The Dissertation Committee for Scott Tyson Matteucci Certifies that this is the approved version of the following dissertation:

Gas Transport Properties of Reverse Selective Nanocomposite Materials

Committee:

Benny D. Freeman, Supervisor

Donald R. Paul

Miguel Jose Yacaman

Charles Mullins

Greg Fleming

Gas Transport Properties of Reverse Selective Nanocomposite Materials

by

Scott Tyson Matteucci, B.S.E.

Dissertation

Presented to the Faculty of the Graduate School of
The University of Texas at Austin
in Partial Fulfillment
of the Requirements
for the Degree of

Doctor of Philosophy

The University of Texas at Austin
December 2007

Dedication

To my family

Acknowledgements

I would like express my appreciation to my advisor, Dr. Benny D. Freeman, for his guidance and support. I would also like to thank my committee Dr. Donald R. Paul, Dr. Charles Mullins, Dr. Miguel Jose Yacaman, and Dr. Greg Fleming, for providing guidance to my research.

I would like to gratefully acknowledge Sande Storey for her general help and enjoyable banter. Dr. Steve Swinnea for conducting and analyzing the wide angle X-ray diffraction experiments, and Steve Werner of the Dow Chemical Company for teaching me the proper preparation and experimentation techniques for performing atomic force microscopy on nanocomposite cross sections. Steve Sorey conducted the NMR experiments for me. Dr. Yangming Sun performed the XPS experiments, and Pam Cook was always very enthusiastic about editing my manuscripts.

It was a pleasure to work with the former and current students of Dr. Freeman's research group especially Dr. Haiqing Lin and Dr. Rajeev Prabhakar who trained me to use the gas transport equipment in our lab and provided guidance in my research as well in my career as a graduate student. Victor Kusuma has also been very helpful in preparing samples for SEM and AFM experiments as well as obtaining TEM images of my samples. I would also like to thank Roy Raharjo, Dr. Ho Bum Park, Scott Kelman, Keith Ashcraft, Alyson Sagle, Brian McCloskey, Hoa Ju, Yuan-Hsuan Wu, Brandon Rowe, Richard Li, and Elizabeth Van Wagner for their camaraderie.

Finally, I would like to thank my family, especially my wife, for their encouragement and support during the years I have spent conducting research and preparing this report.

Gas Transport Properties of Reverse Selective Nanocomposite Materials

Publication No._____________

Scott Tyson Matteucci, Ph.D.
The University of Texas at Austin, 2007

Supervisor: Benny D. Freeman

The effect of dispersing discreet periclase (magnesium oxide) or brookite (titanium oxide) nanoparticles into poly(1-trimethylsilyl-1-propyne) (*i.e.,* a super glassy polymer) and 1,2-polybutadiene (*i.e.,* a rubbery polymer) has been examined. Particle dispersion has been investigated using atomic force microscopy and transmission electron microscopy to determine particle/aggregate size and distribution. Titanium dioxide nanoparticles dispersed into aggregates on the order of nanometers, as did magnesium oxide in 1,2-polybutadiene. However, the magnesium oxide filled poly(1-trimethylsilyl-1-propyne) did not exhibit nanoparticle aggregates below approximately one micron in characteristic dimensions. Nanocomposite transport properties were studied, where permeability and solubility coefficients were determined for light gases with increasing pressure, and diffusion coefficients were calculated from the solution-diffusion model. The permeability of light gases in the heterogeneous films increased with increasing particle loading. Depending on particle loading, brookite filled nanocomposite light gas permeability increased to over four times that of the unfilled polymer, whereas at high periclase loadings the nanocomposites exhibited light gas permeabilities in excess of an order of magnitude higher than the unfilled materials. Even at these high loadings the light gas selectivities were higher than predicted for films containing transmembrane defects. Solubility was relatively unaffected by the void volume concentration, although it did increase to some extent depending on the nanoparticle concentration. Wide angle X-ray diffraction, nuclear magnetic resonance, and Fourier transform infra-red experiments were used to determine if the nanoparticles remained stable during film preparation. TiO_2 nanoparticles did not appear to react with water, the polymer matrixes or test gases used in this research. However, under certain circumstances, periclase reacted with adventitious water to form brucite. A desilylation reaction occurred when brucite was exposed to polymers or small molecule compounds that contained a trimethylsilyl group attached to a conjugated organic backbone. This reaction caused certain disubstituted polyacetylenes to become insoluble in common organic solvents.

Table of Contents

List of Figures

List of Tables

List of Schemes

Chapter 1: Introduction

POLYMER MEMBRANE TECHNOLOGY

Carbon dioxide is believed to be a major component of the greenhouse effect, and its disposal in the atmosphere has raised great international concern.[1,2] Economic CO_2 capture from natural gas,[3-6] industrial flue gases,[7] and steam-reformed H_2[8-11] are necessary to make fossil fuels more efficient and sustainable energy sources.[3,7,12]

There are many shortcomings with current acid gas (*i.e.*, CO_2) removal technologies. Amine scrubbing columns (ASC), physical solvent processes (PSP), and pressure-swing adsorption (PSA) are generally used to remove acid gases from valuable product gas streams.[8,13] Each of these technologies has significant drawbacks, such as high capital cost, complexity of operation, and large space requirements.[8,13] ASC and PSP use solvents which must be regenerated by heat or pressure, thus increasing process complexity.[8] ASC solvents include monoethanolamine, diethanolamine, and methyldiethanolanime, all of which are corrosive, environmentally hazardous, and subject to chemical degradation.[14]

Membranes may represent a viable alternative method for removing acid gases from non-polar gases. Many of the difficulties associated with conventional acid gas separation techniques do not affect membranes. Membranes have a small footprint, low capital cost, are easy to install and operate, and have little environmental impact.[8] Polymeric membranes are used for CO_2/CH_4 separations and could be used for removal of CO_2 from flue gases, and from high pressure H_2 streams.[2,3,9,12] However, the current use of polymer membranes in industry is often limited by their permeability and selectivity.

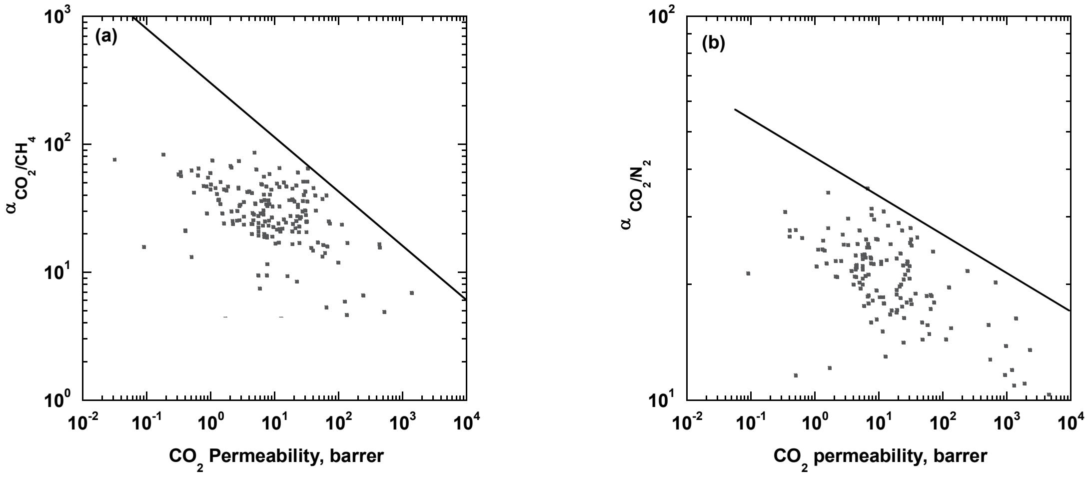

Figure 1.1. Trade off plot for pure gas CO_2 permeability and pure gas (a) CO_2/CH_4 selectivity and (b) CO_2/N_2 selectivity for polymers reported in literature (■). Solid line indicates predicted maximum for CO_2 permeability *vs.* CO_2/light gas selectivity as predicted by Freeman's method (*i.e.,* Eq. (1.1)).[15,16]

Membranes exhibit certain performance limitations that have restricted their acceptance for CO_2 separations.[3,12,15,16] Polymer membranes have a theoretical limit to the purity of gas that may be produced at a given productivity. The relationship between the trade off between these two parameters can be calculated as:[16]

$$\alpha_{A/B} = \beta_{A/B} \Big/ P_A^{\lambda_{A/B}} \tag{1.1}$$

where $\lambda_{A/B}$ is a relationship between penetrant gas kinetic diameters, and $\beta_{A/B}$ is a relationship between the solubility of penetrant gases in the polymer matrix.[15] P_A (*i.e.,* permeability of gas A) is the pressure and thickness normalized flux of gas A in a polymer matrix, and $\alpha_{A/B}$ is the ideal selectivity. Both permeability and selectivity are defined in Chapter 2. The so-called "trade-off" limit is shown in Figure 1.1 for CO_2/CH_4 and CO_2/N_2 and are compared to experimental results for a number of polymers taken from the literature.[15,16]

HETEROGENEOUS MIXED MATRIX MEMBRANES

The increasing variety of available nanoparticles provides new opportunities to prepare and study polymer-based heterogeneous materials. In such heterogeneous materials, as particle size approaches a few nanometers, the interparticle spacing, d_i, can be on the order of nanometers even at low nanoparticle loadings. For example, Figure 1.2 presents the influence of particle loading on interparticle spacing for addition of 3 nm and 10 nm diameter spherical particles or aggregates to a matrix in which the particles are arranged in a body centered cubic structure. The interparticle spacing, d_a, was estimated as follows:

$$d_a = \left(\frac{\pi d_p^3}{6\phi_F} \right)^{\frac{1}{3}} - d_p \tag{1.2}$$

where d_p is the nanoparticle diameter (nm), and ϕ_F is the nanoparticle volume fraction in the composite. These interparticle spacings are much smaller than the persistence length of many polymers[17,18] and approach, at higher loadings, the size of gas molecules of interest.

Recent studies of nanocomposites have included doping polymers with nano-scale metals, fumed silica, nanoclays or other additives.[19-22] For example, oriented nanoparticle vermiculite flakes, where the particles were 1 to 2 nm thick and 200 to 400 nm in length, decrease gas permeability to less than 10 percent of that of the unfilled polymer.[20,22] In another example, the addition of ~27 volume percent trimethylsilylglucose (TMSG), which has characteristic dimensions of 1 nm, to poly(1-trimethylsilyl-1-propyne) (PTMSP) reduced N_2 and CH_4 permeabilities to less than 1 percent of the unfilled PTMSP permeabilities.[23]

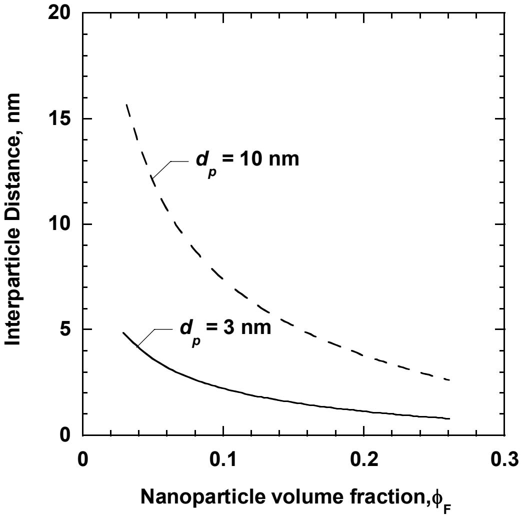

Figure 1.2. Estimated interparticle spacing, d_i, as a function of nanoparticle loading. Interparticle spacing was calculated using Eq. (1.2). The dashed and solid lines represent the interparticle spacing at nanoparticle diameters, d_p, of 10 and 3 nm

In contrast to results in which the introduction of impermeable particles into polymers decrease permeability, dispersing fumed silica (FS) in high free volume, stiff chain, glassy polymers (*e.g.,* PTMSP, poly(2,2-bis(trifluoromethyl)-4,5-difluoro-1,3-dioxole-*co*-tetrafluoroethylene) (AF2400), and poly(4-methyl-2-pentyne) (PMP)) actually increased gas and vapor permeability coefficients.[24-26] Furthermore, in PMP, *n*-butane/CH_4 mixed gas selectivity also increased as FS content increased.[24,25] Dispersion of FS in PTMSP, AF2400, and PMP increased both fractional free volume and gas diffusion coefficients.[24,25] Hill proposed a theoretical model suggesting that the free volume increase occurs primarily in a depletion layer at the polymer-FS interface.[27]

GOALS AND ORGANIZATION OF THE DISSERTATION

In many industrial applications membranes are not competitive with traditional separation technologies due to their low flux and/or purification capabilities. Much effort has already been exerted to improve polymer size-sieving ability or solubility selectivity, with mixed results.[28-30] Mixed-matrix polymer based materials may possibly be used to improve membrane light gas permeability and/or selectivity performance beyond the upper bound. Inorganic zeolites have been incorporated into polymeric materials in order to alter the composites size-sieving capability.[31] Fumed silica has also been widely used to increase permeability in polymeric matrixes by increasing the nanocomposite free volume.[21,24] This dissertation discusses the incorporation of nanoparticles whose surface chemistry may interact with CO_2 in such a way as to increase CO_2 solubility in the nanocomposite. The goal of this research is to increase CO_2 permeability by increasing CO_2 diffusion coefficients and solubility in the resulting mixed matrix material.

This dissertation is divided into 9 chapters including the introduction chapter. Chapter 2 presents background information that is related to gas transport in dense polymer films, modeling gas transport in heterogeneous films, and a discussion of particle selection. Magnesium oxide (MgO) nanoparticles were selected as a promising CO_2-philic material after surveying commercially available nanoparticles and the literature regarding CO_2 interactions with various metal and metal oxide surfaces. This material was selected because of its ability to physisorb CO_2, which allows the gas to sorb and desorb at temperatures and pressures that are relevant to our research. TiO_2 nanoparticles have been incorporated into polymers as a comparison to the CO_2-philic MgO particles, since the TiO_2 particles do not necessarily interact with CO_2. Chapter 3 discusses the materials and experimental techniques that were employed in this research.

The remaining chapters discuss the effects of incorporating nanoparticles into various polymer matrixes. Chapters 4 and 5 investigates nanoparticle dispersion and gas transport properties in poly(1-trimethylsilyl-1-propyne) filled with TiO_2 or MgO nanoparticles, respectively. Chapter 6 discusses a reaction that occurs when MgO is dispersed in a select group of disubstituted polyacetylenes. Chapters 7 and 8 pertain to the incorporation of TiO_2 or MgO nanoparticles into 1,2-polybutadiene. These chapters discuss particle dispersion and gas transport properties in terms of permeability, solubility and diffusion coefficients. Chapters 7 and 8 also discuss the effect dispersed nanoparticles have on the T_g and crystallinity of semi-crystalline 1,2-polybutadiene. Chapter 9 presents conclusions and recommendations for continued work in nanocomposite materials.

REFERENCES

(1) Houghton, J. T. Climate Change 2001: The Scientific Basis; Cambridge University Press: Cambridge, 2001.

(2) Stewart, C.; Hessami, M.-A., A study of methods of carbon dioxide capture and sequestration--The sustainability of a photosynthetic bioreactor approach, *Energy Conversion and Management* **2005**, *46*, 403-420.

(3) Baker, R. W., Future directions of membrane gas separation technology, *Industrial and Engineering Chemistry Research* **2002**, *41*, 1393-1411.

(4) Wind, J. D.; Paul, D. R.; Koros, W. J., Natural gas permeation in polyimide membranes, *Journal of Membrane Science* **2004**, *228*, 227-236.

(5) Henis, J. M. S. *Commercial and practical aspects of gas separation membranes*, In Polymeric Gas Separation Membranes; Yampolskii, Y. P., Ed.; CRC Press: Boca Raton, 1994; pp 441-512.

(6) Minhas, B. S.; Matsura, T.; Sourirajan, S., Formation of asymmetric cellulose acetate membranes for the separation of carbon dioxide-methane gas mixtures, *Industrial and Engineering Chemistry Research* **1987**, *26*, 2344-2348.

(7) Litynski, J. T.; Klara, S. M.; McIlvried, H. G.; Srivastava, R. D., An overview of terrestrial sequestration of carbon dioxide: The United States Department of Energy's Fossil Energy R&D Program, *Climatic Change* **2006**, *74*, 81-95.

(8) Kohl, A.; Nielsen, R. Gas Purification, 5th ed.; Gulf Publishing Company: Houston, 1997.

(9) Lin, H.; van Wagner, E.; Freeman, B. D.; Toy, L. G.; Gupta, R. P., Plasticization-enhanced hydrogen purification using polymeric membranes, *Science* **2006**, *311*, 639-642.

(10) Berchtold, K. A.; Young, J. S.; Dudeck, K. W.; Acquaviva, J.; Onorato, F.; Hopkins, S. D. In *Fifth Annual Conference on Carbon Capture & Sequestration*: Alexandria, VA, 2006.

(11) Joensen, F.; Rostrup-Nielsen, J. R., Conversion of hydrocarbons and alcohols for fuel cells, *Journal of Power Sources* **2002**, *105*, 195-201.

(12) Powell, C. E.; Qiao, G. G., Polymeric CO_2/N_2 gas separation membranes for the capture of carbon dioxide from power plant flue gases, *Journal of Membrane Science* **2006**, *279*, 1-49.

(13) Yang, J.; Lee, C.-H., Adsorption dynamics of a layered bed PSA for H_2 recovery from coke oven gas, *AIChE Journal* **1998**, *44*, 1325-1334.

(14) Richards, R. M.; Volodin, A. M.; Bedilo, A. F.; Klabunde, K. J., ESR study of nanocrystalline aerogel-prepared magnesium oxide, *Physical Chemistry Chemical Physics* **2003**, *5*, 4299-4305.

(15) Freeman, B. D., Basis of permeability/selectivity tradeoff relations in polymeric gas separation membranes, *Macromolecules* **1999**, *32*, 375-380.

(16) Robeson, L. M., Correlation of separation factor versus permeability for polymeric membranes, *Journal of Membrane Science* **1991**, *62*, 165-185.

(17) Pavlov, G. M.; Zaitseva, I. I.; Michailova, N. A.; Rjumtsev, E. I., Molecular characteristic of poly(1-trimethylsilyl-1-propyne) in dilute solutions, *Polymer* **2004**, *45*, 1159-1166.

(18) Mourey, T.; Le, K.; Bryan, T.; Zheng, S.; Bennett, G., Determing persistence length by size-exclusion chromotography, *Polymer* **2005**, *46*, 9033-9042.

(19) Barsema, J. N.; Balster, J.; Jordan, V.; van der Vegt, N. F. A.; Wessling, M., Functionalized carbon molecular sieve membranes containing Ag-nanoclusters, *Journal of Membrane Science* **2003**, *219*, 47-57.

(20) Lape, N. K.; Nuxoll, E. E.; Cussler, E. L., Polydisperse flakes in barrier films, *Journal of Membrane Science* **2004**, *236*, 29-37.

(21) He, Z.; Pinnau, I.; Morisato, A., Nanostructured poly(4-methyl-2-pentyne)/silica hybrid membranes for gas separation, *Desalination* **2002**, *146*, 11-15.

(22) Takahashi, S.; Goldberg, H. A.; Feeney, C. A.; Karim, D. P.; Farrell, M.; O'Leary, K.; Paul, D. R., Gas barrier properties of butyl rubber/vermiculite nanocomposite coatings, *Polymer* **2006**, *47*, 3083-3093.

(23) Qiu, J.; Zheng, J.-M.; Peinemann, K.-V., Gas transport properties in a novel poly(trimethylsilylpropyne) composite membrane with nanosized organic filler trimethylsilylglucose, *Macromolecules* **2006**, *39*, 4093-4100.

(24) Merkel, T. C.; Freeman, B. D.; Spontak, R. J.; He, Z.; Pinnau, I.; Meakin, P.; Hill, A. J., Ultrapermeable, reverse-selective nanocomposite membranes, *Science* **2002**, *296*, 519-522.

(25) Merkel, T. C.; Freeman, B. D.; Spontak, R. J.; He, Z.; Pinnau, I.; Meakin, P.; Hill, A. J., Sorption, transport, and structural evidence for enhanced free volume in poly(4-methyl-2-pentyne)/fumed silica nanocomposite membranes, *Chemistry of Materials* **2003**, *15*, 109-123.

(26) Merkel, T. C.; He, Z.; Pinnau, I.; Freeman, B. D.; Meakin, P.; Hill, A. J., Sorption and transport in poly(2,2-bis(trifluoromethyl)-4,5-difluoro-1,3-dioxole-*co*-tetrafluoroethylene) containing nanoscale fumed silica, *Macromolecules* **2003**, *36*, 8406-8414.

(27) Hill, R. J., Diffusive permeability and selectivity of nanocomposite membranes, *Industrial and Engineering Chemistry Research* **2006**, *45*, 6890-6898.

(28) Paul, D. R.; Yampol'skii, Y. P. *Introduction and Perspective*, In Polymeric Gas Separation Membranes; Yampolskii, Y. P., Ed.; CRC Press: Boca Raton, 1994; pp 1-81.

(29) Lin, H.; Freeman, B. D., Gas solubility, diffusivity and permeability in poly(ethylene oxide), *Journal of Membrane Science* **2004**, *239*, 105-117.

(30) Lin, H.; Freeman, B. D., Gas and vapor solubility in cross-linked poly(ethylene glycol diacrylate), *Macromolecules* **2005**, *38*, 8394-8407.

(31) Zimmerman, C. M.; Singh, A.; Koros, W. J., Tailoring mixed matrix composite membranes for gas separations, *Journal of Membrane Science* **1997**, *137*, 145-154.

Chapter 2: Background

GAS TRANSPORT

Empirical observations of the pressure and thickness dependence of the steady-state gas permeation rate or flux, N, led von Wroblewski [1] to propose the following relation:

$$N = P(\Delta p / l) \tag{2.1}$$

where Δp is the pressure difference across the membrane, and l is its thickness. The proportionality coefficient in this equation, P, was defined as the permeability coefficient. While permeability defines gas transport as an intrinsic physical property for a given polymer/gas pair, this expression does not reveal the molecular basis of permeation.

A more fundamental basis for permeation may be derived by considering a plane polymer film of thickness l separating two regions filled with a single gas. The gas pressure on the upstream (or high pressure) side of the film is p_2, and the gas pressure on the downstream (or low pressure) side is p_1. At steady state, the gas flux at any point inside the polymer is given by Fick's first law:[2]

$$N = \frac{-D_{loc}}{1-w}\frac{dC}{dx} \tag{2.2}$$

where N is the gas flux relative to fixed coordinates, C is the gas concentration, x is the distance across the film, w is the mass fraction of gas in the polymer, and D_{loc} is the binary mutual diffusion coefficient of the gas in the polymer. Integration across the film (from $x = 0$ to $x = l$) yields:

$$N = \frac{1}{l} \int_{C_1}^{C_2} \frac{D_{loc}}{1-w} dC \tag{2.3}$$

where C_1 and C_2 are the gas concentrations in the polymer at the downstream and upstream faces of the membrane, respectively, which are in equilibrium with the external pressures p_1 and p_2, respectively. This relationship can be written as follows:

$$N = \frac{C_2 - C_1}{l} D \tag{2.4}$$

where D, the average effective diffusion coefficient, is defined as:

$$D = \frac{1}{C_2 - C_1} \int_{C_1}^{C_2} \frac{D_{loc}}{1-w} dC \tag{2.5}$$

With this definition, the permeability of a gas in a polymer, P, can be expressed as:

$$P = \frac{Nl}{p_2 - p_1} = \frac{C_2 - C_1}{p_2 - p_1} D \tag{2.6}$$

Eq. (2.6) is derived for pure-gas permeation. To extend the definition to mixtures, the total pressures p_2 and p_1 should be replaced with the corresponding partial pressures of the component of interest on the upstream and downstream sides of the membrane, respectively. To account for effects of gas phase nonidealities on the driving force for permeation, the pressures (or partial pressures, in the case of mixtures) are typically replaced by fugacities in situations where there is substantial departure from ideal gas behavior (*e.g.*, with high pressure CO_2 feed streams).[3]

When the upstream pressure and concentration (p_2 and C_2, respectively) are much greater than their downstream analogs, this result simplifies as follows:

$$P = \frac{C_2}{p_2} D \tag{2.7}$$

The equilibrium solubility coefficient of a gas in a polymer is the ratio of the concentration of gas dissolved in the polymer at equilibrium to the pressure of gas (or partial pressure in the case of mixtures) in the contiguous gas phase:[2]

$$S = C/p \tag{2.8}$$

When this result is applied to Eq. (2.7), one obtains:

$$P = DS \tag{2.9}$$

where the solubility coefficient, S, is evaluated at the upstream face of the membrane (*i.e.,* $S = C_2/p_2$). From this result, P depends upon two factors: (1) a thermodynamic term, S, characterizing the number of gas molecules sorbed into and onto the polymer and (2) a kinetic or mobility term, D, characterizing the mobility of gas molecules as they diffuse through the polymer. In other words, permeability, which is the pressure- and thickness-normalized gas flux through the polymer film (*cf.,* Eq. (2.1)), depends upon the product of the number of gas molecules that dissolve in the polymer and the speed with which they migrate through the polymer matrix. Eq. (2.9) emphasizes that high permeability coefficients can result from large D values, large S values, or both. For example, some so-called "fast" (*i.e.*, high permeability) gases display (i) large diffusion coefficients (*e.g.*, He or H_2), (ii) high solubility coefficients (*e.g.*, CO_2) or (iii) both (*e.g.*, H_2O).

In the SI system, permeability coefficients are expressed in the following units:

$$P = \text{mol/(m s Pa)} \tag{2.10}$$

However, a more widely used and accepted unit for P is:

$$1 \text{ barrer} = 10^{-10} \text{ cm}^3\text{(STP)cm/(cm}^2 \text{ s (cm Hg))} \quad (2.11)$$

Permeability coefficients of common gases in polymers span over a range of more than seven orders of magnitude, from 10^{-3} to 10^{4} barrer or more.

Another key characteristic of gas separation membranes is their selectivity. The ideal selectivity is defined as follows:[2]

$$\alpha_{A/B} = P_A/P_B \quad (2.12)$$

where P_A and P_B are the permeability coefficients of gases A and B, respectively. Commonly, the more permeable gas is taken as A, so that $\alpha_{A/B} > 1$. Bearing in mind Eq. (2.9), the ideal selectivity can be partitioned into diffusivity and solubility selectivity as follows:

$$\alpha_{A/B} = (D_A/D_B)\,(S_A/S_B) = \alpha^D_{A/B}\,\alpha^S_{A/B} \quad (2.13)$$

where S_i and D_i are the solubility and diffusion coefficients of species i, respectively. The independent analysis of $\alpha^D_{A/B}$ and $\alpha^S_{A/B}$ is very helpful in rationalizing gas separation properties in polymers.

PARTICLE LOADING

Often nanoparticles (*i.e.,* filler) and polymer mix in a manner that does not usually obey volume additivity, so the following discussion provides the framework to characterize departures from volume additivity. The filler volume fraction is the volume of filler, V_F, divided by the total volume of the composite sample, V_T. V_T may be written as follows:

$$V_T = V_P + V_F + V_V \tag{2.14}$$

where V_P and V_F are the contributions of the polymer and filler, respectively, to the total nanocomposite volume. These contributions are defined as follows:

$$V_P = \frac{M_P}{\rho_P} \tag{2.15}$$

$$V_F = \frac{M_F}{\rho_F} \tag{2.16}$$

where M_P and ρ_P are the mass and density of the pure polymer, respectively. M_F and ρ_F are the mass and density of the pure filler, respectively. The final term in Eq. (2.14), V_V, accounts for any difference between the actual volume of the nanocomposite sample, V_T, and the ideal contribution of the polymer and filler to the total composite volume, (*i.e.,* $V_P + V_F$). In this study, the nominal filler volume fraction, ϕ_F^N, is defined as follows:

$$\phi_F^N = \frac{V_F}{V_P + V_F} \tag{2.17}$$

If $V_V = 0$, then the nominal volume fraction of filler will be equal to the true volume fraction of filler, ϕ_F^T, which is V_F / V_T. If V_V is not zero, then ϕ_F^N will be either greater than or less than the true volume fraction of filler, depending on whether V_V is positive or negative. In this regard, ϕ_F^N should be viewed as a parameter characterizing the nanocomposite loading, but it only gives an accurate indication of the actual particle volume fraction when $V_V = 0$ (*i.e.,* when the polymer and particles mix ideally).

Density measurements can be used to estimate the true filler volume fraction. The experimental density, ρ_{Exp}, is given by:

$$\rho_{Exp} = \frac{M_P + M_F}{V_P + V_F + V_V} \tag{2.18}$$

When $V_V = 0$, Eq. (2.18) reduces to the ideal additive density, ρ_{Add}:

$$\rho_{Add} = \frac{M_P + M_F}{V_P + V_F} \tag{2.19}$$

Substituting Eq. (2.17) into Eq. (2.19) yields:

$$\rho_{Add} = \rho_F \phi_F^N + \rho_P \left(1 - \phi_F^N\right) \tag{2.20}$$

Eq. (2.20) defines the ideal additive model for the density of a nanocomposite sample and represents the baseline against which experimental density data will be compared. In a semi-crystalline polymer ρ_{Add} is:

$$\rho_{Add} = \phi_F^N \rho_F + \left(1 - \phi_F^N\right)\left(\phi_C \rho_C + \left(1 - \phi_C\right)\rho_A\right) \tag{2.21}$$

where ρ_C and ρ_A are the densities of crystalline and amorphous polymer, respectively. ϕ_C is the volume fraction of crystalline polymer in the polymer phase. In 1,2-polybutadiene ρ_C is (*i.e.,* 0.963 g/cm^3)^4, and ρ_A is (*i.e.,* 0.889 g/cm^3)^5.

Deviations between experimental and additive densities arise if the polymer or particle volume (or both) in the nanocomposite are different from their ideal values.

Deviations between ideal *(i.e.,* ρ_{Add}) and actual (*i.e.,* ρ_{Exp}) density values can be characterized by defining the "void" volume fraction, ϕ_V, as follows:[6]

$$\phi_V = \frac{V_V}{V_P + V_F + V_V} = 1 - \frac{\rho_{Exp}}{\rho_{Add}} \tag{2.22}$$

ϕ_V may be positive (*i.e.,* the composite is less dense than expected based on the additive model Eq. (2.20) or Eq. (2.21)) or negative (*i.e.,* the composite is more dense than expected based on the additive model). ϕ_V can then be used to estimate the true volume fraction of nanoparticles in the nanocomposite, ϕ_F^T:

$$\phi_F^T = \frac{V_F}{V_P + V_F + V_V} = \phi_F^N \left(1 - \phi_V\right) \tag{2.23}$$

As indicated earlier, this framework is used because the system considered in this study exhibits significant deviations from the ideal additive model (*i.e.,* Eq. (2.20) or Eq. (2.21)). A similar approach is used to describe density of foamed materials.[6]

MODELING GAS TRANSPORT PROPERTIES IN HETEROGENEOUS FILMS

A number of models have been used to describe gas transport behavior in filled polymers.[3,7] One model commonly used to describe gas permeability in heterogeneous materials is Maxwell's model. For heterogeneous materials containing a spherical dispersed phase, Maxwell's model is:[8]

$$P_C = P_M \left(\frac{1 - \phi_F^T}{1 + \dfrac{\phi_F^T}{2}} \right) \tag{2.24}$$

where P_C, and P_M are the permeabilities of the composite and the polymer matrix, respectively. Eq. (2.24) has been used to describe permeability behavior in heterogeneous films containing impermeable, spherical particles, and an example is presented in Figure 2.1.[9-12] Maxwell's model and other similar models predict a decrease in permeability as concentration of the impermeable phase increases.[8,13]

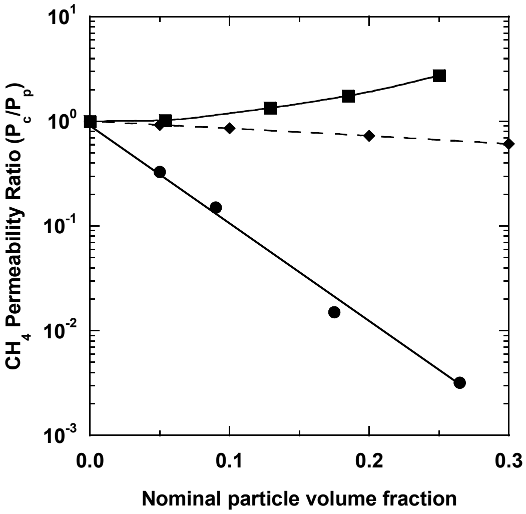

Figure 2.1. Relative CH_4 permeability (P_C/P_P) for PTMSP filled with fumed silica nanoparticles at 25 °C [12] (■), PTMSP filled with trimethylsilylglucose at 30 °C[10] (●), and natural rubber filled with micron-sized ZnO particles at 40 °C (♦).[7] The solid lines are provided to guide the eye. The dashed line was calculated using Maxwell's model, Eq. (2.24).

Maxwell's prediction was derived for a dilute suspension of particles in a matrix, and this model becomes increasingly less accurate as the concentration of the dispersed phase increases.[7] Bruggeman's model was developed to account for streamlines that develop within heterogeneous materials at high particle loadings, and is expressed as:[7,8,13]

$$\frac{\left({}^{P_C}\!/\!_{P_M}\right)-\left({}^{P_D}\!/\!_{P_M}\right)}{1-\left({}^{P_D}\!/\!_{P_M}\right)}\left(\frac{P_C}{P_M}\right)^{-\frac{1}{3}}=1-\phi_D \tag{2.25}$$

where P_C, P_M, and P_D are the permeabilities of the composite, polymer matrix, and dispersed phase, respectively. ϕ_D is the dispersed phase volume percent. Bruggeman's model predicts a minimum permeability in heterogeneous films when P_D is much less than P_M (*i.e.,* when the dispersed phase is impermeable):[13]

$$\frac{P_C}{P_M}=\left(1-\phi_D\right)^{3/2} \tag{2.26}$$

The model also predicts a maximum permeability when P_D is much greater than P_M (*i.e.,* when the dispersed phase is comprised of voids):[13]

$$\frac{P_C}{P_M}=\frac{1}{\left(1-\phi_D\right)^3} \tag{2.27}$$

These limits correlate well with experimental data, as presented in Figure 2.2.[7,14]

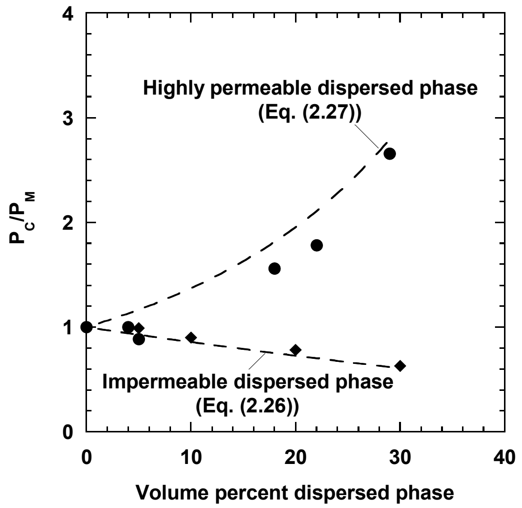

Figure 2.2. Bruggeman's prediction for the ratio of the composite permeability, P_C, and the matrix permeability, P_M, as calculated from Eq. (2.26) and Eq. (2.27) at increasing dispersed phase volume percent, compared to experimental data. Micron-sized ZnO filled natural rubber[7] (♦) represents heterogeneous materials where the dispersed phase (ZnO) has permeability much lower than the matrix, and MgO filled PTMSP (●) represents heterogeneous materials where the dispersed phase (*i.e.*, void space) has permeability much higher than the matrix.

GAS ADSORBING METALS AND METAL OXIDES

Many metals and metal oxides adsorb certain permanent gases more favorably than others.[15-17] For instance, both clean iron and silver readily adsorb atmospheric oxygen without adsorbing other light gases.[15,16] Gases adsorb onto metals and metal oxides by a variety of mechanisms depending on system chemistry (*e.g.,* acid-base interactions, gas dissociation, *etc.*),[18-22] overall system conditions (*e.g.,* temperature, pressure),[20,22] and surface defects[23] of the metal or metal oxides.

Since CO_2 is an acid gas, basic particles readily adsorb CO_2. For example, MgO adsorbs 10 wt. % CO_2 at ambient temperature and 20 Torr CO_2 after 15 minutes,[24] and CaO adsorbs 3.5 wt. % CO_2 at ambient temperature and 10 Torr CO_2.[25] In basic metal oxides, the oxygen atom withdraws electrons from the metal, causing the oxygen to behave as an electron-rich Lewis base and the metal to act as a Lewis acid.[26] The oxygen atoms of metal oxides interact with CO_2.[27] Basic metal oxides can adsorb CO_2 preferentially *vs*. light gases.[18,28]

There are substantial differences in the interactions of metal oxides with CO_2. At ambient temperatures, MgO physisorbs[26] or weakly chemisorbs CO_2,[29] whereas the heavier alkaline earth oxides tend to chemisorb CO_2.[18,19] The binding energy of CO_2 to metal oxides is due to the basicity of the alkaline earth oxides, [20] which increases with the period of the metal (*i.e.*, MgO is less basic than CaO, SrO is less basic than BaO, *etc.*).[18,19] Many rare earth metal oxides (*e.g.,* La_2O_3 and ThO_2) act as bases.[20] Rare earth oxides have a stronger binding energy and adsorb higher concentrations of CO_2 than alkaline earth oxides.[20,21] An ideal CO_2 adsorbing nanoparticle candidate would have a high CO_2 uptake while still being able to desorb CO_2.

Many inorganic materials catalyze reactions (*e.g.*, decomposition of CO_2 to CO on Fe_2O_3),[16] and such reactions could have deleterious effects if they were operative in separation membranes. In many systems, CO_2 and H_2 form CH_4, methanol or alkanes depending on the catalyst (*e.g.*, Ni, Ru, Cu).[30,31] The alkaline earth oxides react with water, which, in a subsequent reaction, can form metal carbonates.[32,33] Since CO is toxic and a poison for fuel cells, metals allowing decomposition of CO_2 to CO should not be used. Hydrogenation of CO_2 reverses the steam reforming reaction, which would reduce the overall efficiency of H_2 synthesis. Although water will be present in the H_2 product stream after steam reforming, flue gases, and natural gas streams, carbonation is an acceptable side reaction since it does not produce harmful byproducts. Possible reactions involving basic nanoparticles should not influence the chemical composition of gases permeating through the membrane.

MgO fits the criteria outlined above for CO_2 adsorbing materials, and it has other desirable attributes as well. CO_2 should readily desorb from MgO at 35 ^{o}C.[34] MgO nanoparticles are commercially available in particle diameters in the size range of interest (*i.e.,* 3 nm). Since gas adsorption cannot occur on defect-free, crystalline MgO surfaces,[35] ideal nanoparticles should offer a combination of high surface area and a large number of defect sites per unit area. Aerogel MgO has surface defects (*e.g.,* steps in the crystal, oxygen vacancies, *etc.*)[27] which permit gas adsorption.[27] These particles are spherical, which results in a large percentage of surface sites being defects.[25] Therefore, MgO nanoparticles will be used as the basic filler in this project.

Brookite nanoparticles are available with approximately the same primary particle diameter as MgO (*i.e.,* 3 nm). TiO_2 nanoparticles do not demonstrate any specific interaction with CO_2. TiO_2 particles are used as a neutral nanoparticle surface for comparison with the basic MgO surface chemistry.

REFERENCES

(1) von Wroblewski, S., Ueber die natur der absorption der gase durch flussigkeiten unter hohen drucken, *Ann Physik u Chem* **1879**, *8*, 29-52.

(2) Ghosal, K.; Freeman, B. D., Gas separation using polymer membranes: An overview., *Polymers for Advanced Technology* **1994**, *5*, 673-697.

(3) Petropoulos, J. H. *Mechanisms and theories for sorption and diffusion of gases in polymers*, In Polymeric Gas Separation Membranes; Yampol'skii, Y. P., Ed.; CRC Press, Inc.: Boca Raton, 1994; pp 17-82.

(4) Natta, G.; Corradini, P., The structure of crystalline 1,2-polybutadiene and of other "syndiotactic polymers", *Journal of Polymer Science* **1956**, *20*, 251-266.

(5) Obata, Y.; Tosaki, C.; Ikeyama, M., Bulk properties of syndiotactic 1,2-polybutadiene. I. Thermal and viscoelastic properties, *Polymer Journal* **1975**, *7*, 207-216.

(6) Shutov, F. A. *Cellular structures and properties of foamed polymers*, In Handbook of Polymeric Foams and Foam Technology; Frisch, K. C., Ed.; Hanser Publishers: New York, 1991; pp 17-46.

(7) Barrer, R. M.; Barrie, J. A.; Rogers, M. G., Heterogeneous membranes: Diffusion in filled rubber, *Journal of Polymer Science, Part A: Polymer Chemistry* **1963**, *1*, 2565-2586.

(8) Vu, D. Q.; Koros, W. J.; Miller, S. J., Mixed matrix membranes using carbon molecular sieves II. Modeling permeation behavior, *Journal of Membrane Science* **2003**, *211*, 335-348.

(9) Vu, D. Q.; Koros, W. J.; Miller, S. J., Mixed matrix membranes using carbon molecular sieves I. Preparation and experimental results, *Journal of Membrane Science* **2003**, *211*, 311-334.

(10) Qiu, J.; Zheng, J.-M.; Peinemann, K.-V., Gas transport properties in a novel poly(trimethylsilylpropyne) composite membrane with nanosized organic filler trimethylsilylglucose, *Macromolecules* **2006**, *39*, 4093-4100.

(11) Merkel, T. C.; Freeman, B. D.; Spontak, R. J.; He, Z.; Pinnau, I.; Meakin, P.; Hill, A. J., Ultrapermeable, reverse-selective nanocomposite membranes, *Science* **2002**, *296*, 519-522.

(12) Merkel, T. C.; He, Z.; Pinnau, I.; Freeman, B. D.; Hill, A. J.; Meakin, P., Effect of nanoparticles on gas sorption and transport in poly(1-trimethylsilyl-1-propyne), *Macromolecules* **2003**, *36*, 6845-6855.

(13) Bouma, R. H. B.; Checchetti, A.; Chidichimo, G.; Drioli, E., Permeation through a heterogeneous membrane: The effect of the dispersed phase, *Journal of Membrane Science* **1997**, *128*, 141-149.

(14) Matteucci, S. T.; Kusuma, V.; Sanders, D.; Swinnea, S.; Freeman, B. D., Gas transport in TiO_2 nanoparticle filled poly(1-trimethylsilyl-1-propyne), *Journal or Membrane Science*, **2007**.

(15) Backx, C.; De Groot, C. P. M.; Biloen; Sachtler, W. M. H., Interaction of O_2, CO_2, CO, C_2H_4, and C_2H_4O with Ag(100), *Surface Science* **1983**, *128*, 81-103.

(16) Erdohelyi, A.; Anneser, E.; Bauer, T.; Stephan, K.; Borgmann, D.; Wedler, G., Interaction of carbon dioxide and oxygen on iron films at 273 K, *Surface Science* **1990**, 57-66.

(17) Rollason, R. J.; Plane, J. M. C., A kinetic study of the reactions of MgO with H_2O, CO_2, and O_2: Implications for magnesium chemistry in the mesosphere, *Physical Chemistry Chemical Physics* **2001**, *3*, 4733-4740.

(18) Zecchina, A.; Lofthouse, M. G.; Stone, F. S., Reflectance spectra of surface states in magnesium oxide and calcium oxide, *Journal of the Chemical Society, Faraday Transactions 1: Physical Chemistry in Condensed Phases* **1975**, *71*, 1476-1490.

(19) Zecchina, A.; Stone, F. S., Reflectance spectra of surface states in strontium oxide and barium oxide, *Journal of the Chemical Society, Faraday Transactions 1: Physical Chemistry in Condensed Phases* **1976**, *72*, 2364-2374.

(20) Auroux, A.; Gervasini, A., Macrocalorimetric study of the acidity and basicitiy of metal oxide surfaces, *Journal of Physical Chemistry* **1990**, *94*, 6371-6379.

(21) Freund, H.-J.; Roberts, M. W., Surface chemistry of carbon dioxide, *Surface Science Reports* **1996**, *25*, 225-273.

(22) Horiuchi, T.; Hiroaki, H.; Takehisa, F.; Kubo, Y.; Horio, M.; Suzuki, K.; Mori, T., Effect of added basic metal oxides on CO_2 adsorption on alumnia at elevated temperatures, *Applied Catalysis A: General* **1998**, *167*, 195-202.

(23) Ferrari, A. M.; Soave, R.; D'Ercole, A.; Pisani, C.; Giamello, E.; Pacchioni, G., Theoretical characterization of charge-transfer reactions between N_2 and O_2 molecules and paramagnetic oxygen vacancies on the MgO surface, *Surface Science* **2001**, 83-97.

(24) Stark, J. V.; Park, D. G.; Lagadic, I.; Klabunde, K. J., Nanoscale metal oxide particles/clusters as chemical reagents. Unique surface chemistry on magnesium oxide as shown by enhanced adsorption of acid gases (sulfur dioxide and carbon dioxide) and pressure dependence, *Chemistry of Materials* **1996**, *8*, 1904-1912.

(25) Koper, O. B.; Lagadic, I.; Volodin, A. M.; Klabunde, K. J., Alkaline-earth oxide nanoparticles obtained by aerogel methods. Characterization and rational for unexpectedly high surface chemical reactivities, *Chemistry of Materials* **1997**, *9*, 2468-2480.

(26) Meixner, D. L.; Arthur, D. A.; George, S. M., Kinetics of desorption, adsorption, and surface diffusion of CO_2 on MgO(100), *Surface Science* **1992**, *261*, 141-154.

(27) Pacchioni, G., Physisorbed and chemisorbed CO_2 at surface and step sites of MgO(100) surface, *Surface Science* **1993**, *281*, 207-219.

(28) Coluccia, S.; Boccuzzi, F.; Ghiotti, G.; Morterra, C., Infrared study of hydrogen adsorption on MgO, CaO, and SrO, *Journal of the Chemical Society, Faraday Transactions 1: Physical Chemistry in Condensed Phases* **1982**, *78*, 2111-2119.

(29) Pacchioni, G.; Ricart, J. M.; Illas, F., Ab initio cluster model calculations of chemisorption of CO_2 and SO_2 probe molecules on MgO and CaO (100) surfaces. A theorhetical measure of oxide basicity, *Journal of the American Chemical Society* **1994**, *116*, 10152-10158.

(30) Rasmussen, P. B.; Kazuta, M.; Chorkendorff, I., Synthesis of methanol from a mixture of H_2 and CO_2 on Cu (100), *Surface Science* **1994**, *318*, 267-280.

(31) Fujita, S.-I.; Takezawa, N., Difference in the selectivity of CO and CO_2 methanation reactions, *Chemical Engineering Journal* **1997**, *68*, 63-68.

(32) Yu, Y.; Guo, Q.; Liu, S.; Wang, E., Partial dissociation of water on a MgO(100) film, *Physical Review B* **2003**, *68*, 1-4.

(33) Beruto, D. T.; Botter, R., Liquid-like H_2O adsorption layers to catalyze the $Ca(OH)_2/CO_2$ solid-gas reaction and to form a non-protective solid product layer at 20°C, *Journal of the European Ceramic Society* **2000**, *20*, 497-503.

(34) Xu, M.; Iglesia, E., Readsorption and adsorption-assisted desorption of CO_2 on basic solids, *Journal of Physical Chemistry Pary B* **1998**, *102*, 961-966.

(35) Onishi, H.; Egawa, C.; Aruga, T.; Iwasawa, Y., Adsorption of Sodium Atoms and Oxygen-containing Molecules on Magnesia(100) and (111) Surfaces, *Surface Science* **1987**, *191*, 479.

Chapter 3: Materials and Experimental Procedures

MATERIALS

Nanoparticles: MgO Plus (Nanoscale, Manhattan, KS) was used in this study. According to the supplier, these MgO nanoparticles have a specific gravity of 3.58 g/cm^3 and a BET surface area between 600 and 680 m^2/g. The resulting average equivalent spherical particle diameter is 2.6 nm, where equivalent spherical particle diameter is defined as 6/(surface area x density). Samples are reported to be spherical, and the metal composition is 99.2% pure Mg, with the remainder being trace impurities. Such MgO aerogels readily deagglomerate in organic solvents such as toluene.[1]

Spherical brookite (*i.e.,* amorphous TiO_2) nanoparticles (Nanoscale, Manhattan, KS) were used throughout this study. According to the supplier, the nanoparticles are 99.999 % titanium, based on metal, with a density of 3.7 g/cm^3 and a BET surface area of 500 m^2/g. The equivalent spherical particle diameter is 3 nm.

Polymers: Poly(1-trimethylsilyl-1-propyne) was kindly supplied by Air Products and Chemicals, Inc. (Allentown, PA) and poly(1-phenyl-2-[*p*-(trimethylsilyl)phenyl]acetylene) was prepared as described elsewhere.[2] Both polymers were high molar mass materials that readily form films from solution in toluene.

1,2-polybutadiene (Scientific Polymer Products, Inc. Ontario, NY) has an approximate molecular weight of 100,000 and was prepared using a cobalt-phosphine catalyst system. The 1,4 *cis* content was 7 percent, with the vinyl structure comprising the remaining 93 percent. The structure of the polymers used in this research as well as polymers discussed in this document are list in Table 3.1

Table 3.1 Structures of polymers

poly(1-trimethylsilyl-1-propyne) [PTMSP]	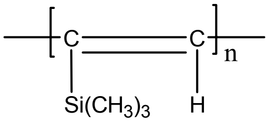 $-[\mathrm{C}(\mathrm{Si(CH_3)_3})=\mathrm{C}(\mathrm{H})]_n-$
poly(1-phenyl-2-[(p-trimethylsilyl)phenyl]acetylene) (PTMSDPA)	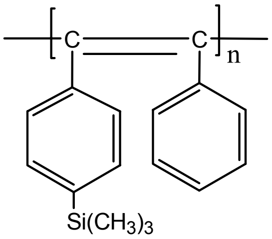
poly(4-methyl-2-pentyne) (PMP)	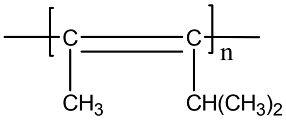 $-[\mathrm{C}(\mathrm{CH_3})=\mathrm{C}(\mathrm{CH(CH_3)_2})]_n-$
poly(methylacetylene)	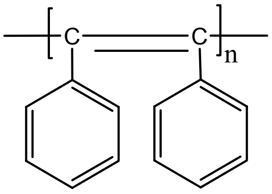
poly(diphenylacetylene) (PDPA)	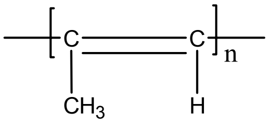 $-[\mathrm{C}(\mathrm{CH_3})=\mathrm{C}(\mathrm{H})]_n-$
1,2-polybutadiene	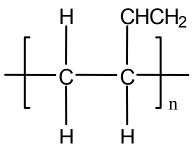 $-[\mathrm{CH_2}-\mathrm{CH}(\mathrm{CHCH_2})]_n-$

SAMPLE PREPARATION

PTMSP nanocomposite film preparation: Glassware used in these studies was cleaned and dried at 80 ^oC overnight. Unless otherwise noted, the glassware was allowed to cool to room temperature at ambient conditions prior to being moved to a N_2 blanketed glove box.

PTMSP was added to 99.8 % anhydrous toluene from Sigma-Adrich (St. Louis, MO) (1.5 g of PTMSP per 100 ml of toluene) and stirred using a magnetic stir bar until the polymer dissolved. Nanoparticles were added to the solution to prepare a final dry film having a target filler volume fraction, ϕ_F^N, which was calculated as described in Eq. (2.17).

The particle-filled solution was then allowed to mix overnight at ambient conditions using a magnetic stir bar. Afterwards, the solution was poured onto a clean, dry, level glass casting plate and allowed to dry at ambient conditions until the toluene had completely evaporated, which usually required about two days. All PTMSP sample preparation steps involving MgO particles were conducted in a glove box under a N_2 blanket, and a relative humidity of 0.0 (as determined by a Tescom Hydrometer (Elk River, Minnesota)) was maintained at all times. The N_2 blanket was used to minimize the exposure of the particles to water, since MgO particles can react with water.[3] No precautions were taken to prevent TiO_2 particles from being exposed to water other than standard drying of glassware, etc.

PTMSDPA nanocomposite film preparation: PTMSDPA was dissolved in toluene (1 g of PTMSDPA in 100 ml of 99.8 % anhydrous toluene). The solution was stirred for 24 hours at ambient conditions using a magnetic stir bar. Afterwards, the solution was stirred for 4 hours at a prescribed temperature (*i.e.,* -10, 0, and 23 ^{o}C) to explore the influence of mixing temperature on the extent of reaction between the particles and polymer. MgO nanoparticles were then added to the solution, and it was shaken to disperse the nanoparticles. The particle-filled solution was stirred for a fixed amount of time using a magnetic stir bar at the prescribed temperature. The solution was then poured onto a clean, dry, level glass casting plate in a fume hood and covered with a Petri dish to slow evaporation. Films were cast at room temperature (~ 23 ^{o}C) and generally required two days for complete solvent removal.

MgO-Treated model compounds: The chemical structures of the low molar mass model compounds used in this study are presented in Table 3.2, and all of the compounds were obtained from Sigma-Aldrich (St. Louis, MO). 0.39 g of 1-phenyl-2-(trimethylsilyl) acetylene (PhTMSA) (*cf.*, Table 3.2), 0.39 g of 1-phenyl-2-(trimethylsilyl)-ethylene (PhTMSE), and 0.35 g of trimethyl(phenyl)silane (TMPS) were each dissolved individually in 10 g of *d*-benzene from Fisher Scientific (Hampton, NH). These masses of model compounds correspond to the TMS molar concentration in 0.25 g of PTMSP dissolved in 10 g of *d*-benzene, which was the sample concentration used for the NMR experiments described below. After mixing for one hour using a magnetic stirring bar, MgO nanoparticles were added to the solution. The amount of MgO added to the solution was characterized by Γ, which is the ratio of moles of TMS per gram of MgO. Γ was calculated as follows:

$$\Gamma = \frac{m_{MC}}{M_{MC} \cdot m_{MgO}} \tag{3.1}$$

where M_{MC} is the molar mass of the model compound (174 for PhTMSA, 176 for PhTMSE, and 150 for TMPS), and m_{MC} and m_{MgO} are the masses of the model compound and MgO added to the solution, respectively. To vary Γ, m_{MC} is held constant and m_{MgO} was changed. The resulting solution was mixed overnight at ambient conditions using a magnetic stir bar.

Table 3.2 Model compounds

Trimethyl(phenyl)silane (TMPS)	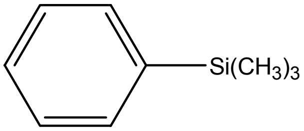
1-phenyl-2-(trimethylsilyl)-ethylene (PhTMSE)	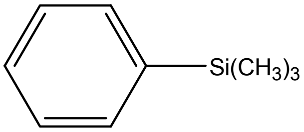
1-phenyl-2-(trimethylsilyl)-acetylene (PhTMSA)	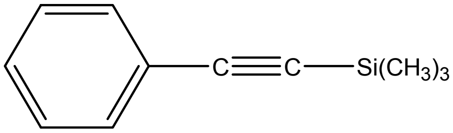

<u>1,2-Polybutadiene nanocomposite film preparation:</u> 1,2-Polybutadiene was added to toluene (1.5 g / 20 ml solution) and stirred at 40 °C until the polymer dissolved, which usually took less than 20 minutes. Nanoparticles were added to the solution in an

amount that would result in a final dry film with a predetermined nominal filler volume percent loading, ϕ_F^N, as defined by Eq. (2.17). The solution viscosity was sufficient to prevent nanoparticle settling. The particle-filled solution was then mixed for 20 minutes at 40 ^{o}C using a magnetic stir bar. The solution was poured onto a clean, dry, level glass casting plate in a fume hood and dried slowly, which is to obtain a cast film with a flat surface suitable for gas permeation experiments (*i.e.,* film thickness variation of less than 10 percent). Casting generally took less than 24 hours and resulted in nanocomposite films around 200 μm thick, with variation were less than 20 μm over the entire film surface.

Sample preparation for atomic force microscopy (AFM): The PTMSP, PB and nanocomposite samples are in the form of thin films of approximately 200 microns. The samples were cut to a convenient size for microtoming, approximately 2 mm wide, using a razor blade. Tapering cuts were made to give a point to the sample, which was then polished using a cryomicrotome at -100 ^{o}C for 1,2-polybutadiene based materials and at room temperature for PTMSP based samples to yield a small protruding rectangular surface. For both materials polishing took place at a temperature that was significantly lower than the glass transition temperature of 1,2-polybutadiene (*i.e.,* -19 to -10 ^{o}C) and PTMSP (*i.e.,* 250 ^{o}C). All samples were polished using an RMC-Boeckeler PowerTome PT-XL (Boeckeler Instruments Inc., Tucson, AZ). A cryo diamond knife (Micro Star Technologies, Huntsville, TX) was used in the polishing step, with a cutting speed of 0.6 mm/s. To ensure sample stability for AFM surface analysis, the polished samples were then mounted on AFM sample holders (Ted Pella Inc., Redding, CA) using 5-minute epoxy (Fisher Scientific International Inc., Hampton, NH), polished side up.

<u>Sample preparation for scanning transmission electron microscopy (STEM) and transmission electron microscopy (TEM)</u>: Samples were trimmed using a razor blade in a manner similar to AFM sample preparation. The trimmed samples were embedded within LR White resin (Electron Microscopy Sciences, Hatfield, PA) by cold curing in a BEEM® capsule container (Ted Pella Inc., Redding, CA). The embedded sample was pre-trimmed using a glass knife at room temperature with a Leica Ultracut UCT microtome (Leica Microsystems GmbH, Wetzlar, Hesse, Germany) to form a small, protruding, truncated pyramidal shape containing the sample with a smooth rectangular face approximately 100-200 μm in length and width. Sections were collected from this pyramid using a cryo diamond knife at -100 ^{o}C for 1,2-polybutadiene based materials and at room temperature for PTMSP samples at a cutting speed of 0.6 mm/s. The sections were floated on water in the diamond knife boat and scooped out with 400-mesh copper TEM grids (Ted Pella Inc.). High-angle annular dark field STEM and TEM experiments employed a FEI TECNAI G^2 F20 transmission electron microscope (FEI Company, Hillsboro, OR) using accelerating voltage of 200 kV at room temperature.

EXPERIMENTAL PROCEDURES

<u>Experimental Procedure for Atomic Force Microscopy (AFM)</u>: Tapping mode AFM using a Digital Instruments Dimension 3100 with Nanoscope IV controller (Woodbury,

New York) was used to characterize particle dispersion in a nanocomposite cross section. Silicon NCH AFM tips from Nanosensors, now Nanoworld (Neuchatel, Switzerland), were used. Phase profiles were obtained at 1 μm by 1 μm surface areas with 512 lines scanned per sample, which yielded a resolution of 2 nm per line. The scan rate was 0.8 Hz, the integral feedback was set to 0.2, and the proportional feedback was set to 1.0.

AFM particle size and particle size distribution were obtained using ImageJ software from the National Institutes of Health, using a technique that is consistent with the ImageJ instructions for particle analysis.[4] AFM tapping mode phase profiles were cropped using the software and converted to an 8-bit image. A threshold was applied to the image so that only the hardest phase (corresponding to the nanoparticles) would be resolved. The "analyze particles" feature was then utilized to determine average nanoparticle size, nanoparticle surface area fraction within the image area, and nanoparticle agglomerate size distributions.

The area distribution produced by ImageJ from an AFM image was divided into 100 bins of equal area increments. As long as at least 50 bins were used in the data analysis, the nanoparticle aggregate diameter results were not significantly influenced by the number of bins used. The area of bin j of nanoparticle aggregates, A_j, was converted to an effective aggregate diameter, d_j, using a spherical model:

$$d_j = \sqrt{\frac{4A_j}{\pi}} \tag{3.2}$$

The fraction of aggregates, F_j, of diameter d_j was calculated as follows:

$$F_j = \frac{N_j}{N_T} \tag{3.3}$$

where N_j is the number of nanoparticle aggregates of diameter d_j. N_T is the total number of distinguishable aggregates characterized, which varied from 700 to 1500 particles depending upon particle loading and polymer matrix. These data were then fit to the Weibull distribution, which is an empirical model often used to characterize particle size distributions, and it is defined as:[5-8]

$$F_j = \frac{\beta}{\alpha}\left(\frac{d_j - \upsilon}{\alpha}\right)^{\beta-1} \exp\left[-\left(\frac{d_j - \upsilon}{\alpha}\right)^{\beta}\right] \tag{3.4}$$

where υ is the smallest possible value of d_j (3 nm in this case since this is the diameter of a single nanoparticle), and β and α are model fitting parameters.

The average aggregate size, $\overline{d}$, was calculated as follows:[7]

$$\overline{d} = \frac{1}{N_T}\sum_{j=1}^{m} d_j N_j \tag{3.5}$$

where m is the total number of bins, which was set to 100 in this study. The standard deviation in aggregate size, σ, is:[7]

$$\sigma = \left(\frac{1}{N_T}\sum_{j=1}^{m}\left[(d_j - \overline{d})^2 N_j\right]\right)^{\frac{1}{2}} \tag{3.6}$$

Low Pressure Sorption: Kinetic gravimetric sorption experiments were performed using an automated spring balance (described elsewhere [9]). These studies characterized the adsorption of permanent gases (*i.e.,* CO_2, CH_4, and N_2) onto nanoparticles. An analytical balance was used to determine sample weight. The nanoparticle sample to be studied was placed in a hemispherical quartz pan suspended on a quartz spring from Ruska Instruments (Houston, TX). An initial reading of spring extension was recorded, vacuum was applied overnight to degas the film and the system, and, at this point, a second spring extension reading was made to determine the weight loss due to degassing.

Spring extension data were acquired while the sample was exposed to a gas at a fixed pressure for 20 minutes. Adsorption generally reached equilibrium well before 20 minutes. Afterwards, the system pressure was increased, and the spring extension was remeasured. This process was repeated until system pressure was just below atmospheric pressure (the test limit for this apparatus). Gas concentration (cm^3(STP)/cm^3particles) on the particles, C_F, was calculated as follows:

$$C_F = \frac{22414 \rho_F k \left(l_p - l_v \right)}{W_F M_w} \tag{3.7}$$

where the constant 22414 has units of cm^3(STP)/mol, W_F is the mass of filler (g), ρ_F is the nanoparticle density (g/cm^3), l_p is the spring extension at equilibrium at a given pressure (mm), l_v is the spring extension at equilibrium at vacuum (mm), M_w is the molar mass of the test gas (g/mol), and k is the spring constant (mg/mm). The spring constant for the kinetic gravimetric measurements was $2.82\text{x}10^{-4}$ g/mm. The least count is the equivalent of 1 pixel (*i.e.,* $8.9\text{x}10^{-6}$ g).

<u>High Pressure Sorption:</u> A high-pressure barometric sorption apparatus[10,11] was used to determine the sorption of gases in PTMSP and TiO_2 filled nanocomposites. Vacuum was

applied for at least 18 hours prior to beginning measurements with a new gas. Gases were applied at pressure intervals of ~3 atm from vacuum to ~20 atm. All experiments were conducted at 35 ^{o}C. Equilibrium was reached in, at most, a few hours.

Density: Density was measured via a hydrostatic weighing method that employed a Mettler Toledo balance Model AG204 (Switzerland) equipped with a density determination kit. Samples were tested in deionized water.

In 1,2-polybutadiene, the volume fraction crystallinity of the pure polymer, ϕ_C, was estimated from the experimentally determined polymer density, ρ_P, as follows:[13]

$$\phi_C = \frac{\rho_P - \rho_A}{\rho_C - \rho_A} \tag{3.8}$$

where ρ_C and ρ_A are the densities of crystalline (*i.e.,* 0.963 g/cm^3) and amorphous (*i.e.,* 0.889 g/cm^3) 1,2-polybutadiene, respectively.[12] For the 1,2-polybutadiene samples considered in these studies, ρ_P was 0.911 ± 0.05 g/cm^3.

Wide angle X-ray diffraction (WAXD): Wide angle X-ray diffraction was performed using a Scintag X1 theta-theta diffractometer. CuKα radiation with a wavelength of 1.54 Å was used. The power settings were 45 kV and 40 ma. The software used for data processing was Jade v. 7.5 from Materials Data Inc., Livermore, CA. The powder diffraction database used for comparing the experimental data to known powder diffraction patterns was PDF-2 Release 2004 from the International Centre for Diffraction Data, Newton Square, PA.

To determine crystalline polymer concentration in semi-crystalline materials, backgrounds were modeled and removed from each diffraction pattern in a manner consistent with the literature.[12] An amorphous peak centered at about 14.5° 2θ was modeled for height, location, full width half maximum (FWHM), and skew. Additionally, peaks for the 1,2-polybutadiene were modeled for height, location and FWHM. The weight fraction of crystalline polymer was calculated as follows:[13]

$$\chi_C = \frac{I_C}{I_C + I_A} \tag{3.9}$$

where I_C and I_A are the integrated area under the crystalline and amorphous peaks, respectively.

Fourier transform infrared spectroscopy (FTIR): Polymer and polymer composite samples were examined using FTIR (Thermo Nicolet Nexus 470, Madison, WI) with an ATR Smart Avatar attachment (Thermo Nicolet Nexus, Madison, WI). The crystal was cleaned with isopropyl alcohol prior to collecting the background. Whenever possible, samples were tested immediately after removal from the glove box. Small model compounds were prepared in KBr (Sigma-Aldrich) pellet samples and examined using transmission FTIR (Thermo Nicolet Nexus 470, Madison, WI).

Toluene or chloroform solubility test: PTMSDPA, PTMSP and polymethylacetylene (*i.e.,* desilylated PTMSP) are highly soluble in toluene or chloroform.[14] In contrast, desilylated PTMSDPA (*i.e.,* PDPA) is insoluble in these solvents.[14] So, extracting PTMSDPA-MgO nanocomposites in toluene or chloroform and monitoring the solids content of the sample provides an indication of the influence of the nanoparticles on nanocomposite solubility. Nanoparticle-filled PTMSDPA films weighing approximately 0.1 g were placed in sealed containers with 50 ml of either toluene (Sigma-Aldrich) or chloroform (Sigma-Aldrich). This ratio of polymer to solvent is well below the solubility limit of PTMSDPA in either solvent.[14] The films were extracted for at least two weeks at ambient conditions in solvent. After two weeks, the films were removed from solvent either using tweezers, if the film had sufficient mechanical strength, or the films were removed by filtering the solvent from the solids using a filter that was attached to a vacuum. Samples that required filtering were either in a gel-like state or appeared to be fragile polymer films. After removal from solvent, samples were dried for two days in a fume hood. The fraction weight loss, ΔM, was estimated as follows:

$$\Delta M = 1 - \frac{M_S}{M_0} \tag{3.10}$$

where M_0 and M_S are the weights of the dry nanocomposite sample before and after extraction in toluene or chloroform, respectively. This calculation does not distinguish between polymer and/or particle extraction from the film. Therefore, it provides a qualitative demonstration of the effects of mixing time, solution temperature, and particle loading on the chemical stability of PTMSDPA nanocomposites in solvents that are quite effective for dissolving the native polymer and for dispersing the particles.

<u>X-ray photoelectron spectroscopy (XPS):</u> An XPS system equipped with a monochromatic Al $K\alpha_{1,2}$ X-ray source (PHI 5700, Physical Electronics Inc., Chanhassen,

MN) was used to examine films for evidence of reaction. Operating conditions were: 1×10^{-9} Torr chamber pressure; 14 kV; 250W for the Al X-ray source.

Proton and Carbon Nuclear Magnetic Resonance (^{1}H NMR) and (^{13}C NMR): ^{1}H and ^{13}C solution NMR spectra were observed on an RT Quad Probe Unity +300 (Varian, Palo Alto, CA). Proton NMR experiments were conducted at 500 MHz, and ^{13}C NMR experiments were conducted at 125 MHz. Nanocomposite films were dissolved in *d*-benzene such that each sample contained 0.25 g of polymer, regardless of particle volume fraction. This procedure assured that all NMR samples would have sufficient polymer present to obtain meaningful data. Model compounds were added directly to *d*-benzene containing MgO and allowed to stir overnight at ambient conditions prior to testing. All samples were referenced to the solvent, *d*-benzene. ^{1}H NMR experiments were conducted over one hour. ^{13}C NMR experiments were taken over a period of at least 16 hours to improve resolution.

Permeability in substituted polyacetylenes based materials: Pure gas permeability was determined using a constant pressure/variable volume apparatus.[15] Films were 150 to 300 μm thick. Samples were masked with aluminum tape. After a film was placed in the permeation cell, it was exposed to the test gas at 3.4 atm upstream pressure for at least thirty minutes to ensure that steady state was established. Gas permeability (cm^3(STP) cm/(cm^2 s cmHg)) was calculated from the steady state permeate flowrate through a bubble flow meter according to:[16]

$$P_A = \frac{273 p_{atm}}{76T} \frac{l}{A(p_2 - p_1)} \frac{dV}{dt} \tag{3.11}$$

where *dV/dt* is the permeate volumetric flowrate (cm^3/s), *l* is the film thickness (cm), p_2 is the upstream absolute pressure (cmHg), p_1 is the downstream absolute pressure (cmHg), p_{atm} is atmospheric absolute pressure (cmHg), *A* is the area of the film available for transport (cm^2), and *T* is absolute temperature (K). All experiments were performed at atmospheric downstream pressure (76 cmHg).

Permeability in 1,2-polybutadiene based materials: Pure gas permeability was determined using a constant volume/variable pressure apparatus.[17] A 13.8 cm^2 unmasked film was secured in a permeation cell. The film was exposed to vacuum for at least 18 hours on both the upstream and downstream surfaces in order to degas the system. After degassing, both the upstream and downstream volumes were sealed, and the system was tested for leakage. If the leak test demonstrated a change in downstream pressure of less than 0.01 cmHg over a period of 2 hours, then the permeation experiments continued. Otherwise, the film was resecured in the cell to reduce gas leakage. After a successful leak test, the downstream volume was sealed at vacuum and the upstream film surface was exposed to a pure gas at a known pressure. Gas permeability (cm^3(STP) cm/(cm^2 s cmHg)) was calculated from the steady state pressure increase in the downstream volume as follows:

$$P = \frac{dp}{dt} \frac{l \cdot V}{T \cdot p \cdot A \cdot R} \tag{3.12}$$

where *dp/dt* is the pseudo-steady state rate of pressure increase in the downstream volume, l is the film thickness (cm), p is the upstream absolute pressure, A is the area of the film available for transport (cm^2), V is the downstream volume (cm^3), and T is absolute temperature (K). R is the gas constant. All experiments were performed with downstream pressure values below 1 cmHg.

<u>Mixed gas permeability:</u> The CO_2 and CH_4 mixed gas permeabilities were determined using a constant pressure/variable volume apparatus.[15,18] The system is equipped with a mass flow controller (MKS Instruments, Inc., Wilmington, MA) on the upstream side to regulate the residue flow rate. Helium was used to sweep the downstream side of the membrane and carry the permeate (*i.e.,* CO_2 and CH_4) to a gas chromatograph. The total flowrate on the downstream side (*i.e.*, helium plus permeate) was measured with a soap film flowmeter. The system temperature was controlled to ±0.1°C using a constant temperature water bath.

The feed compositions contained 20/80, 50/50, and 80/20 mole fraction CO_2/CH_4. A sufficient residue flowrate at the upstream side was maintained (*i.e.*, a stage cut of less than 1%) to prevent concentration polarization. The feed pressure was varied from 4.5 to 14.6 atm. The partial pressure of the penetrants in the downstream was maintained at practically zero (< 0.05 atm) by adjusting the helium flowrate.

The steady state gas permeability was calculated using the expression:

$$P_A = \frac{l}{f_{A,2} - f_{A,1}} \frac{273}{TA} \frac{p_{atm}}{76} \left(y_{A,1} \frac{dV}{dt} \right) \tag{3.13}$$

where $f_{A,2}$ and $f_{A,1}$ are the fugacities of gas A (cmHg) in the upstream and downstream, respectively, which were determined using Soave-Redlich-Kwong (SRK) equation based on the total pressure and the mole fraction of A in the feed and downstream.[19] $y_{\mathrm{A},1}$ is the mole fraction of gas A in the downstream, p_{atm} is atmospheric pressure (cmHg), A is the membrane area (cm^2), T is temperature (K), l is the membrane thickness (cm), and dV/dt is the volumetric displacement rate of the soap film in the bubble flowmeter at steady state (cm^3/s).

Differential scanning calorimeter (DSC): Polymer and nanocomposite samples weighing 10 to 20 mg were placed into steel DSC pans from TA Instruments. DSC sweeps were conducted using a Q-100 DSC from TA Instruments. The sweep began by lowering the sample temperature to -80 °C at 20 °C/minute. The sample was held at -80 °C for 5 minutes and then heated at 20 °C/minute to 150 °C. The maximum and minimum temperatures used in these sweeps were at least 40 °C from the PB melt temperature, 100 °C, and the range was sufficient to observe a complete melting event. Only the initial heating sweep is of use for this study, because subsequent sweeps would not have the same thermal history as the solution cast samples. DSC sweeps were conducted using an empty steel DSC pan as a reference.

The weight fraction of crystallinity in the unfilled polymer, χ_C (g crystals/ g polymer), was calculated by comparing the polymer enthalpy of melting, ΔH_m, in the initial temperature sweep to the estimated enthalpy of melting of the pure crystalline polymer, ΔH_C:

$$\chi_C = \frac{\Delta H_m}{\Delta H_C} \quad (3.14)$$

ΔH_C for 1,2-polybutadiene is 60.7 J/g crystals.[20] This method was used to estimate the crystallinity in the unfilled polymer only. Neat TiO_2 particles showed an endothermic event at temperatures greater than 100 °C. As a result, in the nanocomposite films, there was an endothermic event between 120 and 150 °C that prevented reliable measurements of ΔH_m, so it was not possible to estimate the crystallinity level in the nanocomposites from DSC data.

In the DSC thermograms of each of the nanocomposite samples, there was a broad exotherm beginning at approximately 60 and extending, in some cases, to approximately 140°C. This exotherm completely masked the melting endotherm of the polymer crystals, which, as indicated above, was observed between about 50°C and 115°C. The pure particles exhibit a broad endotherm beginning at temperatures above about 100°C, which may be due to desorption of sorbed atmospheric gases. Thus, the exotherm in the nanocomposite samples did not correspond to any thermal event in either the pure polymer or the particles, suggesting that it might be indicative of an interaction or reaction of the particles with the polymer. PB is known to be sensitive to oxidative degradation that can be markedly accelerated in the presence of appropriate catalysts.[21,22] Also, metal oxides, such as MgO and ZnO, vulcanize polybutadiene.[23,24]

REFERENCES

(1) Koper, O. B.; Lagadic, I.; Volodin, A. M.; Klabunde, K. J., Alkaline-Earth Oxide Nanoparticles Obtained by Aerogel Methods. Characterization and Rational for Unexpectedly High Surface Chemical Reactivities, *Chemistry of Materials* **1997**, *9*, 2468-2480.

(2) Sakaguchi, T.; Yumoto, K.; Shiotsuki, M.; Sanda, F.; Yoshikawa, M.; Masuda, T., Synthesis of Poly(diphenylacetylene) Membranes by Desilylation of Various Precursor Polymers and Their Properties, *Macromolecules* **2005**, *38*, 2704-2709.

(3) Utamapanya, S.; Klabunde, K. J.; Schlup, J. R., Nanoscale metal oxide particles/clusters as chemical reagents. Synthesis and properties of ultrahigh surface area magnesium hydroxide and magnesium oxide, *Chemistry of Materials* **1991**, *3*, 175-181.

(4) Reinking, L., Examples of Image Analysis Using ImageJ, *Online: http://rsweb.nih.gov/ij/docs/pdfs/examples.pdf* **2001**, 1-2.

(5) Bevington, P. R.; Robinson, D. K. Data Reduction and Error Analysis for the Physical Sciences, 3rd ed.; McGraw-Hill, Inc.: New York, 2002.

(6) Weibull, W., A statistical distribution function of wide applicability, *Journal of Applied Mechanics* **1951**, *18*, 293-297.

(7) Olkin, I.; Gleser, L. J.; Derman, C. Probability Models and Applications, 2nd ed.; Macmillan College Publishing Company: New York, 1980.

(8) Bryant, G.; Martin, S.; Budi, A.; van Megen, W., Accurate measurement of small polydispersities in colloidal suspensions, *Langmuir* **2003**, *19*, 616-621.

(9) McDowell, C. C.; Coker, D. T.; Freeman, B. D., An automated spring balance for kinetic gravimetric sorption of gases and vapors in polymers, *Review of Scientific Instruments* **1998**, *69*, 2510-2513.

(10) Sanders, E. S.; Koros, W. J.; Hopfenberg, H. B.; Stannett, V., Pure and mixed gas sorption of carbon dioxide and ethylene in poly(methyl methacrylate), *Journal of Membrane Science* **1984**, *18*, 53-74.

(11) Bondar, V. I.; Freeman, B. D.; Pinnau, I., Gas sorption and characterization of poly(ether-b-amide) segmented block copolymers, *Journal of Polymer Science: Part B: Polymer Physics* **1999**, *37*, 2463-2475.

(12) Natta, G., Determination of the polypropylene crystallinity, *Atti della Accademia Nazionale dei Lincei Rendiconti-Classe de Scienze Fisiche-Matematiche and Naturali* **1957**, *22*, 11-17.

(13) Dhoot, S. N.; Freeman, B. D.; Stewart, M.; Hill, A. J., Sorption and transport of linear alkane hydrocarbons in biaxially oriented poly(ethylene terephthalate), *Journal of Polymer Science Part B: Polymer Physics* **2001**, *39*, 1160-1172.

(14) Teraguchi, M.; Masuda, T., Poly(diphenylacetylene) Membranes with High Gas Permeability and Remarkable Chiral Memory, *Macromolecules* **2002**, *35*, 1149-1151.

(15) Stern, S. A.; Gareis, P. J.; Sinclair, T. F.; Mohr, P. H., Performance of a versatile variable-volume permeability cell. Comparison of gas permeability measurements by the variable-volume and variable-pressure methods, *Journal of Applied Polymer Science* **1963**, *7*, 2035-2051.

(16) Merkel, T. C.; Bondar, V.; Nagai, K.; Freeman, B. D., Sorption and transport of hydrocarbon and perfluorocarbon gases in poly(1-trimethylsilyl-1-propyne), *Journal of Polymer Science: Part B: Polymer Physics* **2000**, *38*, 273-296.

(17) Bondar, V.; Freeman, B. D.; Pinnau, I., Gas transport properties of poly(ether-b-amide) segmented block copolymers, *Journal of Polymer Science Part B: Polymer Physics* **2000**, *38*, 2051-2062.

(18) O'Brien, K. C.; Koros, W. J.; Barbari, T. A., A new technique for the measurement of multicomponent gas transport through polymeric films, *Journal of Membrane Science* **1986**, *29*, 229-238.

(19) Raharjo, R. D.; Lin, H.; Sanders, D. F.; Freeman, B. D.; Kalakkunnath, S.; Kalika, D. S., Relation between network structure and gas transport in crosslinked poly(propylene glycol diacrylate), *Journal of Membrane Science* **2006**, *283*, 253-265.

(20) Obata, Y.; Tosaki, C.; Ikeyama, M., Bulk properties of syndiotactic 1,2-polybutadiene. I. Thermal and viscoelastic properties, *Polymer Journal* **1975**, *7*, 207-216.

(21) Iraqi, A.; Cole-Hamilton, D. J., Preparation and reactivity of polyepoxides and polyketones: Catalytic oxidation of polybutadienes, *Journal of Material Chemistry* **1992**, *2*, 183-190.

(22) Ajjou, A. N.; Alper, H., Catalitic oxidation of polybutadienes based on a Wicker-type reaction, *Macromolecules* **1996**, *29*, 5072-5074.

(23) Yin, D.; Zhang, Y.; Pend, Z.; ZHang, Y., Effect of fillers and additives on the properties of SBR vulcanizates, *Journal of Applied Polymer Science* **2003**, *88*, 775-782.

(24) Westlinning, H.; Fleischhauer, H. *Properties of White Reinforcing FIllers in Elastomers*, In Reinforcement of Elastomers; Kraus, G., Ed.; John Wiley and Sons: New York, 1965; pp 425-490.

Chapter 4: Gas transport in TiO_2 nanoparticle filled poly(1-trimethylsilyl-1-propyne)

The study of nanocomposites prepared using impermeable particles has been dominated by the use of fumed silica as nanoparticles.[1-4] Although some grades of fumed silica contains primary particles as small as 13 nm in diameter, these particles are chemically fused together so that it is not possible to disperse the primary particles individually or in nanoscale aggregates. This chapter reports the influence of impermeable brookite (*i.e.,* TiO_2) nanoparticles on pure gas permeability coefficients in PTMSP-based nanocomposites. The primary particles of TiO_2 are approximately 3 nm in diameter, and they are not inherently fused together, so they have the potential to be dispersed individually or in nanoscale aggregates.

This chapter is part of a larger study investigating the influence of particle surface chemistry on nanocomposite gas transport properties. This study investigates how very small particles that are interactive or non-interactive with PTMSP influence gas transport properties, and this paper presents results based on non-interactive particles. Particle dispersion, nanocomposite density, and light gas permeability coefficients are reported as a function of particle content. The influence of physical aging on nanocomposite gas permeation properties was also characterized.

RESULTS AND DISCUSSION

Polymer-particle stability

Some nanoparticles can react with test gases (*e.g.,* carbonation of MgO)[6], water or with the polymer matrix (*e.g.*, MgO induced desilylation of certain substituted polyacetylenes)[5]. WAXD and FTIR experiments demonstrated that TiO_2 nanoparticles were chemically stable in PTMSP, and TiO_2 did not react with the polymer matrix or the gases considered. WAXD confirmed that both the neat TiO_2 particles and those embedded in PTMSP were brookite (*i.e.,* TiO_2). TiO_2 nanoparticles soaked in deionized water (*i.e.,* 18.2 MΩ-cm) for two weeks prior to WAXD studies maintained the brookite structure, so presumably exposure to adventitious humidity in the laboratory did not influence the particle structure. This result is in contrast to that observed with MgO nanoparticles, which are known to react with water and PTMSP.[5]

Particle dispersion

In nanocomposites, the morphology of the discontinuous phase has a significant effect on gas transport properties.[3,7,8] Discontinuous phase (*i.e.,* TiO_2 nanoparticles and/or voids) dispersion was examined by TEM and AFM. TEM images could not be obtained at magnifications sufficient to resolve individual particles or nanometer scale aggregates due to the instability of PTMSP upon exposure to a highly focused electron beam. Also, a typical TEM sample was at least 40 nm thick. At even modest particle loadings, interparticle spacing could be significantly less than 40 nm (*cf.*, Figure 1.2).

Since TEM images are planar projections of the three-dimensional structure of the sample being imaged, apparent particle overlap could appear in the TEM images even if the particles were well-separated simply because the sample thickness was many times the average interparticle spacing. For this reason, AFM was used to provide a more faithful characterization of particle dispersion in these samples.

Representative examples of AFM tapping mode phase profiles of cross sections of neat and TiO_2-filled PTMSP samples are presented in Figure 4.1. Although AFM can resolve individual nanoparticles and nanoscale aggregates at low particle loadings (*i.e.,* ≤ 10 volume percent TiO_2), the interparticle spacing at high TiO_2 loadings becomes sufficiently small that AFM cannot resolve the polymer phase between dispersed particles and aggregates. Also, the AFM tip cannot effectively maintain contact with the sample due to abrupt changes in surface topography that appear more frequently, even in carefully microtomed sections, at higher particle loadings. AFM phase profiles resolve relative surface hardness.[9] In this study, the harder phase, shown in white, is presumed to be the inorganic TiO_2 particles. The softer phase (*i.e.,* the non-white regions) is ascribed to the polymer.

As expected, unfilled PTMSP, which is amorphous,[10] did not exhibit regions that were significantly out-of-phase (*cf.* Figure 4.1a). The lines in Figures 4.1a-4.1c are attributed to sample preparation artifacts (*i.e.,* from scratches in the diamond knife, which cause sufficient change in surface topography to distort the AFM cantilever, resulting in apparent deviations in the phase profile). In contrast, AFM images of the nanocomposite films containing 0.03 and 0.10 volume fraction TiO_2 exhibit regions that are significantly harder than the continuous phase (*cf*., white regions of Figures 4.1b and 4.1c). These regions are attributed to nanoparticles or nanoparticle aggregates.

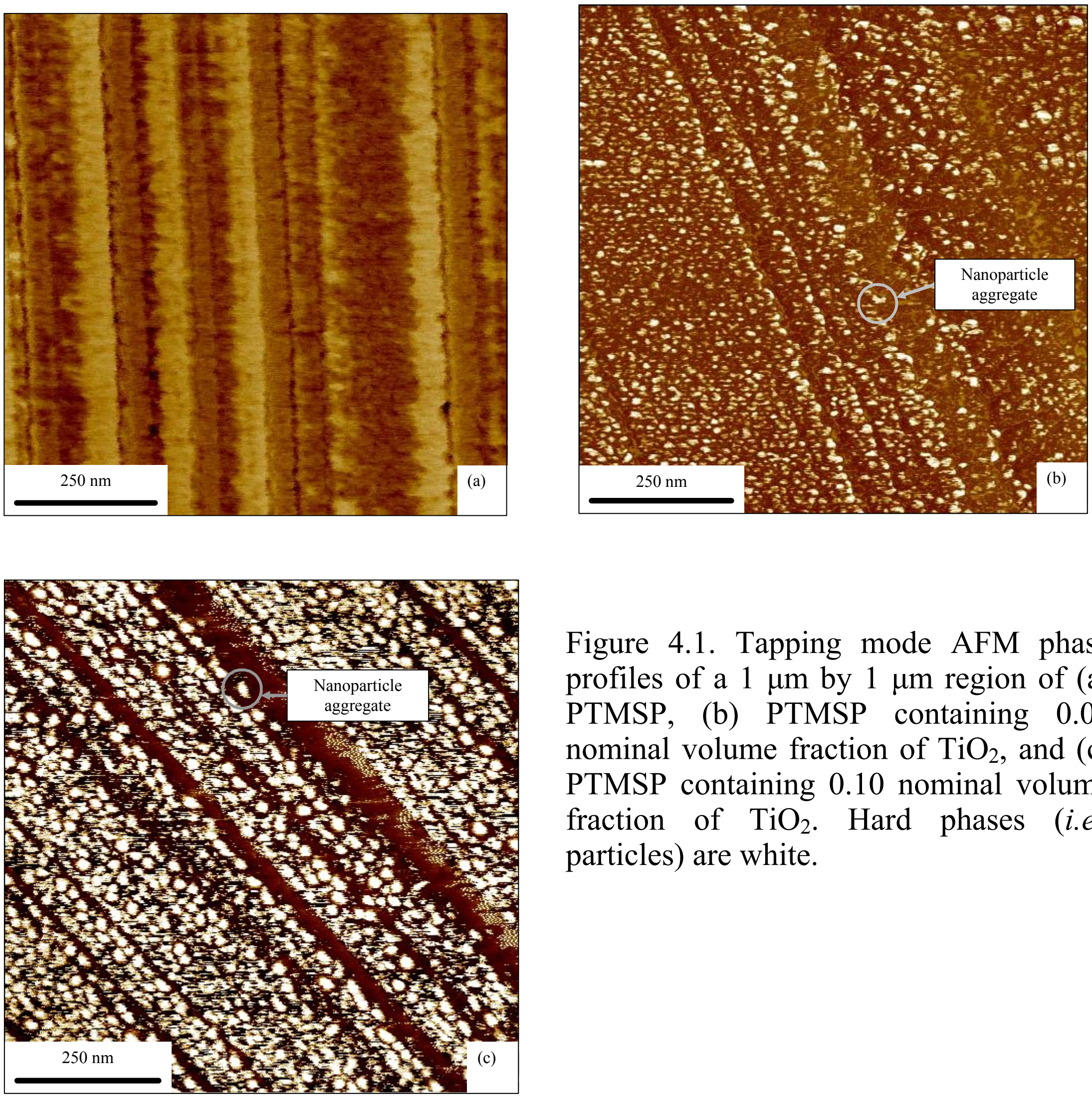

Figure 4.1. Tapping mode AFM phase profiles of a 1 μm by 1 μm region of (a) PTMSP, (b) PTMSP containing 0.03 nominal volume fraction of TiO_2, and (c) PTMSP containing 0.10 nominal volume fraction of TiO_2. Hard phases (*i.e.,* particles) are white.

The nanoparticle aggregate diameter distributions are shown in Figure 4.2. The distributions were estimated using the ImageJ software as described earlier to analyze AFM images, such as those shown in Figure 4.1. Regions of the AFM images that contain processing artifacts (*i.e.,* scratches from polishing, which appear as black streaks in the AFM image) have been excluded from the nanoparticle aggregate diameter analysis. However, in Figure 4.1c some of the smaller artifacts were included in the image analysis since the concentration of such artifacts made it impossible to remove 100% of them.

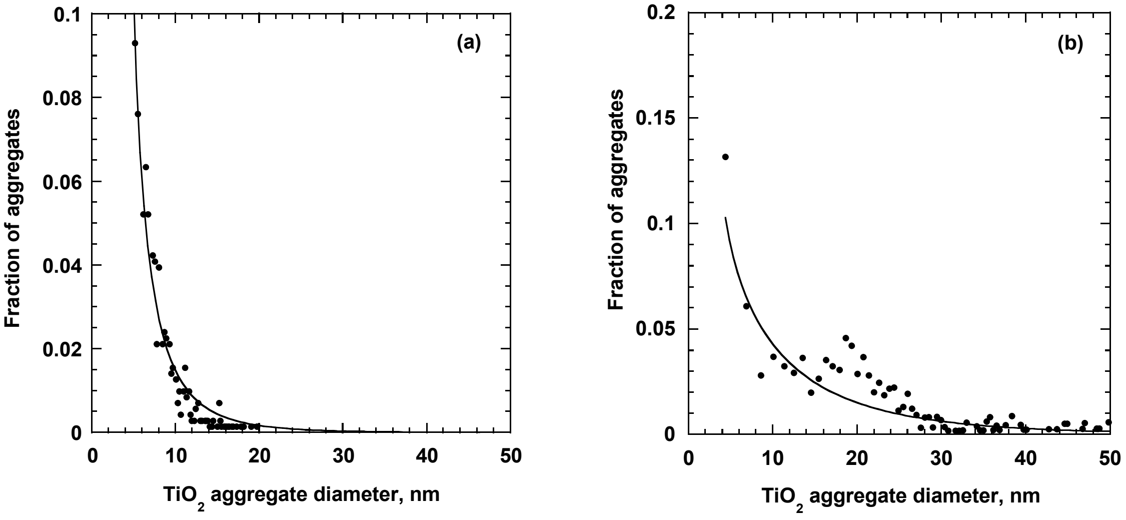

Figure 4.2. TiO_2 aggregate diameter distribution from tapping mode phase profiles of (a) 0.03 nominal TiO_2 volume fraction, and (b) 0.10 nominal TiO_2 volume fraction in PTMSP. The solid line represents a fit of Weibull's distribution to the data using $v = 3.0$ nm, $\beta = 1.15 \pm 0.44$ and $\alpha = 0.58 \pm 0.2$ for (a) and $v = 3.0$ nm, $\beta = 8.07 \pm 3.87$ and $\alpha = 0.8 \pm 0.26$ for plot (b).[11,12] The uncertainty in the Weibull distribution parameters was determined as described in Bevington.[13]

The aggregates in the nanocomposites containing 0.03 and 0.10 nominal TiO_2 volume fraction have an average diameter, $\overline{d}$, of 7 nm ± 3 nm and 12 nm ± 8 nm, respectively. These values are in good agreement with the $\overline{d}$ values calculated from the Weibull distribution (*i.e.,* 8 ± 6 nm and 15 ± 11 nm for the nanocomposites containing

0.03 and 0.10 nominal TiO_2 volume fraction, respectively). The particle distributions indicate that at least some of the particles are dispersed individually or in small nanoparticle aggregates.

The AFM images in Figure 4.1 have a resolution limit of around 2 nm, which is near the individual particle size (*i.e.,* ~ 3 nm). If there are particles smaller than 2 nm in these samples, they will not be accounted for by this particle analysis. Not counting such particles would, of course, introduce error into $\overline{d}$ and σ. Treating the aggregates as spheres is another potential source of error. Also, as shown in Figure 4.1c, many aggregates are either touching or nearly touching one another. In these cases, the apparent aggregate shape may significantly deviate from spherical, and this issue will be more significant at higher particle loadings, where the inter-aggregate spacing is less than at lower loadings. Once inter-aggregate spacing is within the resolution limit of the AFM, multiple aggregates will register as a single, larger aggregate. These experimental limitations may cause the value of $\overline{d}$ to be less than the reported value. Also, large (*i.e.,* micron sized aggregates) have been excluded from this calculation, since abrupt changes in aggregate topography, that were possibly caused by sample processing, resulted in poor quality AFM images. The exclusion of such aggregates artificially, and possibly substantially, causes the reported average particle size to be lower than the true $\overline{d}$. Although the interparticle spacing and average aggregate diameters have numerous sources of error, they demonstrate at least some of the particles are dispersed individually or in nanoscale aggregates, which has not be reported to date in the nanocomposite membrane literature.

The aggregate size distributions are wide, and no single microscopic technique can capture the full range of aggregates. Both AFM and TEM have limitations, and future work in this field is required to allow for accurate measurement of aggregate size and interparticle as well as interaggregate spacing. The data presented in this manuscript represent a step towards that goal.

The aggregates are sufficiently small that inter-aggregate spacing should be on the order of nanometers. Using Eq. (1.2) and the average aggregate size determined from AFM, the inter-aggregate spacing would be approximately 9 ±3 nm and 11 ±6 nm in PTMSP containing 3 and 10 nominal volume percent TiO_2, respectively. The higher inter-aggregate spacing in the sample at higher particle loading reflects the larger average aggregate size in the sample containing a higher loading of particles. In principle, increasing particle loading should decrease interparticle spacing, if the particle size is constant. However, the particles exhibit a stronger tendency to aggregate at higher loadings, which would act to increase spacing between particle aggregates. The reported values reflect the competition between these opposing factors. These inter-aggregate spacings are smaller than the persistence length for PTMSP, which is 48 nm.[14] Thus, one might expect the dispersion of these particles in PTMSP to significantly influence chain packing and, in turn, transport properties.

In a two phase system, the area fraction of each phase should be similar to its true volume fraction.[15] The nanoparticle area fractions are 0.04 and 0.16 cm^2 nanoparticles per cm^2 of nanocomposite for the films containing 3 and 10 nominal volume percent TiO_2, respectively (*i.e.,* 3.5 and 8.9 true volume percent). The area of the image occupied by nanoparticles was calculated as the sum of the area occupied by aggregates, determined from the ImageJ analysis, divided by the total image area considered for the calculation. These calculations are sensitive to aggregate shape, which is taken to be spherical, and to the resolution limit of the AFM. The errors associated with AFM resolution and aggregate shape may account for at least some of the difference between the aggregate area and the nominal volume fraction. Also, if voids are located in the aggregates, the AFM may overestimate the area fraction of nanoparticles, since not all of the resolved aggregate would be in the same plane.

While TEM is not useful for resolving the fine structure of the composites due to sample instability at high magnification, it can image larger structural features since the instability issues are markedly diminished at low magnification. TEM differentiates between materials by electron density, so it is possible to distinguish regions of high and low particle loadings.[2] As indicated in Figure 4.3a, at low TiO_2 loading (*i.e.,* 3 nominal volume percent), micron-sized aggregates were present. The light colored region within the nanoparticle aggregate may be void space, however; this void could be an artifact of sample preparation rather than a structural feature of the aggregate. As shown in Figure 4.3b, the aggregate concentration and size were higher in the sample containing 10 nominal volume percent TiO_2. The aggregates may be caused by the polymer's inability to disperse particles at high loadings, which results in less effective mixing at higher particles loadings.

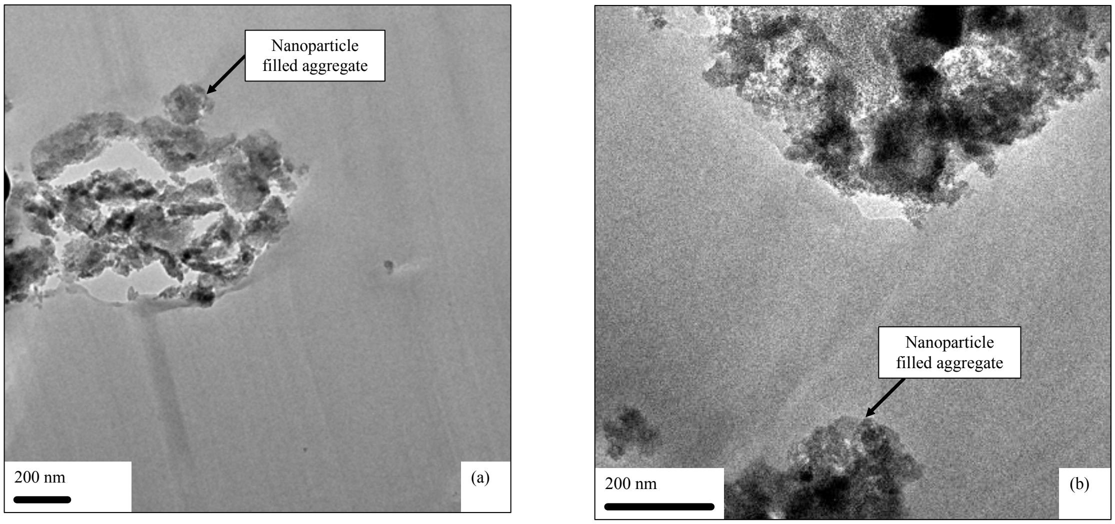

Figure 4.3. TEM images of (a) PTMSP containing 3 nominal volume percent TiO_2, and (b) PTMSP containing 10 nominal volume percent TiO_2.

Figure 4.4a presents experimental nanocomposite density, ρ_{Exp}, as a function of TiO_2 concentration at particle loadings less than 6 volume percent. At these loadings, the nanocomposite density is perhaps slightly greater than predicted by the additive model (*i.e.,* Eq. (2.20)), although the deviation between the model and the data is near the resolution of the measurement. Thus, the nanocomposites exhibit slightly more compact structures than expected based on pure component properties. Such deviations could also be observed if there were errors in the pure polymer or pure particle density. For ρ_{Exp} to equal ρ_{Add} at the highest loading considered in Figure 4.4a would require the polymer density to be 0.80 g/cm^3 (rather than 0.75 g/cm^3) or require the particle density to be 4.5 g/cm^3 (rather than 3.7 g/cm^3). The reported error in particle density (*i.e.,* ± 0.05 g/cm^3) is too small to account for the observed difference between ρ_{Exp} and ρ_{Add}. Based on the uncertainty in the polymer density measurements (*i.e.,* ± 7 percent), the difference between ρ_{Exp} and ρ_{Add} may be insignificant at the loadings shown in Figure 4.4a. However, as presented later, the permeability data are also consistent with densification occurring in nanocomposites containing less than 0.07 nominal volume percent TiO_2.

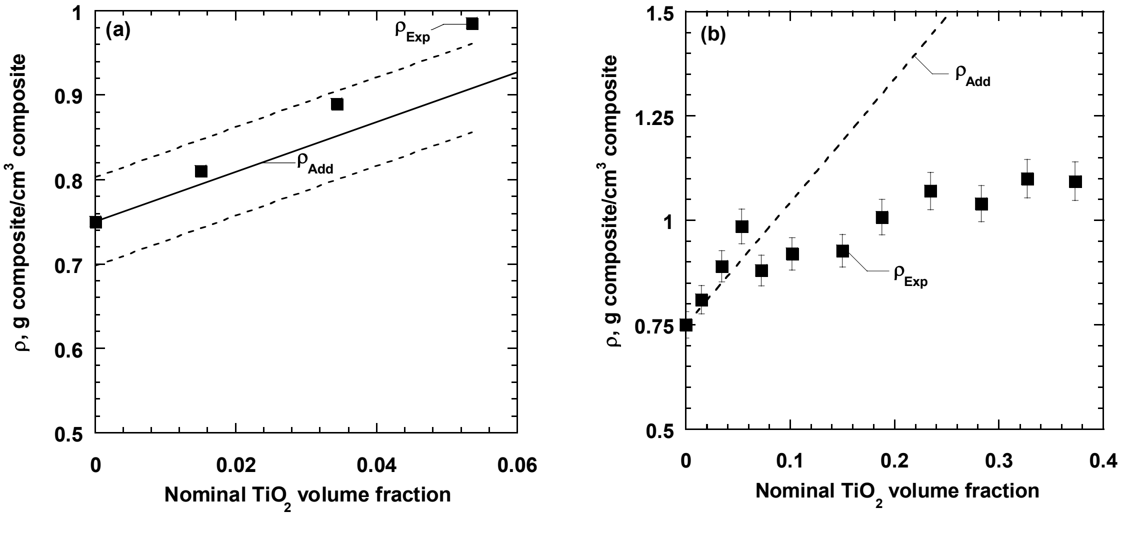

Figure 4.4. Effect of TiO_2 concentration in nanocomposites on experimental density (ρ_{Exp}, ■) at low particle loadings (a) and over the full range of particle loadings (b). The solid line represents the additive density, ρ_{Add}, calculated Eq. (2.20). Error bars were estimated from the standard deviation in density for multiple experiments at each point according to the propagation of errors method described by Bevington.[13] In Figure 4.4a, the dashed lines represent the possible ρ_{Add} values based on this uncertainty analysis.

Figure 4.4b presents nanocomposite density data over a much wider composition range. At TiO_2 concentrations higher than 7 volume percent, the deviation between ρ_{Exp} and ρ_{Add} increased significantly with increasing TiO_2 content. One interpretation of this observation is the creation of void space (*i.e.,* volume containing neither polymer chains nor particles) within the composite. The density experiments provide a macroscopic indicator consistent with the presence of such voids, but they do not reveal how the void volume is distributed within the composite.

There is an apparent discontinuity between decreasing void volume fraction at increasing particle loadings up to around 0.07 ϕ_F^N, and a positive and increasing void volume fraction as TiO_2 concentration increases beyond 0.07 nominal volume fraction. It is not clear why this discontinuity occurs.

The difference between the experimental and additive density can be characterized in terms of an apparent void volume fraction resulting from mixing the particles with the polymer. Figure 4.5 presents ϕ_V values calculated using Eq. (2.22). ϕ_V decreases with increasing particle content up to about 6 volume percent particles. However, the uncertainty in these estimated ϕ_V values is high, and the ϕ_V values are, of course, sensitive to the pure polymer and pure particle density values, so any deviations in ρ_P or ρ_F would directly impact ϕ_V. Native PTMSP has a very high fractional free volume (FFV) (*i.e.,* void space within the polymer structure) of 0.29.[10] The physical significance of negative ϕ_V values could indicate that the particles are reducing this free volume.

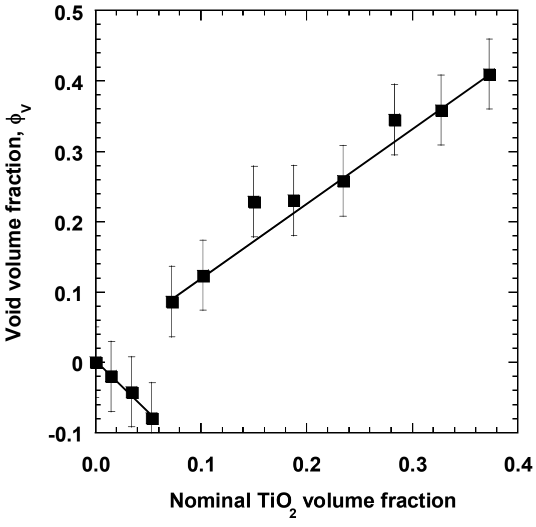

Figure 4.5. Calculated void volume fraction in PTMSP/TiO_2 nanocomposite films. Error bars were estimated from the standard deviation in density for multiple experiments at each point according to the propagation of errors method described by Bevington.[13]

In contrast, at particle loadings greater than 7 nominal volume percent, ϕ_V values are significantly greater than zero and increase approximately linearly with particle loading. The void space may exist in macrovoids (*i.e.,* void volumes that are larger than the inherent polymer free volume elements) within the composite. These macrovoids could occur within the nanoparticle aggregates, at the nanoparticle-polymer interface, or as a result of nanoparticle-induced disruption of polymer chain packing. This macroscopic measure of the presence of such voids does not distinguish between these various contributions, and each of these mechanisms could contribute to the observed void volume. Such morphologies have been proposed for other glassy polymer based nanocomposites.[2]

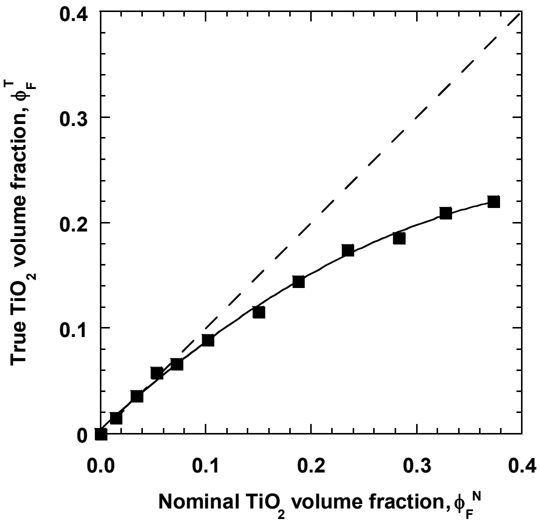

Figure 4.6. Comparison of true particle volume fraction and nominal particle volume fraction TiO_2 in PTMSP/TiO_2 nanocomposite films as calculated using Eq. (2.23). The dashed line represents the case where true and nominal volume fractions are equal and is shown for comparison. The solid line is drawn to guide the eye.

Figure 4.6 presents the true volume fraction of TiO_2, calculated using Eq. (2.23), as a function of the nominal particle volume fraction in PTMSP/TiO_2 nanocomposites. The voids in the nanocomposites cause the true nanoparticle volume fraction (and the true polymer volume fraction) to be considerably lower than their nominal values over much of the range of particle concentrations explored. The difference between true and nominal volume fractions becomes more significant at high loadings, where ϕ_F^T is as much as 40% lower than ϕ_F^N. Therefore, even at high nominal volume fractions, the true volume fraction of particles is still below the fundamental limits of particle packing (*i.e.,* 0.583 in a body centered cubic lattice, or 0.491 in a randomly packed lattice).[16,17]

Gas transport

As presented in Figures 4.7a and 4.7b, at low TiO_2 particle loadings light gas (*i.e.,* CO_2, CH_4, N_2, H_2) permeability decreased as particle loading increased. Although the trend agrees qualitatively with composite models such as Maxwell's model (*i.e.,* gas permeability decreases as impermeable filler content increases), the 50 percent permeability reduction at 5 percent particle loading greatly exceeds the reduction expected based on Maxwell's model, which predicts a 7.5 percent permeability reduction at an impermeable particle loading of 5 volume percent.[8]

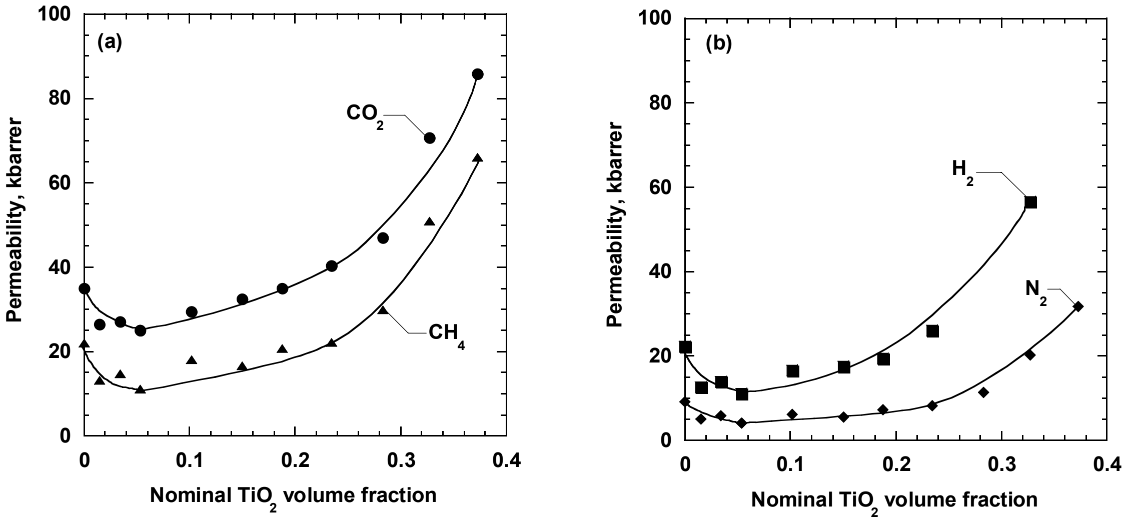

Figure 4.7. Effect of TiO_2 concentration on (a) CO_2 (●), CH_4 (▲), (b) H_2 (■), and N_2 (♦) permeability at $\Delta p = 3.4$ atm and 35 ^{o}C. The lines are drawn to guide the eye.

The magnitude of the initial permeability reduction is more consistent with the gas transport behavior of PTMSP filled with trimethylsilylglucose, where the nanoparticles block/fill free volume elements of the polymer (*cf.*, Figure 2.1).[18] The particle loadings at which permeability was less than that of the unfilled polymer coincided with the loadings where density is slightly greater than predicted by Eq. (2.20), which is consistent with the nanoparticles acting to reduce the polymer free volume. The size of the free volume elements in PTMSP has been studied using positron annihilation lifetime spectroscopy.[19] These studies report a bimodal distribution of free volume elements with characteristic dimensions of 2.5 to 4.0 and 5 to 7.5 Å, respectively.[19] The free volume elements are substantially smaller than the 3 nm primary particle diameter reported for TiO_2. Therefore, it is unlikely that such free volume elements could be occupied by particles. However, the presence of the particles in the initial casting solution may influence the processing history (solvent removal rate, etc.) in such a way as to slightly increase polymer density, thereby lowering permeability.

At higher particle loadings (*i.e.,* greater than 7 volume percent), light gas permeability increased with increasing particle loading (*cf.*, Figure 4.7). This is the same concentration range where ρ_{Exp} was significantly lower than ρ_{Add} (*cf.*, Figure 4.4a) and apparent void volume, ϕ_V, was significantly greater than zero (*cf.*, Figure 4.5).

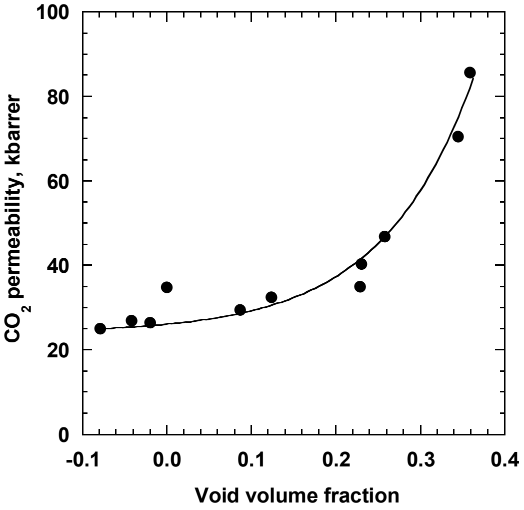

Figure 4.8. Effect of void volume fraction as calculated by Eq. (2.22) on CO_2 permeability, where the trend line is drawn to assist the eye. The experimental data were collected at 35 °C and $\Delta P = 3.4$ atm.

Often, the natural logarithm of permeability is linearly related to the inverse of the polymer fractional free volume.[20] However, in this study, permeability does not obey such a model, even when the void volume fraction is included in the overall fractional free volume. As shown in Figure 4.8, permeability is roughly correlated with nanocomposite void volume fraction. The trend illustrated for CO_2 is consistent with the trends observed for H_2, CH_4 and N_2.

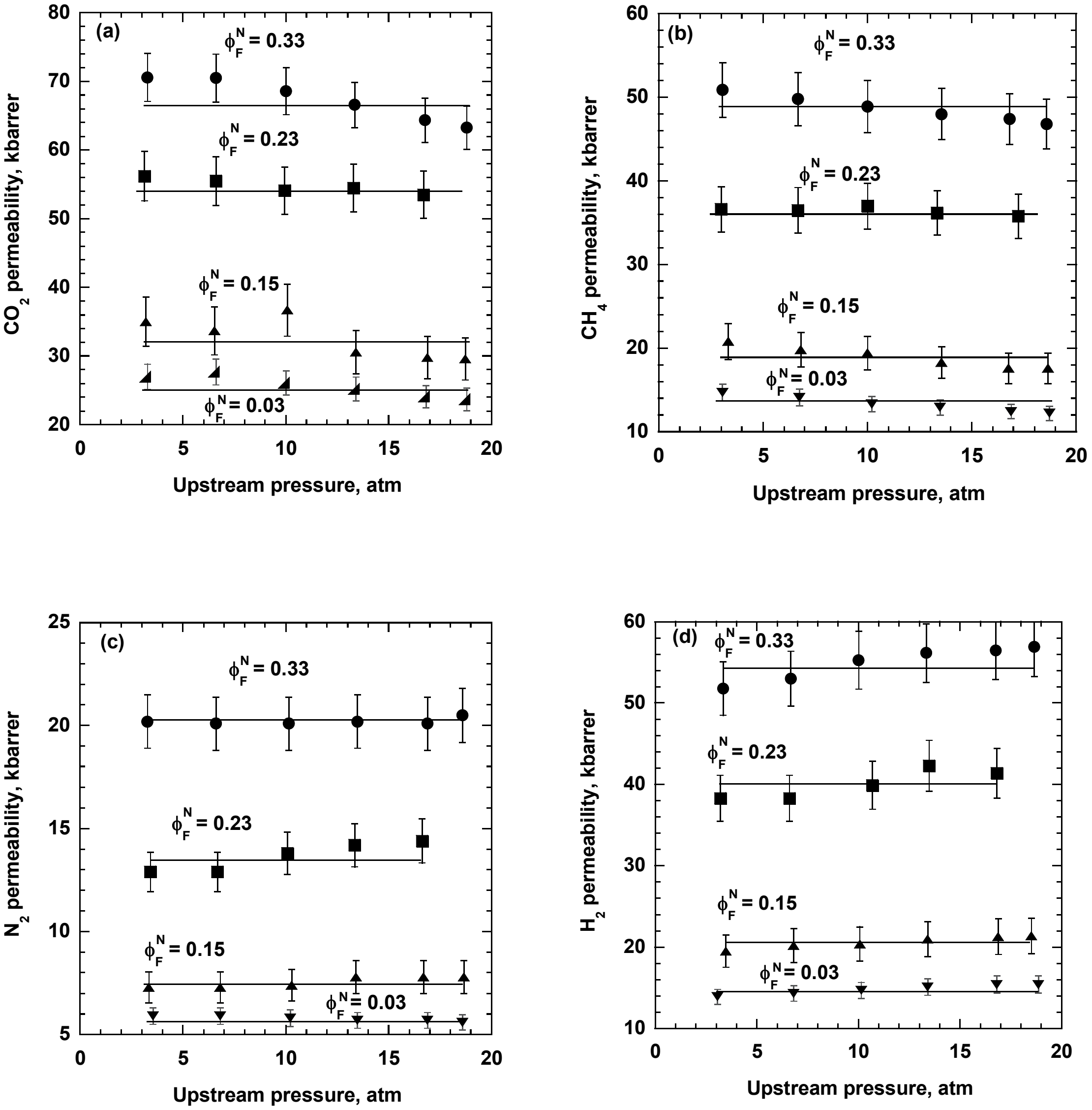

Figure 4.9. Effect of upstream pressure on pure gas permeability of PTMSP containing various nominal volume fractions, ϕ_F^N, of TiO_2 for (a) CO_2, (b) CH_4, (c) N_2, and (d) H_2. These measurements were conducted at 35 °C. Error bars were estimated from the standard deviation in permeability for multiple experiments at each point according to the propagation of errors method described by Bevington.[13] The solid lines are provided to guide the eye.

In principle, permeability enhancements could also be caused by trans-film defects. Two methods to test for defects rely on measuring the pressure dependence of permeability and comparing selectivity values with those observed in porous systems. First, a trans-film defect can cause the apparent gas permeability to increase with increasing feed pressure.[21,22] Figures 4.9a through 4.9d present the influence of upstream pressure on permeability of four gases for films of varying TiO_2 content. In the TiO_2/PTMSP nanocomposites, the permeability values for both CO_2 and CH_4 decrease with increasing feed pressure, which is in agreement with the literature.[23] While the permeability of N_2 and H_2 did not readily exhibit a reduction in permeability with increasing feed pressure, such as has been reported elsewhere for PTMSP,[23] these results are consistent for permeability results in nanoparticle filled PTMSP.[21]

Another method to test for trans-film defects involves penetrant selectivity. When a trans-film defect is present, selectivity often tends towards the Knudsen limit, $\alpha^{K}_{A/B}$, or the Poiseuille limit, $\alpha^{P}_{A/B}$. Knudsen selectivity is given by:[24]

$$\alpha^{K}_{A/B} = \sqrt{\frac{M_B}{M_A}} \tag{4.1}$$

where M_A and M_B are the molar masses of species A and B. The Poiseuille limit for selectivity is given by:[25]

$$\alpha^{P}_{A/B} = \frac{\mu_B}{\mu_A} \tag{4.2}$$

where μ_A and μ_B are the viscosities of gas A and B, respectively. The selectivity values presented in this study were calculated as the ratio of pure gas permeability coefficients (*cf.,* Eq. (2.12)). Therefore, the selectivity in Eq. (4.2) is based on the ratio of pure gas permeability coefficients for a pair of pure gases undergoing Poiseuille flow in a cylindrical tube.[16,18] Obviously, if mixtures of gases were copermeated in Poiseuille flow through a cylindrical tube, the selectivity would be 1 (*i.e.*, the flow would be non-selective).[16]

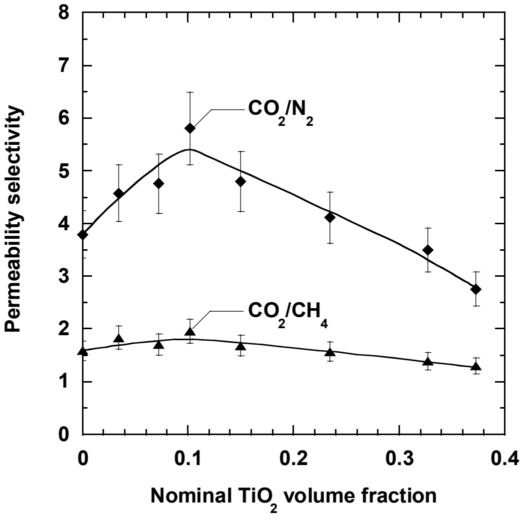

Figure 4.10. Effect of TiO_2 concentration on pure gas CO_2/N_2 (♦) and CO_2/CH_4 (▲) selectivity at Δp = 3.4 atm. Measurements were made at 35 °C and atmospheric downstream pressure. Trend lines are drawn to guide the eye. Error bars were estimated from the standard deviation in permeability for multiple experiments at each point according to the propagation of errors method described by Bevington.[13]

Pure gas CO_2/CH_4 and CO_2/N_2 selectivities are presented as a function of TiO_2 particle loading in Figure 4.10. Other pure gas selectivities are recorded in Table 4.1. While there is a hint of a maximum in the CO_2/N_2 selectivity, the uncertainties in the measurement are near a level that makes it difficult to draw a definitive conclusion regarding this issue. Therefore, selectivity changes, at most, modestly with particle loading. The CO_2/CH_4 and CO_2/N_2 selectivities were not at their Knudsen (*i.e.,* 0.6 and 0.8, respectively) or Poiseuille limits (*i.e.,* 0.7 and 1.2, respectively) at any particle concentration. Therefore, based on the pressure independence of permeability and the fact that selectivities are far from values associated with porous materials, the PTMSP/TiO_2 nanocomposite films are presumed to be defect free at or below 38 nominal volume percent particles. In nanocomposites films containing more than 38 volume percent particles, the CO_2/CH_4 and CO_2/N_2 selectivities were indicative of the presence of transmembrane defects in the nanocomposites at such high particle concentrations.

Table 4.1. Light gas selectivity of TiO_2 filled PTMSP at 35 °C and Δp = 3.4 atm

ϕ_{F,TiO_2}^{N}	$\alpha_{\frac{CO_2}{H_2}}$	$\alpha_{\frac{CO_2}{CH_4}}$	$\alpha_{\frac{CO_2}{N_2}}$	$\alpha_{\frac{H_2}{CH_4}}$	$\alpha_{\frac{H_2}{N_2}}$	$\alpha_{\frac{CH_4}{N_2}}$
0.00	1.6 ± 0.2	1.6 ± 0.3	3.8 ± 0.7	1.0 ± 0.2	2.4 ± 0.4	2.4 ± 0.4
0.03	1.9 ± 0.3	1.8 ± 0.3	4.6 ± 0.9	0.9 ± 0.2	2.4 ± 0.4	2.5 ± 0.4
0.07	1.8 ± 0.3	1.6 ± 0.2	4.8 ± 0.9	0.9 ± 0.2	2.7 ± 0.5	2.9 ± 0.5
0.10	1.9 ± 0.3	2.0 ± 0.4	5.8 ± 1.0	1.1 ± 0.2	3.1 ± 0.5	3.0 ± 0.5
0.15	1.8 ± 0.3	1.7 ± 0.3	4.8 ± 0.9	0.9 ± 0.2	2.7 ± 0.5	2.8 ± 0.5
0.23	1.7 ± 0.3	1.6 ± 0.3	4.1 ± 0.8	0.9 ± 0.2	2.5 ± 0.4	2.6 ± 0.5
0.33	1.2 ± 0.2	1.4 ± 0.2	3.5 ± 0.6	1.1 ± 0.2	2.8 ± 0.5	2.5 ± 0.4

Error bars were estimated from the standard deviation in permeability for multiple experiments at each point according to the propagation of errors method described by Bevington.[13]

Permeability changes derive from changes in penetrant diffusivity, penetrant solubility, or both. Both inorganic fillers and the polymer matrix sorb light gases. PTMSP is a glassy polymer, and its sorption behavior follows the dual mode sorption model:[26]

$$C_P = k_D + \frac{C_H^{'} bp}{1 + bp} \tag{4.3}$$

where C_P is the equilibrium penetrant concentration, k_D is the Henry's law constant, $C_H^{'}$ is the Langmuir sorption capacity, and b is the Langmuir affinity constant. Figure 4.11 presents CO_2, CH_4 and N_2 sorption in unfilled PTMSP at low pure penetrant pressures calculated using the dual mode parameters reported by Merkel *et al.*; these parameters are recorded in Table 4.2.[27]

The low pressure adsorption isotherms of CO_2, CH_4, and N_2 on TiO_2 nanoparticles are also shown in Figure 4.11. These data are described by the empirical Freundlich model:[28]

$$C_F = Kp^{\frac{1}{n}} \tag{4.4}$$

where C_F is the equilibrium penetrant concentration, and K and n are temperature dependent fitting parameters. Values for these parameters are listed in Table 4.2 for the adsorption of CO_2, CH_4, and N_2 on TiO_2 nanoparticles. Many empirical equations can be used to estimate the effect of pressure on gas adsorption on mineral surfaces; the Freundlich model (*i.e.,* Eq. (4.4)) was used because it does not impose a limit on gas adsorption on particle surfaces.[28] For comparison, the Langmuir model accurately estimates the nanoparticle gas adsorption in Figure 4.12. However, the Langmuir model does not accurately predict the sorption behavior of the nanocomposites, as discussed below.

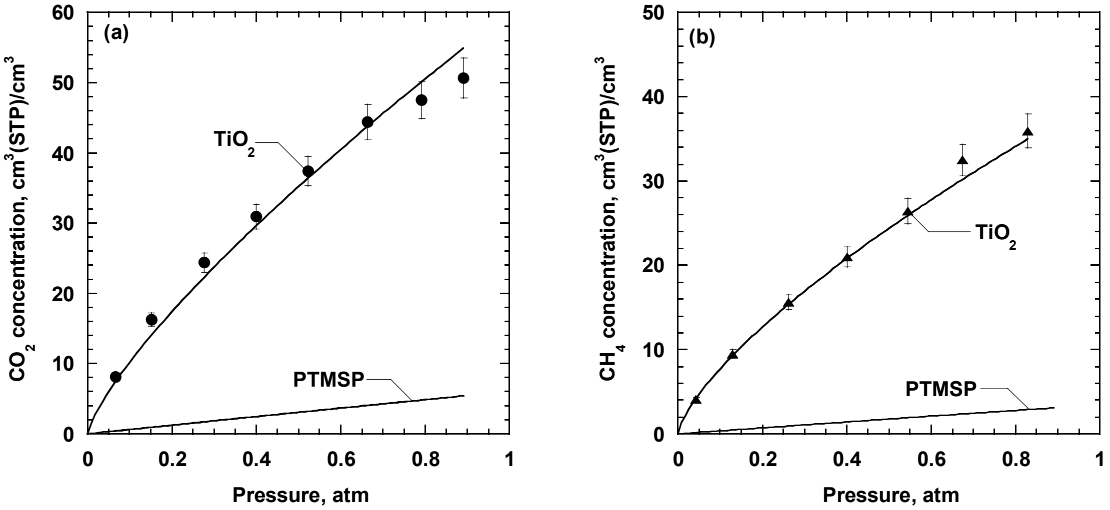

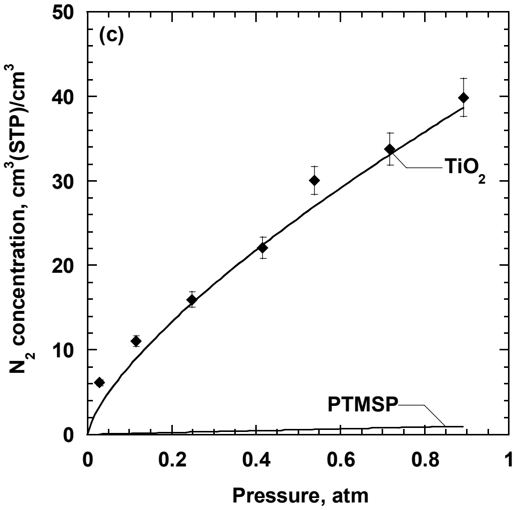

Figure 4.11. Calculated sorption isotherm in PTMSP and experimental adsorption isotherm on TiO_2 particles at 35 °C for pure (a) CO_2, (b) CH_4 and (c) N_2. The PTMSP sorption isotherms are calculated using dual mode model parameters from Merkel *et al.*[27] The line through TiO_2 data represents a best fit to the Freundlich model.[28] Error bars were estimated from the standard deviation in concentration for multiple experiments at each point according to the propagation of errors method described by Bevington.[13]

Table 4.2. Freundlich isotherm parameters for adsorption onto TiO_2 and dual mode sorption parameters for PTMSP at 35 °C

Penetrant	$K, \frac{cm^3(STP)}{cm^3 TiO_2 \ atm^{\frac{1}{n}}}$	n, -	$k_D, \frac{cm^3(STP)}{cm^3 PTMSP \ atm}$	$C'_H, \frac{cm^3(STP)}{cm^3 PTMSP}$	$b, \frac{1}{atm}$
N_2	42 ± 2.89	1.43 ± 0.02	0.1	74	0.14
CH_4	40 ± 2.63	1.43 ± 0.02	0.5	62	0.05
CO_2	60 ± 4.05	1.29 ± 0.02	1.1	130	0.02

The Freundlich isotherm parameter uncertainties are estimated using the least-squares fit method.[13]. PTMSP dual mode sorption parameters are from the literature.[27]

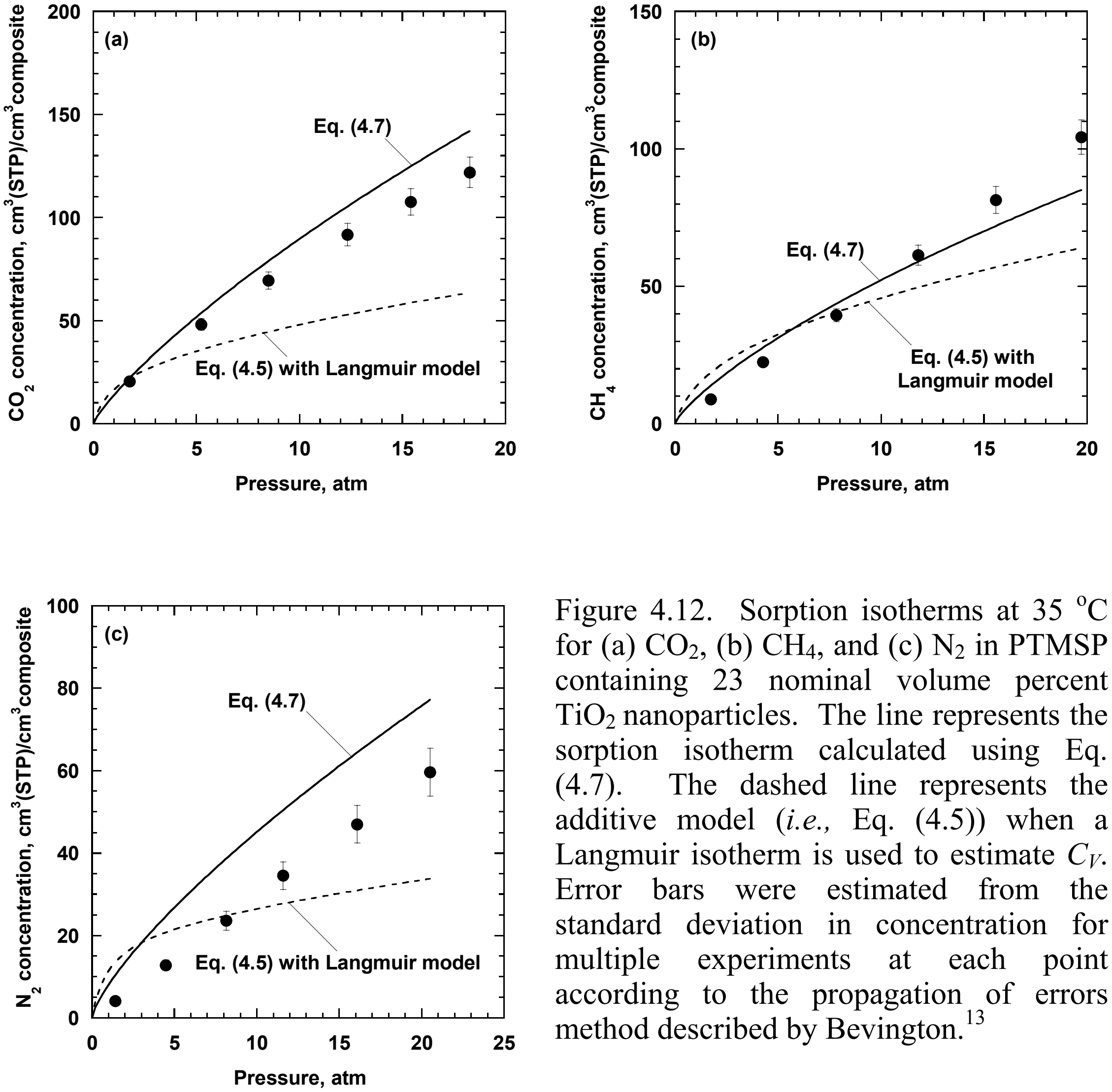

Figure 4.12. Sorption isotherms at 35 °C for (a) CO_2, (b) CH_4, and (c) N_2 in PTMSP containing 23 nominal volume percent TiO_2 nanoparticles. The line represents the sorption isotherm calculated using Eq. (4.7). The dashed line represents the additive model (*i.e.,* Eq. (4.5)) when a Langmuir isotherm is used to estimate C_V. Error bars were estimated from the standard deviation in concentration for multiple experiments at each point according to the propagation of errors method described by Bevington.[13]

If incorporation of nanoparticles does not cause any deviation in either the polymer or particle phase gas sorption properties, then the gas sorption level in the nanocomposite, C_C, could be estimated by an additive combination of the sorption properties of the independent phases (*i.e.,* filler, polymer, and voids):[29]

$$C_C = \left(\phi_F^N C_F + \left(1-\phi_F^N\right) C_P\right)\left(1-\phi_V\right) + \phi_V C_V \tag{4.5}$$

The concentration of gas in the voids volume, C_V, is given by the gas law:

$$C_V = \left(\frac{p}{RT}\right) \tag{4.6}$$

where T is the experimental temperature (K), and R is the gas constant. $\left(1-\phi_V\right)$ is used in this calculation to correct the nominal filler and polymer volume fractions to true volume fractions.

Substituting Eqs. (4.3), (4.4) and (4.6) into Eq. (4.5) yields:

$$C_C = \left(\phi_F^N K p^{\frac{1}{n}} + \left(1-\phi_F^N\right)\left(k_D + \frac{C_H' bp}{1+bp}\right)\right)\left(1-\phi_V\right) + \phi_V \frac{p}{RT} \tag{4.7}$$

where the adsorption isotherm for light gases on TiO_2 has been extrapolated beyond the measurement range of 1 atm using the parameters listed in Table 4.2. As shown in Figure 4.12, the gas sorption levels in the nanocomposites were slightly less than those predicted by Eq. (4.7) over the range of loadings tested. Such discrepancies have been reported for gas sorption in composites prepared by dispersing ZnO particles in natural rubber, and they were attributed to wetting of the particle surface by the polymer, because the polymer occupies potential sorption sites on the particles.[29] This phenomenon competes with gas adsorption on the particle surface and acts to reduce the total amount of gas sorbed by the composite relative to that expected based on the pure polymer and filler sorption properties.[29] Similar effects may occur in TiO_2 filled PTMSP nanocomposites.

When a Langmuir isotherm was used to predict C_F in Eq. (4.5) the resulting fit to the experimental data was much poorer than that obtained by using the Freundlich model (*cf.*, Figure 4.12).

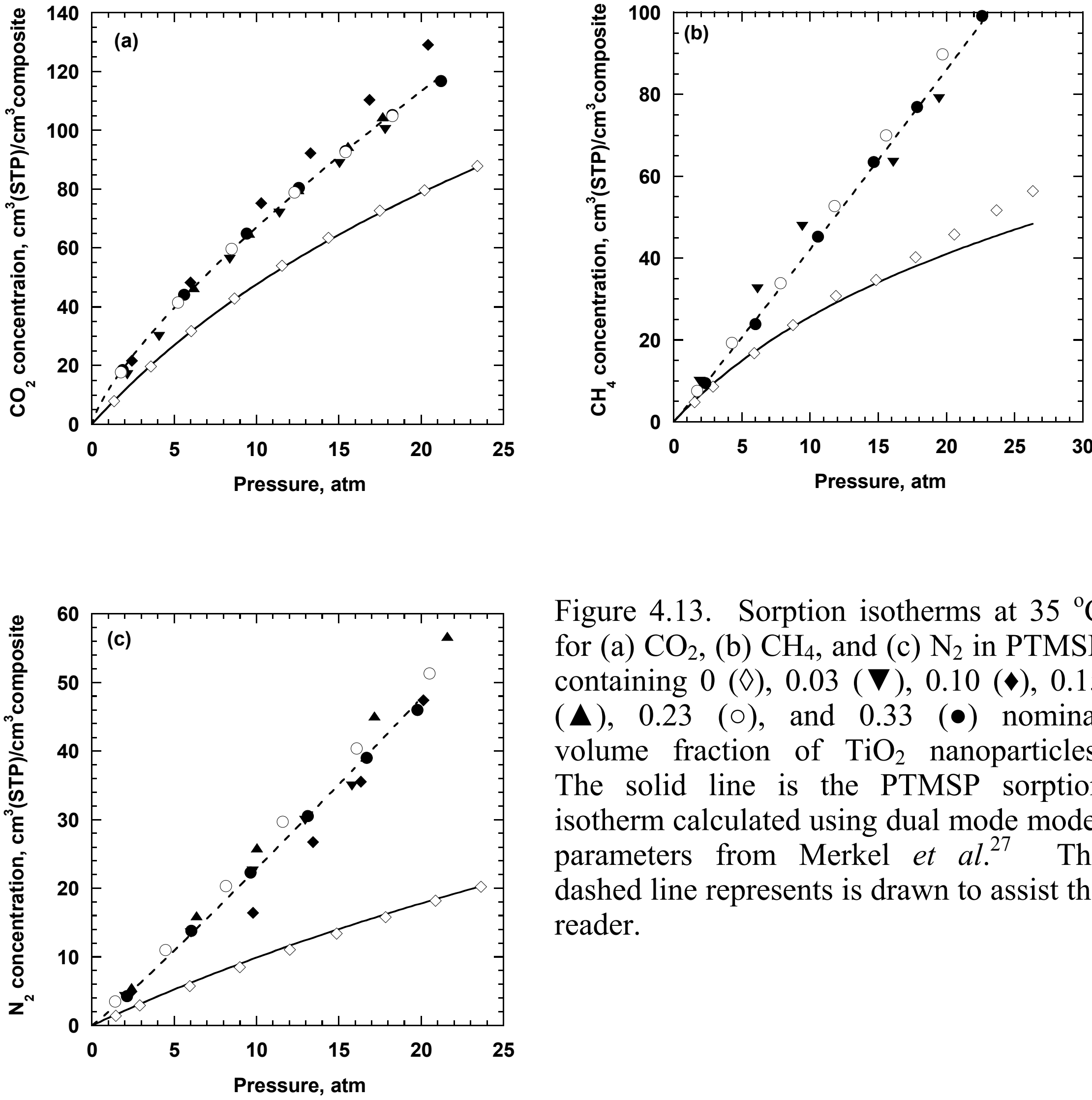

Figure 4.13. Sorption isotherms at 35 °C for (a) CO_2, (b) CH_4, and (c) N_2 in PTMSP containing 0 (◊), 0.03 (▼), 0.10 (♦), 0.15 (▲), 0.23 (○), and 0.33 (●) nominal volume fraction of TiO_2 nanoparticles. The solid line is the PTMSP sorption isotherm calculated using dual mode model parameters from Merkel *et al.*[27] The dashed line represents is drawn to assist the reader.

The extent to which nanoparticle content influences gas sorption varies among the gases. The nanoparticles adsorb 9.3, 12, and 20 times more CO_2, CH_4, and N_2, respectively, than an equivalent volume of unfilled PTMSP at 35 ^{o}C and 1 atm (*cf.*, Figure 4.11). As shown in Figure 4.13, the experimental CO_2 concentration was over 50% higher in a nanocomposite sample than in an unfilled PTMSP film, (*i.e.,* 130 cm^3(STP)/cm^3 in PTMSP containing 33 nominal volume percent TiO_2, and 80 cm^3(STP)/cm^3 in PTMSP at 20 atm). The increase in CH_4 and N_2 sorption levels in PTMSP containing 33 nominal volume percent TiO_2 were 90% and 160% higher than in unfilled PTMSP, respectively. Values for permeability, solubility, and diffusion coefficients for PTMSP films containing varying concentrations of TiO_2 are listed in Table 4.3.

In Figure 4.13 the light gas concentration in the nanocomposites appears to follow the same trend and have nearly the same values at all sample loadings. This is an artifact of the manner in which concentration is reported. When light gas concentration is presented in units of cm^3(STP)/(cm^3 nanocomposite), where void volume is included in the nanocomposite volume, the light gas concentration falls, more or less, on a single trend line. However, when light gas concentration is presented in units of cm^3(STP)/(cm^3 nanocomposite solids), where the nanocomposite solids include only the volume of polymer and the volume of particles in the nanocomposite, the light gas concentration increases with increasing particle loadings over the range of pressures investigated, as shown in Figure 4.14. This result is consistent with substantial gas adsorption on the particles in the nanocomposite.

Table 4.3. CO_2, N_2, and CH_4 permeability, solubility, and diffusion coefficients in TiO_2 filled PTMSP at 35 °C

ϕ_{F,TiO_2}^{N}	Permeability[a], kbarrer			Solubility[b], $\frac{cm^3(STP)}{cm^3\ atm}$			Diffusivity[c] x 10^6, $\frac{cm^2}{s}$		
	CO_2	N_2	CH_4	CO_2	N_2	CH_4	CO_2	N_2	CH_4
0.00	35 ± 4	9.2 ± 0.9	22 ± 2	5.5 ± 0.5	1.1 ± 0.1	2.8 ± 0.3	48 ± 7	63 ± 9	60 ± 9
0.03	27 ± 3	5.9 ± 0.6	15 ± 2	6.8 ± 0.7	2.2 ± 0.2	4.8 ± 0.5	30 ± 4	20 ± 3	23 ± 3
0.07	30 ± 3	6.2 ± 0.6	18 ± 2	5.3 ± 0.5	2.1 ± 0.2	4.4 ± 0.4	43 ± 6	23 ± 3	31 ± 4
0.10	33 ± 3	5.6 ± 0.6	17 ± 2	7.5 ± 0.8	2.1 ± 0.2	5.7 ± 0.6	33 ± 5	21 ± 3	22 ± 3
0.15	35 ± 4	7.3 ± 0.7	21 ± 2	7.5 ± 0.8	2.5 ± 0.3	8.5 ± 2.0	36 ± 5	22 ± 3	19 ± 7
0.23	56 ± 5	13 ± 1	36 ± 3	7.5 ± 0.8	2.5 ± 0.3	4.5 ± 0.5	57 ± 8	39 ± 6	61 ± 9
0.33	71 ± 7	20 ± 2	51 ± 5	7.5 ± 0.8	2.2 ± 0.2	4.1 ± 0.1	72 ± 10	70 ± 10	93 ± 13

[a] The upstream pressure was 7.4 atm, and the downstream pressure was 1 atm.

[b] The solubility coefficients were determined by linearly interpolating the data in Figure 4.13 to 7.4 atm.

[c] The diffusion coefficients were calculated from permeability and solubility using Eq. (2.9).

Uncertainties in permeability, solubility and diffusion coefficients were estimated using the propagation of errors method.[13]

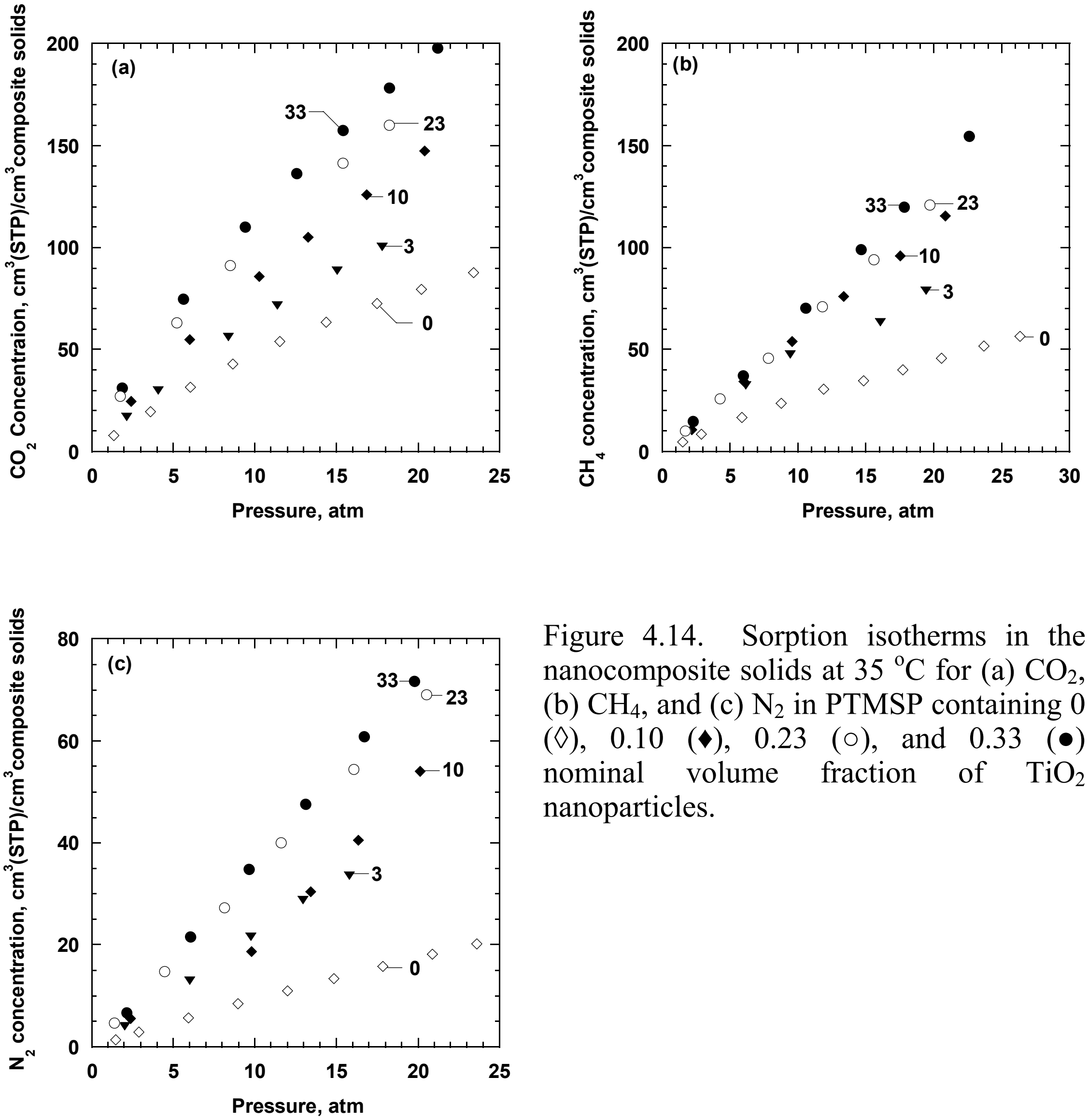

Figure 4.14. Sorption isotherms in the nanocomposite solids at 35 °C for (a) CO_2, (b) CH_4, and (c) N_2 in PTMSP containing 0 (◊), 0.10 (♦), 0.23 (○), and 0.33 (●) nominal volume fraction of TiO_2 nanoparticles.

Estimation of light gas diffusion coefficients from steady state permeability data requires gas solubility data. Therefore, the experimental sorption data in Figure 4.13 were linearly interpolated to calculate solubility coefficients as a function of pressure using Eq. (2.8), and the resulting solubility coefficients are presented in Figure 4.15. CO_2

solubility decreased with increasing pressure in the unfilled polymer as well as the nanocomposites. The N_2 and CH_4 solubility in the nanocomposites are relatively pressure independent. The observed solubility behavior for these gases is consistent with previously reported light gas solubility in PTMSP based nanocomposites.[21]

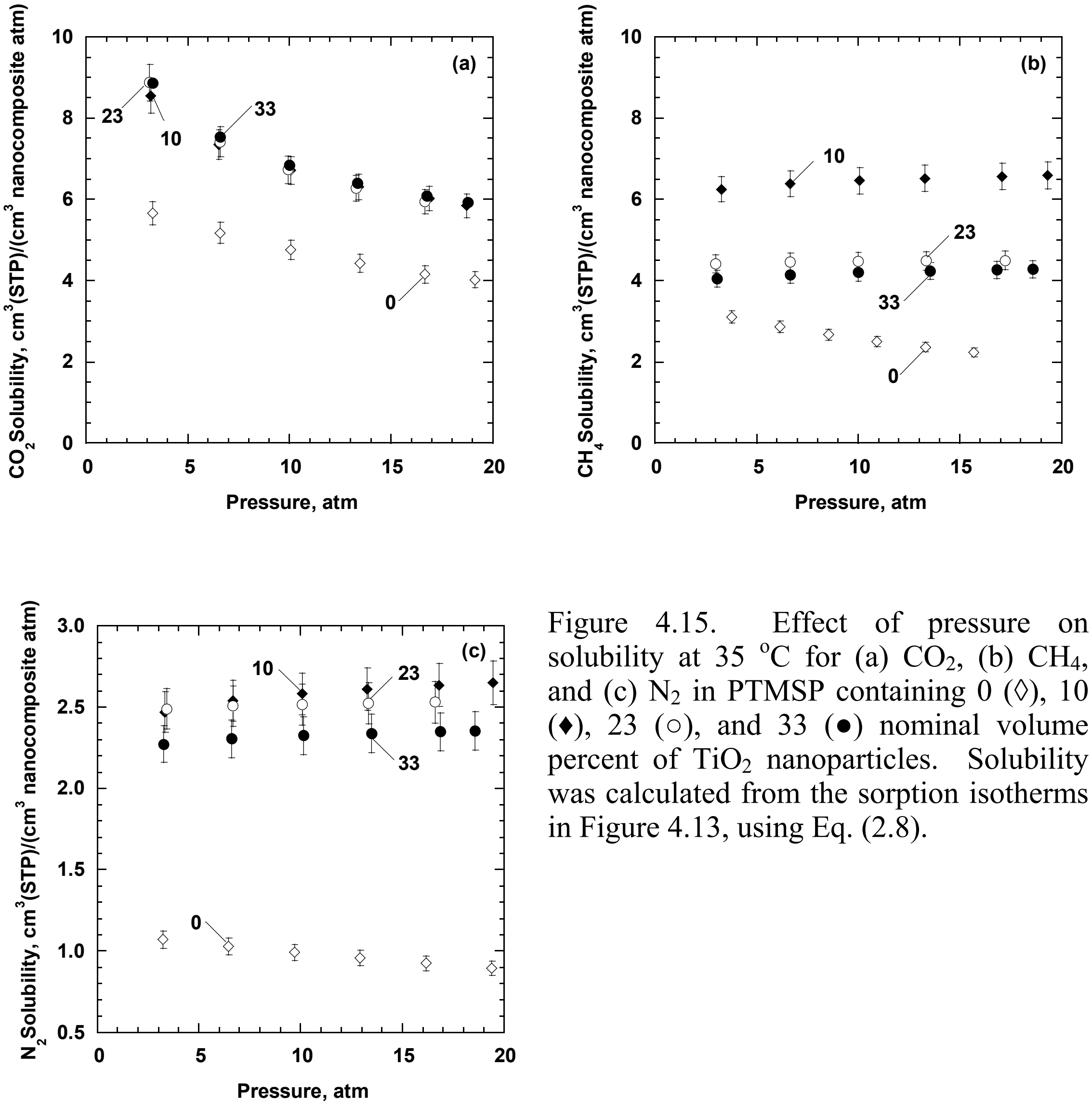

Figure 4.15. Effect of pressure on solubility at 35 °C for (a) CO_2, (b) CH_4, and (c) N_2 in PTMSP containing 0 (◊), 10 (♦), 23 (○), and 33 (●) nominal volume percent of TiO_2 nanoparticles. Solubility was calculated from the sorption isotherms in Figure 4.13, using Eq. (2.8).

The influence of particle content on gas permeability can only partially be attributed to the effect of particles on gas solubility. For instance, at 6 atm CO_2, solubility is 36 percent higher in PTMSP containing 33 volume percent TiO_2 than in unfilled PTMSP. However, CO_2 permeability in PTMSP containing 33 volume percent TiO_2 is twice that of the unfilled polymer. Thus, the particles also affect gas diffusivity.

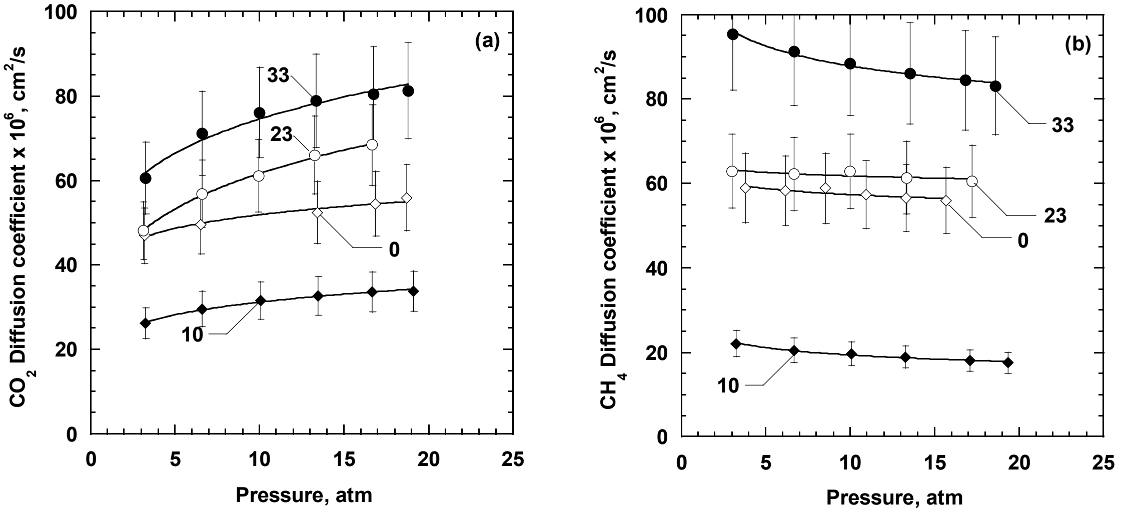

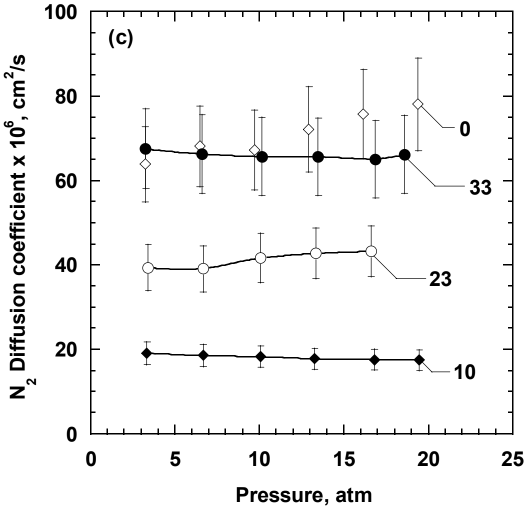

Figure 4.16. Concentration averaged diffusion coefficients for (a) CO_2, (b) CH_4, and (c) N_2 in PTMSP containing 0 (◊), 10 (♦), 23 (○), and 33 (●) nominal volume percent of TiO_2 nanoparticles. The diffusion coefficients were calculated from the permeability and solubility for each penetrant in each nanocomposite film using Eq. (2.9). The permeability used in these calculations came from experimental results, and solubility was linearly interpolated to the upstream pressure of the permeability experiments. Trend lines are drawn to guide the eye. Error bars were estimated from the propagation of errors method described by Bevington.[13]

Figure 4.16 presents diffusion coefficients for CO_2, N_2, and CH_4 in PTMSP filled with TiO_2. The diffusion coefficients were calculated from the permeability and solubility in each nanocomposite film using Eq. (2.9). The permeability used in these calculations came from experimental results, and solubility was linearly interpolated at the upstream pressure at which the corresponding permeability.

The diffusion coefficients of CO_2, N_2, and CH_4 in nanocomposites containing 10 nominal volume percent TiO_2 are lower than the diffusion coefficients of unfilled PTMSP, which is consistent with the permeability data presented in Figure 4.7. At particle loadings of 23 and 33 nominal volume percent, the diffusion coefficients were higher than those of the film containing 10 nominal volume percent TiO_2, and for CO_2 and CH_4 the diffusion coefficients were higher than in unfilled PTMSP. The elevated diffusion coefficients may be associated with the onset of high concentrations of voids through which penetrant gases can diffuse rapidly.

The diffusion coefficients were somewhat pressure dependent, as seen in Figure 4.16. The observed increase in CO_2 diffusion coefficient values with increasing pressure is consistent with the behavior exhibited by CO_2 in other glassy polymers.[23] The CH_4 and N_2 diffusion coefficients decrease slightly with increasing pressure, which is also consistent with the behavior of such light gases in unfilled PTMSP.[23] However, these changes in diffusivity, particularly for N_2 and CH_4, are near or at the resolution limits of the experiment, so the changes in diffusivity with pressure are a weak effect.

Table 4.4 presents the solubility and diffusivity selectivities for TiO_2 filled PTMSP nanocomposites. For CO_2/CH_4 and CH_4/N_2, the solubility selectivity of the nanocomposite sample is essentially equal to that of PTMSP. For CO_2/N_2, the pure polymer CO_2/N_2 solubility selectivity, 4.9, appears to be somewhat higher than that of the nanocomposites, which have an average CO_2/N_2 solubility selectivity value of 3.0. The nanocomposite CO_2/N_2 solubility selectivity is unaffected by particle loading. It is not clear why the CO_2/N_2 solubility selectivity behaves in this manner.

The CO_2/nonpolar gas diffusivity selectivity appears to increase with increasing particle loading up to around 15 volume percent TiO_2, while at higher loadings the CO_2/nonpolar gas selectivity appears to decrease with increasing particle concentration. However, due to the uncertainty of the diffusivity selectivity values reported in this study, both trends would need to be verified in a more detailed study.

Table 4.4. Light gas solubility and diffusivity selectivity of TiO_2 filled PTMSP at 35 °C

ϕ^{N}_{F,TiO_2}	Solubility Selectivity			Diffusivity Selectivity		
	CO_2/N_2	CO_2/CH_4	CH_4/N_2	CO_2/N_2	CO_2/CH_4	CH_4/N_2
0.00	4.9 ± 1.0	2.0 ± 0.3	2.5 ± 0.6	0.8 ± 0.2	0.8 ± 0.2	1.0 ± 0.3
0.03	3.1 ± 0.5	1.4 ± 0.2	2.1 ± 0.5	1.5 ± 0.5	1.3 ± 0.4	1.2 ± 0.4
0.07	2.5 ± 0.5	1.2 ± 0.2	2.1 ± 0.5	1.9 ± 0.6	1.4 ± 0.5	1.4 ± 0.5
0.10	3.6 ± 0.7	1.3 ± 0.2	2.8 ± 0.6	1.6 ± 0.5	1.5 ± 0.5	1.1 ± 0.4
0.15	3.0 ± 0.6	0.9 ± 0.2	3.4 ± 0.8	1.6 ± 0.5	1.9 ± 0.6	0.8 ± 0.2
0.23	3.0 ± 0.6	1.7 ± 0.3	1.8 ± 0.4	1.4 ± 0.5	0.9 ±0.3	1.6 ± 0.5
0.33	3.4 ± 07	1.8 ± 0.3	1.9 ± 0.4	1.0 ± 0.3	0.8 ± 0.2	1.3 ±0.4

Note: Solubility and diffusivity selectivity values were calculated from the data in Table 4.3. Uncertainties in solubility and diffusion selectivities were estimated using the propagation of errors method.[13]

Physical aging in nanocomposite films

The propensity for gas permeability in PTMSP to decrease with time is well known.[10,30] Figure 4.17 presents CO_2 permeability aging behavior, which is representative of that observed for CH_4, N_2 and H_2 for PTMSP filled with varying amounts of TiO_2. CO_2 permeability in unfilled PTMSP and in the two nanocomposite films decreased with time. Figure 4.18 presents the CO_2 permeability aging data normalized by the CO_2 permeability of a given film on the first day after drying. The unfilled PTMSP and the nanocomposite film containing 20 nominal volume percent TiO_2 took 35 and 154 days, respectively, to reach approximately 60 percent of the initial permeability, whereas the nanocomposite film containing 0.33 nominal volume fraction of TiO_2 retained almost 80 percent of its initial permeability after 181 days.

The loss of permeability due to physical aging appears to be retarded by the presence of nanoparticles in the polymer matrix, and the severity of permeability loss is moderated at higher particle loadings. It is not clear how the particles reduce the rate of permeability loss due to aging. One explanation for this behavior might be that most of the permeability enhancement exhibited by nanocomposites containing high TiO_2 loadings may be due to the voids. Such void spaces might not decrease in size or volume over time, since they are not necessarily associated with non-equilibrium polymer structure. Any permeability loss exhibited by these filled films may be attributed to the aging of the native polymer and not the voids. However, this speculative hypotheses have not been proven.

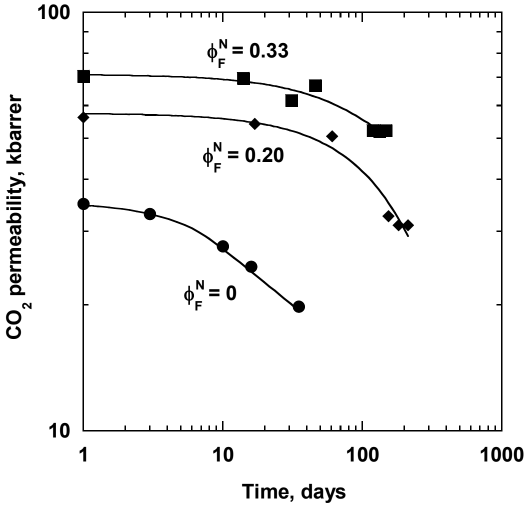

Figure 4.17. CO_2 permeability at 35 °C and $\Delta p = 3.3$ atm as a function of time for PTMSP containing 0 (●), 0.20 (♦), and 0.33 (■) nominal volume fraction of TiO_2. Samples were stored in the laboratory air at room temperature between permeation measurements. Trend lines are drawn to guide the eye.

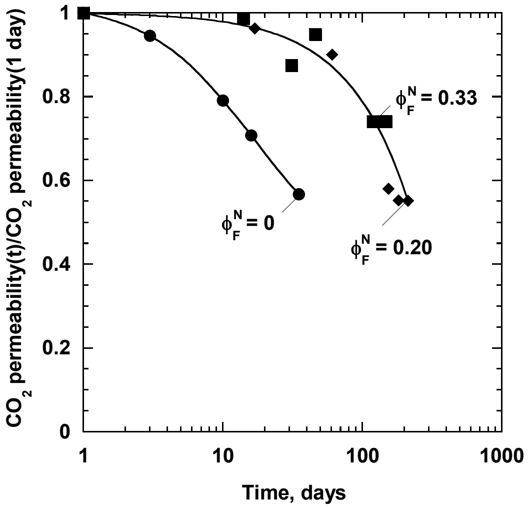

Figure 4.18. Aging ratio (CO_2 permeability of an aged sample / CO_2 permeability at day 1) at 35 °C and $\Delta p = 3.3$ atm as a function of time for PTMSP containing 0 (●), 0.20 (♦), and 0.33 (■) nominal volume fraction of TiO_2. Samples were stored in the laboratory air at room temperature between permeation measurements. Trend lines are drawn to guide the eye.

CONCLUSIONS

TiO_2 nanoparticles dispersed in PTMSP formed nanoscale and micron-sized aggregates. The TiO_2 filled PTMSP nanocomposite exhibited two different regimes in terms of density and gas transport properties. At low particle concentrations (*i.e.,* less than 6 nominal volume percent), permeability was lower than that of the native polymer. At these particle loadings, the nanocomposite density was slightly greater than that predicted by a simple additive model for density. However, at particle concentrations greater than 7 nominal volume percent, nanocomposite densities were much lower than anticipated by the additive density model, suggesting that these nanocomposite samples contained significant levels of voids. At these loadings nanocomposites exhibited permeability that was as much as four times that of the unfilled polymer.

REFERENCES

(1) De Sitter, K.; Winberg, P.; D'Haen, J.; Dotremont, C.; Leysen, R.; Martens, J. A.; Mullens, S.; Maurer, F. H. J.; Vankelecom, I. F. J., Silica filled poly(1-trimethylsilyl-1-propyne) nanocompsite membranes: Relation between gas transport and structural characteristics, *Journal of Membrane Science* **2006**, *278*, 83-91.

(2) Takahashi, S.; Paul, D. R., Gas permeation in poly(ether imide) nanocomposite membranes based on surface-treated silica. Part 1: Without chemical coupling to matrix, *Polymer* **2006**, *47*, 7519-7534.

(3) Merkel, T. C.; Freeman, B. D.; Spontak, R. J.; He, Z.; Pinnau, I.; Meakin, P.; Hill, A. J., Ultrapermeable, reverse-selective nanocomposite membranes, *Science* **2002**, *296*, 519-522.

(4) Merkel, T. C.; Freeman, B. D.; Spontak, R. J.; He, Z.; Pinnau, I.; Meakin, P.; Hill, A. J., Sorption, transport, and structural evidence for enhanced free volume in poly(4-methyl-2-pentyne)/fumed silica nanocomposite membranes, *Chemistry of Materials* **2003**, *15*, 109-123.

(5) Matteucci, S.; van Wagner, E.; Swinnea, S.; Freeman, B. D.; Sakaguchi, T.; Masuda, T., Desilylation of substituted polyacetylenes in the presence of nanoparticles, *Macromolecules* **2007**, *40*, 3337-3347.

(6) Utamapanya, S.; Klabunde, K. J.; Schlup, J. R., Nanoscale metal oxide particles/clusters as chemical reagents. Synthesis and properties of ultrahigh surface area magnesium hydroxide and magnesium oxide, *Chemistry of Materials* **1991**, *3*, 175-181.

(7) Bouma, R. H. B.; Checchetti, A.; Chidichimo, G.; Drioli, E., Permeation through a heterogeneous membrane: The effect of the dispersed phase, *Journal of Membrane Science* **1997**, *128*, 141-149.

(8) Vu, D. Q.; Koros, W. J.; Miller, S. J., Mixed matrix membranes using carbon molecular sieves II. Modeling permeation behavior, *Journal of Membrane Science* **2003**, *211*, 335-348.

(9) Wan, T.; Wang, Y.-C.; Feng, F., Preparation of titanium dioxide/polyacrylate nanocomposites by sol-gel process in reverse micelles and *in situ* photopolymerization, *Journal of Applied Polymer Science* **2006**, *102*, 5105-5112.

(10) Nagai, K.; Masuda, T.; Nakagawa, T.; Freeman, B. D.; Pinnau, I., Poly[1-(trimethylsilyl)-1-propyne] and related polymers: Synthesis, properties and functions, *Progress in Polymer Science* **2001**, *26*, 721-798.

(11) Olkin, I.; Gleser, L. J.; Derman, C. Probability Models and Applications, 2nd ed.; Macmillan College Publishing Company: New York, 1980.

(12) Weibull, W., A statistical distribution function of wide applicability, *Journal of Applied Mechanics* **1951**, *18*, 293-297.

(13) Bevington, P. R.; Robinson, D. K. Data Reduction and Error Analysis for the Physical Sciences, 3rd ed.; McGraw-Hill, Inc.: New York, 2002.

(14) Pavlov, G. M.; Zaitseva, I. I.; Michailova, N. A.; Rjumtsev, E. I., Molecular characteristic of poly(1-trimethylsilyl-1-propyne) in dilute solutions, *Polymer* **2004**, *45*, 1159-1166.

(15) Brandon, D.; Kaplan, W. D. Microstructural Characterization of Materials; John Wiley and Sons: New York, 1999.

(16) van der Marck, S. C., Percolation thresholds of the duals of the face-centered-cubic, hexagonal-close-packed, and diamond lattices, *Physical Review E* **1997**, *55*, 6593 LP - 6597.

(17) Mezzasalma, S. A., Percolating Behavior of Solid Bimodal (Polymethylmethacrylate + Inert) Particle Packings during Polymerization, *Journal of Colloid and Interface Science* **1997**, *195*, 51-58.

(18) Qiu, J.; Zheng, J.-M.; Peinemann, K.-V., Gas transport properties in a novel poly(trimethylsilylpropyne) composite membrane with nanosized organic filler trimethylsilylglucose, *Macromolecules* **2006**, *39*, 4093-4100.

(19) Shantarovich, V. P.; Kevdina, I. B.; Yampolskii, Y. P.; Alentiev, A. Y., Positron annihilation lifetimes of high and low free volume glassy polymers: Effects of free volume sizes on the permeability and permselectivity, *Macromolecules* **2000**, *33*, 7453-7466.

(20) Lee, W. M., Selection of barrier materials from molecular structure, *Polymer Engineering and Science* **1980**, *20*, 65-69.

(21) Merkel, T. C.; He, Z.; Pinnau, I.; Freeman, B. D.; Hill, A. J.; Meakin, P., Effect of nanoparticles on gas sorption and transport in poly(1-trimethylsilyl-1-propyne), *Macromolecules* **2003**, *36*, 6844-6855.

(22) Rao, M. B.; Sircar, S., Performance and pore characterization of nanoporous carbon membranes for gas separation, *Journal of Membrane Science* **1996**, *110*, 109-118.

(23) Merkel, T. C.; Bondar, V.; Nagai, K.; Freeman, B. D., Sorption and transport of hydrocarbon and perfluorocarbon gases in poly(1-trimethylsilyl-1-propyne), *Journal of Polymer Science Part B: Polymer Physics* **1999**, *38*, 273-296.

(24) Lindbrathen, A.; Hagg, M.-B., Glass membranes for purification of aggressive gases: Part II. Adsorption measurements and diffusion coefficient estimations, *Journal of Membrane Science* **2005**, *259*, 154-160.

(25) Bird, R. B.; Stewart, W. E.; Lightfoot, E. L. Transport Phenomena, 2nd ed.; John Wiley & Sons: New York, 2002.

(26) Koros, W. J.; Chan, A. H.; Paul, D. R., Sorption and transport of various gases in polycarbonate, *Journal of Membrane Science* **1977**, *2*, 165-190.

(27) Merkel, T. C.; Bondar, V.; Nagai, K.; Freeman, B. D., Sorption and transport of hydrocarbon and perfluorocarbon gases in poly(1-trimethylsilyl-1-propyne), *Journal of Polymer Science: Part B: Polymer Physics* **2000**, *38*, 273-296.

(28) Do, D. D. Adsorption Analysis: Equilibria and Kinetics; Imperial College Press: London, 1998; Vol. 2.

(29) Barrer, R. M.; Barrie, J. A.; Rogers, M. G., Heterogeneous membranes: Diffusion in filled rubber, *Journal of Polymer Science, Part A: Polymer Chemistry* **1963**, *1*, 2565-2586.

(30) Nagai, K.; Sugawara, A.; Kazama, S.; Freeman, B. D., Effects of physical aging on solubility, diffusivity, and permeability of propane and *n*-butane in poly(4-methyl-2-pentyne), *Journal of Polymer Science Part B: Polymer Physics* **2004**, *42*, 2407-2418.

Chapter 5: Gas Transport Properties of MgO Filled Poly(1-trimethylsilyl-1-propyne) Nanocomposites

This chapter reports the influence of impermeable periclase (*i.e.,* MgO) nanoparticles on pure gas permeability coefficients in poly(1-trimethylsilyl-1-propyne) (PTMSP) based nanocomposites. The MgO/PTMSP nanocomposites exhibited very high gas permeability values. Particle dispersion was characterized using transmission electron microscopy (TEM). Nanocomposite density and gas permeation properties of CO_2, CH_4, N_2, and H_2 are reported as a function of particle concentration. Nanocomposite physical aging was also studied by monitoring changes in gas permeability over time. For all of the gases except H_2, gas solubility was also measured. From the measured permeability and solubility data, gas diffusion coefficients were calculated.

Magnesium oxide (MgO) nanoparticles were dispersed via solution processing in poly(1-trimethylsilyl-1-propyne) (PTMSP) to form polymer nanocomposites. Transmission electron microscopy was used to determine the extent of particle aggregation in the composites. Both nanocomposite density and CO_2, CH_4, N_2, and H_2 permeability were influenced by nanoparticle loading. Nanocomposite densities were markedly lower than predicted by a two phase additive model. For example, in films containing 75 nominal volume percent MgO, the polymer/particle composite density was 68 percent lower than expected based on an additive model. At this loading, gas permeability coefficients were, depending on the gas, 17 to 50 times higher than in unfilled PTMSP at similar conditions. The changes in permeability with particle content were interpreted in terms of measured changes in gas solubility with particle content and diffusion coefficients calculated from the permeability and solubility data.

RESULTS AND DISCUSSION

Polymer-particle interactions

In the presence of water, periclase nanoparticles and PTMSP undergo a chemical reaction that results in partial desilylation of the polymer, as discussed in Chapter 6.[1] The desilylation reaction removes, at most, approximately 9 percent of the trimethylsilyl groups from PTMSP.[1] The sample preparation protocol discussed in Chapter 3 do eliminating adventitious water was developed to minimize the reaction between the polymer and particles by limiting sample exposure to adventitious water, and this protocol was used in preparing the nanocomposites discussed in this chapter. In the samples considered in this study, WAXD studies confirm that the particle structure did not change from periclase to brucite, which would be observed if the particles had reacted with water.[1] The hydration reaction of MgO (*i.e.*, the conversion of periclase to brucite) is the first step in the reaction of the particles with the polymer.[1] Additionally, FTIR and ^{1}H NMR studies did not show any evidence of reaction between the particles and polymer. Based on this experimental protocol, any reaction between the polymer and particles was at a level that was below the detection limit of FTIR and ^{1}H NMR, which were used previously to characterize the reaction of these particles with PTMSP.[1]

Characterization of particle dispersion

Nanoparticle dispersion strongly influences gas transport properties in heterogeneous films. For instance, incorporation of trimethylsilylglucose reduces gas permeability in PTMSP by up to 99% relative to that of unfilled PTMSP.[2] In contrast, permeability increases substantially when brookite nanoparticles are added to PTMSP.[3] The influence of particles on transport properties is determined, in part, by the degree of dispersion of the particles in the polymer. When the particles disperse individually or in nanometer-scale aggregates, tapping mode phase profile AFM has been used to observe nanoparticle dispersion in PTMSP at a resolution of around 2 nm.[3] In PTMSP filled with TiO_2 and 1,2-polybutadiene filled with MgO nanoparticles, AFM revealed that at least some of the nanoparticles were dispersed individually.[3,4] However, for MgO dispersed in PTMSP, this was not the case. There were no individual nanoparticles or nanometer-scale aggregates of particles observed in these samples, suggesting that the MgO particles did not disperse as completely in PTMSP as other particles in PTMSP or as MgO in other polymers.[3,4]

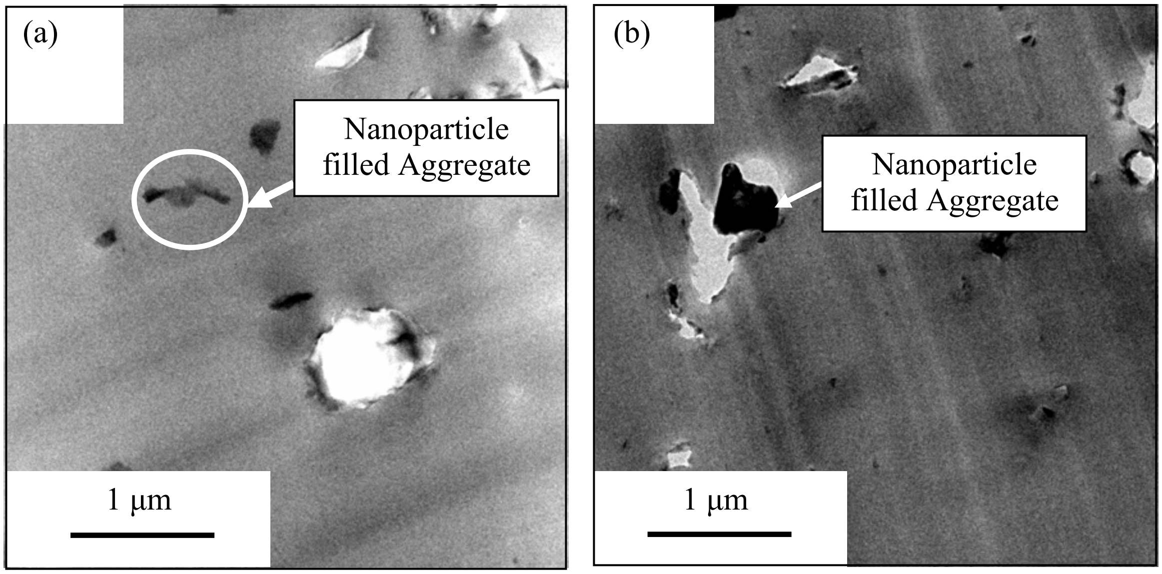

Figure 5.1. TEM images of (a) PTMSP containing 5 nominal volume percent MgO, and (b) PTMSP containing 10 nominal volume percent MgO.

Figure 5.1 presents TEM images of PTMSP filled with MgO nanoparticles. Even at low nanoparticle loading (*i.e.,* 5 nominal volume percent), the nanoparticles (*i.e.*, the dark regions in Figure 5.1) form micron-sized aggregates, suggesting that these particles are dispersed into aggregates that are many times the size of individual particles. As indicated above, this result is in contrast to other nanocomposites, such as PTMSP filled with TiO_2 or 1,2-polybutadiene filled with MgO, which exhibit a substantial amount of nanometer-sized particle aggregates at similar loadings.[3,4] The TEM images also show numerous micron-sized voids (*i.e.,* light gray areas in the TEM images). It is not clear if these voids are artifacts caused by the microtoming during the sample preparation or if they are an inherent feature of the dispersion of MgO particles in PTMSP.

A number of factors probably contribute to the observed wide variation in the degree of dispersion of nanoparticles in different polymers and to the possibility of void formation, such as particle/polymer interactions, casting conditions, polymer chain stiffness, particle loading, *etc*. Currently, there is not enough information available to definitively predict which particles will disperse well in which polymers and whether or not small scale voids (to be discussed in the next section) will be formed in the resulting nanocomposite samples.

Density and voids in nanocomposite samples

Figure 5.2 presents the density of nanocomposite samples as a function of particle loading. A notable feature of Figure 5.2 is that free-standing nanocomposite films may be prepared at loadings as high as 75 nominal volume percent particles, which corresponds to 94 wt. % particles in the polymer. To the best of our knowledge, such high loadings of particles in polymers considered for gas permeation properties have not been reported previously. Often, as inorganic particle content increases, polymer-based composites become brittle and, therefore, too fragile to test in gas permeation experiments, or the samples develop transmembrane defects that render the materials non-selective in gas permeation tests.[3,5,6] So, most studies do not report samples with particle loadings as high as those discussed in this study. For example, the maximum zeolite 4A content in poly(vinyl acetate) considered by Mahajan and Koros was 40 wt % before samples could no longer be prepared without selectivity-destroying defects.[5] While there is no evidence of chemical reaction between the particles and the polymer, the ability to reach such high loadings suggests somewhat favorable interactions between the particles and the polymer.

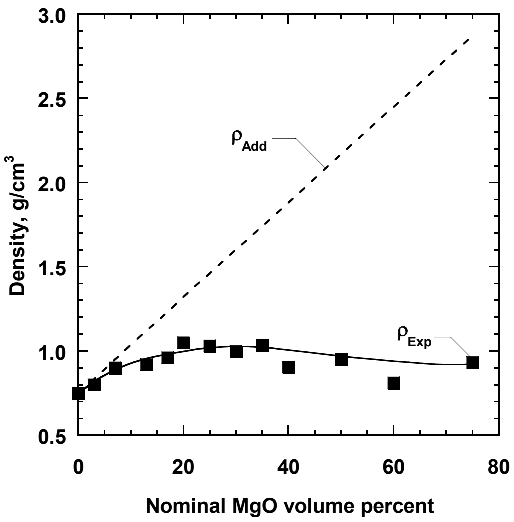

Figure 5.2. Effect of MgO concentration in nanocomposites on density (ρ_{Exp}, ■). The dashed line represents the additive density, ρ_{Add}, as calculated by Eq. (2.20). The solid trend line is drawn to guide the eye.

The simplest model of nanocomposite density would be that in which the nanocomposite density, ρ_{Add}, would obey an additive model, such as Eq. (2.20).[3] However, as indicated by the density data in Figure 5.2, the PTMSP/MgO system shows significant deviations from this model. The experimentally observed density is considerably lower than that expected based on the additive model, and the deviation between the data and the model increases as particle concentration increases. These data strongly suggest that these nanocomposites samples contain rather high levels of voids, either within the polymer or particle phases or at the interface between them.

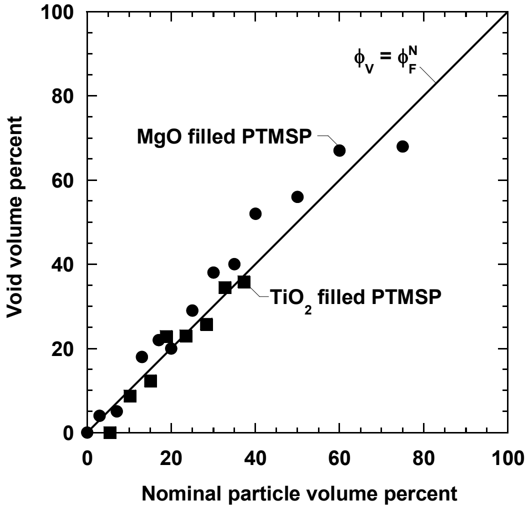

Figure 5.3. Correlation between particle loading and void volume percent in PTMSP/MgO (●) and PTMSP/TiO_2 (■) nanocomposite films.[3] The solid line represents $\phi_V = \phi_F^N$.

The deviation between the additive model and the experimental density can be quantified in terms of the volume fraction of voids, ϕ_V, as calculated using Eq. (2.22).[3] Figure 5.3 presents the effect of nanoparticle concentration on void volume percent in PTMSP containing MgO and in PTMSP/TiO_2 nanocomposites based on TiO_2 nanoparticles having a primary particle diameter of approximately 3 nm.[3] Interestingly, the trend in void volume with particle loading does not depend on particle type. The void volume percent increases with increasing particle loading to the point where the composite materials are predominantly void space at high particle loadings. The line shown in this figure corresponds to the case where the void volume and nominal particle volume percent are equal. While it is not clear why the void volume and nominal particle volume percent are equal, it is interesting that this trend is observed. The location of the voids within the nanocomposite could not be identified using common microscopic techniques, but the existence of void space in mixed matrix polymer-based materials has been reported in the literature for a variety of particle-polymer combinations.[7-10] The data in Figure 5.3 extend significantly farther for MgO-based composites than for TiO_2-based composites because the TiO_2 samples exhibit non-selective permeation (*i.e.,* defects) in the films when the nominal volume fraction is above 38 %, providing another indication that the interactions between the polymer and particles more strongly favors preparation of samples with high particle loadings in the MgO case.

The true volume fraction of particles in the nanocomposite, ϕ_F^T, which is the volume of particles per unit volume of sample (including polymer, particles, and void space) can be calculated using Eq. (2.23). For the samples considered in this study, the maximum value of the true volume percent of particles was 24 percent at 75 nominal volume percent MgO, which is well below the maximum packing limit for spherical particles in a matrix, which is 49 volume percent.[11]

Gas permeability in PTMSP/MgO nanocomposites

Generally, dispersing impermeable particles in polymer matrixes decreases gas permeability.[2,7,12] However, this trend is not always obeyed in nanoparticle filled polymers. Nanoparticles can disrupt chain packing in glassy polymers, thereby increasing free volume in the polymer phase, which acts to increase permeability.[13] In other heterogeneous systems, voids at the polymer-particle interface or between particles in particle aggregates cause permeability to be greater in nanocomposites than in unfilled polymers.[3,8] In this regard, Figure 5.4 shows strong increases in gas permeability in PTMSP as MgO loading increases. The unfilled PTMSP permeability values at $\Delta p = 3.4$ atm are 35, 18, 7, and 18 kbarrer for CO_2, CH_4, N_2, and H_2, respectively. These values are similar to those reported in the literature. For instance, Pinnau and Toy report CO_2,

CH_4, N_2, and H_2 permeability values at 23 °C and $\Delta p = 3.4$ atm of 34, 16, 6, and 17 kbarrer, respectively.[14] At the highest particle loadings in Figure 5.4, which correspond to 94 wt. % particles, the CO_2, CH_4, N_2, and H_2 permeability coefficients are 17, 28, 30, and 40 times higher than in unfilled PTMSP.

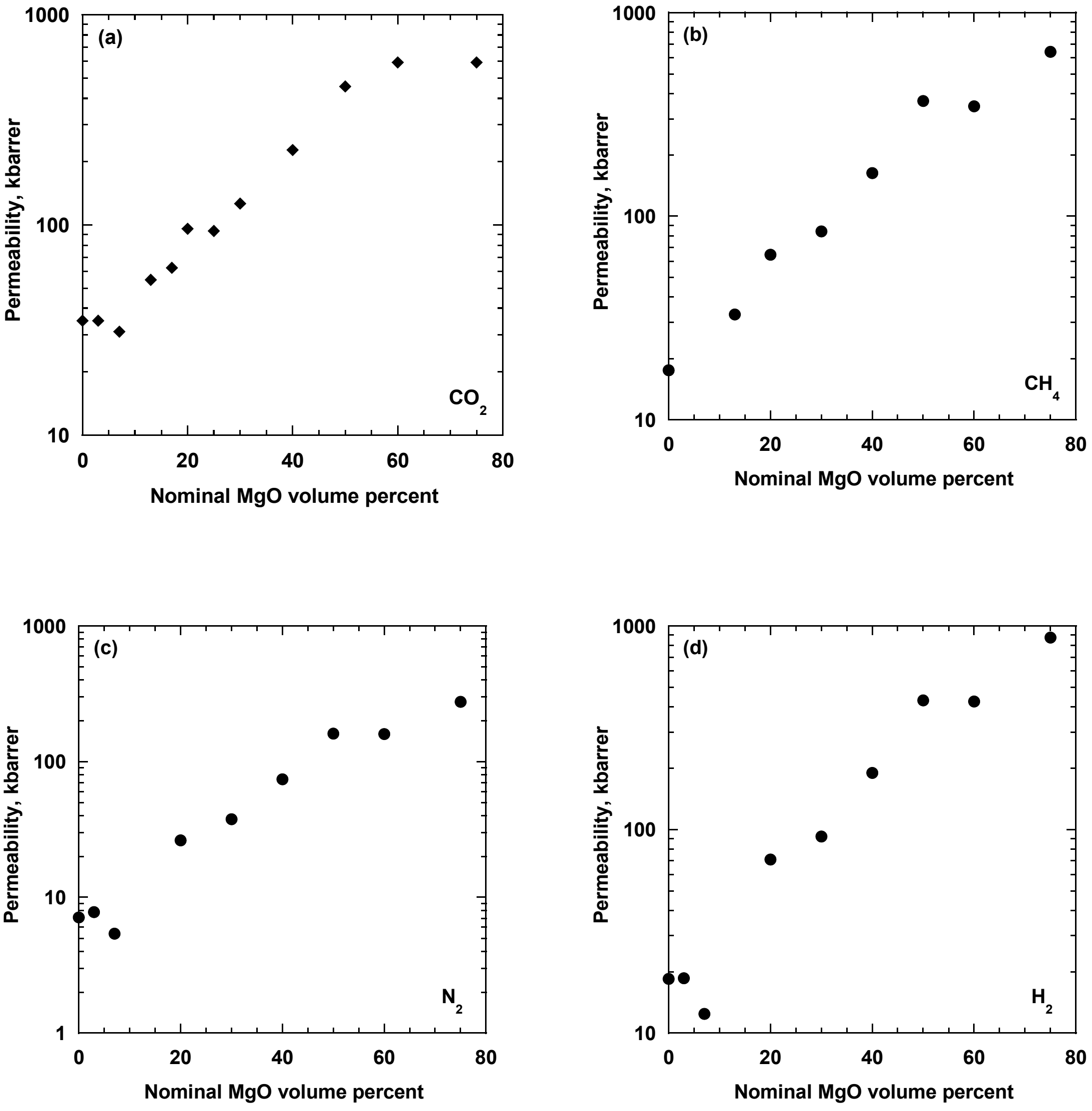

Figure 5.4. Effect of MgO concentration on (a) CO_2, (b) CH_4, (c) N_2, and (d) H_2 permeability at $\Delta p = 3.4$ atm. These measurements were made at 35 °C and atmospheric downstream pressure.

Figure 5.5 presents a correlation of the CO_2 permeability with void volume. Applying Bruggeman's model in the limit where the dispersed phase (the voids, in this case) is much more permeable than the matrix phase (*i.e.*, setting $\phi_V = \phi_D$ in Eq. (2.27)), one obtains a reasonable fit of the experimental permeability data to the model, as indicated in Figure 5.5. There are no adjustable parameters in Eq. (2.27). The dependence of gas permeability on the amount of void space in the nanocomposites is similar among a variety of nanoparticle fillers dispersed in PTMSP. For instance, CO_2 permeability values in PTMSP filled with either MgO or TiO_2 nanoparticles are similar at the same void volume content, as demonstrated in Figure 5.6.[3] Similar results have been observed for the other gases considered in this study. Therefore, the basic permeation properties of the polymer are not affected by the presence of the particles or, at least, any change in polymer transport properties is overshadowed by the dominant effect of the voids on the permeability of the nanocomposites.

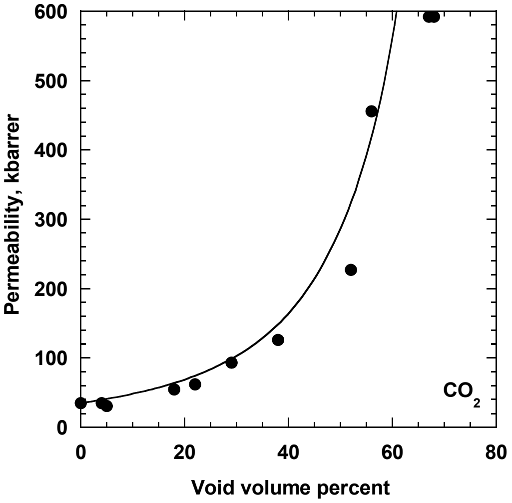

Figure 5.5. Effect of void volume, ϕ_V, concentration on CO_2 permeability (●) at Δp = 3.4 atm. The solid line represents Eq. (2.22), where the voids are treated as the dispersed phase (*i.e.,* setting $\phi_D = \phi_V$ in Eq. (2.27)). These measurements were made at 35 °C and atmospheric downstream pressure.

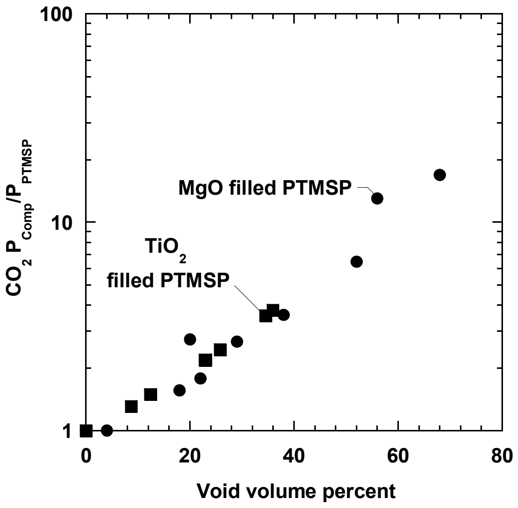

Figure 5.6. Effect of void volume percent, as calculated by Eq. (2.22) on the ratio of CO_2 permeability in the nanocomposite, P_{Comp}, to CO_2 permeability in PTMSP, P_{PTMSP}, in PTMSP/MgO (●) and PTMSP/TiO_2 (■) nanocomposite films.[3]

The permeability coefficients in PTMSP/MgO nanocomposites are very high. For instance, in PTMSP containing 75 nominal volume percent MgO, CO_2 permeability is ~600 kbarrer at $\Delta p = 3.4$ atm and 35 °C, and *n*-butane permeability is 1,200 kbarrer at $\Delta p = 0.9$ atm and 35 °C. A key question is whether the observed permeability coefficients are consistent with gas transport in a polymer without transmembrane defects or whether the results are simply due to the particle's ability, particularly at high loadings, to introduce defects that span the sample.

Permeability in systems exhibiting Poiseuille flow, which would be observed if large defects (*i.e.,* > 50 nm or so [15]) were present in the films, would typically increase with increasing pressure difference across the film.[16] Figure 5.7 presents permeability coefficients in PTMSP nanocomposites containing MgO. CO_2 and CH_4 permeability in unfilled PTMSP decreases slightly with increasing pressure, which is consistent with reports in the literature.[3,17] However, the decrease in permeability with increasing CO_2 and CH_4 pressure is small enough to be masked by the scale of Figures 5.7a and 5.7b. In summary, gas permeability does not increase with increasing upstream pressure, which indicates that the gas transport behavior does not obey Poiseuille flow.

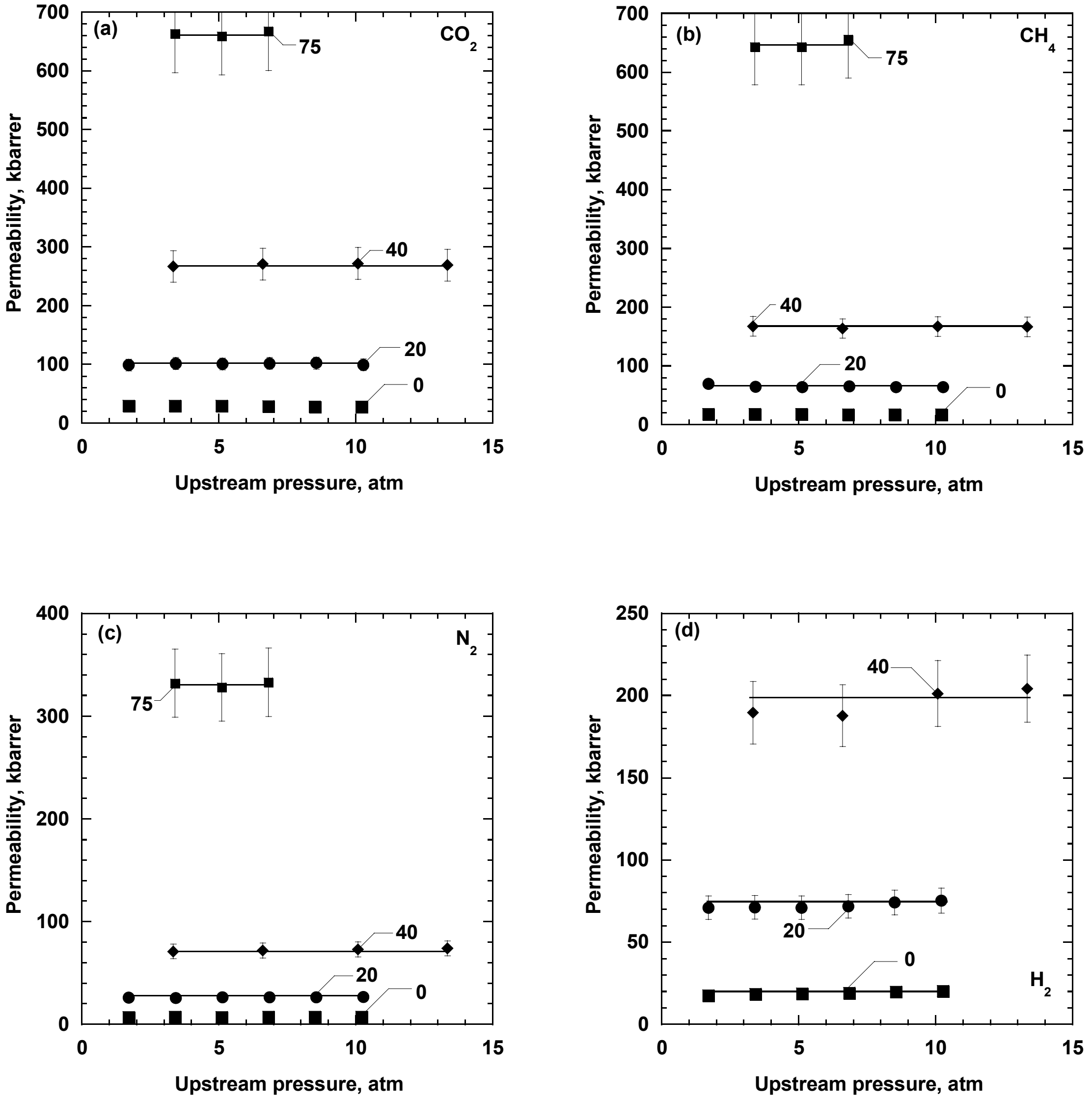

Figure 5.7. Effect of upstream pressure on pure gas permeability of PTMSP containing various nominal volume percents, ϕ_F^N, of MgO for (a) CO_2, (b) CH_4, (c) N_2, and (d) H_2. These measurements were conducted at 35 °C and at atmospheric downstream pressure. Error bars were estimated from the variance in permeability for multiple experiments at each loading and pressure according to the propagation of errors method described by Bevington.[36] The solid lines are drawn to guide the eye.

Gas selectivity values provide further evidence regarding the presence of selectivity-destroying defects in the PTMSP/MgO nanocomposites. Depending upon the defect or pore size, in a polymer film containing a pore or defect that is connected across the entire sample, the ideal selectivity can reach the Poiseuille limit, $\alpha^{P}_{A/B}$, if the pore are large enough, or the Knudsen limit, $\alpha^{K}_{A/B}$, if the pores are smaller.[15] $\alpha^{P}_{A/B}$ is:[16,18]

$$\alpha^{P}_{A/B} = \frac{\mu_B}{\mu_A} \tag{4.2}$$

where μ_A and μ_B are the viscosities of gas A and B, respectively. The Knudsen selectivity limit, $\alpha^{K}_{A/B}$, is:[18]

$$\alpha^{K}_{A/B} = \sqrt{\frac{M_B}{M_A}} \tag{4.1}$$

where M_A and M_B are the molecular masses of gases A and B, respectively. Poiseuille and Knudsen flow selectivity limits are presented in Table 5.1 for the gas pairs of interest to this study. The viscosity data used to generate the selectivity values in Table 5.1 are at 35 °C.[19]

Table 5.1. Knudsen diffusion and Poiseuille flow selectivities

Flow regime	CO_2/N_2	CO_2/CH_4	CO_2/H_2	H_2/N_2	H_2/CH_4	CH_4/N_2
Knudsen Diffusion	0.8	0.6	0.2	3.7	2.8	1.3
Poiseuille Flow	1.2	0.7	0.6	2.0	1.2	1.7

The selectivity data provide some information regarding the transport mechanism governing gas transport in these nanocomposite samples and changes in transport mechanism with particle content. In this regard, Figure 5.8 presents the pure gas selectivity values as a function of particle content. Interestingly, the CO_2/CH_4, CO_2/N_2, and CO_2/H_2 selectivity values generally decrease with increasing particle content. In contrast, the H_2/N_2 and H_2/CH_4 selectivity values increase somewhat with increasing particle content. The CH_4/N_2 selectivity exhibits little to no change with particle content. In each of these cases, as the particle content increases, the selectivity values trend towards, but do not reach, selectivity values expected based on Knudsen flow (*cf.*, Table 5.1). These results suggest that as particle content increases, transport in the nanocomposites becomes more similar to transport through interconnected pores, of a size characteristic of that required for Knudsen flow[15,18], that span the sample. For some of the gas pairs (*e.g.*, H_2/CH_4 and CO_2/H_2) the selectivity values also achieve values consistent with Poiseuille flow. For the other gas pairs, this is not the case. Given that the permeability coefficients do not exhibit the pressure dependence expected for Poiseuille flow, it is unlikely that this flow mechanism is active in these materials.

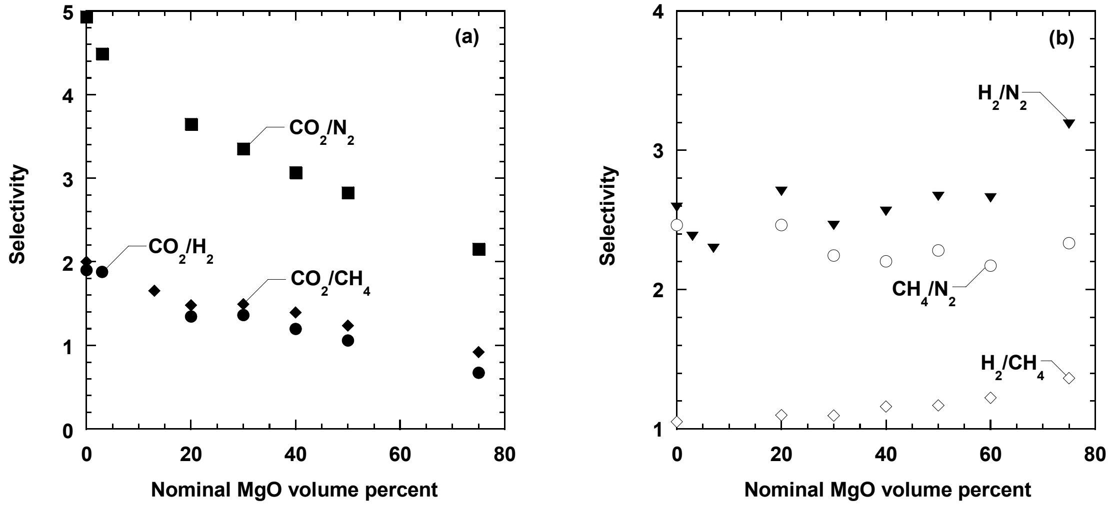

Figure 5.8. Effect of MgO concentration on pure gas selectivities at Δp = 3.4 atm for: (a) CO_2/N_2 (■), CO_2/CH_4 (♦), and CO_2/H_2 (●), as well as (b) H_2/N_2 (▼), H_2/CH_4 (◊), and CH_4/N_2 (○). Measurements were made at 35 °C and atmospheric downstream pressure.

These results appear to be consistent with those reported earlier by Merkel *et al.* For example, they observed that H_2/CH_4 increased from about 0.9 in PTMSP to 1.2 in PTMSP containing 50 wt. % fumed silica nanoparticles.[15] Merkel *et al.* argued that, as nanoparticle content increased, contributions from pore flow modes of transport (*e.g.,* Knudsen flow) to the overall rate of gas transport became more important relative to solution-diffusion transport. Merkel *et al.* reasoned that, in the transition from solution-diffusion to pore flow, the solubility selectivity, which, in the solution-diffusion limit, favors CH_4 in the case of H_2/CH_4, would come to be unity, which is the value of the solubility selectivity expected for pore flow. This change in solubility selectivity would act to increase H_2/CH_4, permeability selectivity, which is consistent with the results shown in Figure 5.8b. In this picture, the permeability selectivity would approach that of Knudsen transport as the contribution of pore flow to the overall gas transport increased (*i.e.,* as particle content increased). In the PTMSP/MgO case presented in Figure 5.8b, the Knudsen selectivity limit (2.8 for H_2/CH_4) is not reached, suggesting that solution-diffusion transport still contributes substantially to the total rate of transport even in the nanocomposites containing the highest concentrations of particles. Similar reasoning would also explain why H_2/N_2 selectivity appears to exhibit a slight increase, towards the Knudsen limit of 3.7 (*cf.*, Table 5.1) with increasing particle content. In the case of CH_4/N_2, the solubility selectivity in the polymer favors CH_4[20] so transition to a pore flow regime would favor a reduction in permeability selectivity. However, this trend might be partially offset by the fact that, in the solution-diffusion limit, nitrogen would typically be expected to have a higher diffusion coefficient than methane, since the kinetic diameter of nitrogen (3.64 Å) is slightly less than that of methane (3.8Å),[21] while the situation would be reversed, with methane having the higher diffusion coefficient, in the Knudsen flow limit. The resulting combination of factors apparently act to keep the selectivity largely unchanged as particle content increases.

In the case of the selectivity values involving CO_2 (*i.e.,* Figure 5.8a), the solubility selectivity in the solution-diffusion limit always favors CO_2. Therefore, at higher particle contents, if there is a transition to pore flow modes of transport, such as Knudsen flow, the solubility selectivity favoring CO_2 would be lost, resulting in an overall decrease in selectivity, which is consistent with that observed in Figure 5.8a. In each case, the selectivity decreases towards, but does not reach, selectivity values indicative of pore flow (*i.e.,* Knudsen diffusion). In summary, the permeability results are independent of pressure, suggesting that there are no large defects, which would allow flow mechanisms such as Poiseuille flow. However, the permeability selectivity results suggest a stronger influence of Knudsen flow on the overall transport properties as particle concentration increases.

In the remainder of this manuscript, the influence of particle concentration on gas permeability is analyzed further in terms of the influence of particle concentration on gas solubility and diffusivity using the solution-diffusion model, which presumes that the samples are free from trans-film defects. As a first step in this process, Figure 5.9 presents gas sorption isotherms for the MgO nanoparticles alone. The Freundlich isotherm can adequately describe the adsorption of gases onto the particles, and this model is given by:[4,22]

$$C_F = Kp^{\frac{1}{n}} \tag{4.4}$$

where K and n are fitting parameters, and p is the gas pressure. Gas sorption in glassy polymers, C_P, typically obeys the dual mode sorption model:[23,24]

$$C_P = k_D + \frac{C_H' bp}{1 + bp} \tag{4.3}$$

where k_D is the Henry's law constant, C_H' is the Langmuir sorption parameter, and b is the Langmuir affinity constant. Table 5.2 presents Freundlich isotherm parameters for CO_2, CH_4, and N_2 adsorption on MgO nanoparticles from this study as well as dual mode parameters for PTMSP from the literature.[20]

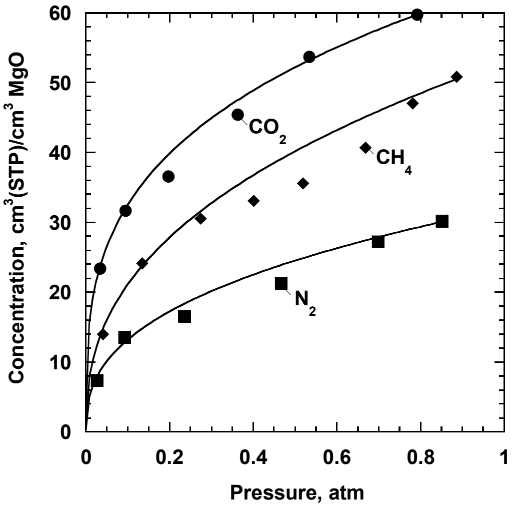

Figure 5.9. Pure gas CO_2 (●), CH_4 (♦), and N_2 (■) adsorption isotherms on MgO at 35 °C. The lines represent the Freundlich model (*i.e.,* Eq. 4.4)).

Figure 5.10 presents sorption isotherms in unfilled PTMSP and nanocomposite samples. The sorption in unfilled PTMSP is in good agreement with that predicted by Eq. (4.3) using dual mode sorption parameters from the literature (*cf.*, Table 5.2).[17] Due to the good agreement between sorption isotherms in the unfilled polymer with the literature data, the dual mode sorption model parameters from the literature are used in the calculation described below. In some, but not all, cases, the gas solubility in the nanocomposites is higher than in the unfilled polymer. Because the gas sorption levels are not a monotonic function of particle content, these results suggest that competing factors may contribute to the observed gas uptake. In the following paragraphs, these factors are discussed in more detail.

Table 5.2. Freundlich isotherm parameters for adsorption onto MgO and dual mode sorption parameters for PTMSP at 35 °C

Penetrant	K, $\frac{\text{cm}^3\left(\text{STP}\right)}{\text{cm}^3\text{MgO atm}^{\frac{1}{n}}}$	n, -	$k_D, \frac{\text{cm}^3\left(\text{STP}\right)}{\text{cm}^3\text{PTMSP atm}}$	$C'_H, \frac{\text{cm}^3\left(\text{STP}\right)}{\text{cm}^3\text{PTMSP}}$	b, $\frac{1}{\text{atm}}$
N_2	31 ± 7	2.6 ± 0.2	0.1	74	0.014
CH_4	50 ± 8	2.5 ± 0.2	0.5	62	0.05
CO_2	63 ± 10	3.4 ± 0.2	1.1	130	0.04

Note: PTMSP dual mode parameters are from the literature.[17] Uncertainties in the Freundlich isotherm parameters were estimated as described in the literature.[36]

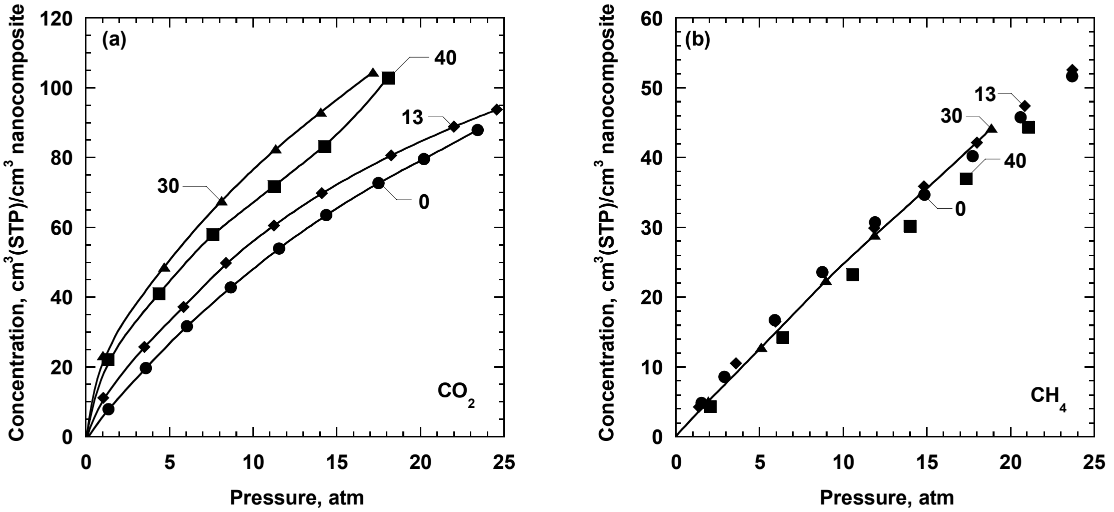

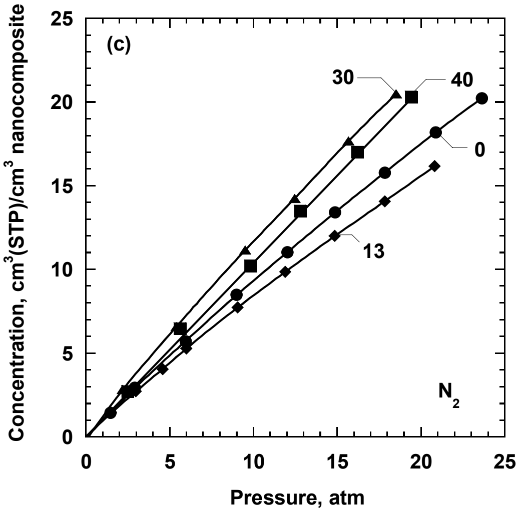

Figure 5.10. Sorption isotherms at 35 °C for (a) CO_2, (b) CH_4, and (c) N_2 in PTMSP containing 0 (●), 13 (♦), 30 (▲), and 40 (■) nominal volume percent MgO nanoparticles. Trend lines are drawn to guide the eye in the nanocomposite samples. For pure PTMSP, the line through the data is the dual mode model (Eq. (4.3)) using the parameters shown in Table 5.2.[36]

If the polymer and particles contributed their pure component gas sorption properties to the gas uptake in nanocomposite samples, then the gas sorption properties of the nanocomposite would obey the following additive model:[3,7]

$$C_C = \left(\phi_F^N C_F + \left(1-\phi_F^N\right) C_P\right)\left(1-\phi_V\right) + \phi_V C_V \tag{4.5}$$

where C_C is the gas concentration in the nanocomposite (cm^3(STP)/cm^3 nanocomposite), and C_V is the concentration of gas in the voids, which is given by the ideal gas law:[16]

$$C_V = \frac{p}{RT} \tag{4.6}$$

To put this contribution in perspective with that of the polymer and particles (*cf.*, Table 5.2), the concentration of gas in a void at 35 ^{o}C and 1 atm would be 0.88 cm^3(STP)/(cm^3 void), which is less than that of the gas concentration in the polymer or on the particles. Substituting Eqs. (4.3), (4.4), and (4.6) into Eq. (4.5) yields:[3]

$$C_C = \left(\phi_F^N K p^{\frac{1}{n}} + \left(1-\phi_F^N\right)\left(k_D + \frac{C_H^{'} bp}{1+bp} \right) \right)\left(1-\phi_V\right) + \phi_V \frac{p}{RT} \tag{4.7}$$

According to Eq. (4.7) and the data from Table 5.2, sorption on the nanoparticle surface and sorption into the polymer phase dominate the overall sorption of gas into the nanocomposite. For instance, for CO_2 sorption in a PTMSP film containing 13 nominal volume percent MgO (and 12 volume percent voids) at 4.4 atm, adsorption on the nanoparticle surface (extrapolated from the experimental data in Figure 5.9 and the Freundlich model) accounts for 47 % of the overall sorbed gas concentration, and sorption in the polymer phase accounts for 50 % of the total sorbed gas concentration. In this case, the voids contribute only ~3 % of the total sorbed gas in the nanocomposite. The contributions of particles, polymer, and voids to the total amount of gas uptake will vary with pressure, gas, and particle concentration. However, this example is representative of the typical contributions of each phase to the gas concentration in the nanocomposites. Since the void volume makes a small, but non-negligible, contribution to the concentration of gas in the nanocomposite, certain nanocomposites adsorb less gas than the unfilled polymer (*cf.,* Figure 5.10). In these cases, the increase in gas sorption due to incorporation of highly gas sorbing particles is more than offset by the low gas sorption in the voids. As indicated earlier, gas sorption levels in the voids, based on Eq. (4.6), are lower than gas sorption by either the polymer or particles.

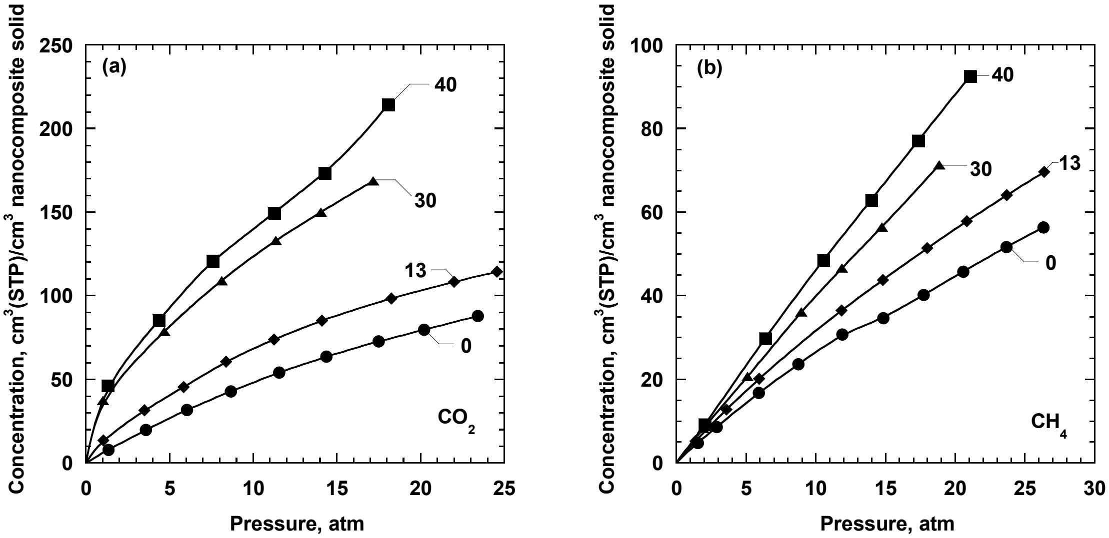

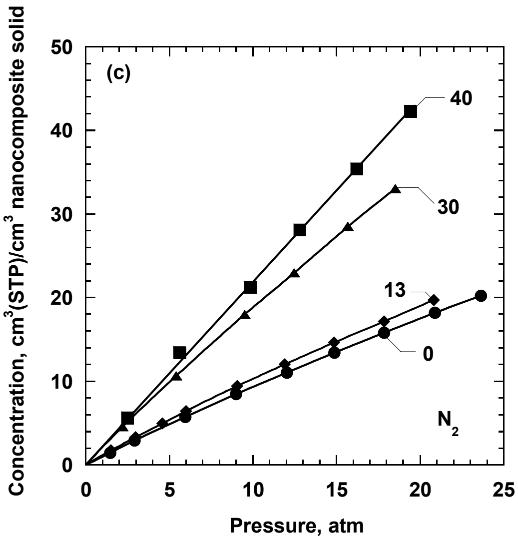

Figure 5.11. Sorption isotherms in the nanocomposite solids for (a) CO_2, (b) CH_4, and (c) N_2 in PTMSP containing 0 (●), 13 (♦), 30 (▲), and 40 (■) nominal volume percent MgO nanoparticles at 35 °C. Trend lines are drawn to guide the eye in the nanocomposite samples. For pure PTMSP, the line through the data is the dual mode model (Eq. (4.3)) using the parameters shown in Table 5.2.[36]

At the same pressure, the gas concentration in nanocomposites containing 13 nominal volume percent particles is lower than the gas concentration in the unfilled polymer. This results from the manner in which gas concentration is normalized. The sorption isotherms in Figure 5.10 are reported based on the concentration of gas in the nanocomposite volume (*i.e.,* in the entire volume of the sample, including polymer, particles, and void volume). When calculated in this fashion, the sorption isotherms do not follow a systematic trend with nanoparticle loading. However, sorption levels per unit volume of nanocomposite solids (*i.e.,* the polymer and particle volume, but not including the void volume) increases systematically with increasing particle loading, as shown in Figure 5.11. These results appear reasonable, since the neat particles sorb more gas than the unfilled polymer.

Figure 5.12 presents a comparison of Eq. (4.7) to experimental sorption data in a PTMSP/MgO nanocomposite containing 30 nominal volume percent MgO. Results for other particle concentrations are qualitatively consistent with those presented in Figure 5.12. Eq. (4.7) overestimates the concentration of CH_4 and N_2, but it underestimates the CO_2 concentration in the nanocomposite. A reduction in gas sorption in polymer/inorganic particle composites relative to that predicted by an additive model such as Eq. (4.7) is often observed and has been ascribed to wetting of the particles by the polymer chains.[3,7,25] That is, any polymer chains that wet the particle surface occupy sorption sites that would otherwise be available to the gases, thereby reducing gas solubility in the composite below levels expected based on pure polymer and pure particle sorption properties.[7]

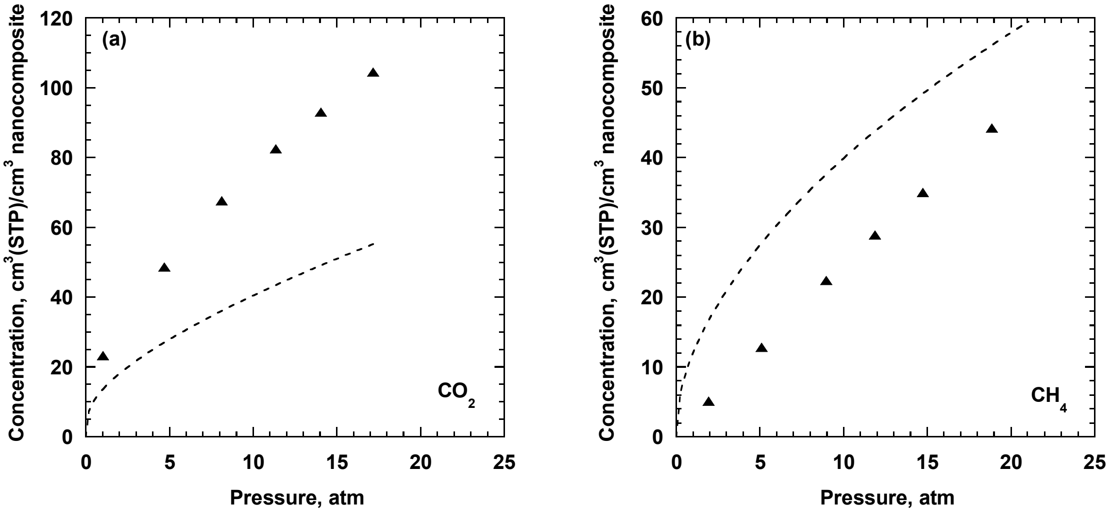

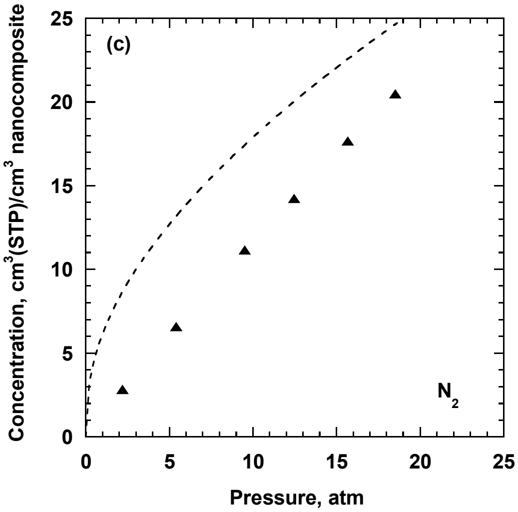

Figure 5.12. Sorption isotherms of: (a) CO_2, (b) CH_4, and (c) N_2 in a PTMSP nanocomposite containing 30 nominal volume percent MgO. The sorption level expected based on Eq. (4.7) using the parameters from Table 5.2 and void volume values from Figure 5.3 is the dashed line.

It is not clear why Eq. (4.7) underestimates CO_2 concentration in the nanocomposites while it substantially overestimates the concentration of non-polar gases. However, CO_2 is the most strongly sorbing penetrant considered in this study, and MgO is basic,[26] so it might have specific interactions with acidic CO_2 that are not accessible to CH_4 and N_2. Also, the low pressure sorption experiments used in this study may not accurately characterize the CO_2 sorption capacity of the MgO surface in the nanocomposites. For instance, Stark *et al.* report after preheating MgO nanoparticles overnight at 500 °C under vacuum, the nanoparticles sorbed approximately 150 cm^3(STP) CO_2 per cm^3 of nanoparticles at 20 Torr (0.03 atm) and 23 °C,[27] which indicates that MgO nanoparticles can sorb significantly more CO_2, depending on preparation method, than the 60 cm^3(STP) CO_2 per cm^3 of nanoparticles we report at 0.8 atm and 35 °C. Stark's sorption values may represent an upper limit to the concentration of CO_2 that can be adsorbed to MgO nanoparticles. It is possible the nanoparticles adsorb more CO_2 in the nanocomposites than the neat particles did during low pressure sorption experiments, which may account for the difference between the CO_2 sorption isotherms predicted by Eq. (4.7) and the CO_2 sorption isotherms determined experimentally. However, further studies, including high pressure sorption studies of the gases onto the neat particles, which are not possible with our equipment, would be required to resolve this issue.

Since our adsorption studies of the particles could not be performed beyond atmospheric pressure, if there were any changes in the shape of the gas adsorption isotherms or the level of gas uptake on the particles at higher pressures, this information would not be captured by the Freundlich isotherm model we have used. That is, the calculated isotherms in Figure 5.12 were based on gas adsorption data on the polymers obtained at pressures only as high as 1 atm, so the predictions represent a considerable extrapolation of the gas adsorption behavior on the particles. It is not known how much this extrapolation might contribute to the error in the calculated sorption isotherms.

To determine how much of the increase in permeability with increasing particle content was due to changes in gas solubility and how much was due to changes in diffusivity, the sorption isotherms in Figure 5.10 were used to estimate gas solubility values according to Eq. (2.8). The resulting solubility coefficients are presented in Figure 5.13. Gas solubility in the nanocomposites is, at most, slightly higher than in the unfilled

PTMSP, so the effect of the particles on gas solubility does not account for the increase in permeability values at increasing particle loadings. Therefore, increases in gas diffusion coefficients with increasing particle loading must account for the high permeability in MgO filled PTMSP.

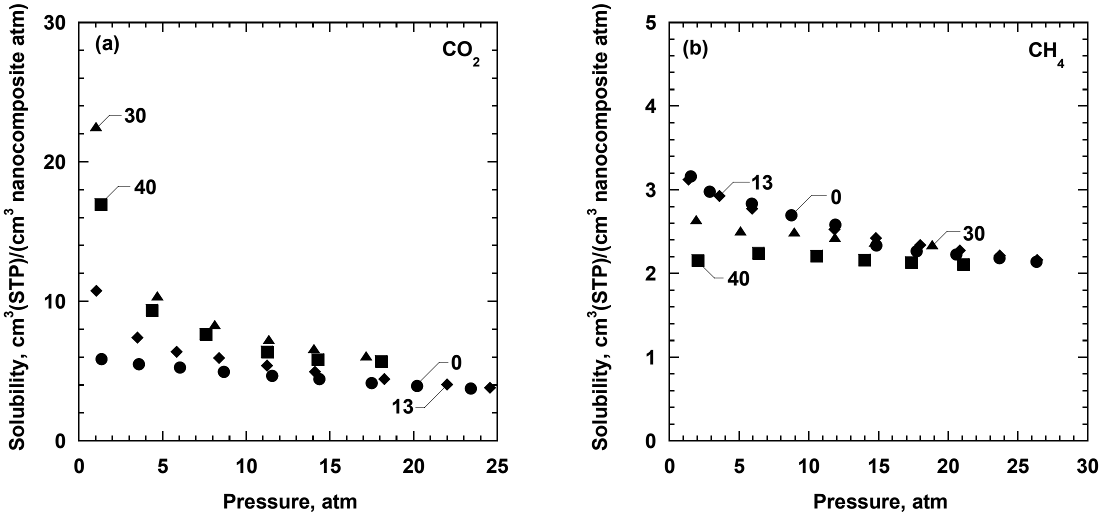

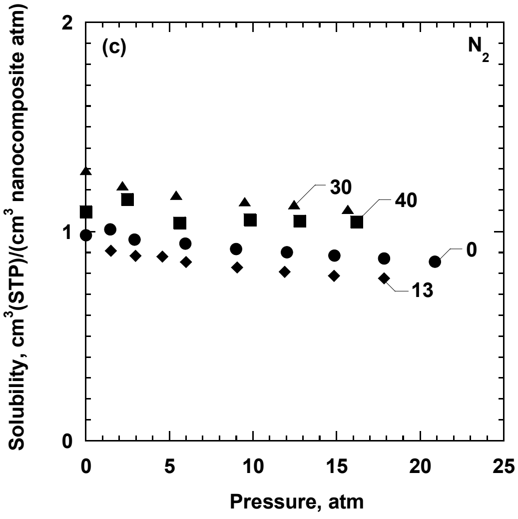

Figure 5.13. Solubility coefficients at p = 4.4 atm for (a) CO_2, (b) CH_4, and (c) N_2 in PTMSP nanocomposites containing 0 (●), 13 (♦), 30 (▲), and 40 (■) nominal volume percent MgO at 35 °C. Solubility coefficients were calculated using Eq. (2.8).

Gas diffusion coefficients were determined according to Eq. (2.9), using permeability data at $\Delta p = 3.4$ atm. Gas diffusion coefficients in unfilled PTMSP from this study are within the range of values reported in the literature, as shown in Table 5.3.[28-30] The rather large range of gas diffusion coefficients for unfilled PTMSP has been attributed to the sensitivity of gas permeability and diffusivity in PTMSP to film preparation protocols.[31]

Table 5.3. Pure gas diffusion coefficients in unfilled PTMSP

Penetrant	Diffusion coefficient x 10^6, cm^2/s				
	This work, 35 °C	Srinivasan *et al.*,[29] 25 °C	Ichiraku *et al.*,[28] 30 °C	Merkel *et al.*,[17] 35 °C	Raharjo *et al.*,[30] 35 °C
CO_2	48 ± 5	30	22	33	--
CH_4	60 ± 6	32	23	36	70
N_2	63 ± 6	36	26	44	--

Error bars were estimated according to the propagation of errors method described by Bevington.[36]

Figure 5.14 presents the influence of particle concentration on gas diffusion coefficients in the nanocomposites relative to their values in pure PTMSP. The diffusion coefficients increase with increasing particle loadings. Interestingly, gas diffusion coefficients exhibit a similar trend when compared to the nanocomposite void content, as shown in Figure 5.15.

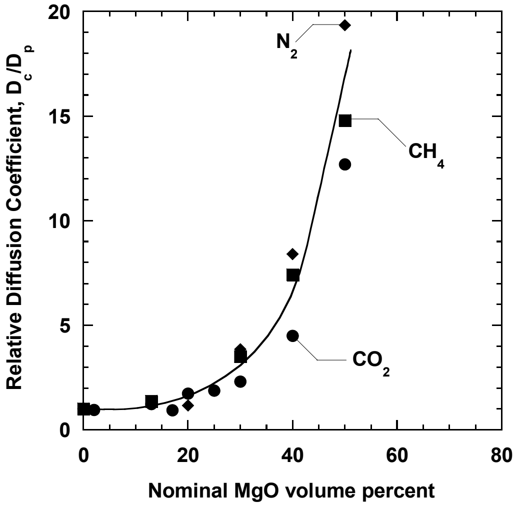

Figure 5.14. Relative concentration averaged diffusion coefficients at $\Delta p = 3.4$ atm for CO_2 (●), CH_4 (■), and N_2 (♦) as a function of MgO particle loading in PTMSP. D_c is the concentration averaged diffusion coefficient in the nanocomposite, and D_p is the concentration averaged diffusion coefficient in the unfilled polymer. Concentration averaged diffusion coefficients were calculated from Eqs. (2.8) and (2.9), where P was obtained from experimental data at 35 ^{o}C, and solubility was linearly interpolated to 4.4 atm. The trend line is drawn to guide the eye.

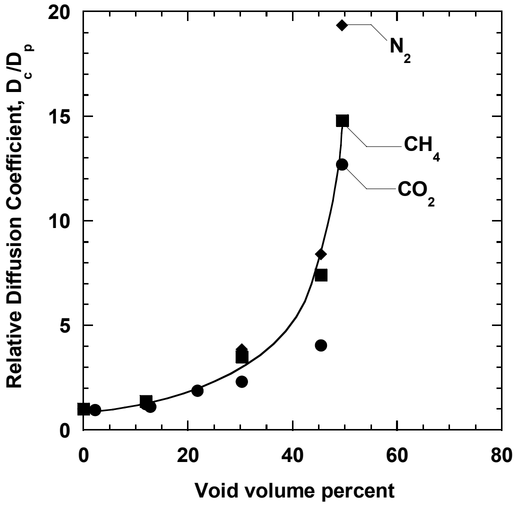

Figure 5.15. Relative concentration averaged diffusion coefficients at $\Delta p = 3.4$ atm for CO_2 (●), CH_4 (■), and N_2 (♦) as a function of void volume percent as calculated by Eq. (2.22). D_c is the concentration averaged diffusion coefficient in the nanocomposite, and D_p is the concentration averaged diffusion coefficient in the unfilled polymer. Concentration averaged diffusion coefficients were calculated from Eqs. (2.8) and (2.9), where P was obtained from experimental data at 35 ^{o}C, and solubility was linearly interpolated to 4.4 atm. The trend line is drawn to guide the eye.

The overwhelming source of the increase in permeability with increasing particle loading comes from the increase in diffusion coefficients, which is attributed to the void space in the nanocomposites. For example, in PTMSP containing 40 nominal volume percent MgO, the increase in CO_2 diffusion coefficients accounts for approximately 75 percent of the increase in permeability of CO_2, whereas the solubility behavior only accounts for approximately 25 percent of CO_2 permeability enhancement. Although the exact contributions of diffusivity and solubility to the nanocomposite permeability depends on particle loading and the gas, these results illustrate the relative scale of the contributions. The Bruggeman model correlates the permeability data reasonably well (*cf.*, Figure 5.5), because the model is mainly designed to capture the influence of diffusivity on permeability,[32] and diffusivity is the main source of permeability enhancement.

Aging

Gas permeability decreases with time in glassy polymers, in a process commonly referred to as physical aging.[31,33] PTMSP often shows more extensive decreases in permeability over time than other, lower free volume, glassy polymers.[34] However, the dispersion of brookite nanoparticles into PTMSP slowed the rate of permeability reduction with time.[3] In PTMSP films containing 20 nominal volume percent MgO, the CO_2 permeability decreases at approximately the same rate as in unfilled PTMSP, as shown in Figure 5.16. However, a film containing 75 volume percent MgO does not exhibit a permeability loss over time. Aging in glassy polymers is associated with polymer chain motion and non-equilibrium excess free volume associated with the polymer.[35] The film containing 75 nominal volume percent MgO is predominantly void space (*cf.*, Figure 5.3), and this void space is not necessarily associated with the polymer non-equilibrium free volume. Any voids at the particle-polymer interface or in the interparticle spacing might not be influenced by physical aging in the polymer phase, which would account for the permeability stability in PTMSP films containing high concentrations of MgO. It is not clear why permeability in the film containing 75 nominal volume percent MgO increases over time. However, the uncertainty in relative permeability is approximately ±14 %, so it is feasible that the permeability in the film containing 75 nominal volume percent MgO is essentially equal to that of a fresh, unaged sample. However; it is also conceivable that a reaction involving exposure of the film to ambient laboratory conditions (*i.e.,* sorption of water, reaction with water, *etc.*) over an extended period of time could occur, and the influence of such events on permeability is not known.

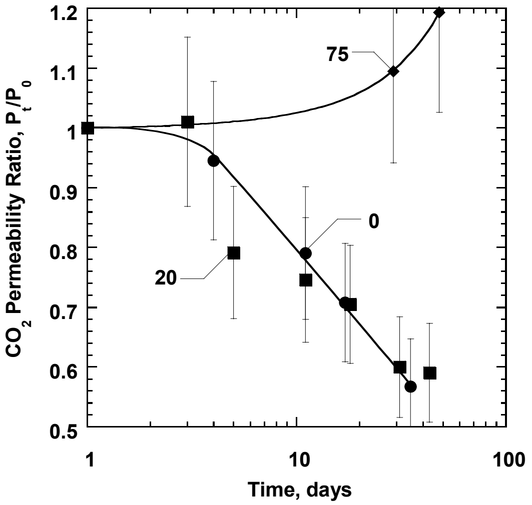

Figure 5.16. CO_2 aging ratio (permeability of a sample at time t, P_t, relative to the permeability at time 0, P_0) at 35 ^{o}C and Δp = 3.4 atm as a function of time for PTMSP containing 0 (●), 20 (■), and 75 (♦) nominal volume percent MgO. Samples were stored in air at room temperature between permeation measurements. Trend lines are drawn to guide the eye. Error bars were estimated from the variance in permeability for multiple experiments using the propagation of errors method described by Bevington.[36]

CONCLUSIONS

Based on TEM imaging, MgO nanoparticles dispersed in PTMSP form micron size aggregates. As the nanoparticle concentration increases, void volume and gas permeability increase strongly. The permeability enhancement was due in large part to an increase in gas diffusion coefficients with increasing void space in the nanocomposite. For example, CO_2 permeability in a sample containing 40 nominal volume percent MgO was 4.5 times higher than that of the unfilled polymer, and 75 percent of this increase was due to an increase in the CO_2 diffusion coefficient. Although both gas permeability and diffusion coefficients increase substantially with particle loading, the nanocomposites used in this study were defect-free. There is a good correlation between void volume and permeability, and the increase in permeability with increasing void volume can be modeled using Bruggeman's model. In this system, the dominant impact of the nanoparticles on permeability is to form voids that do not span the sample, which provides high gas transport rates and results in the polymer controlling, to a large extent, the resulting selectivity. Perhaps the aggregates observed in TEM are the locus of this void volume (*i.e.*, between loosely packed particles) but this hypothesis could not be definitively verified. The pure gas selectivity data suggest a stronger role of flow mechanisms, such as Knudsen flow, at the highest particle loadings, suggesting that at high enough particle contents, pore flow transport mechanisms begin to play a role in the overall transport properties in these materials.

REFERENCES

(1) Matteucci, S.; van Wagner, E.; Swinnea, S.; Freeman, B. D.; Sakaguchi, T.; Masuda, T., Desilylation of substituted polyacetylenes in the presence of nanoparticles, *Macromolecules* **2007**, *40*, 3337-3347.

(2) Qiu, J.; Zheng, J.-M.; Peinemann, K.-V., Gas transport properties in a novel poly(trimethylsilylpropyne) composite membrane with nanosized organic filler trimethylsilylglucose, *Macromolecules* **2006**, *39*, 4093-4100.

(3) Matteucci, S.; Kusuma, V.; Sanders, D.; Swinnea, S.; Freeman, B. D., Gas transport in TiO_2 nanoparticle filled poly(1-trimethylsilyl-1-propyne), *Journal of Membrane Science* **In Press**.

(4) Matteucci, S.; Raharjo, R.; Kusuma, V. A.; Swinnea, S.; Freeman, B. D., Permeability, solubility and diffusion coefficients in 1,2-polybutadiene containing magnesium oxide, *Macromolecules* **Submitted**.

(5) Mahajan, R.; Koros, W. J., Factors controlling successful formation of mixed-matrix gas separation materials, *Industrial and Engineering Chemistry Research* **2000**, *39*, 2692-2696.

(6) Mahajan, R.; Koros, W. J., Mixed matrix membrane materials with glassy polymers. Part 2, *Polymer Engineering and Science* **2002**, *42*, 1432-1441.

(7) Barrer, R. M.; Barrie, J. A.; Rogers, M. G., Heterogeneous membranes: Diffusion in filled rubber, *Journal of Polymer Science, Part A: Polymer Chemistry* **1963**, *1*, 2565-2586.

(8) Takahashi, S.; Paul, D. R., Gas permeation in poly(ether imide) nanocomposite membranes based on surface-treated silica. Part 1: Without chemical coupling to matrix, *Polymer* **2006**, *47*, 7519-7534.

(9) Merkel, T. C.; Freeman, B. D.; Spontak, R. J.; He, Z.; Pinnau, I.; Meakin, P.; Hill, A. J., Sorption, transport, and structural evidence for enhanced free volume in poly(4-methyl-2-pentyne)/fumed silica nanocomposite membranes, *Chemistry of Materials* **2003**, *15*, 109-123.

(10) Barsema, J. N.; Balster, J.; Jordan, V.; van der Vegt, N. F. A.; Wessling, M., Functionalized carbon molecular sieve membranes containing Ag-nanoclusters, *Journal of Membrane Science* **2003**, *219*, 47-57.

(11) van der Marck, S. C., Percolation thresholds of the duals of the face-centered-cubic, hexagonal-close-packed, and diamond lattices, *Physical Review E* **1997**, *55*, 6593 LP - 6597.

(12) Lape, N. K.; Nuxoll, E. E.; Cussler, E. L., Polydisperse flakes in barrier films, *Journal of Membrane Science* **2004**, *236*, 29-37.

(13) Merkel, T. C.; Freeman, B. D.; Spontak, R. J.; He, Z.; Pinnau, I.; Meakin, P.; Hill, A. J., Ultrapermeable, reverse-selective nanocomposite membranes, *Science* **2002**, *296*, 519-522.

(14) Pinnau, I.; Toy, L. G., Transport of organic vapors through poly(1-trimethylsilyl-1-propyne), *Journal of Membrane Science* **1996**, *116*, 199-209.

(15) Merkel, T. C.; He, Z.; Pinnau, I.; Freeman, B. D.; Hill, A. J.; Meakin, P., Effect of nanoparticles on gas sorption and transport in poly(1-trimethylsilyl-1-propyne), *Macromolecules* **2003**, *36*, 6844-6855.

(16) Bird, R. B.; Stewart, W. E.; Lightfoot, E. L. Transport Phenomena, 2nd ed.; John Wiley & Sons: New York, 2002.

(17) Merkel, T. C.; Bondar, V.; Nagai, K.; Freeman, B. D., Sorption and transport of hydrocarbon and perfluorocarbon gases in poly(1-trimethylsilyl-1-propyne), *Journal of Polymer Science Part B: Polymer Physics* **1999**, *38*, 273-296.

(18) Kesting, R. E.; Fritzsche, A. K. Polymer Gas Separation Membranes; John Wiley and Sons: New York, 1993.

(19) Eletskii, A. V. *Viscosity*, In Handbook of Physical Quantities; Grigoriev, I. S.; Meilikhov, E. Z., Eds.; CRC Press: New York, 1997; pp 451-464.

(20) Merkel, T. C.; Bondar, V.; Nagai, K.; Freeman, B. D., Sorption and transport of hydrocarbon and perfluorocarbon gases in poly(1-trimethylsilyl-1-propyne), *Journal of Polymer Science: Part B: Polymer Physics* **2000**, *38*, 273-296.

(21) Breck, D. W. Zeolite Molecular Sieves: Structure, Chemistry, and Use; John Wiley & Sons: New York, 1974.

(22) Do, D. D. Adsorption Analysis: Equilibria and Kinetics; Imperial College Press: London, 1998; Vol. 2.

(23) Koros, W. J.; Chan, A. H.; Paul, D. R., Sorption and transport of various gases in polycarbonate, *Journal of Membrane Science* **1977**, *2*, 165-190.

(24) Paul, D. R., Gas sorption and transport in glassy polymers, *Berichte der Bunsen-Gesellschaft-Physical Chemistry Chemical Physics* **1979**, *83*, 294-302.

(25) Matteucci, S.; Kusuma, V. A.; Swinnea, S.; Freeman, B. D., Light gas permeability, solubility and diffusion in 1,2-polybutadiene containing brookite nanoparticles, *Polymer* **Submitted**.

(26) Mekhemer, G. A. H.; Halaway, S. A.; Mohamed, M. A.; Zaki, M. I., Qualitative and quantitative assessments of acid and base sites exposed on polycrystalline MgO surfaces: Thermogravimetric, calorimetric, and in-situ FTIR spectroscopy study combination, *Journal of Physical Chemistry Part B* **2004**, *108*, 13379-13386.

(27) Stark, J. V.; Park, D. G.; Lagadic, I.; Klabunde, K. J., Nanoscale metal oxide particles/clusters as chemical reagents. Unique surface chemistry on magnesium oxide as shown by enhanced adsorption of acid gases (sulfur dioxide and carbon dioxide) and pressure dependence, *Chemistry of Materials* **1996**, *8*, 1904-1912.

(28) Ichiraku, Y.; Stern, S. A.; Nakagawa, T., An investigation of the high gas permeability of poly(1-trimethylsilyl-1-propyne), *Journal of Membrane Science* **1987**, *34*, 5-18.

(29) Srinivasan, R.; Auvil, S. R.; Burban, P. M., Elucidating the mechanism(s) of gas transport in poly[1-(trimethylsilyl)-1-propyne] (PTMSP) membranes, *Journal of Membrane Science* **1994**, *86*, 67-86.

(30) Raharjo, R. D.; Freeman, B. D.; Paul, D. R.; Sanders, E. S., Pure and mixed gas CH_4 and n-C_4H_{10} permeability and diffusivity in poly(1-trimethylsilyl-propyne), **In Press**.

(31) Nagai, K.; Masuda, T.; Nakagawa, T.; Freeman, B. D.; Pinnau, I., Poly[1-(trimethylsilyl)-1-propyne] and related polymers: Synthesis, properties and functions, *Progress in Polymer Science* **2001**, *26*, 721-798.

(32) Barrer, R. M. *Diffusion and Permeation in Heterogeneous Media*, In Diffusion in Polymers; Crank, J.; Park, G. S., Eds.; Academic Press: New York, 1968; pp 165-219.

(33) McCaig, M. S.; Paul, D. R., Effect of film thickness on the changes in gas permeability of a glassy polyarylate due to physical aging. Part I. Experimental observations, *Polymer* **2000**, *41*, 629-637.

(34) Nagai, K.; Nakagawa, T., Effects of aging on the gas permeability and solubility in poly(1-trimethylsilyl-1-propyne) membranes synthesized with various catalysts, *Journal of Membrane Science* **1995**, *105*, 261-272.

(35) Pfromm, P. H. *The Impact of Physical Aging of Amorphous Glassy Polymers on Gas Separation Membranes*, In Materials Science of Membranes for Gas and Vapor Separation; Yampol'skii, Y. P.; Pinnau, I.; Freeman, B. D., Eds.; John Wiley and Sons: London, 2006; pp 293-306.

(36) Bevington, P. R.; Robinson, D. K. Data Reduction and Error Analysis for the Physical Sciences, 3rd ed.; McGraw-Hill, Inc.: New York, 2003.

Chapter 6: Desilylation of Substituted Polyacetylenes by Nanoparticles

The purpose of this study is to demonstrate the ability of reactive nanoparticles to alter solvent resistance and light gas permeation properties in polymeric membranes. In this study, we report partial desilylation of highly soluble PTMSDPA to insoluble PDPA resulting from dispersing magnesium oxide (MgO) nanoparticles in PTMSDPA by solution blending and film casting. We report desilylation of PTMSP by the same process. The reaction products were characterized using X-ray photoelectron spectroscopy (XPS), Fourier transform infrared spectroscopy (FTIR), and nuclear magnetic resonance (NMR) spectroscopy. Low molar mass model compounds were used to further study this desilylation reaction in the presence of nanoparticles. CO_2 and CH_4 permeabilities are reported for PTMSDPA/MgO nanocomposite films for comparison with permeation results reported for stable substituted polyacetylene films prepared using other desilylation mechanisms.

BACKGROUND

Advantages of substituted polyacetylenes membranes

Recent membrane-based gas separation applications have focused on the removal of organic vapors from mixtures with permanent gases.[1-4] These separations include, for example, the removal of higher hydrocarbons from natural gas and hydrogen mining from mixtures with hydrocarbons in refineries.[2] As a class of materials, substituted polyacetylenes exhibit high permeability and high selectivity in such applications.[5] For example, poly(1-trimethylsilyl-1-propyne) (PTMSP) (*cf.*, Table 3.1) has an n-C_4H_{10} permeability of 80,000 barrer (35 °C, $\Delta p = 1.1$ atm) and an n-C_4H_{10}/CH_4 selectivity of 48 when exposed to a 98 mol % CH_4/ 2% n-C_4H_{10} gas mixture (25 °C, $\Delta p = 11.2$ atm).[6] Similarly, poly(1-phenyl-2-[*p*-(trimethylsilyl)phenyl]acetylene) (PTMSDPA) has a pure gas *n*-butane permeability of 20,000 barrer and a pure gas CH_4 permeability of 1,600 barrer (25 °C, $\Delta p = 0.6$ atm for n-C_4H_{10} and 3.4 atm for CH_4).[7] The n-C_4H_{10}/CH_4 separation has been used as a marker for the removal of higher hydrocarbons from natural gas, which is a separation required to adjust the heating value and dew point of natural gas to pipeline specifications.[1,2] This separation is currently performed using energy-intensive condensation processes.[2] Membranes that are sufficiently permeable to higher hydrocarbons and highly selective for higher hydrocarbons over CH_4 could be of interest for this separation.[1]

The addition of impermeable, surface-treated fumed silica (FS) nanoparticles increases the permeability of some substituted polyacetylenes.[8-10] Furthermore, the addition of 45 wt. % FS increases n-C_4H_{10} permeability of poly(4-methyl-2-pentyne) (PMP) (from 9,200 to 27,000 barrer) and mixed gas n-C_4H_{10}/CH_4 selectivity (from 13 to

21) (25 °C, Δp = 10.2 atm).[9] From a gas transport perspective, substituted polyacetylenes exhibit the best combinations of permeation and selectivity of all known polymers for selective removal of larger organic vapors from mixtures with smaller permanent gases, and nanoparticles can enhance their separation properties.[11,12]

Disadvantages of substituted polyacetylenes

A limitation of substituted polyacetylenes as viable membrane materials is their high solubility in higher hydrocarbons or aromatics such as toluene; such compounds could be present in the gas streams that would be candidates for separation using such polymers, thereby limiting the utility of these materials for vapor separations.[2,13,14] PTMSP, PTMSDPA, and poly(methylacetylene) (*cf.*, Table 3.1) dissolve readily in hydrocarbon solvents such as toluene, hexane, and benzene.[9,15-17] However, many materials from the same family of polymers, such as poly(acetylene) and poly(diphenylacetylene) (PDPA), are insoluble in organic solvents.[17,18] Due to the insolubility of PDPA in organic solvents, films and membranes of this material have only been prepared via desilylation of a soluble substituted precursor, such as PTMSDPA.[19] The desilylation was accomplished by exposing a PTMSDPA film to a mixture of hexane and trifluoroacetic acid for 24 hours at room temperature as presented in Scheme 6.1.[20] After neutralizing the excess acid with triethylamine, impurities were removed by immersing the film in methanol for 5 hours and then washing it with methanol.[20] Desilylation, while imparting chemical stability, was accompanied by a marked diminution in permeability.[19,20] For example, CO_2 permeability in PTMSDPA is 4,000 barrer, but it is only 1,500 barrer in desilylated PTMSDPA (*i.e.,* PDPA) (35°C, Δp = 10.2 atm).[21]

Scheme 6.1. PTMSDPA desilylation reaction with trifluoroacetic acid treatment[20]

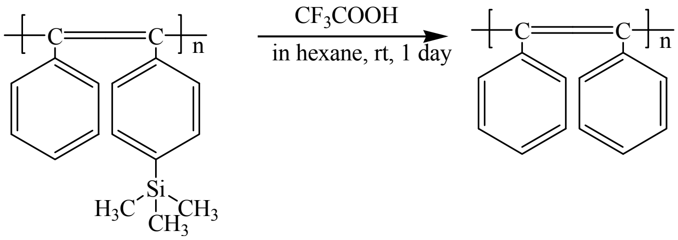

Trimethylsilyl chemistry

Polymers containing trimethylsilyl (TMS) groups often exhibit higher gas and vapor permeability than their analogs without TMS groups.[4,5] For example, materials such as PTMSDPA and poly(vinyltrimethyl silane) have higher diffusivity and permeability coefficients than their non-TMS-containing analogs.[21-23] The diffusivity enhancement has been attributed to disruption of chain packing by bulky TMS groups.[21-23]

The TMS group has several attributes which are relevant to the study of polymer desilylation by metal oxide nanoparticles. Silicon atoms have 3d orbitals available for bonding, and they allow silicon to form transition states with pentavalent bonds.[24] The 3d bond orbital conjugates effectively with adjacent p orbitals such as lone pair electrons on oxygen, nitrogen, and sulfur or with pi-bonded carbon.[24] The $(d\text{-}p)_\pi$ bonding has been credited with increasing the reactivity of Si-Y bonds relative to C-Y bonds.[25] These composite characteristics render TMS groups chemically reactive under certain circumstances.[24]

Teraguchi and Masuda reported the use of trifluoroacetic acid to desilylate PTMSDPA as shown in Scheme 6.1.[20] FTIR indicated complete PTMSDPA conversion to PDPA based upon the disappearance of peaks ascribed to TMS groups in PTMSDPA (*i.e.,* 1250 cm^{-1} for SiC-H as well as 1119, 855, and 812 cm^{-1} for Si-CH_3).[20] The CO_2 permeability of the resulting PDPA membrane is 1,500 barrer as compared to 4,000 barrer for PTMSDPA.[21] The CO_2/CH_4 selectivity was the same for both PTMSDPA and PDPA.[21]

Basic alcohols desilylate small organic molecules containing TMS groups.[24] For instance, Henglein and Scheinost report the desilylation of small molecules, as shown in Scheme 6.2,[26] where R represents either glucose or pectin. In the second step, the positive charge on the nitrogen atom is stabilized by conjugation with the pyridine ring. Such stabilization by conjugation is reported to be important for this reaction.[24] In general, basic alcohol lone pair electrons form a p-d bond with the silicon atom of trimethylsilyl groups.[24] Desilylation is most probable when the TMS donor is less basic than the acceptor and when the donor is conjugated to stabilize the p-d bond. The desilylation reaction mechanism of basic alcohols and organic compounds containing TMS groups is presented in Scheme 6.3,[24] where Y is a TMS acceptor and X is a TMS donor.

Scheme 6.2. Reaction between basic compounds and compounds containing trimethylsilyl groups[26]

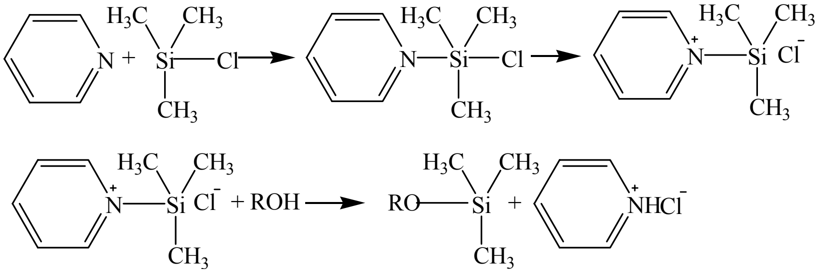

Scheme 6.3. Generic desilylation reaction mechanism for basic molecules[24]

$$\mathrm{HY{:}} + \mathrm{X\text{-}Si(CH_3)_3} \longrightarrow \mathrm{Y{-}Si(CH_3)_3} + \mathrm{HX}$$

RESULTS AND DISCUSSION

Reaction of MgO nanoparticles with water

A reaction was observed between MgO and the polymers under study (*i.e.,* PTMSDPA and PTMSP). As explained in more detail below, this reaction resulted in removal of at least some TMS groups from the polymer. The first step in the desilylation reaction mechanism is believed to be reaction of MgO (*i.e.,* periclase) with adventitious water to form brucite, the mineral form of magnesium hydroxide (-MgOH), as shown in Scheme 6.4.[35] In this way, the particles become partially functionalized with $-\mathrm{MgOH}$ groups.[38,39] Since the brucite formed in this reaction is a part of the overall nanoparticle structure (*e.g.,* -Mg-O-MgOH),[35,40] and does not disassociate in solution,[35,41] it is labeled as $-\mathrm{MgOH}$ rather than $\mathrm{Mg(OH)_2}$.

Scheme 6.4. MgO hydration reaction[40]

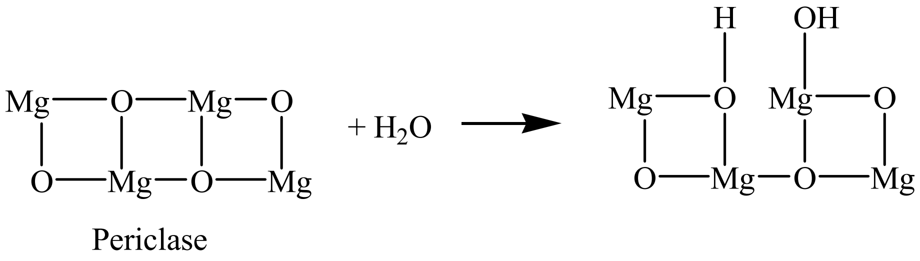

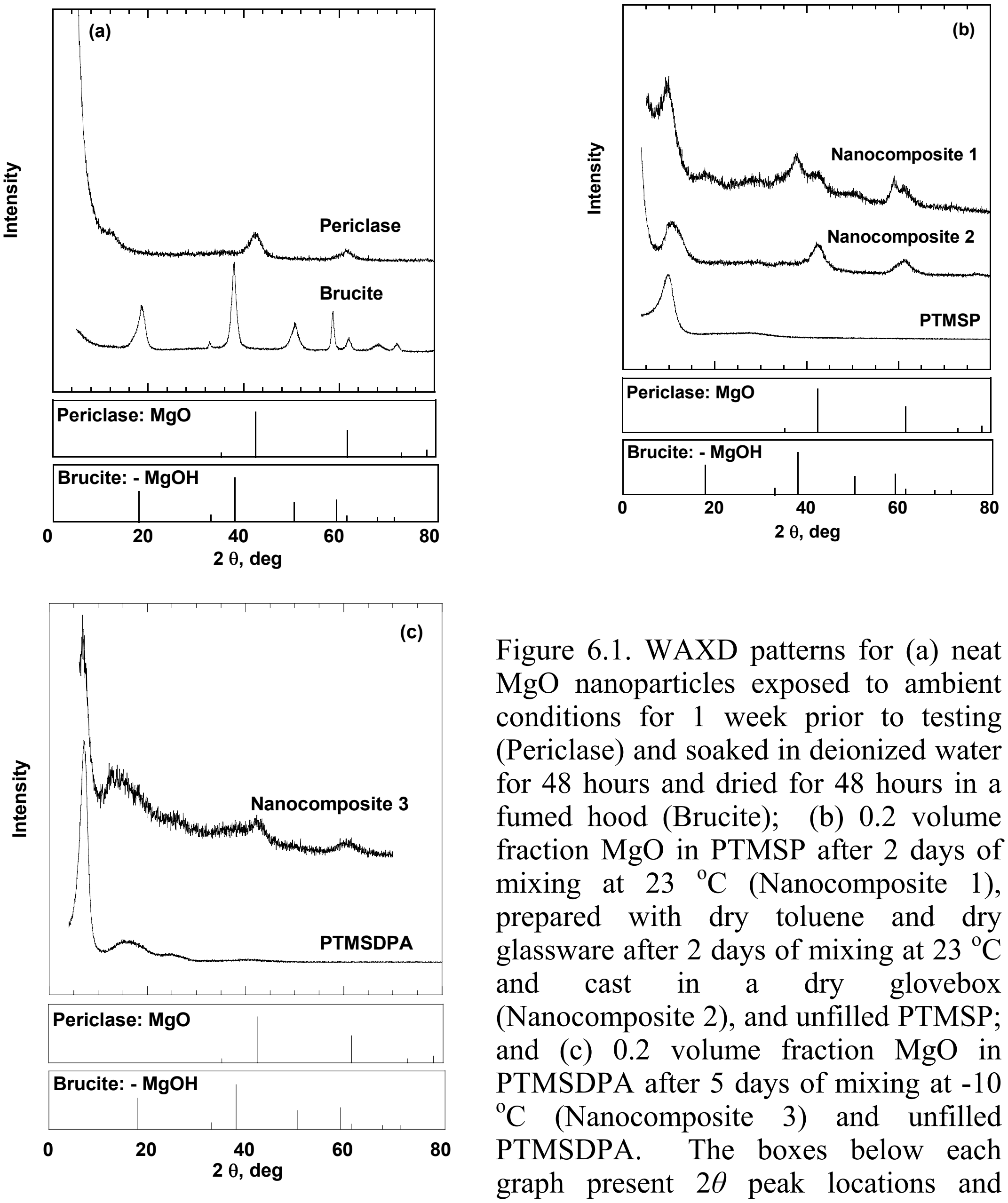

Figure 6.1. WAXD patterns for (a) neat MgO nanoparticles exposed to ambient conditions for 1 week prior to testing (Periclase) and soaked in deionized water for 48 hours and dried for 48 hours in a fumed hood (Brucite); (b) 0.2 volume fraction MgO in PTMSP after 2 days of mixing at 23 °C (Nanocomposite 1), prepared with dry toluene and dry glassware after 2 days of mixing at 23 °C and cast in a dry glovebox (Nanocomposite 2), and unfilled PTMSP; and (c) 0.2 volume fraction MgO in PTMSDPA after 5 days of mixing at -10 °C (Nanocomposite 3) and unfilled PTMSDPA. The boxes below each graph present 2*θ* peak locations and intensities associated with periclase and brucite crystal structures from the powder diffraction database, PDF-2 Release 2004 from the International Centre for Diffraction Data, Newton Square, PA. The WAXD spectra were shifted vertically for easier viewing.

As shown in Figure 6.1a, the WAXD data indicated that the particle structure prior to mixing with the polymer solution was predominantly periclase, which is the crystalline structure of MgO.[40] There was no discernable evidence of brucite in the WAXD spectrum of the neat particles even after exposure to ambient conditions for one week. When the MgO nanoparticles were soaked in deionized water with a resistance of 18.2 MΩ-cm prepared by a Milli-Q plus TOC (Millipore, Billerica, MA) for 48 hours, the particles converted to brucite as shown in Figure 6.1a.

The spectrum of PTMSP filled with 0.2 vol. fraction MgO particles exhibits peaks indicating the presence of both periclase and brucite (*cf.*, Nanocomposite 1 in Figure 6.1b). That is, $-\mathrm{MgOH}$ functional groups were present in the nanocomposite but not in the particles prior to being mixed with the polymer solution. The brucite peaks did appear in the WAXD spectrum of MgO particles soaked in 99.8 % anhydrous toluene for two days and allowed to dry in a fume hood for two days, so the partial conversion of periclase to brucite did not require the presence of PTMSP in the solution. Thus, using the protocol described in the experimental section except that the glassware was allowed to cool to room temperature at ambient conditions prior to being moved to a N_2 blanketed glove box, a reaction between MgO and water takes place. Although the nanocomposite solution and films were prepared in a dry glovebox, it seems likely that there were traces of water adsorbed on glassware or in the solvent with which the particles could have reacted.

A more rigorous drying procedure suppresses conversion of periclase to brucite as described in Chapter 3. Adventitious water introduced from the glassware can be suppressed by drying the glassware at 80 ^{o}C overnight and placing the warm glassware into the N_2 blanketed glove box. Using anhydrous toluene from Acros Organics (Geel, Belgium) containing less than 50 ppm water reduces another potential source of moisture. Nanocomposite 2 in Figure 6.1b was prepared under these conditions, and it exhibited no peaks associated with brucite in WAXD. The peak at around 9.5° is associated with PTMSP (*cf.,* Figure 6.1b), and it is consistent with the PTMSP WAXD spectrum in the literature.[15] The results discussed below were obtained using the protocol described in the experimental section, that is, using the sample preparation method that results in the conversion of some periclase to brucite.

The spectrum of MgO-filled PTMSDPA, when the particles are mixed with the polymer at low temperatures, did not exhibit peaks associated with brucite (*cf.*, Nanocomposite 3 in Figure 6.1c). The spectrum of PTMSDPA exhibited peaks at 6.3 and 14.5° as presented in Figure 6.1c, which is consistent with the spectrum reported in the literature.[16] As discussed in more detail below, the absence of brucite in the WAXD spectrum of this sample may result from the consumption of most of the available $-\mathrm{MgOH}$ groups by the desilylation reaction.

Desilylation of PTMSP

The proposed reaction mechanism of PTMSP with brucite alcohol groups is presented in Scheme 6.5. The alcohol groups on magnesium hydroxide are electron rich and basic,[42] which favors their participation in reactions of the type shown in Scheme 6.3. The PTMSP backbone could serve as a TMS donor. Also, the polymer backbone is somewhat conjugated,[5] which allows p-d bond stabilization, and this effect also favors reactions of the type illustrated in Schemes 6.3 and 6.5.[24] From Scheme 6.3, Y would represent MgO-, and X would represent the PTMSP backbone. The lone pair electrons on -Mg-OH groups may form a p-d bond with silicon, which would be stabilized by conjugation with the PTMSP backbone.

Scheme 6.5. Proposed PTMSP desilylation reaction by hydrolyzed MgO nanoparticles

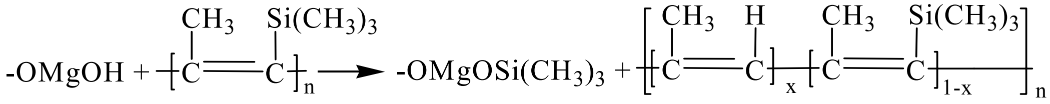

$$\text{-OMgOH} + \left[\overset{CH_3}{\overset{|}{C}}=\overset{Si(CH_3)_3}{\overset{|}{C}}\right]_n \longrightarrow \text{-OMgOSi}(CH_3)_3 + \left[\left[\overset{CH_3}{\overset{|}{C}}=\overset{H}{\overset{|}{C}}\right]_x\left[\overset{CH_3}{\overset{|}{C}}=\overset{Si(CH_3)_3}{\overset{|}{C}}\right]_{1-x}\right]_n$$

ATR FTIR spectra of pure MgO, pure PTMSP and a nanocomposite film of PTMSP containing MgO are presented in Figure 6.2. The MgO nanoparticles did not exhibit any peaks between 675 to 4000 cm^{-1}, and this result is consistent with the literature.[43] The PTMSP spectrum exhibits a peak at 1540 cm^{-1}, which is attributed to carbon-carbon double bonds, as well as peaks at 1240, 820 and 740 cm^{-1}, which are attributed to $\mathrm{SiC-H}$ and Si-CH$_3$ bonds, respectively. These peaks and their assignments are consistent with those reported by Masuda *et al.*[15] The spectrum for PTMSP/MgO films contains PTMSP peaks and several additional peaks. The MgO-Si peak at 1092 cm^{-1} suggests that desilylation occurred.[44] Other differences between the spectra of the PTMSP and PTMSP/MgO samples were at 2300 to 2400 cm^{-1} and at 1400 to 1550 cm^{-1}, consistent with physisorption[45] and chemisorption[35,43] of CO$_2$ on MgO, respectively. CO$_2$ chemisorbed to MgO leads to the formation of -MgCO$_3$.[35,43] Any differences in the peaks associated with physisorbed CO$_2$ (*i.e.,* the peak at 2200 to 2400 cm^{-1}) can be attributed to differences in the background levels of CO$_2$ present when the background and sample scans were collected.

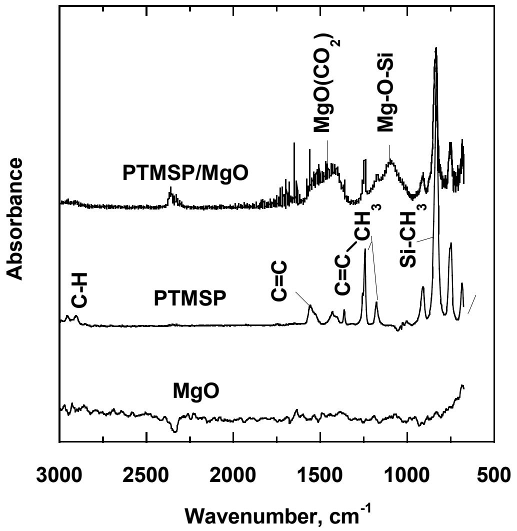

Figure 6.2. ATR FTIR of MgO, PTMSP and PTMSP containing 0.2 volume fraction MgO. The PTMSP/MgO spectrum was shifted vertically for easier viewing. Peak assignments for PTMSP are from Masuda *et al.*[15] Peak assignments for MgOH,[35] physisorbed CO_2,[45] chemisorbed CO_2 (i.e., $MgO(CO_2)$),[35,43] and Mg-O-Si[24] are consistent with the literature.

Figure 6.3 presents XPS characterization of the silicon 2p orbital of PTMSP and a PTMSP/MgO nanocomposite. From these spectra, Si had bonds to two different elements in the nanocomposite sample, but not in the polymer. The peak at 101 eV corresponds to Si-C bonds,[46] and this peak is observed in both the PTMSP film and the PTMSP/MgO film. The peak at 105 eV is ascribed to the presence of Si-O bonds.[47] The particles provide the only oxygen source in the PTMSP/MgO film. The PTMSP provides the only source of Si in these materials since XPS did not detect Si in the neat MgO nanoparticles, as expected. Therefore, the XPS results corroborate the existence of Mg-O-Si bonds, which should be present if PTMSP were partially desilylated according to Scheme 6.5.

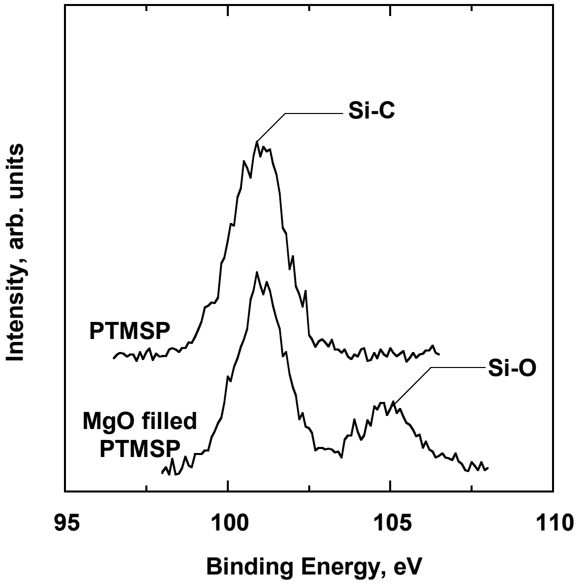

Figure 6.3. XPS of Si 2p orbital for PTMSP and PTMSP containing 0.2 volume fraction MgO.

One advantage of using PTMSP in the desilylation studies is that the desilylated product, a copolymer of PTMSP and poly(methylacetylene), remains soluble in organic solvents, including d-benzene. This feature allows the reaction products to be characterized by solution NMR. ^{1}H NMR solution spectroscopy was conducted on PTMSP and PTMSP/MgO samples to characterize changes in the polymer structure due to the reaction, and the results are presented in Figure 6.4. As shown in Figure 6.4a, the ^{1}H NMR spectrum for PTMSP exhibited peaks at 0.8 and 2.1 ppm, and they are attributed to protons on the TMS methyl groups and the lone methyl group, respectively. These results are consistent with those reported by Masuda *et al.*[15] As shown in Figure 4b, these peaks were also present in the ^{1}H NMR spectrum for the PTMSP nanocomposite. The peak at 0.8 ppm (*i.e.,* protons on the TMS groups) in the nanocomposite indicates that the desilylation reaction did not proceed to completion. Also, a singlet peak was observed at 3.1 ppm the PTMSP/MgO spectrum, and this peak is not observed in the spectrum of the polymer alone (*cf.*, Figure 6.4a). Since PTMSP did not have a peak at 3.1 ppm, it is assigned to the olefinic proton produced by the desilylation reaction. The 3.1 ppm peak is at a different location than the olefinic proton peak value of 5.9 ppm reported for pure poly(methylacetylene).[48] However, the silylated constituents on the polymer chain may shift the olefinic proton peak to a lower value. The chemical shift of olefinic protons in polyacetylenes often varies widely depending on the secondary polymer structure.[49]

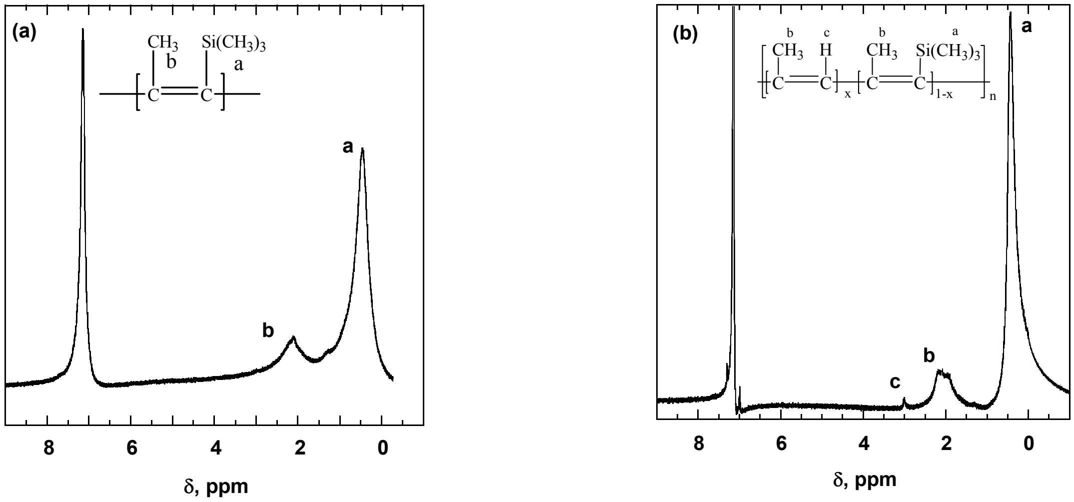

Figure 6.4. ^{1}H NMR of (a) PTMSP and (b) PTMSP containing 0.2 volume fraction MgO. The peak at 7.2 ppm is ascribed to the hydrogen atoms in the *d*-benzene solvent.

Using the NMR data, the fractional desilylation, X_{TMS} (moles of TMS removed / moles of TMS in the polymer before desilylation) can be estimated as follows:

$$X_{TMS} = \frac{i_c}{i_c + \frac{i_a}{9}} \times 100 \tag{6.1}$$

where i_a is the integral value of the TMS group of PTMSP at peak (a), and i_c is the proton integral value of the desilylated PTMSP olefinic proton peak (c). In this case, i_a is divided by nine because there are nine hydrogen atoms on a TMS group, and they are replaced by one hydrogen when desilylation occurs. Based on Eq. (6.1) and the data in Figure 6.4b, 9 % of the TMS groups were removed from the polymer due to contact with MgO according to the sample preparation protocol described earlier.

Desilylation of PTMSDPA

If the desilylation of PTMSDPA follows a similar mechanism to that of PTMSP, the reaction would proceed as indicated in Scheme 6.6. The phenyl groups may increase the conjugation of the PTMSDPA polymer backbone,[16,20] which may, in turn, stabilize the MgOH–TMS bond more effectively than in PTMSP. PTMSDPA and nanocomposites containing 0.2 volume fraction MgO in PTMSDPA were examined by FTIR, and the results are presented in Figure 6.5. The PTMSDPA peaks at 1250 cm^{-1} (SiC-H) and at 1119, 855, and 812 cm^{-1} (Si-CH_3) are in agreement with the spectrum reported for PTMSDPA by Tsuchihara *et al.*[16] and by Teraguchi and Masuda.[16,20] The PTMSDPA/MgO film contained a new peak at 1092 cm^{-1}. This new peak is consistent with the peak at 1092 cm^{-1} in the PTMSP/MgO spectrum, and it is attributed to Mg-O-Si bonds formed as a result of the desilylation reaction shown in Scheme 6.6.

Scheme 6.6. MgO induced PTMSDPA desilylation reaction

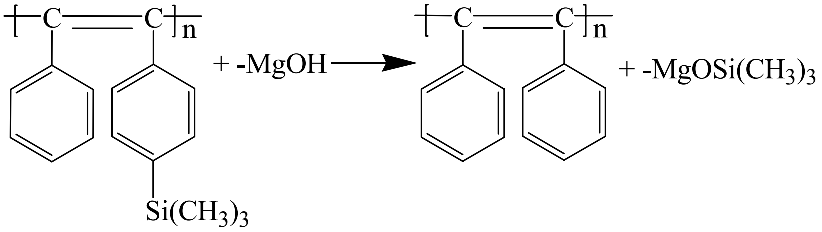

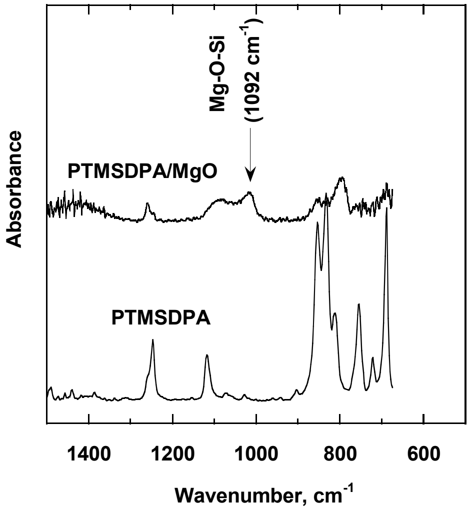

Figure 6.5. ATR FTIR spectra of PTMSDPA and PTMSDPA containing 0.2 volume fraction MgO. The spectrum of PTMSDPA/MgO was shifted vertically for easier viewing.

Like PDPA (*i.e.,* desilylated PTMSDPA), the PTMSDPA/MgO samples were insoluble in d-benzene, so solution NMR studies could not be performed. Testing nanocomposite solubility in known solvents for PTMSDPA provides indirect evidence for the desilylation of PTMSDPA by MgO nanoparticles. As demonstrated below, the weight loss of PTMSDPA/MgO nanocomposites after extraction in toluene depends on MgO loading, PTMSDPA/MgO solution mixing time, and solution mixing temperature. Increasing MgO loading, while holding the other parameters constant, substantially decreased weight loss due to extracting the nanocomposite in toluene, as shown in Figure 6.6. Since PTMSDPA is soluble in toluene and the MgO particles are readily dispersed in toluene, if there were no interaction between the polymer and particles, the weight loss would be 100%, which is the result obtained in the absence of particles (*i.e.,* 0 vol. fraction MgO in Figure 6.6). On the other hand, if the polymer/particle film is completely insoluble in toluene, then the weight loss upon extraction in toluene would be 0%. This limit is achieved in samples containing 0.35 and 0.5 volume fraction nanoparticles. Similar insolubility results were found for PTMSDPA/MgO films in chloroform extraction experiments, and chloroform is another good solvent for PTMSDPA.[20]

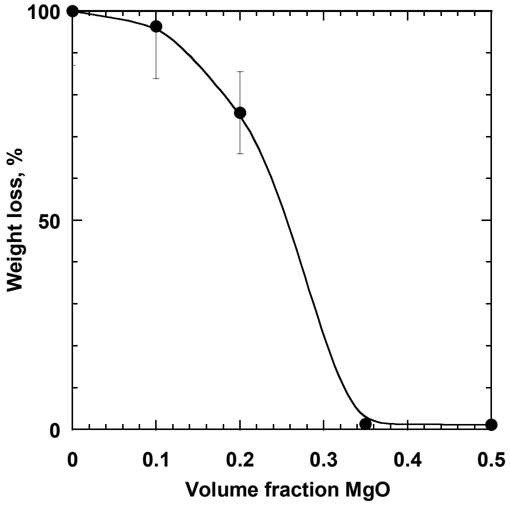

Figure 6.6. Influence of MgO nanoparticle content in PTMSDPA on weight loss after extraction in toluene for 2 weeks, as calculated by Eq. (3.10). Solutions were mixed for 5 days at -10 °C. The uncertainty in sample weight after toluene extraction is indicated by the error bars on the data points, and they represent the standard deviation from multiple experiments. The volume fraction MgO corresponds to the particle content in the polymer films prior to the start of the extraction study.

Similar behavior was observed with respect to the PTMSDPA/MgO solution mixing time. As shown in Figure 6.7, increasing mixing time generally decreased nanocomposite weight loss due to toluene extraction. As mixing time increased, the solution turned from orange (*i.e.*, the typical color of a PTMSDPA/toluene solution) to dark red, which is the color of PDPA reported by Teraguchi and Masuda.[20] When a PTMSDPA/MgO solution was allowed to mix for extended periods of time (*e.g.,* 6 days at room temperature), it would gel. This observation is another qualitative indication consistent with the formation of toluene-insoluble PDPA in the presence of MgO nanoparticles.

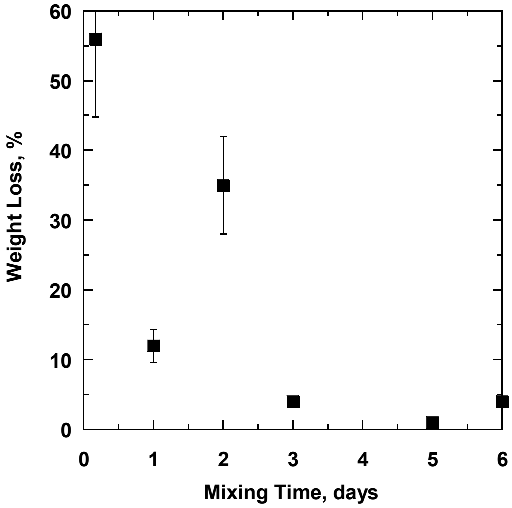

Figure 6.7. Influence of mixing time on PTMSDPA/MgO film weight loss after extracting in toluene for 2 weeks, as calculated using Eq. (3.10). Samples were mixed at 23 °C, and the film before extraction contained 0.2 volume fraction MgO. The uncertainty in sample weight after toluene extraction is indicated by the error bars on the data points, and they represent the standard deviation from multiple experiments.

The effect of temperature on desilylation was similar to that of mixing time and MgO loading. Increasing the mixing temperature decreased the weight loss of PTMSDPA/MgO samples after toluene extraction. After 5 days of mixing the solution at -10 °C, there was substantial weight loss (*i.e.,* 76 %), whereas at higher solution mixing temperatures, PTMSDPA/MgO films were essentially insoluble in toluene and experienced practically no detectable weight loss (*i.e.,* weight loss was 2 % at 0 °C and 4 % at 23 °C). Presumably, the reaction between the particles and polymer was favored at higher temperatures. Therefore, at a fixed mixing time, the extent of reaction, as characterized by weight loss upon extraction in toluene, was higher at higher temperatures.

Table 6.1 presents pure gas CO_2 and CH_4 permeability in filled PTMSDPA. The gas permeability generally increases with increasing particle loading. At 0.1 volume fraction MgO, CO_2 permeability was similar to that of PTMSDPA, (*i.e.,* 6 kbarrer), which is somewhat higher than the CO_2 permeability in PTMSDPA reported by Raharjo *et al*. (*i.e.,* 4 kbarrer).[21] The difference between the unfilled PTMSDPA permeability reported here and that reported by Raharjo *et al.* may be attributed to differences in sample processing history.[21] However, at 0.1 volume fraction MgO, CH_4 permeability is higher than that of the particle-free polymer. At MgO loadings greater than 0.1 volume fraction, the permeability of both gases increased. The nanocomposite film with 0.5 volume fraction MgO exhibited a CO_2 permeability of 40.3 kbarrer and a CO_2/CH_4 selectivity of 2.2. The CO_2 permeability of the 0.5 volume fraction filled PTMSDPA is approximately 25 times higher than the CO_2 permeability reported for PDPA (*i.e.,* 1.5 kbarrer)[21] and over 6 times higher than PTMSDPA, whereas the CO_2/CH_4 selectivity is somewhat lower than the CO_2/CH_4 selectivity values reported by Raharjo *et al.* for PDPA and PTMSDPA, which were 3.3 for both materials.[21] Transmission electron microscopy were used to characterize the nanoparticle dispersion in the polymers, and the results from this study are reported in Chapter 5.

Table 6.1. Permeability of MgO filled PTMSDPA films mixed at -10 °C for 5 days

MgO volume fraction	CO_2 Permeability, kbarrer	CH_4 Permeability, kbarrer	α_{CO_2/CH_4}
0	6.0 (± 0.6)	2.7 (± 0.3)	2.2 (± 0.2)
0.1	6.0 (± 0.6)	3.8 (± 0.4)	1.6 (± 0.2)
0.25	8.6 (± 0.8)	5.3 (± 0.5)	1.6 (± 0.2)
0.5	40 (± 4)	19 (± 1.9)	2.2 (± 0.2)

Experiments were conducted at 35 °C and $\Delta p = 3.4$ atm. Permeability is expressed in kbarrer (kilobarrer), where 1 kbarrer = $10^{-7}\ \frac{\text{cm}^3(\text{STP})\text{cm}}{\text{cm}^2\text{s cmHg}}$

Desilylation of model compounds

One obstacle encountered in the study of PTMSDPA desilyation is that the resulting product, PDPA, is insoluble, which limits structural characterization of the resulting desilylated compound. To provide further evidence of this reaction and to study it in more detail, low molar mass model compounds (*cf.*, Table 3.2) containing a TMS unit connected to an aromatic ring (trimethyl(phenyl)silane (TMPS)) or via an ethylene linkage, (1-phenyl-2-(trimethylsilyl)-ethylene (PhTMSE)), or an acetylene linkage (1-phenyl-2-(trimethylsilyl)-acetylene (PhTMSA)), were selected to study desilylation in the presence of MgO nanoparticles. Since these are low molar mass compounds, they remain soluble even after reaction with the particles, which enables characterization via NMR.

Treating TMPS with MgO does not transfer the TMS group as discussed with PTMSP and PTMSDPA, but MgO treatment results in an interaction between the nanoparticles and the small molecule as proposed in Scheme 6.7. Proton and ^{13}C NMR did not show any reaction products for MgO treated TMPS. Any material bound to a nanoparticle (*i.e.,* any TMPS molecule whose silicon atom has a p-d bond with the nanoparticle) would not be in solution since the MgO particles are not soluble in d-benzene. However, a chalky residue formed on the side of the mixing vessel during treatment was presumed to be MgO-treated TMPS. The FTIR spectrum of the chalky material (*cf.* Figure 6.8) shows peaks at 1160 cm^{-1} and at 1090 cm^{-1} that are not present in the neat TMPS. The chalky residue (*i.e.,* MgO-treated TMPS) also has a peak that is shifted relative to that of untreated TMPS. The new peak at 1160 cm^{-1} is attributed to the in-plane CH bending vibrations of monosubstituted benzene.[44] This vibration is more pronounced in the MgO-treated TMPS than in untreated TMPS, which might indicate a change in the monosubstituted benzene, such as the formation of a p-d bond between Si and the nanoparticle oxygen lone pair electrons. The peak at 1090 cm^{-1} is attributed to Si-O bonds.[44,51] The broadly shifted peak between 1200 and 1275 cm^{-1} in the chalky residue spectrum is ascribed to the SiC-H,[19,44] and it is consistent with FTIR spectra of other molecules containing TMS groups or phenyl-silicon bonds where the silicon atom is bound to substituents of varying chemistry (*i.e.,* alcohols, amines, halogens, *etc.*).[44]

Scheme 6.7. Interaction between MgO and TMPS

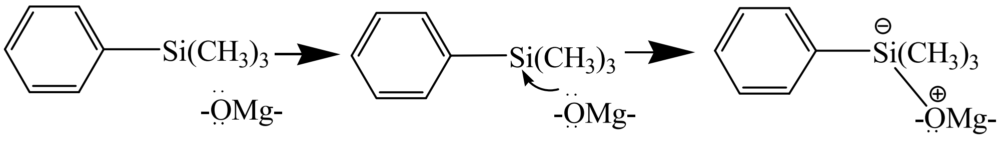

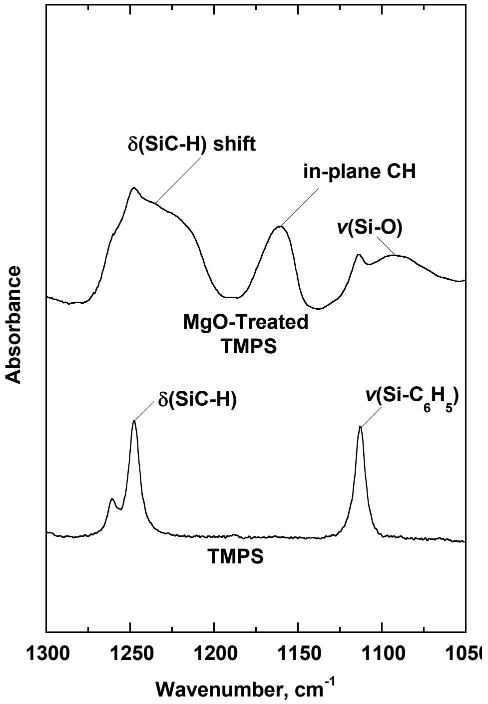

Figure 6.8. FTIR transmission spectra of TMSP and MgO-treated TMPS in KBr pellets. The spectra have been shifted vertically for easier viewing.

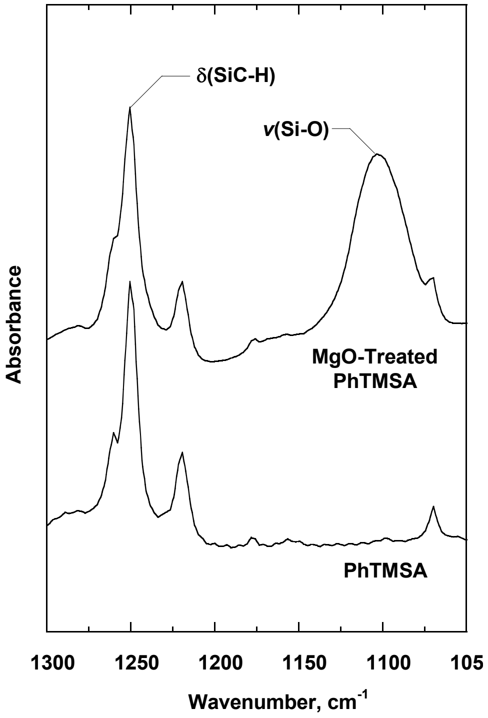

Figure 6.9. FTIR transmission spectra of PhTMSA and MgO-treated PhTMSA in KBr pellets. The spectra have been shifted vertically for easier viewing.

^{1}H NMR revealed several new peaks in the MgO treated PhTMSE spectrum that were not present in the untreated PhTMSE spectrum. The TMS peaks (*i.e.,* peaks near 0 ppm) were not changed upon treatment with MgO. A reaction is believed to occur between PhTMSE and the MgO particles which does not involve the TMS group. Therefore, PhTMSE was not a good model compound for the study of the MgO nanoparticle induced desilylation reaction, and studies of this compound were discontinued.

The acetylene group in PhTMSA did not react with MgO. The aromatic group of PhTMSA mimics, albeit crudely, conjugation of the PTMSDPA phenyl rings and also stabilizes oxygen-silicon p-d bonds.[24] To be consistent with the reaction mechanism proposed in the literature for basic alcohol groups reacting with TMS-containing compounds (*i.e.,* Scheme 6.3), the desilylation reaction of PhTMSA would follow Scheme 6.8. Figure 6.9 presents the FTIR spectrum of PhTMSA and the spectrum of MgO-treated PhTMSA with a TMS content of 0.08 mol TMS/g MgO, which is equivalent to the TMS/MgO ratio for a PTMSP film containing 0.2 volume fraction MgO. There is a broad peak in the MgO-treated PhTMSA spectrum at 1107 cm^{-1}, which is not present in the spectrum of PhTMSA. This peak is consistent with the presence of Si-O bonds,[44] and it is ascribed to -Mg-O-Si bonds.

Scheme 6.8. MgO induced PhTMSA desilylation reaction

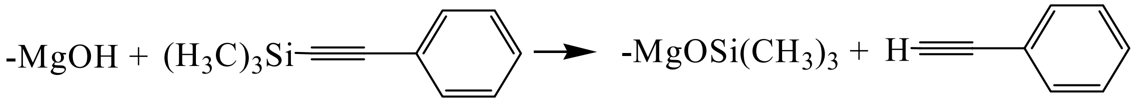

As shown in Figure 6.10a, the PhTMSA ^1H NMR spectrum exhibited peaks at 7.4, 6.8, and 0.3 ppm, which are attributed to the para-hydrogen, meta and ortho hydrogens, and the TMS hydrogen, respectively. These peaks are consistent with those reported in the literature.[52] The peak at 7.2 ppm is attributed to the hydrogen atoms on the d-benzene solvent. As shown in Figure 6.10b, relative to PhTMSA, there were three new peaks in the ^1H NMR spectrum of MgO-treated PhTMSA (TMS/MgO ratio = 0.08 mol/g) at 7.39, 2.72, and 0.10 ppm. The peak at 7.39 ppm (g,h) corresponds to the *m*-phenyl protons on desilylated PhTMSA samples.[53] The peak at 2.72 ppm (e) is assigned to the proton bound to the acetylene unit,[53] confirming the hydrogen-TMS transfer between -MgOH and PhTMSA. Peak (i) has a chemical shift slightly lower than that of the TMS proton peak in PhTMSA, *i.e.,* peak (a); therefore, peak (i) is ascribed to the

TMS protons in $-\mathrm{OTMS}$. The $-\mathrm{OTMS}$/acetylene proton integral ratio (*i.e.,* the ratios of the peaks at 0.20 and 0.10 ppm) is 9:1, which is the stoichiometric ratio required by the proposed reaction (*cf.*, Scheme 6.8).

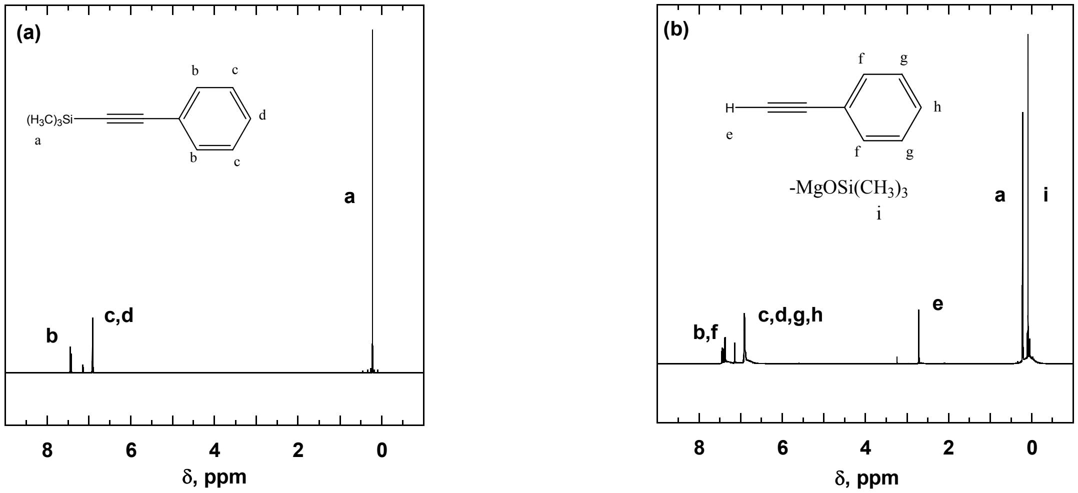

Figure 6.10. ^{1}H NMR spectrum of (a) PhTMSA and (b) MgO-treated PhTMSA.

Using the NMR data in Figure 6.10, the fractional desilylation, X_{TMS} (percentage of moles of TMS removed / total moles of TMS), was characterized by two methods. First, if the TMS groups are conserved, a TMS balance of the proton integral values of peaks (a) and (i) yields the following estimate:

$$X_{TMS} = \frac{i_i}{i_i + i_a} \times 100 \tag{6.2}$$

where i_i and i_a are the proton integral values for peak (i) (the TMS group of –OTMS) and peak (a) (the TMS group of PhTMSA), respectively. The second method involves comparing the integral of peak (a), the TMS group of PhTMSA, to that of the desilylated PhTMSA proton peak (e):

$$X_{TMS} = \frac{i_e}{i_e + \frac{i_a}{9}} \times 100 \qquad (6.3)$$

where i_e is the proton integral value of the desilylated PhTMSA proton peak (e). In this case, i_a is divided by nine because there are nine hydrogen atoms on a TMS group, and they are replaced by one hydrogen when desilylation occurs. Eq. (6.3) is generally the better method of calculating X_{TMS} since the -OTMS peak does not always appear in solution state NMR spectrum in samples where the nanoparticles could not be adequately dispersed in d-benzene to be detected. The fractional desilylation of MgO-treated PhTMSA based upon Eqs. (6.2) and (6.3) yield similar results, as shown in Figure 6.11. Both methods indicated an increase in fractional desilylation with increasing particle loading and essentially complete desilylation (*i.e.,* X_{TMS} equals 100 %) of PhTMSA at a volume fraction of MgO equal to 0.5.

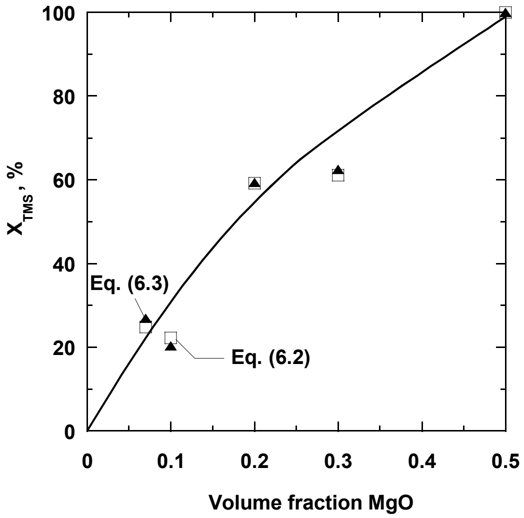

Figure 6.11. Influence of MgO content on estimated percentage desilylation of PhTMSA, X_{TMS}, as calculated by Eq. (6.2) and estimated percentage of trimethylsilyl groups on the MgO particles as calculated by Eq. (6.3).

The ^{13}C NMR spectrum revealed a chemical change when PhTMSA was contacted with MgO (*cf.*, Figures 6.12a and b). As shown in Figure 6.12a, PhTMSA peaks at 106 ppm (c) and 94 ppm (b) represent the acetylene carbons, while the peak at 0 ppm (a) corresponds to the TMS carbons,[53] and it is consistent with the ^{13}C NMR spectrum reported in the literature.[52] As shown in Figure 6.12b, three new peaks appeared for the MgO-treated PhTMSA at 84, 78, and 2 ppm. The peaks at 84 ppm (i) and 78 ppm (h) represent desilylated acetylene carbons.[53] The peak at 2 ppm (n) is attributed to -OTMS since the chemical shift is near 0, as expected for a TMS group, yet it is not equivalent to the TMS chemical shift observed for untreated PhTMSA. In this case, the -OTMS peak is present due to its high concentration in the solution (60 mol % based on Eq. (6.3)).

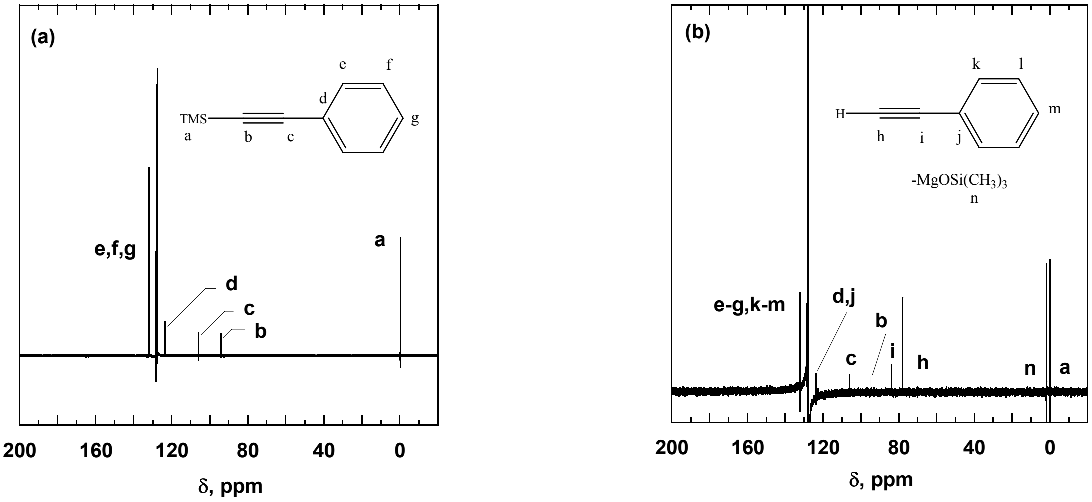

Figure 6.12. ^{13}C NMR spectrum of (a) PhTMSA and (b) MgO-treated PhTMSA.

Mixed gas selectivity in desilylated polyacetylene nanocomposites

The combination of improved solvent resistance and increased permeability makes these materials interesting for applications involving the removal of light gases from organic vapors. However, mixed gas *n*-butane/CH$_4$ selectivity decreases with increasing particle loading in the PTMSDPA/MgO nanocomposites. For instance, for a 98:2 (mol/mol) CH$_4$/*n*-butane feed, mixed gas *n*-butane/CH$_4$ selectivity in PTMSDPA was 3.3, and that of PTMSDPA filled with 35 nominal volume percent MgO was 2.2 at 35 ^{o}C over a feed pressure range of 5 to 15 atm.

CONCLUSIONS

In much of the literature on polymer nanocomposites for gas separation applications, the nanoparticles are presumed to be chemically inert with the polymer. However, this assumption is not obeyed by metal oxides such as MgO in materials such as those considered in this study. The reaction and permeation data presented in this report demonstrate that metal oxide nanoparticles can alter the chemical properties and enhance the gas transport properties of polymeric membranes. The desilylation reaction between TMS-bearing compounds and MgO nanoparticles was substantiated via model compound studies. The chemical stability and gas permeability of the polymers increase with increasing particle loading. At high MgO loadings (*i.e.,* 0.5 volume fraction), the nanocomposite films are insoluble in common solvents and exhibit CO_2 permeability coefficients nearly one order of magnitude greater than that of the native polymer. Although this is only one example of nanoparticle-treated polymeric membranes, the technique of adding nanoparticles that react with the polymer matrix presents one relatively unexplored route to prepare membrane materials with enhanced gas transport properties and improved chemical stability. So far, it is not known to what extent particle size affects these results and whether other particles might behave similarly.

REFERENCES

(1) Baker, R. W., Future directions of membrane gas separation technology, *Industrial and Engineering Chemistry Research* **2002**, *41*, 1393-1411.

(2) Baker, R. W. Membrane Technology and Applications, 2nd ed.; McGraw-Hill: New York, 2004.

(3) Freeman, B. D.; Pinnau, I., Separation of gases using solubility-selective polymers, *Trends in Polymer Science* **1997**, *5*, 167-173.

(4) Matteucci, S. T.; Yampol'skii, Y. P.; Freeman, B. D.; Pinnau, I. *Transport of gases and vapors in glassy and rubbery polymers*, In Materials Science of Membranes for Gas and Vapor Separations; Pinnau, I., Ed.; John Wiley and Sons: London, 2006; pp 1-48.

(5) Nagai, K.; Masuda, T.; Nakagawa, T.; Freeman, B. D.; Pinnau, I., Poly[1-(trimethylsilyl)-1-propyne] and related polymers: Synthesis, properties and functions, *Progress in Polymer Science* **2001**, *26*, 721-798.

(6) Merkel, T. C.; He, Z.; Pinnau, I.; Freeman, B. D.; Hill, A. J.; Meakin, P., Effect of nanoparticles on gas sorption and transport in poly(1-trimethylsilyl-1-propyne), *Macromolecules* **2003**, *36*, 8406-8414.

(7) Toy, L. G.; Nagai, K.; Freeman, B. D.; Pinnau, I.; He, Z.; Masuda, T.; Teraguchi, M.; Yampolskii, Y. P., Pure-Gas and Vapor Permeation and Sorption Properties of Poly{1-phenyl-2-[*p*-(trimethylsilyl)phenyl]acetylene] (PTMSDPA), *Macromolecules* **2000**, *22*, 2516-2524.

(8) Merkel, T. C.; Freeman, B. D.; Spontak, R. J.; He, Z.; Pinnau, I.; Meakin, P.; Hill, A. J., Ultrapermeable, reverse-selective nanocomposite membranes, *Science* **2002**, *296*, 519-522.

(9) Merkel, T. C.; Freeman, B. D.; Spontak, R. J.; He, Z.; Pinnau, I.; Meakin, P.; Hill, A. J., Sorption, transport, and structural evidence for enhanced free volume in poly(4-methyl-2-pentyne)/ fumed silica nanocomposite membranes, *Chemistry of Materials* **2003**, *15*, 109-123.

(10) He, Z.; Pinnau, I.; Morisato, A., Nanostructured poly(4-methyl-2-pentyne)/silica hybrid membranes for gas separation, *Desalination* **2002**, *146*, 11-15.

(11) Teplyakov, V. V.; Roizard, D.; Farve, E.; Khotimsky, V. S., Investigations on the Peculiar Permeation Properties of Volatile Organic Compounds and Permanent Gases Through PTMSP, *Journal of Membrane Science* **2003**, *220*, 165-175.

(12) Pinnau, I.; Toy, L. G., Transport of organic vapors through poly(1-trimethylsilyl-1-propyne), *Journal of Membrane Science* **1996**, *116*, 199-209.

(13) White, L. S.; Blinka, T. A.; Kloczewski, H. A.; Wang, I., Properties of a polyimide gas separation membrane in natural gas streams, *Journal of Membrane Science* **1995**, *103*, 73-82.

(14) Ratcliffe, C. T.; Diaz, A.; Nopasit, C.; Munoz, G. In *Laurence Reid Gas Conditioning Conference*: Norman, OK, 1999; pp 118-140.

(15) Masuda, T.; Isobe, E.; Higashimura, T., Polymerization of 1-(trimethylsilyl)-1-propyne by halides of niobium(V) and tantalum(V) and polymer properties, *Macromolecules* **1985**, *18*, 841-845.

(16) Tsuchihara, K.; Masuda, T.; Higashimura, T., Polymerization of Silicon-Containing Diphenylacetylenes and High Gas Permeability of the Product Polymers, *Macromolecules* **1992**, *25*, 5816-5820.

(17) Chien, J. C. W.; Wnek, G. E.; Karasz, F. E.; Hirsch, J. A., Electrically Conducting Acetylene-Methylacetylene Copolymers. Synthesis and Properties, *Macromolecules* **1981**, *14*, 479-485.

(18) Niki, A.; Masuda, T.; Higashimura, T., Effects of organometallic cocatalysts on the polymerization of distributed acetylenes by tantalum chloride and niobium clhoride, *Journal of Polymer Science Part A: Polymer Chemistry* **1987**, *25*, 1553-1562.

(19) Sakaguchi, T.; Yumoto, K.; Shiotsuki, M.; Sanda, F.; Yoshikawa, M.; Masuda, T., Synthesis of Poly(diphenylacetylene) Membranes by Desilylation of Various Precursor Polymers and Their Properties, *Macromolecules* **2005**, *38*, 2704-2709.

(20) Teraguchi, M.; Masuda, T., Poly(diphenylacetylene) Membranes with High Gas Permeability and Remarkable Chiral Memory, *Macromolecules* **2002**, *35*, 1149-1151.

(21) Raharjo, R. D.; Lee, H. J.; Freeman, B. D.; Sakaguchi, T.; Masuda, T., Pure gas and vapor permeation properties of poly[1-phenyl-2-[p-(trimethylsilyl)phenyl]acetylene] (PTMSDPA) and its desilylated analog, poly[diphenylacetylene] (PDPA), *Polymer* **2005**, *46*, 6316-6324.

(22) Teplyakov, V. V.; Durgaryan, S. G., Correlation analysis of permeation parameters for polymers, *Vysokomolekuliarnye Soedineniia, A* **1984**, *26*, 1498-1505.

(23) Teplyakov, V. V.; Meares, P., Correlation aspects of the selective gas permeabilities of polymeric materials and membranes, *Gas Separation & Purification* **1990**, *4*, 66-73.

(24) Pierce, A. E. Silylation of Organic Compounds; Pierce Chemical Company: Rockford, Illinois, 1968.

(25) Sommer, L. H. Stereochemistry, Mechanism, and Silicon; McGraw Hill: New York, 1965.

(26) Henglein, F. A.; Scheinost, K., Substituted silyl derivatives of pectin and glucose, *Makromolekulare Chemie* **1956**, *21*, 59-73.

(27) Ghosal, K.; Freeman, B. D., Gas separation using polymer membranes: An overview., *Polymers for Advanced Technology* **1994**, *5*, 673-697.

(28) Freeman, B. D.; Pinnau, I. *Polymeric materials for gas separations*, In Polymer Membranes for Gas and Vapor Separation, ACS Symposium Series; Pinnau, I., Ed.: Washington, D.C., 1999; Vol. 733, pp 1-27.

(29) Vu, D. Q.; Koros, W. J.; Miller, S. J., Mixed matrix membranes using carbon molecular sieves II. Modeling permeation behavior, *Journal of Membrane Science* **2003**, *211*, 335-348.

(30) Bouma, R. H. B.; Checchetti, A.; Chidichimo, G.; Drioli, E., Permeation through a heterogeneous membrane: The effect of the dispersed phase, *Journal of Membrane Science* **1997**, *128*, 141-149.

(31) Barrer, R. M.; Barrie, J. A.; Rogers, M. G., Heterogeneous membranes: Diffusion in filled rubber, *Journal of Polymer Science, Part A: Polymer Chemistry* **1963**, *1*, 2565-2586.

(32) Merkel, T. C.; Freeman, B. D.; Spontak, R. J.; He, Z.; Pinnau, I.; Hill, A. J., Sorption, transport and structural evidence for enhanced free volume in poly(4-methyl-2-pentyne)/fumed silica nanocomposite membranes, *Chemistry of Materials* **2003**, *15*, 109-123.

(33) Koper, O. B.; Lagadic, I.; Volodin, A. M.; Klabunde, K. J., Alkaline-Earth Oxide Nanoparticles Obtained by Aerogel Methods. Characterization and Rational for Unexpectedly High Surface Chemical Reactivities, *Chemistry of Materials* **1997**, *9*, 2468-2480.

(34) Matteucci, S. T.; Kusuma, V.; Sanders, D.; Freeman, B. D., Gas transport in TiO_2 nanoparticle filled poly(1-trimethylsilyl-1-propyne), *Journal of Membrane Science* **In Press**.

(35) Utamapanya, S.; Klabunde, K. J.; Schlup, J. R., Nanoscale metal oxide particles/clusters as chemical reagents. Synthesis and properties of ultrahigh surface area magnesium hydroxide and magnesium oxide, *Chemistry of Materials* **1991**, *3*, 175-181.

(36) Stern, S. A.; Gareis, P. J.; Sinclair, T. F.; Mohr, P. H., Performance of a versatile variable-volume permeability cell. Comparison of gas permeability measurements by the variable-volume and variable-pressure methods., *Journal of Applied Polymer Science* **1963**, *7*, 2035-2051.

(37) Merkel, T. C.; Bondar, V.; Nagai, K.; Freeman, B. D., Sorption and transport of hydrocarbon and perfluorocarbon gases in poly(1-trimethylsilyl-1-propyne), *Journal of Polymer Science: Part B: Polymer Physics* **2000**, *38*, 273-296.

(38) Yu, Y.; Guo, Q.; Liu, S.; Wang, E., Partial Dissociation of Water on a MgO(100) Film, *Physical Review B* **2003**, *68*, 1-4.

(39) Rollason, R. J.; Plane, J. M. C., A Kinetic Study of the Reactions of MgO with H_2O, CO_2, and O_2: Implications for Magnesium Chemistry in the Mesosphere, *Physical Chemistry Chemical Physics* **2001**, *3*, 4733-4740.

(40) Wang, J. A.; Novaro, O.; Bokhimi, X.; Lopez, T.; Gomez, R.; Navarrete, J.; Llanos, M. E.; Lopez-Salinas, E., Structural defects and acidic and basic sites in sol-gel MgO, *Journal of Physical Chemistry B* **1997**, *101*, 7448-7451.

(41) Atteya, M.; Klabunde, K. J., Nanoscale Metal Oxide Particles as Chemical Reagents. Heats of Adsorption of Heteroatom-Containing Organics on Heat-Treated Magnesium Oxide Samples of Various Surface Areas, *Chemistry of Materials* **1991**, *3*, 182-187.

(42) Mekhemer, G. A. H.; Halaway, S. A.; Mohamed, M. A.; Zaki, M. I., Qualitative and quantitative assessments of acid and base sites exposed on polycrystalline MgO surfaces: Thermogravimetric, calorimetric, and in-situ FTIR spectroscopy study combination, *Journal of Physical Chemistry Part B* **2004**, *108*, 13379-13386.

(43) Rethwisch, D. G.; Dumesic, J. A., Effect of Metal-Oxygen Bond Strength on Properties of Oxides. 1. Infrared Spectroscopy of Adsorbed CO and CO_2, *Langmuir* **1986**, *2*, 73-79.

(44) Colthup, N. B.; Daly, L. H.; Wiberly, S. E. Introduction to Infrared and Raman Spectroscopy, 2nd ed.; Academic Press: New York, 1975.

(45) Gregg, S.; Ramsay, J. D., Adsortpion of Carbon Dioxide by Magnesia Studied by Use of Infrared and Isotherm Measurements, *Journal of Chemical Society A* **1970**, 2784-2787.

(46) Sherrill, A. B.; Barteau, M. A., Oligomerization of Trimethylsilyl Acetylene to Form Large Molecules on Reduced Surfaces of TiO_2 (001), *Journal of Molecular Catalysis A: Chemical* **2002**, *184*, 301-310.

(47) Paparazzo, E.; Fanfoni, M.; Severini, E., Studies on the Structure of the $SiOx/SiO_2$ Interface, *Applied Surface Science* **1992**, *56-58*, 866-872.

(48) Leclerc, M.; Prud'homme, R. E.; Soum, A.; Fontanille, M., Determination of the geometric structure of substituted polyacetylenes: polymethylacetylene, polypentylacetylene, and poly(tert-butylacetylene). *Journal of Polymer Science Part B: Polymer Physics Edition* **1985**, *23*, 2031-2041.

(49) Sone, T.; Asako, R.; Masuda, T.; Tabata, M.; Wada, T.; Sasabe, H., Polymerization of o-Trifluoromethyl(phenylacetylene) initiated by [Rh(norbornadiene)Cl]$_2$ and MoCl$_4$-*n*-Bu$_4$Sn-EtOH catalysts. Formation of order and disorder trans sequences., *Macromolecules* **2001**, *34*, 1586-1592.

(50) Matteucci, S. T.; Kusuma, V.; Freeman, B. D., Gas transport properties of MgO filled poly(1-trimethylsilyl-1-propyne), *Polymer* **Submitted**.

(51) Helmy, R.; Wenslow, R. W.; Fadeev, A. Y., Reaction of Organosilicon Hydrides with Solid Surfaces: An Example of Surface-Catalyzed Self-Assembly, *Journal of the American Chemical Society* **2004**, *126*, 7595-7600.

(52) Bartik, T.; Happ, B.; Iglewsky, M.; Bandmann, H.; Boese, R.; Helmbach, P.; Hoffmann, T.; Wenschuh, E., Synthesis and characterization of bis(phosphine)nickel(0) complexes containing nonsymmetrically substituted acetylenes, *Organometallics* **1992**, *11*, 1235-1241.

(53) Silverstein, R. M.; Webster, F. X. Spectrometric Identification of Organic Compounds, 6th ed.; John Wiley & Sons: New York, 1998.

Chapter 7: Gas Permeability, Solubility and Diffusivity in 1,2-Polybutadiene Containing Brookite Nanoparticles

So far, only nanocomposites based on stiff chain, glassy polymers have been reported to exhibit light gas permeabilities higher than those of the comparable unfilled polymer. Rubbery polymers have not been shown to exhibit permeability enhancements with increasing nanoparticle concentration.[1] This chapter presents the influence of 3 nm diameter titanium dioxide (TiO_2) nanoparticles on gas transport properties of 1,2-polybutadiene (PB) –based nanocomposites. Pure gas permeability, solubility and diffusion coefficients are reported as a function of nanocomposite particle concentration. Atomic force microscopy and scanning transmission electron microscopy were used to characterize particle dispersion. Changes in polymer glass transition temperature and crystallinity with particle content were characterized using differential scanning calorimetry and wide angle X-ray diffraction, respectively.

Brookite (*i.e.,* titanium dioxide) nanoparticles having a nominal diameter of 3 nm were dispersed in 1,2-polybutadiene (PB) via solution processing to form polymer nanocomposites. Atomic force microscopy and scanning transmission electron microscopy were used to characterize particle dispersion. A significant population of nanoparticle aggregates exhibited characteristic dimensions below 50 nm. However, some aggregates were over one micron in size. At high nanoparticle loadings (*e.g.*, 27 nominal volume percent TiO_2), the permeability coefficients of CO_2, CH_4, N_2 and H_2 were more than 3 times higher than in unfilled PB, which is opposite to the trend typically observed when impermeable particles are added to rubbery polymers. Gas solubility coefficients generally increased with increasing particle loading, whereas diffusion coefficients decreased with increasing particle loading. Therefore, the increase in permeability was due to an increase in gas solubility upon incorporating highly sorbing nanoparticles into the polymer. Interestingly, there was virtually no change in pure gas selectivity in the nanocomposites as compared to unfilled PB.

RESULTS AND DISCUSSION

Nanocomposite stability

Nanoparticles have the potential to react either with the polymer matrix (*e.g.,* desilylation of poly[1-phenyl-2-[*p*-(trimethylsilyl)phenyl]acetylene] by MgO nanoparticles)[2] or with penetrant gases (*e.g.,* reaction of MgO with water).[3] Therefore, care was taken to insure that such effects were not operative in this study. In this regard, TiO_2 is stable in the presence of water and the gases used in this study.[4] No chemical reaction was observed between TiO_2 and PB, based upon Fourier transform infrared spectroscopy of PB and PB-based nanocomposites.

Crystallinity and glass transition temperature in 1,2-polybutadiene and 1,2-polybutadiene based nanocomposites

Figure 7.1 presents the WAXD sweeps for PB and PB-TiO_2 nanocomposites. The peaks in the unfilled PB are located at 13.2°, 16.0°, 21.6°, 24.0°, 35.0°, and 39.1° (2θ), and these values are consistent with the peak locations reported by Obata *et al.* for PB containing 32 wt % crystals.[8] All peaks in the unfilled polymer were also present in the nanocomposites. The crystalline peak located at 13.2° (2θ) in the unfilled polymer shifts to higher 2θ values in the nanocomposites as particle loading increases. Such a drift in this peak has been reported for unfilled PB samples as crystal content decreases.[8] As will be discussed below, the crystalline fraction of the polymer decreases as particle content increases. Thus, the shift in the peak at 13.2° (2θ) to higher values at higher particle loadings is consistent with the reduction in crystallinity observed as particle loading increases. On this basis, it appears that the nanoparticles have not changed the crystal structure.

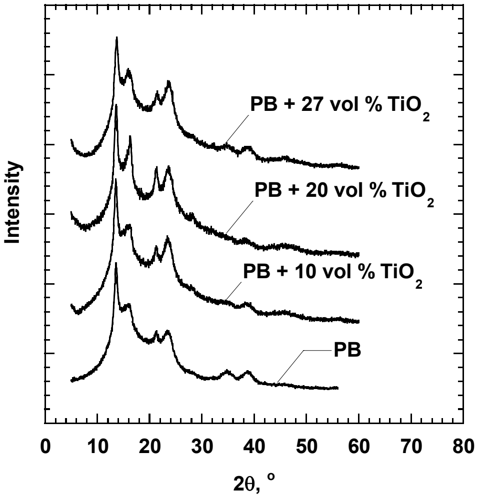

Figure 7.1. WAXD patterns for TiO_2 nanoparticles, unfilled 1,2-polybutadiene, and 1,2-poybutadiene filled with 10, 20, and 27 nominal volume percent TiO_2. These spectra were displaced vertically for easier viewing.

Nanoparticles dispersed in rubbery polymers have been reported to nucleate polymer crystallite growth, which increases the crystalline content of the polymer in nanocomposites,[5] or interfere with polymer crystallization, resulting in lower polymer crystallinity levels in the nanocomposite than in the unfilled polymer.[6] Table 7.1 presents crystallinity values for PB and PB-based nanocomposites. Figure 7.2 presents the DSC scan from which the unfilled PB crystallinity was estimated. There are two discernable melting points for unfilled PB. The lower melting point, $T_{m,1}$, occurs at 60 °C, and the higher melting point, $T_{m,2}$, was 100 ^{o}C. Both melting point values agree with those reported by Obata *et al.*[8]

In some discussion to follow, it will be useful to have the crystallinity expressed in volume percent. Therefore, the volume fraction of crystalline PB in the polymer phase of the samples (*i.e.,* volume of crystalline polymer / total volume of polymer), ϕ_C, was estimated as follows:[9]

$$\phi_C = \chi_C \frac{\rho_P^N}{\rho_C} \tag{7.1}$$

where ρ_P^N is the density of the polymer in the nanocomposite (*i.e.,* g polymer/cm^3 polymer), which was estimated as follows:[8]

$$\frac{1}{\rho_P^N} = \frac{\chi_C}{\rho_C} + \frac{\chi_C - 1}{\rho_A} \tag{7.2}$$

Eq. (7.2) assumes that the amorphous and crystalline phase polymer densities in the nanocomposite are not influenced by the presence of the nanoparticles. The volume fraction crystallinity values are recorded in Table 7.1.

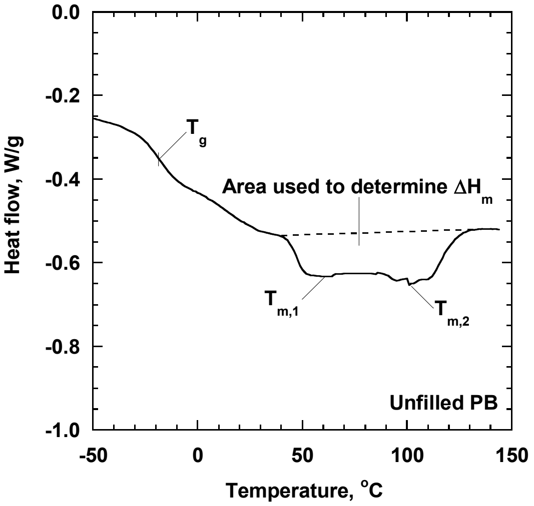

Figure 7.2. DSC thermogram of unfilled PB. The data are from the first scan. The area between the dashed line and the thermogram (*i.e.,* the solid line) was used to determine ΔH_m. The glass transition temperature (T_g), the broad melting event, and the location of the melting temperatures ($T_{m,1}$ and $T_{m,2}$), are consistent with literature.[8]

The estimates of crystallinity in the unfilled polymer from WAXD (*i.e.,* 32 ± 3 wt % as estimated by Eq. (3.9)) and density (*i.e.,* 30 ± 5 wt % as estimated by Eqs. (3.8) and (7.1)) are quite similar, and these values are consistent with the value measured by DSC (*i.e.,* 34 ± 3 wt % as estimated by Eq. (3.14)). However, as shown in Table 7.1, the weight fraction of crystalline polymer in the polymer, χ_C, determined from WAXD and Eq. (3.8), is influenced by particle loading. χ_C decreases from about 32 wt % in the unfilled polymer to about 20 wt % in the samples containing 27 nominal volume percent nanoparticles. Such behavior is qualitatively consistent with the literature in which nanoparticles are reported to interfere with polymer crystallization.[6]

Table 7.1. Polymer and nanocomposite crystallinity and glass transition temperatures

ϕ_F^N (%)	Technique for estimating crystallinity	χ_C,(%)	ϕ_C,(%)	T_g, $^oC^b$
0	density [a]	30 ± 5	28 ± 4	--
0	DSC	34 ± 3	32 ± 3	-17 ± 3
0	WAXD	32 ± 3	30 ± 3	--
10	WAXD	24 ± 1	22 ± 2	-9 ± 3
20	WAXD	23 ± 1	18 ± 2	-10 ± 3
27	WAXD	20 ± 1	15 ± 2	-9 ± 3

Note: Uncertainties were estimated using the propagation of errors method.[7]

[a] Density measurements yield a value of ϕ_C, which was converted to χ_C using Eq. (7.1). The other techniques considered (*i.e.,* DSC and WAXD) yield estimates of χ_C, which were converted to ϕ_C using Eq. (7.1).

[b] All glass transition temperatures were determined using first scan DSC data.

In some polymer nanocomposites, the polymer glass transition temperature, T_g, is influenced by the concentration of nanoparticles.[10,11] For example, the bulk T_g of poly(2-vinyl pyridine) increased with alumina nanoparticle content from 100 °C in the unfilled polymer to 117 °C in a film containing 4 volume percent alumina nanospheres.[11] Such increases in T_g have been ascribed to strong interactions between the polymer and the nanoparticles.[11] Table 7.1 presents T_g values in PB and the PB-based nanocomposites considered in this study. The thermograms from which the glass transition values are obtained are presented in Figure 7.3. The T_g of the unfilled polymer is approximately 8 °C lower than that of the nanocomposite samples. This increase in T_g suggests reduced polymer chain mobility in the nanocomposite samples relative to the unfilled polymer. Such reductions in polymer chain mobility have been attributed to adsorption of polymer chains to nanoparticles, which effectively tethers the polymer to the particle.[10,11]

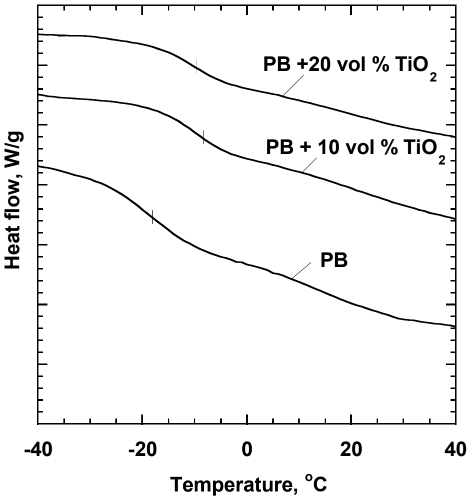

Figure 7.3. Influence of nominal particle volume percent on the glass transition temperature of 1,2-polybutadiene filled with TiO_2 nanoparticles. The tick marks represent the T_g, which is identified as the midpoint of the endothermic step change in the heat capacity in the DSC thermograms. The data are from the first scan. The DSC traces have been displaced vertically for easier viewing.

The T_g of PB is known to decrease as crystallinity decreases.[8] For example, Obata *et al*. report that the T_g decreases from 7 °C to -38 °C as crystallinity goes from 46 to 0 wt %.[8] On this basis, T_g should decrease, not increase, with increasing particle content if the only effect of the particles were to disrupt crystallinity. Therefore, the observed increase in T_g due to the presence of the particles is even more significant when viewed in the light of the observed decrease in crystallinity, which should decrease T_g, with increasing particle content. Also, data to be presented later suggest that other phenomena (*e.g.,* voids or larger particle aggregates) may not interact with the bulk polymer in the same manner as individually dispersed particles or nanoscale particle aggregates. Such effects might explain why there is little change in T_g as nanoparticle content increases from 10 to 27 nominal volume percent. Therefore, several competing factors could be influencing the glass transition behavior of the nanocomposites.

Particle dispersion

Particle and aggregate dispersion influence gas transport in heterogeneous nanocomposite films.[4,12-16] AFM tapping mode phase profiles can be used to resolve the relative modulus of polymer and nanocomposite samples.[17] This technique can resolve individual nanoparticles that are on the order of several nanometers in primary particle diameter since the nanoparticle modulus is expected to be much greater than that of the polymer. That is, the nanoparticles typically constitute the hard phase, and the polymer is the soft phase in nanocomposite samples. This situation is somewhat more complex in PB-based nanocomposites, since the polymer contains hard crystalline regions in addition to soft amorphous regions. This issue is discussed in more detail below.

Figure 7.4 presents AFM phase profiles for unfilled PB and PB-based composites containing 7 and 20 nominal volume percent TiO_2. In Figure 7.4a, the neat PB exhibits two distinct phases. The phase with the higher modulus appears lighter, while the softer, lower modulus phase is darker. The phase with the higher modulus in this image is attributed to crystalline PB, and the softer phase is ascribed to amorphous PB. The high modulus phase occupies approximately 27 area percent of Figure 7.4a, which is consistent with the crystalline volume percent (28-32 %) recorded in Table 7.1.

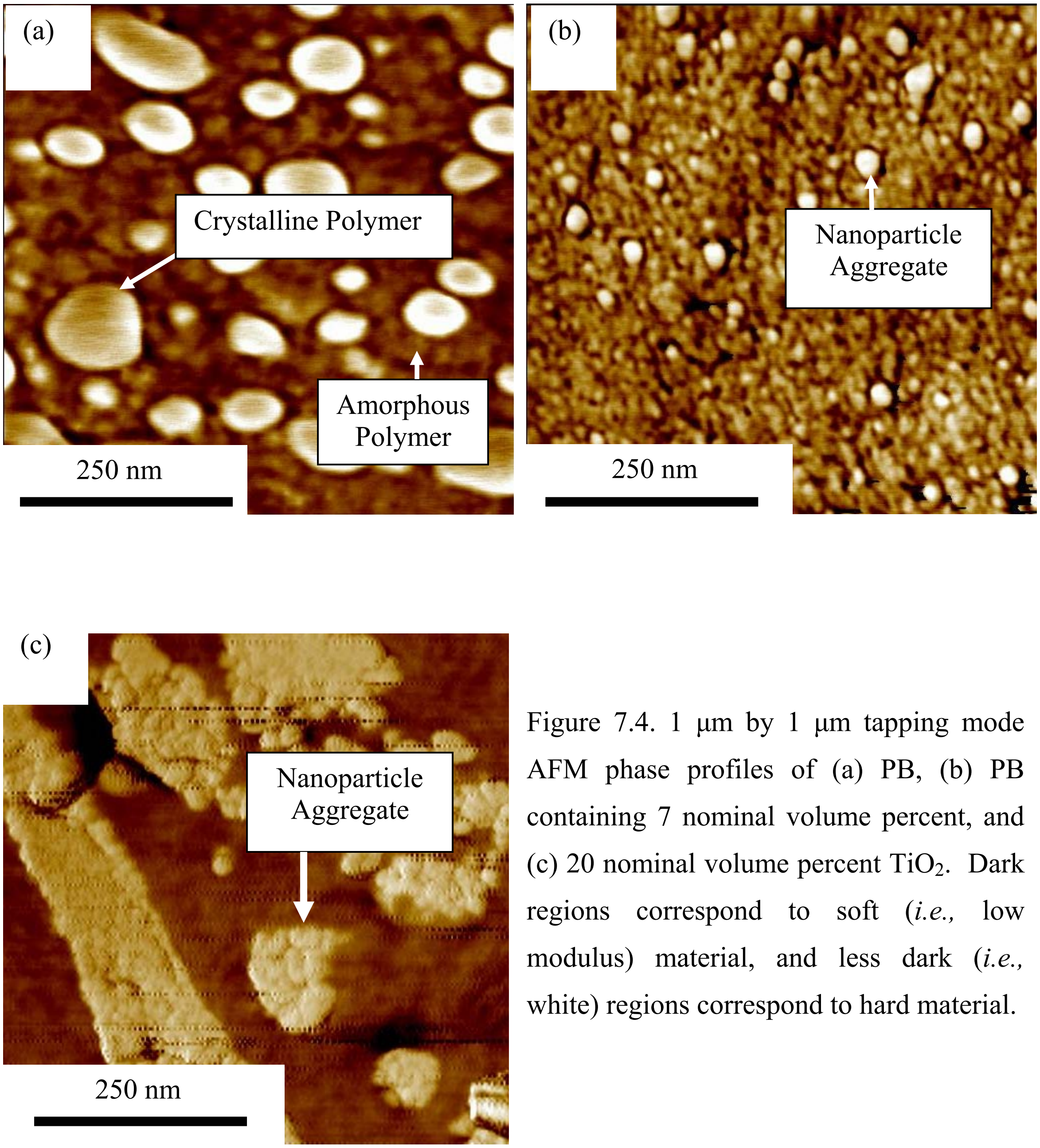

Figure 7.4. 1 μm by 1 μm tapping mode AFM phase profiles of (a) PB, (b) PB containing 7 nominal volume percent, and (c) 20 nominal volume percent TiO_2. Dark regions correspond to soft (*i.e.,* low modulus) material, and less dark (*i.e.,* white) regions correspond to hard material.

Figures 7.4b and 7.4c present images of PB nanocomposites. The dark lines in Figure 7.4c are artifacts caused by contaminants (*i.e.,* nanoparticles) on the sample surface or AFM cantilever tip.[18] There are also two distinct phases in these images. The hard phase occupies ~7 and 23 percent of the area of Figures 7.4b and 7.4c, respectively, which are essentially the same as the nominal volume percent nanoparticles in the sample (*i.e.,* 7 and 20 nominal volume percent, respectively), suggesting that the hard phase in the nanocomposites is particles or particle-rich regions.

The nanoparticle modulus may be sufficiently high, relative to that of the polymer matrix, that it is not possible to distinguish between the crystalline and amorphous polymer phases. Based on the literature, AFM phase profile images have produced mixed results when used to characterize nanoparticle filled semi-crystalline polymers. In certain systems, the crystalline polymer phase cannot be resolved.[19] In other cases, the nanoparticles did not appear on the images.[20] Finally, some groups have resolved both crystalline polymer and nanoparticles in such systems.[21]

According to the WAXD results in Table 7.1, the crystallinity of the polymer (*i.e.*, the volume of crystals per unit volume of polymer) decreases as particle loading increases, which is opposite to the trend observed in Figures 7.4b and 7.4c, where the area fraction occupied by the hard phase increases with increasing particle concentration. Based on all of this information, the hard phase in Figures 7.4b and 7.4c is ascribed to nanoparticles, not polymer crystals.

Image analysis can be used to estimate the average diameter, $\overline{d}$, of the harder phase in the nanocomposite AFM images using Eq. (3.5). The nanoparticle aggregates in Figure 7.4b have an estimated average diameter of 9 nm ± 4 nm. Distributions were not estimated for Figure 7.4c, since there are relatively few aggregates in this image, and many of the aggregates do not fit within the image boundaries.

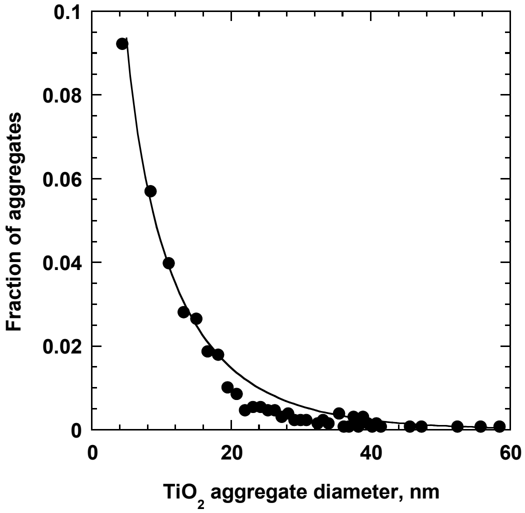

Figure 7.5. TiO_2 aggregate diameter distribution from tapping mode phase profiles of PB containing 7 nominal volume percent TiO_2. The solid line represents a Weibull distribution using v = 3.0 nm, β = 8.40 ± 5.00 and α = 0.86 ± 0.59.[22,23] Uncertainties in the Weibull distribution parameters were determined by a least-squares fit method.[7]

The nanoparticle aggregate diameter distribution is presented in Figure 7.5 for PB containing 7 nominal volume percent TiO_2. The distribution of aggregate diameters can be further characterized by fitting the data in Figure 7.5 to a Weibull distribution. Based on the particle distribution data in Figure 7.5, a significant percentage of particles are dispersed individually or in small nanoparticle aggregates in PB filled with 7 nominal volume percent TiO_2.

The average inter-aggregate distance, d_a, can be estimated by assuming the aggregates are spherical and dispersed in a body centered cubic structure:[4]

$$d_a = \bar{d}\left[\left(\frac{\pi}{6\phi_F^N}\right)^{\frac{1}{3}} - 1\right] \tag{1.2}$$

where $\bar{d}$ is the average aggregate diameter (nm), and ϕ_F^N is the nanoparticle volume fraction in the composite as calculated from Eq. (2.17). The use of either nominal or true volume fraction MgO (*i.e.,* a particle volume fraction that takes into account the presence of any nanoparticle induced voids)[4] in Eq. (1.2) does not change the results significantly.

ϕ_F^N is used in Eq. (1.2) since it is used in other calculations in this study, as will be presented below. A body centered cubic aggregate structure is assumed to simplify estimates of d_a. More realistic structures, such as a random aggregate distribution[24], yield very similar values for d_a. PB films containing 7 nominal volume percent TiO_2 exhibit d_a values of approximately 9 nm, which is similar to the inter-aggregate spacing for TiO_2 nanoparticles dispersed in a glassy polymer, PTMSP, where d_a was 9 nm and 11 nm for 3 and 10 nominal volume percent TiO_2, respectively.[4] The interparticle spacing in these nanocomposites is comparable to the size of structural features of PB molecules. For instance, the radius of gyration of 1,2-polybutadiene of a molecular weight of 100,000 is 8.5 nm.[25] On this basis, one might anticipate that having nanoparticles dispersed at spacings that are comparable to the polymer chain size could have a substantial influence on the properties of such systems.

Since the individual nanoparticles are approximately the same size as the resolution of the AFM images, any particles with characteristic diameters below the resolution limits would not be included in calculations of $\overline{d}$ or d_a. This may represent a substantial fraction of the particles and may cause the reported average aggregate diameter and average inter-aggregate spacing value to be somewhat higher than the true values. Therefore, the $\overline{d}$ or d_a values reported in this paper are most likely higher than the actual values.

Many aggregates in Figure 7.4c are on the order of microns in characteristic dimensions. At these loadings, individually dispersed nanoparticles and small aggregates (*i.e.,* aggregates with < 100 nm characteristic diameter) cannot be resolved. It is possible at these loadings that TiO_2 nanoparticles can not effectively disperse in the polymer, which may be related, in part, to the elevated solution viscosity and, therefore, to a lack of effective mixing, when large amounts of nanoparticles are added to the polymer-toluene solution.

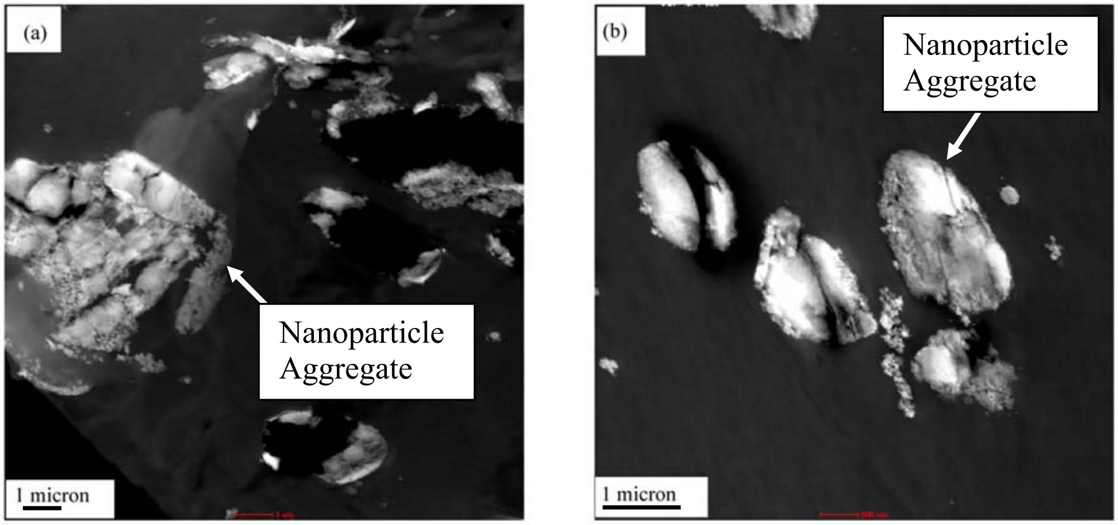

Figure 7.6. STEM dark field image of (a) PB containing 7 nominal volume percent and (b) PB containing 13 nominal volume percent TiO_2. Electron rich phases (*i.e.,* nanoparticles) are shown in white.

Dark field STEM can be used to resolve micron-sized aggregates. Examples of such aggregates are present in Figure 7.6 for PB containing 7 and 13 nominal volume percent TiO_2. Since the nanoparticles are expected to have the highest electron density of the phases present in the nanocomposite, the large light structures in the STEM images are attributed to nanoparticle aggregates. The aggregates shown at these loadings are representative of aggregates observed in other TiO_2 filled PB nanocomposite samples. Since STEM distinguishes features in materials based on differences in electron density, the nanoparticle-rich (*i.e.,* electron-rich, as shown in white) and the polymer-rich (*i.e.,* electron-poor, as shown in black or dark gray) regions are readily observed. The presence of these aggregates may be due to poor particle mixing with the polymer, poor polymer-particle interaction, or the nanoparticle concentration reaching levels beyond which the nanoparticles cannot readily disperse individually or in small aggregates.

In summary, the dispersion of these nanoparticles in PB ranges from single particles dispersed in the particle matrix to micron-sized aggregates of many particles. No single microscopy tool considered can capture the complete distribution of particles and particle aggregates in these samples. The use of multiple techniques, such as AFM and STEM, provides a better understanding of the particle dispersion, but this is clearly an area where better analytical tools, capable of characterizing a very wide range of particle sizes, would be useful.

Nanocomposite density and void space

If the density of the nanoparticles, crystalline polymer and amorphous polymer phases have their pure component values in the nanocomposites, then the density of a nanocomposite sample, ρ_{Exp}, would be equal to the theoretical additive density, ρ_{Add}, which is defined as follows:

$$\rho_{Add} = \phi_F^N \rho_F + \left(1-\phi_F^N\right)\left(\phi_C \rho_C + \left(1-\phi_C\right)\rho_A\right) \tag{2.21}$$

where ρ_F is the pure filler density. ϕ_C is the volume fraction of crystalline polymer (*i.e.,* volume of crystals per unit volume of polymer in the nanocomposites) (*cf.*, Table 7.1). That is, the additive density is the density of a semincrystalline nanocomposite sample if each phase contributed to the nanocomposite density according to its pure component density value and the amount of each phase present.

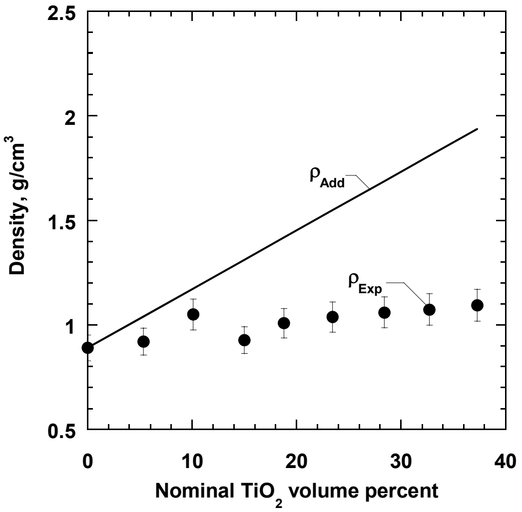

Figure 7.7. Effect of TiO$_2$ concentration on nanocomposite density. ρ_{Exp} is the experimentally measured density, and ρ_{Add} is the additive density predicted by Eq. (2.21). Error bars were estimated from the variance in density for multiple experiments at each point according to the propagation of errors method.[7]

Dispersing TiO$_2$ nanoparticles in PB increases the density of the nanocomposites, as shown in Figure 7.7. However, ρ_{Exp} is less than ρ_{Add} at all TiO$_2$ loadings. The difference between ρ_{Exp} and ρ_{Add} can be rationalized by the creation of void space in the composite with increasing particle loading.[4] The void space can be expressed in terms of a void volume fraction, ϕ_V, defined as follows:[4]

$$\phi_V = \left(1 - \frac{\rho_{Exp}}{\rho_{Add}}\right) \tag{2.22}$$

Using Eq. (2.22), void volume fraction values were calculated and are presented as a function of nanoparticle concentration in Figure 7.8. The void content increases with increasing particle loading, qualitatively consistent with previous results reported for glassy PTMSP filled with TiO$_2$,[4] and glassy polyether imide (*i.e.*, Ultem 1000) filled with surface treated fumed silica.[16] So far, microscopy has not been able to determine the location of such voids. We speculate that the voids may be located at the polymer-particle interface, in the interparticle spacing, or within nanoparticle aggregates.[16,26,27]

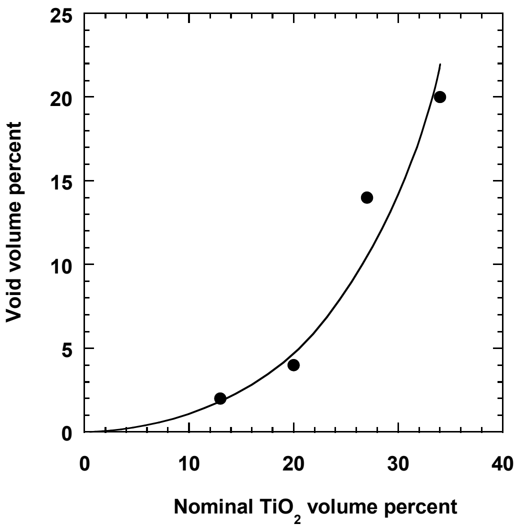

Figure 7.8. Effect of particle concentration on nanocomposite void volume percent as estimated by Eq. (2.22). The trend line is drawn to guide the eye.

Gas transport in TiO$_2$ filled 1,2-polybutadiene

Figure 7.9a presents the influence of particle loading on CO_2, CH_4, N_2, and H_2 permeability relative to the permeability of each gas in the unfilled polymer. As indicated in this figure, the permeability increases with increasing particle concentration. These data are compared to Bruggeman's model in the limit when the dispersed phase concentration is equal to the void volume (*i.e.,* Eq. (2.27) with $\phi_D = \phi_V$) in Figure 7.9b. The permeability for all gases increases with increasing void volume, although the observed increase in permeability exceeds the increase anticipated by this model. Bruggeman's model does not account for any changes in the continuous phase permeability due to changes in solubility (*e.g.,* from adsorption of light gases on a nanoparticle surface) or changes in polymer phase crystallinity.[28] Bruggeman's model, as presented in Eq. (2.27), assumes that the dispersed phase is spherical.[29] If the dispersed phase is arranged in a non-spherical geometry, Eq. (2.27) becomes less accurate.[30]

Deviations from these assumptions could cause the permeability of the filled polymer, based on expectations from the model calculations, to differ from the experimental data. Nonetheless, using Bruggeman's model in this fashion provides a rough estimate of the influence of the voids on the gas permeability in these nanocomposites. Within the scope of the approximations described above, a substantial portion of the increase in permeability cannot be due simply to the presence of the voids and must, therefore, result from the effect of the TiO_2 nanoparticles on the gas transport properties of the solids (*i.e.,* polymer and particles) in the nanocomposite samples.

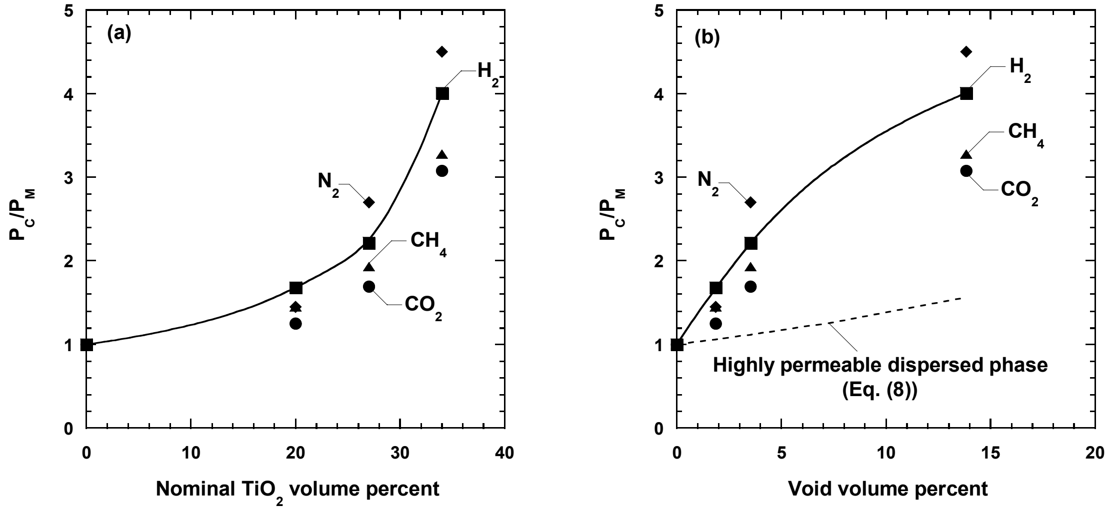

Figure 7.9. Effect of dispersed phase concentration on the ratio of nanocomposite CO_2 (●), CH_4 (▲), N_2 (♦) and H_2 (■) permeability, P_C, to that of unfilled PB, P_M, where the dispersed phase is: (a) nominal TiO_2 volume percent, and (b) void volume percent calculated from Eq. (2.21). The dashed line represents Bruggeman's model (*i.e.,* Eq. (2.27)). The experimental data were measured at 35 ^{o}C and Δp = 4.4 atm. The solid line is drawn to guide the eye.

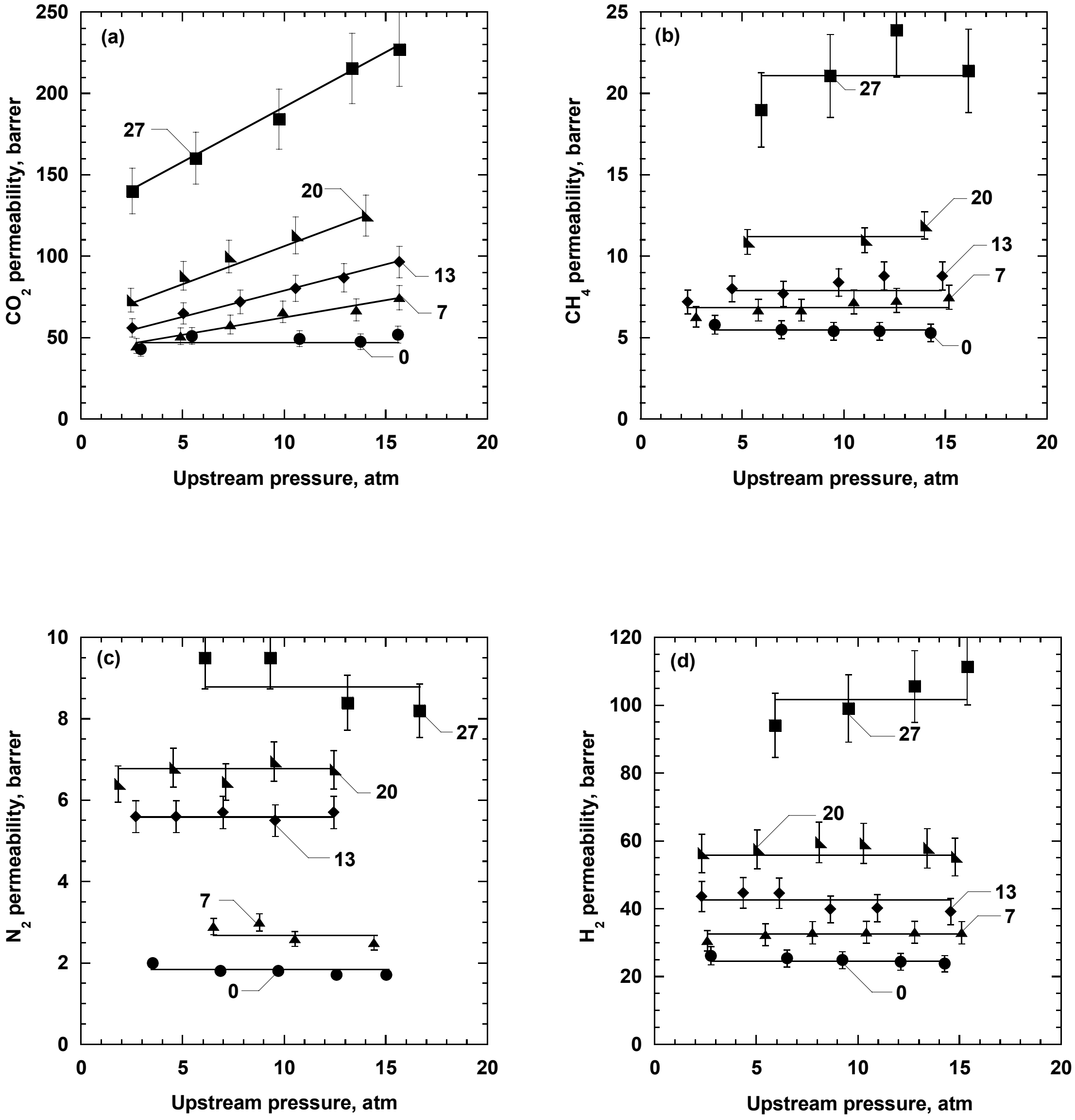

Figure 7.10. Effect of upstream pressure on pure gas permeability in PB containing TiO_2: (a) CO_2, (b) CH_4, (c) N_2, and (d) H_2. The numbers next to the data indicate the nominal volume percent of TiO_2. Measurements were conducted at 35 °C and with downstream pressure less than 0.01 atm. Error bars were estimated from the variance in permeability for multiple experiments at each point according to the propagation of errors method.[7] Trend lines are drawn to guide the eye.

If the permeability enhancements were caused by trans-film defects, light gas permeability would increase with increasing upstream pressure, and/or selectivity values would trend towards values expected based on Knudsen or Poiseuille flow, depending on the size of the defects.[31-33] As will be demonstrated, neither of these effects are observed, suggesting that the increase in permeability does not derive from pinhole defects in the nanocomposite samples. For example, Figure 7.10 presents gas permeability as a function of pressure for PB and a representative group of nanocomposites. The permeability values for unfilled PB are in good agreement with those reported by Naito *et al.*, where CO_2, CH_4, N_2, and H_2 permeabilities were 43 barrer, 5.5, barrer, 1.9 barrer, and 30 barrer at 25 °C, respectively.[34] As Figure 7.10 shows, CH_4, N_2, and H_2 permeabilities are independent of upstream pressure. Only CO_2 permeability increases with increasing pressure in the nanocomposite samples, which is attributed to plasticization of the polymer by CO_2.[35] The permeability of CO_2 also increases slightly in unfilled PB with increasing pressure, which agrees with the literature.[34] However, the increase is masked by the overall scale of Figure 7.10a. Loading particles into PB may intensify the increase in CO_2 permeability with increasing pressure, because the nanoparticles increase the concentration of CO_2 in the film, as discussed below, which may facilitate plasticization.

The Knudsen selectivity, $\alpha^{K}_{A/B}$, is given by:[32]

$$\alpha^{K}_{A/B} = \sqrt{\frac{M_B}{M_A}} \tag{4.1}$$

where M_A and M_B are the molecular masses of penetrant A and B, respectively. The Poiseuille selectivity limit, $\alpha^{P}_{A/B}$, is:[33]

$$\alpha^{P}_{A/B} = \frac{\mu_B}{\mu_A} \tag{4.2}$$

where μ_A and μ_B are the viscosities of gas A and B, respectively. Table 7.2 presents the selectivity limits for Knudsen and Poiseuille flow regimes for a number of gas pairs.[36] As shown in Figure 7.11 for CO_2/light gas pairs, selectivity values in the nanocomposite samples do not vary perceptibly from those observed in the unfilled polymer. These selectivity values are not consistent with either Knudsen or Poiseuille selectivities. Since CH_4, N_2, and H_2 permeabilities are independent of upstream pressure, and the ideal selectivities are not at the Knudsen or Poiseuille flow limits, the permeability enhancements shown in Figures 7.9 and 7.10 are not caused by transmembrane defects introduced by having the TiO_2 particles in the samples. Interestingly, as will be shown below, the permeability enhancement is due to an increase in gas solubility as particle concentration increased.

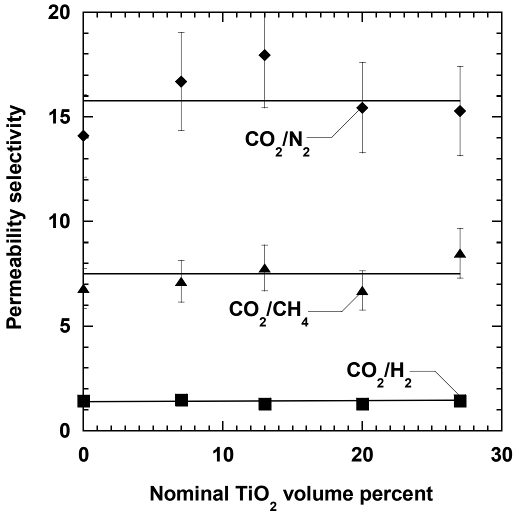

Figure 7.11. Effect of particle concentration on pure gas CO_2/N_2 (♦), CO_2/CH_4 (▲), and CO_2/H_2 (■) permeability selectivity in PB nanocomposites. Experimental conditions were 35 °C and $\Delta p = 4.4$ atm. Trend lines are drawn to assist the reader. Error bars were estimated according to the propagation of errors method.[7]

Table 7.2. Knudsen diffusion and Poiseuille flow selectivities[36]

Flow regime	CO_2/N_2	CO_2/CH_4	CO_2/H_2
Knudsen Diffusion	0.8	0.6	0.2
Poiseuille Flow	1.2	0.7	0.6

At high nanoparticle loadings (*i.e.,* greater than 30 nominal volume percent), light gas selectivity values decreased to values suggesting the presence of transmembrane defects. Therefore, at high enough particle loadings, transmembrane defects develop in the samples. Such non-selective nanocomposite materials have not been considered further in this study.

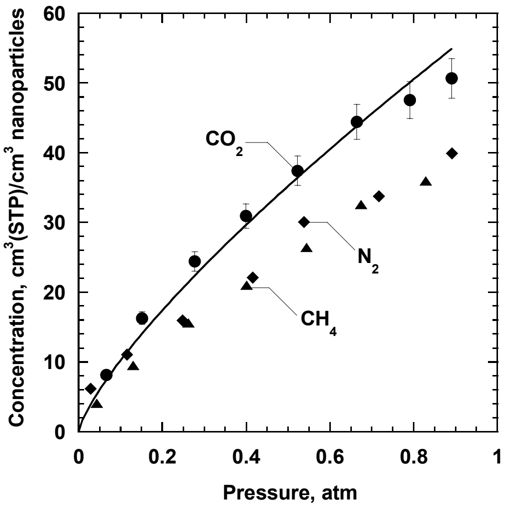

Figure 7.12. Pure gas CO_2, CH_4, and N_2 adsorption isotherms on TiO_2 at 35 °C from Matteucci *et al.*[4] The solid line represents the Freundlich model (*i.e.,* Eq. (4.4)) for CO_2 adsorption on TiO_2 calculated using parameters from Table 7.3. Error bars were estimated from the variance in concentration for multiple experiments according to the propagation of errors method.[7]

The permeability behavior can be further explored by examining the influence of nanoparticle content on gas solubility and diffusivity. TiO_2 nanoparticles adsorb significant amounts of light gases, as shown in Figure 7.12.[4] In fact, as will be demonstrated shortly, the particles sorb far more gas per unit volume than the polymer.

Interestingly, the particles do not become saturated with absorbed gases (*i.e.,* CO_2, CH_4 and N_2) up to at least 1 atm.[4]

The Freundlich isotherm has been used to characterize gas adsorption on TiO_2 nanoparticles, C_F : [37]

$$C_F = Kp^{\frac{1}{n}} \tag{4.4}$$

where K and n are temperature dependent fitting parameters[37], which are listed in Table 7.3. The Freundlich model is used in our studies because it does not limit sorption of gases to one monolayer on the particle surface, whereas many models (*e.g.,* the Langmuir model) have this limitation.[37] As demonstrated elsewhere for another polymer/particle combination,[4] the Freundlich isotherm results in a better estimate of gas sorption in nanocomposites than the Langmuir model.

Table 7.3. Freundlich isotherm parameters for adsorption onto TiO_2 and Henry's law sorption parameters for 1,2-polybutadiene at 35 °C

Penetrant	$K, \frac{cm^3(STP)}{cm^3 TiO_2\ atm^{\frac{1}{n}}}$	n, -	$k_D, \frac{cm^3(STP)}{cm^3 PB\ atm}$ (This work)	$k_D, \frac{cm^3(STP)}{cm^3 PB\ atm}$ (Naito *et al.*)
N_2	24 ± 7	1.8 ± 0.2	0.03 ± 0.01	0.04
CH_4	28 ± 8	1.4 ± 0.2	0.22 ± 0.02	0.23
CO_2	38 ± 10	1.4 ± 0.2	0.71 ± 0.06	0.81

Note: The Freundlich isotherm parameter are from the literature.[4] The Henry's law constants were obtained from sorption experiments. Uncertainties were estimated using the least-squares fit method.[7] Naito *et al*. Henry's law parameters were determined at 25 °C.[34]

Light gas sorption in rubbery polymers, C_P, typically obeys Henry's law:[35]

$$C_P = k_D p \tag{7.3}$$

where k_D is the Henry's law constant, and p is the gas pressure.[35] As Figure 7.13 demonstrates, sorption isotherms in unfilled PB are linear, which is consistent with Henry's law and with the literature.[34] Henry's law parameters for CO_2, CH_4, and N_2 are recorded in Table 7.3. The k_D values obtained in this study are quite similar to those reported by Naito *et al.*[34]

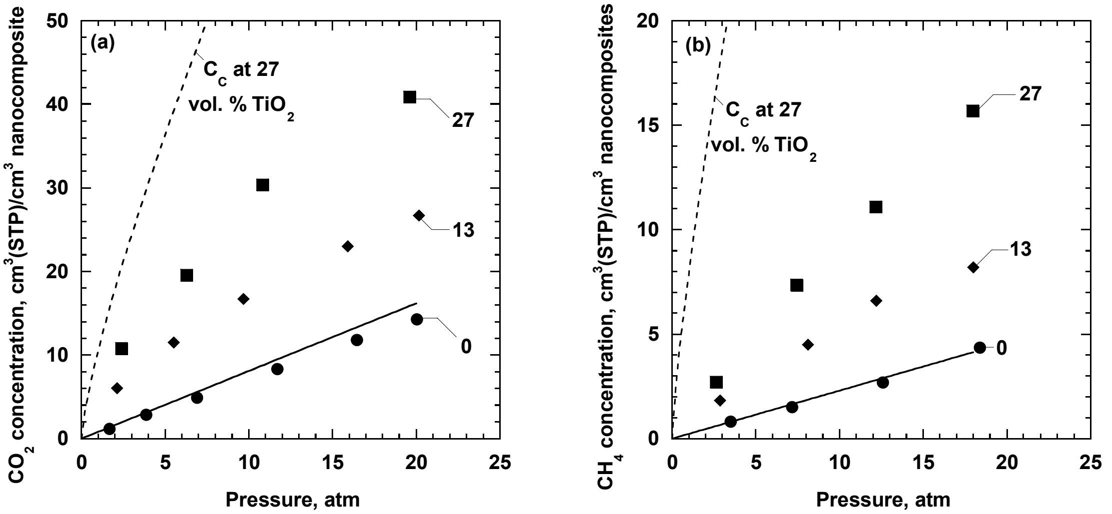

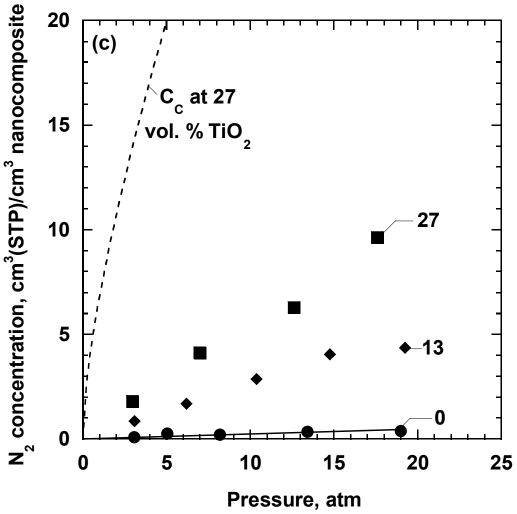

Figure 7.13. Sorption isotherms at 35 °C for (a) CO_2, (b) CH_4, and (c) N_2 in PB containing 0 (●), 13 (♦), and 27 (■) nominal volume percent TiO_2. The dashed line represents the estimated gas concentration in the nanocomposite, C_C, according to Eq. (7.5) for a PB film containing 27 nominal volume percent TiO_2. The solid line represents gas concentration in unfilled PB from the work of Naito *et al.*[34]

k_D values should increase as crystallinity decreases. In general, crystalline polymer sorbs a negligible amount of gas as compared to amorphous polymer.[38] Therefore, a first estimate of the Henry's law parameter in the amorphous regions of a polymer is:[39]

$$k_{D,A} = \frac{k_D}{1-\phi_{C,0}} \tag{7.4}$$

where $k_{D,A}$ is the estimated Henry's law parameter for amorphous polymer, and $\phi_{C,0}$ is the unfilled PB crystalline polymer volume fraction.

The concentration of gas in the void volume of a nanocomposite, C_V, can be estimated using the gas law:[33]

$$C_V = \left(\frac{p}{RT}\right) \tag{4.6}$$

The gas concentration in a nanocomposite, C_C, can be estimated using an additive model, where each phase is assumed to contribute its native gas sorption capacity to the overall gas concentration in the composite:[4]

$$C_C = \left(\phi_F^N K p^{\frac{1}{n}} + \left(1-\phi_F^N\right)\left(1-\phi_C\right)k_{D,A}\,p\right)\left(1-\phi_V\right) + \frac{p\phi_V}{RT} \tag{7.5}$$

The first term in Eq. (7.5) represents the nanoparticle contribution. The second term is associated with the gas sorbed in the amorphous polymer phase, and the final term accounts for the concentration of gas in the voids.

According to Eq. (7.5), the contribution of the void volume and the amorphous polymer phase to the overall concentration of gas sorbed into the nanocomposite are linear with pressure. Generally, the contribution of the void volume to concentration of the gas is small relative to that of the polymer, due to the low concentration of voids in the nanocomposites. For instance, in a film containing 20 nominal volume percent TiO_2 (and 5 volume percent voids), the polymer phase contribution to CO_2 and CH_4 concentration is approximately 24 and 7 times that of the voids, respectively. However, for low sorbing gases such as N_2, the contribution of the voids may be similar to or greater than that of the polymer. For example, in the film containing 20 nominal volume percent TiO_2, the concentration of N_2 in the polymer is roughly equivalent to that of the void space. However, when C_F is extrapolated to pressures greater than atmospheric, the nanoparticles are estimated adsorb almost two orders of magnitude more gas than either the polymer or the voids, so the particle contribution to the overall concentration of gas sorbed in the nanocomposite, as estimated by Eq. (7.5), is the dominant contribution to gas uptake in the nanocomposites.

As shown in Figure 7.13, the gas concentration in the nanocomposite predicted by Eq. (7.5) overestimates gas concentration in the nanocomposites. Eq. (7.5) does not account for the influence of polymer-particle interactions on gas sorption levels. Similar non-additive solubility behavior has been reported for gas solubility in natural rubber filled with micron-sized ZnO.[26] This behavior was attributed to polymer adsorption on the particle surface, which restricts the ability for penetrant gases to sorb on the particle surface.[26] Also, the light gas sorption isotherms in the nanocomposites do not increase linearly with increasing pressure, as expected of gas sorption in polymer alone. The curvature in the influence of gas sorption isotherms presumably derives from the sorption of gases on the nanoparticle surface on the overall gas uptake in the samples. Additionally, the gas sorption isotherms on the particles are only available up to 1 atm, so the model is being extrapolated to much higher pressure than where experimental data are available for the gas sorption on the particles, so any inaccuracy in that extrapolation would also contribute to the observed differences between the model and the experimental data.

Figure 7.13 also shows that the gas concentration in the nanocomposites is higher than that in the polymer. For example, in films containing 27 nominal volume percent TiO_2, the CO_2, CH_4, and N_2 gas concentrations are 2.7, 4, and 18 times higher, respectively, than in unfilled PB at ~18 atm. The ratio of gas concentration in the nanocomposite to that in the unfilled polymer changes substantially from one gas to another. These differences are ascribed to the difference between the amount of gas that can be adsorbed on the neat particle surface relative to the amount of gas that sorbs in the unfilled polymer. That is, the neat nanoparticles adsorb approximately 70, 170, and 1600 times more CO_2, CH_4, and N_2 than unfilled PB, respectively, at 1 atm. It is reasonable that the ratio of the gas concentration in the nanocomposites to that in unfilled PB varies from one gas to another.

Using the measured permeability and gas sorption coefficients, gas diffusion coefficients were calculated as a function of particle loading. Nanoparticles have been reported to increase diffusion coefficients, as in brookite filled PTMSP,[4] or decrease diffusivity as in PTMSP filled with trimethylsilylglucose.[40] Many studies of transport in heterogeneous systems and the standard composites models of transport in polymer/particle mixtures suggest that impermeable particles in polymers decreases diffusion coefficients by increasing the tortuosity of the pathway that diffusing gas molecules must travel to traverse a polymer film.[14,26,29]

Diffusion coefficients were calculated from Eq. (2.7), using permeability coefficients measured at 35 ^{o}C and $\Delta p = 4.4$ atm. Solubility was estimated by linearly interpolating the concentration data to 4.4 atm and using Eq. (2.8). Figure 7.14 presents the results of these calculations. In all cases, gas diffusivity initially decreases substantially with increasing particle loading before increasing slightly at the highest loadings considered. These data suggest a competition between particle-induced increases in tortuosity at lower loadings, which acts to reduce diffusion coefficients, and increasing contribution of voids at high particle loadings, which acts to increase diffusion coefficients. Also the effect of decreasing crystallinity and increasing T_g in the nanocomposites should influence diffusion coefficients though it was not possible to isolate these factors. The combination of lower diffusivity and significantly enhanced solubility is a 3-4 fold increase in gas permeability as nanoparticle content increases.

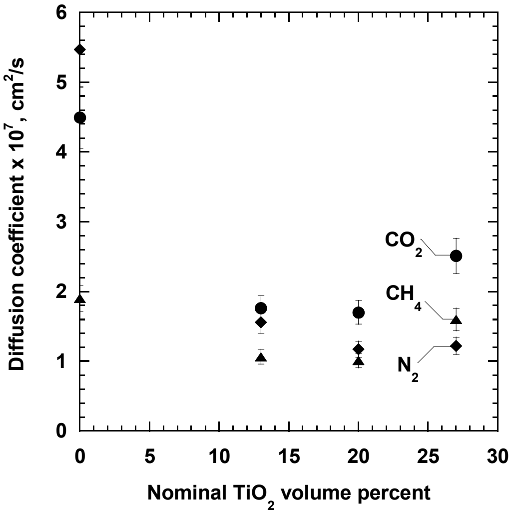

Figure 7.14. Concentration averaged diffusion coefficients for CO_2 (●), CH_4 (▲), and N_2 (♦) as a function of TiO_2 content. Diffusivity was calculated from Eq. (2.7), using permeability data measure at 35 °C and $\Delta p = 4.4$ atm. Solubility was estimated by linearly interpolating the concentration data to 4.4 atm and using Eq. (2.8). Error bars were estimated from permeability and solubility according to the propagation of errors method.[7]

CONCLUSIONS

TiO_2 nanoparticles were dispersed in 1,2-polybutadiene via solution processing, resulting in particle aggregates ranging in characteristic diameter from nanometers to microns. The nanocomposites exhibit density values below those predicted by an additive density model, suggesting the presence of voids within the nanocomposite films.

Gas permeability is 3-4 times higher in 1,2-polybutadiene filled with TiO_2 than in the unfilled polymer. This permeability enhancement is due to an increase in gas solubility coefficients in the nanocomposite films. Diffusion coefficients initially decrease with increasing particle loading, presumably due to the increase in tortuosity caused by the presence of substantial amounts of impermeable particles in the nanocomposites, and then increase at the highest loadings considered.

REFERENCES

(1) Patel, N. P.; Miller, A. C.; Spontak, R. J., Highly CO2-permeable and -selective membranes derived from crosslinked poly(ethylene glycol) and its nanocomposites, *Advanced Functional Materials* **2004**, 15, 699-707.

(2) Matteucci, S.; van Wagner, E.; Swinnea, S.; Freeman, B. D.; Sakaguchi, T.; Masuda, T., Desilylation of substituted polyacetylenes in the presence of nanoparticles, *Macromolecules* **2007**, 40, 3337-3347.

(3) Utamapanya, S.; Klabunde, K. J.; Schlup, J. R., Nanoscale metal oxide particles/clusters as chemical reagents. Synthesis and properties of ultrahigh surface area magnesium hydroxide and magnesium oxide, *Chemistry of Materials* **1991**, 3, 175-181.

(4) Matteucci, S.; Kusuma, V.; Sanders, D.; Swinnea, S.; Freeman, B. D., Gas transport in TiO2 nanoparticle filled poly(1-trimethylsilyl-1-propyne), *Journal of Membrane Science* **In Press.**

(5) Liu, L.; Qi, Z.; Zhu, X., Studies on nylon 6/clay nanocomposites by melt-intercalation process, *Journal of Applied Polymer Science* **1998**, 71, 1133-1138.

(6) Chaudhary, D. S.; Prasad, R.; Gupta, R. K.; Bhatacharya, S. N., Clay intercalation and influence on crystallinity of EVA-based clay nanocomposites, *Thermochimica Acta* **2005**, 433, 187-195.

(7) Bevington, P. R.; Robinson, D. K. Data Reduction and Error Analysis for the Physical Sciences, 3rd ed.; McGraw-Hill, Inc.: New York, **2003**.

(8) Obata, Y.; Tosaki, C.; Ikeyama, M., Bulk properties of syndiotactic 1,2-polybutadiene. I. Thermal and viscoelastic properties, *Polymer Journal* **1975**, 7, 207-216.

(9) Dhoot, S. N.; Freeman, B. D.; Stewart, M.; Hill, A. J., Sorption and transport of linear alkane hydrocarbons in biaxially oriented poly(ethylene terephthalate), *Journal of Polymer Science Part B: Polymer Physics* **2001**, 39, 1160-1172.

(10) Tasagaropoulos, G.; Eisenberg, A., Dynamic mechanical study of the factors affecting the two glass transition behavior of filled polymers. Similarities and differences with random ionomers, *Macromolecules* **1995**, 28, 6067-6077.

(11) Rittigstein, P.; Torkelson, J. M., Polymer-nanocomposite interfacial interactions in polymer nanocomposites: Confinement effects on glass transition temperature and suppression of physical aging, *Journal of Polymer Science Part B: Polymer Physics* **2006**, 44, 2935-2943.

(12) Merkel, T. C.; Freeman, B. D.; Spontak, R. J.; He, Z.; Pinnau, I.; Meakin, P.; Hill, A. J., Sorption, transport, and structural evidence for enhanced free volume in poly(4-methyl-2-pentyne)/fumed silica nanocomposite membranes, *Chemistry of Materials* **2003**, 15, 109-123.

(13) Merkel, T. C.; Freeman, B. D.; Spontak, R. J.; He, Z.; Pinnau, I.; Meakin, P.; Hill, A. J., Ultrapermeable, reverse-selective nanocomposite membranes, *Science* **2002**, 296, 519-522.

(14) Lape, N. K.; Nuxoll, E. E.; Cussler, E. L., Polydisperse flakes in barrier films, *Journal of Membrane Science* **2004**, 236, 29-37.

(15) Takahashi, S.; Goldberg, H. A.; Feeney, C. A.; Karim, D. P.; Farrell, M.; O'Leary, K.; Paul, D. R., Gas barrier properties of butyl rubber/vermiculite nanocomposite coatings, *Polymer* **2006**, 47, 3083-3093.

(16) Takahashi, S.; Paul, D. R., Gas permeation in poly(ether imide) nanocomposite membranes based on surface-treated silica. Part 1: Without chemical coupling to matrix, *Polymer* **2006**, 47, 7519-7534.

(17) Wan, T.; Wang, Y.-C.; Feng, F., Preparation of titanium dioxide/polyacrylate nanocomposites by sol-gel process in reverse micelles and in situ photopolymerization, *Journal of Applied Polymer Science* **2006**, 102, 5105-5112.

(18) Stark, R. W.; Drobek, T.; Heckl, W. M., Tapping-mode atomic force microscopy and phase-imaging in higher eigenmodes, *Applied Physics Letters* **1999**, 74, 3296-3298.

(19) Sengupta, R.; Bandyopadhyay, A.; Sabharwal, S.; Chaki, T. K.; Bhomick, A. K., Polyamide-6,6/in situ silica hybrid nanocomposites by sol-gel technique: synthesis, characterization, and properties, *Polymer* **2005**, 46, 3343-3354.

(20) Ma, D.; Akpalu, Y. A.; Li, Y.; Siegel, R. W.; Schadler, L. S., Effect of titania nanoparticles on the morphology of low density polyethylene, *Journal of Polymer Science Part B: Polymer Physics* **2005**, 43, 488-497.

(21) Yang, H.; Bhimaraj, P.; Yang, L.; Siegel, R. W.; Schadler, L. S., Crystal growth in alumina/poly(ethylene terephthalate) nanocomposite films, *Journal of Polymer Science Part B: Polymer Physics* **2007**, 45, 747-757.

(22) Olkin, I.; Gleser, L. J.; Derman, C. Probability Models and Applications, 2nd ed.; Macmillan College Publishing Company: New York, **1980**.

(23) Weibull, W., A statistical distribution function of wide applicability, *Journal of Applied Mechanics* **1951**, 18, 293-297.

(24) Mackay, M. E.; Dao, T. T.; Tuteja, A.; Ho, D. L.; Van Horn, B.; Kim, H.-C.; Hawker, C. J., Nanoscale effects leading to non-Eistein-like decrease in viscosity, *Nature Materials* **2003**, 2, 762-766.

(25) Gestoso, P.; Nicol, E.; Doxastakis, M.; Theodorou, D. N., Atomistic Monte Carlo simulation of polybutadiene isomers: cis-1,4-polybutadiene and 1,2-polybutadiene, *Macromolecules* **2003**, 36, 6925-6938.

(26) Barrer, R. M.; Barrie, J. A.; Rogers, M. G., Heterogeneous membranes: Diffusion in filled rubber, *Journal of Polymer Science, Part A: Polymer Chemistry* **1963**, 1, 2565-2586.

(27) Hill, R. J., Diffusive permeability and selectivity of nanocomposite membranes, *Industrial and Engineering Chemistry Research* **2006**, 45, 6890-6898.

(28) Bouma, R. H. B.; Checchetti, A.; Chidichimo, G.; Drioli, E., Permeation through a heterogeneous membrane: The effect of the dispersed phase, *Journal of Membrane Science* **1997**, 128, 141-149.

(29) Barrer, R. M. Diffusion and Permeation in Heterogeneous Media, In Diffusion in Polymers; Crank, J.; Park, G. S., Eds.; Academic Press: New York, **1968**; pp 165-219.

(30) Petropoulos, J. H. Mechanisms and theories for sorption and diffusion of gases in polymers, In Polymeric Gas Separation Membranes; Paul, D. R.; Yampol'skii, Y. P., Eds.; CRC Press, Inc.: Boca Raton, **1994**; pp 17-82.

(31) Merkel, T. C.; He, Z.; Pinnau, I.; Freeman, B. D.; Hill, A. J.; Meakin, P., Effect of nanoparticles on gas sorption and transport in poly(1-trimethylsilyl-1-propyne), *Macromolecules* **2003**, 36, 6844-6855.

(32) Lindbrathen, A.; Hagg, M.-B., Glass membranes for purification of aggressive gases: Part II. Adsorption measurements and diffusion coefficient estimations, *Journal of Membrane Science* **2005**, 259, 154-160.

(33) Bird, R. B.; Stewart, W. E.; Lightfoot, E. L. Transport Phenomena, 2nd ed.; John Wiley & Sons: New York, **2002**.

(34) Naito, Y.; Kamiya, Y.; Terada, K.; Mizoguchi, K.; Wang, J.-S., Pressure dependence of gas permeability in a rubbery polymer, *Journal of Applied Polymer Science* **1996**, 61, 945-950.

(35) Matteucci, S.; Yampol'skii, Y. P.; Freeman, B. D.; Pinnau, I. Transport of gases and vapors in glassy and rubbery polymers, In Materials Science of Membranes for Gas and Vapor Separations; Yampol'skii, Y. P.; Freeman, B. D.; Pinnau, I., Eds.; John Wiley and Sons: London, **2006**; pp 1-48.

(36) Matteucci, S.; Kusuma, V.; Kelman, S.; Freeman, B. D., Gas transport properties in MgO nanoparticle filled poly(1-trimethylsilyl-1-propyne), *Polymer* **Submitted**.

(37) Do, D. D. Adsorption Analysis: Equilibria and Kinetics; Imperial College Press: London, **1998**; Vol. 2.

(38) Weinkauf, D. H.; Paul, D. R. Effects of structural order on barrier properties, In Barrier Polymers and Structures; Koros, W. J., Ed.; American Chemical Society: Washington, D.C., **1990**; pp 60-91.

(39) Michaels, A. S.; Bixler, H. J., Solubility of gases in polyethylene, *Journal of Polymer Science* **1961**, 50, 393-412.

(40) Qiu, J.; Zheng, J.-M.; Peinemann, K.-V., Gas transport properties in a novel poly(trimethylsilylpropyne) composite membrane with nanosized organic filler trimethylsilylglucose, *Macromolecules* **2006**, 39, 4093-4100.

Chapter 8: Gas permeability, solubility, and diffusion coefficients in 1,2-polybutadiene containing magnesium oxide

This chapter describes the incorporation of magnesium oxide nanoparticles in 1,2-polybutadiene. The nanoparticles have a high surface area (*i.e.,* greater than 600 m^2/g) and are basic, so they physisorb CO_2.[17,18] These nanoparticles can adsorb large concentrations of CO_2 even at low pressures.[20] Gas permeability and acid gas/non-polar gas selectivity in nanocomposite films are reported for pure and mixed gas feed streams. The influence of the particles on gas permeability is discussed in terms of the effects of the particles on gas solubility and gas diffusivity. Particle dispersion is characterized by atomic force microscopy and transmission electron microscopy.

2.6 nm magnesium oxide nanoparticles were dispersed in 1,2-polybutadiene via solution casting. Particles were observed to be dispersed into submicron aggregates using atomic force microscopy and transmission electron microscopy. The nanocomposite density was consistently lower than that anticipated based on an additive model, suggesting the presence of voids in the nanocomposites. The incorporation of nanoparticles into 1,2-polybutadiene increased acid gas (*i.e.,* CO_2) and non-polar gas (*i.e.,* CH_4, N_2) permeability with increasing particle loading. For instance, CO_2 permeability increased from 52 barrer in the unfilled polymer to 650 barrer in a nanocomposite containing 27 nominal volume percent MgO, at 35 ^{o}C and a feed pressure of 12 atm. CO_2/nonpolar gas selectivity decreased with increasing particle loading, while CH_4/N_2 selectivity was not influenced by the particles. Gas solubility increased systematically with increasing particle loading. In contrast, gas diffusion coefficients initially decreased with increasing particle loading and then increased with increasing loading at particle loadings greater than 10 nominal volume percent.

RESULTS AND DISCUSSION

Nanoparticle reactivity

Periclase (*i.e.,* MgO) nanoparticles can react with water to form brucite (*i.e.,* MgOH).[18,19] To determine if this reaction occurred in the samples considered in this study, wide angle x-ray diffraction spectroscopy was used to characterize the as-received particles, particles that had been soaked in water, and PB-based nanocomposite samples. The WAXD spectra from these studies are presented in Figures 8.1 and 8.2. As explained in more detail below, the location of the amorphous and crystalline peaks in the PB sample presented these figures is consistent with the literature.[20] Based on the results in Figure 8.1, the nanoparticles soaked in water exhibit a rather complete conversion from periclase to brucite. Even when precautions were taken to limit exposure of the samples to water during preparation, some of the nanoparticles in the PB-based nanocomposites also convert to brucite. Figure 8.2 shows that this reaction takes place in nanocomposites over the range of particle loadings used in this study. However, in contrast to previous studies, in which MgO particles were shown to react with a substituted acetylene polymer,[37] no evidence of reaction of the particles with PB was observed in FTIR studies.

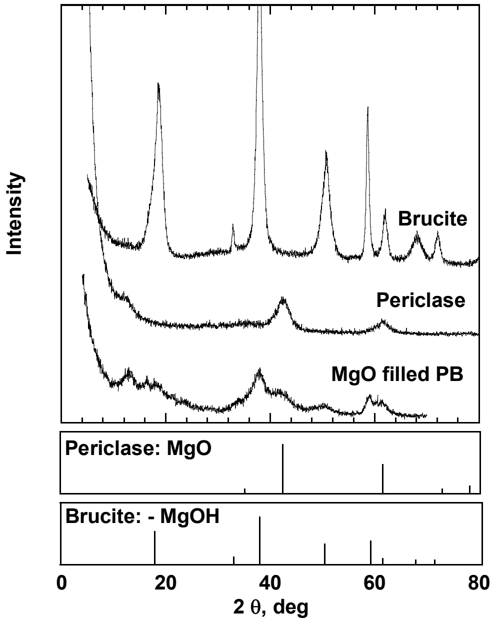

Figure 8.1. WAXD spectra of neat MgO nanoparticles that were exposed to ambient conditions for 1 week prior to testing (periclase)[2], MgO particles that were soaked in deionized water for 48 hours and then dried for 48 hours in a fumed hood (brucite),[2] and a nanocomposite sample containing 20 nominal volume percent MgO in 1,2-polybutadiene after 1 day of mixing at 40 °C (MgO filled PB). The boxes below the figure present 2 θ peak locations and intensities associated with crystal structures of periclase and brucite from the powder diffraction database, PDF-2 Release 2004 from the International Centre for Diffraction Data, Newton Square, PA.

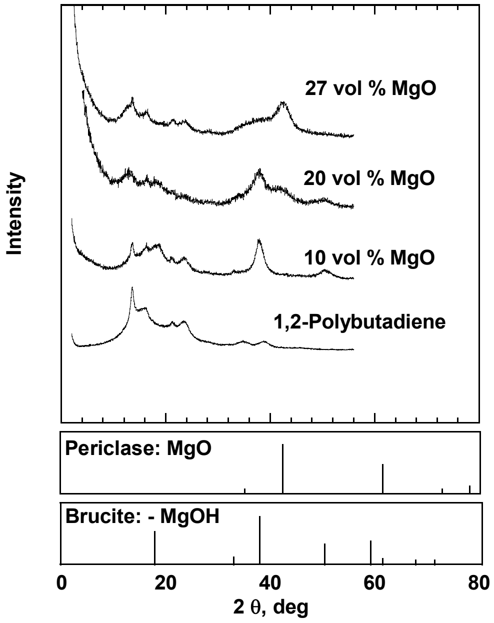

Figure 8.2. WAXD spectra of 1,2-polybutadiene and nanocomposites containing 10, 20, and 27 nominal volume percent MgO in 1,2-polybutadiene after 1 day of mixing at 40 °C. The boxes below the graph present 2 θ peak locations and intensities associated with crystal structures from the powder diffraction database, PDF-2 Release 2004 from the International Centre for Diffraction Data, Newton Square, PA.

Crystallinity and glass transition temperature in PB and nanocomposite samples

Figure 8.2 presents the WAXD spectra for PB and PB-MgO nanocomposites. In unfilled PB, peaks are located at 13.2°, 16.0°, 21.6°, 24.0°, 35.0°, and 39.1° (2θ). The peak locations are consistent with literature values for PB containing 32 wt % crystallinity.[20] Generally, the peaks in the unfilled polymer were also observed in the PB-MgO nanocomposites. However, some of the PB peaks appear near or are overlapped by peaks attributed to either brucite or periclase. The peak located at approximately 13.2° (2θ) in the unfilled polymer shifts to higher 2θ values as particle loading increases in the nanocomposites. A similar shift has been reported for unfilled PB samples as crystal content decreases.[20] As will be discussed below, the concentration of crystalline PB decreases as particle content increases, so the peak shift at 13.2° (2θ) to higher 2θ values as particle loading increases agrees with the reduction in crystallinity observed at high particle concentrations.

Based on the WAXD data in Figures 8.1 and 8.2, the weight fraction of crystalline polymer in the polymer phase decreases as particle loading increases. The crystallinity values are presented in Table 8.1.[21] This trend is qualitatively consistent with that of PB filled with TiO_2 nanoparticles, where the weight fraction of crystals decreased from 32 % in the unfilled polymer to 20 % in samples containing 27 nominal volume percent TiO_2.[12] The volume fraction of crystalline polymer in the polymer phase, ϕ_C (*i.e.,* volume of crystalline polymer per total volume of polymer), was estimated as follows:[22]

$$\phi_C = \chi_C \frac{\rho_P^N}{\rho_C} \tag{7.1}$$

where ρ_P^N is the polymer density in the nanocomposite samples, which was calculated using the following equation:[20]

$$\frac{1}{\rho_P^N} = \frac{\chi_C}{\rho_C} + \frac{\chi_C - 1}{\rho_A} \qquad (7.2)$$

The crystalline volume fraction values, which are presented in Table 8.1, are useful in estimating the contribution of the polymer to the nanocomposite density, which is discussed below.

Table 8.1. Concentration of crystalline 1,2-polybutadiene and polymer/nanocomposite glass transition temperature

ϕ_F^N (%)	Technique for estimating crystallinity	χ_C (%)	ϕ_C (%)	T_g, °C [b]
0	density [a]	30 ± 5	28 ± 4	--
0	DSC	35 ± 3	33 ± 3	-17 ± 3
0	WAXD	32 ± 3	30 ± 3	--
10	WAXD	22 ± 2	20 ± 2	-10 ± 3
20	WAXD	16 ± 2	15 ± 2	-9 ± 3
27	WAXD	15 ± 2	14 ± 2	-8 ± 3

Uncertainties were estimated using the propagation of errors method.[21]

[a] χ_C values were estimate from density using Eq. (7.1), ϕ_C values for DSC and WAXD were estimated using Eq. (7.1).

[b] All T_g values were determined from first scan DSC thermograms.

DSC thermograms of PB and representative nanocomposite samples are presented in Figure 8.3. The nanocomposite T_g increased with increasing particle loading, and the values obtained from the DSC results are recorded in Table 8.1. The T_g of the unfilled polymer is approximately 9 °C lower than that of the PB containing 27 nominal volume percent MgO. Such behavior has been observed in other nanocomposites.[12,23] In the literature, such a shift in T_g is attributed to the adsorption of polymer onto the particle surface, which reduces the chain mobility of the bulk polymer.[23,24]

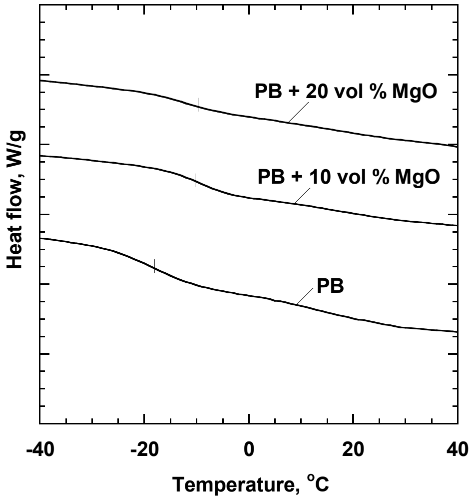

Figure 8.3. Influence of nominal volume percent MgO on the T_g of 1,2-polybutadiene filled with MgO nanoparticles. The T_g is recorded as the middle of the endothermic heat capacity step change in the DSC thermograms, are represented by tick marks. All T_g values are from first run DSC scans. The thermograms have been displaced vertically for easier viewing.

Nanoparticle dispersion

Particle distribution in polymer matrixes can influence gas transport properties.[25,26,33] Traditionally, transmission electron microscopy (TEM) has been used to image particle dispersion in nanocomposites.[25,27] However, the nanoparticles used in such experiments generally had primary particle diameters greater than 10 nm, and such nanoparticles could be imaged using TEM without damaging the polymer phase.[25,26,33] Resolving individual nanoparticles with primary particle diameters below 5 nm often requires the TEM electron beam to be so focused that the polymer could be degraded upon even short exposure to the beam. Also, TEM samples are generally at least 40 nm thick. Since sample thickness could be many times the average interparticle spacing, as discussed below. Therefore, a 2-dimensional image of a 3-dimensional dispersion would show nanoparticles and nanoparticle aggregates overlapping even if the particles were well dispersed. Such overlap could cause errors in the determination of particle aggregate size from TEM images.

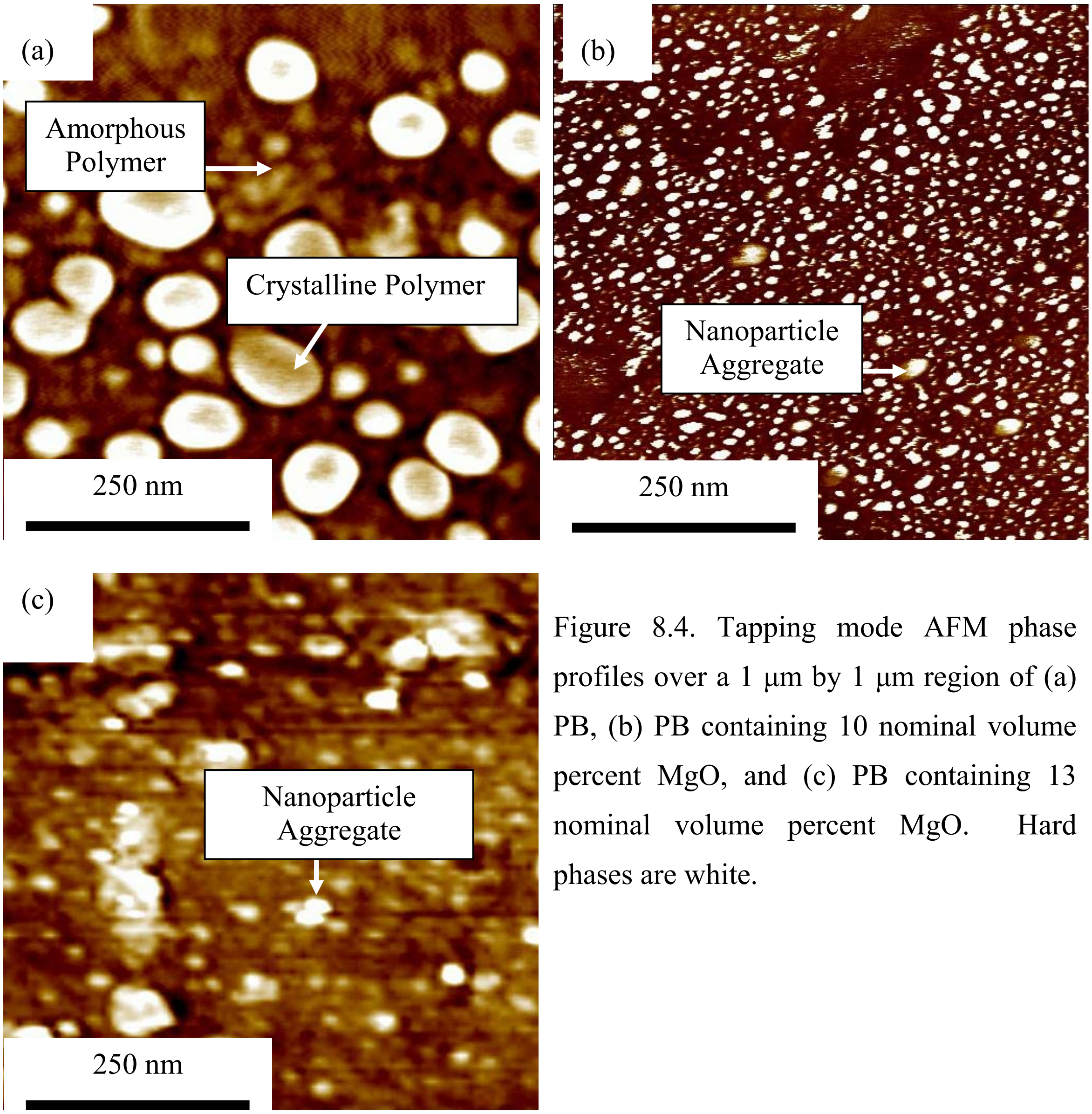

Figure 8.4. Tapping mode AFM phase profiles over a 1 μm by 1 μm region of (a) PB, (b) PB containing 10 nominal volume percent MgO, and (c) PB containing 13 nominal volume percent MgO. Hard phases are white.

Tapping mode atomic force microscopy (AFM) provides images of the nanoparticle cross-sections (*i.e.,* nanocomposite bulk) with sufficient resolution to observe individually dispersed particles and small nanoparticle aggregates.[11] Figure 8.4 presents AFM tapping mode phase profile images for PB and nanocomposite cross-sections. The unfilled PB (*cf.*, Figure 8.4a) has two distinct phases that are attributed to amorphous and crystalline regions of the polymer.[12] The harder phase (*i.e.,* white regions) in Figure 8.4a occupies approximately 27 area percent of the AFM image, which is in good agreement with the volume percent of crystalline polymer as determined by density (28 ± 4 vol %), WAXD (30 ± 3 vol %), and DSC (34 ± 3 vol %). Therefore, the hard phase in unfilled PB is attributed to crystalline polymer.

Nanocomposite AFM images (*i.e.*, Figures 8.4b and 8.4c) also contain two distinct phases. AFM phase profile images resolve the relative hardness of the surface being probed. The nanoparticles may be sufficiently hard that the modulus difference between crystalline and amorphous polymer cannot readily be resolved in the presence of particles, and such behavior has been reported.[12,28] Depending on the polymer and particle, AFM phase profile images have yielded mixed results for resolving amorphous polymer, crystalline polymer and nanoparticles in such systems.[28-30]

Nearly 16 and 18 area percent of the images in Figure 8.4b and Figure 8.4c, respectively, are occupied by the hard phase, which is in the same order as the particle concentration in the composites (*i.e.,* 10 and 20 nominal volume percent MgO, respectively). However, the area fraction of the hard phase in these AFM images (*i.e.,* Figures 8.4b and 8.4c) is higher than concentration of crystalline polymer in the nanocomposite samples; the crystalline content of the nanocomposite samples are recorded in Table 8.1. Therefore, the hard phase in the phase profiles is attributed solely to the nanoparticles.

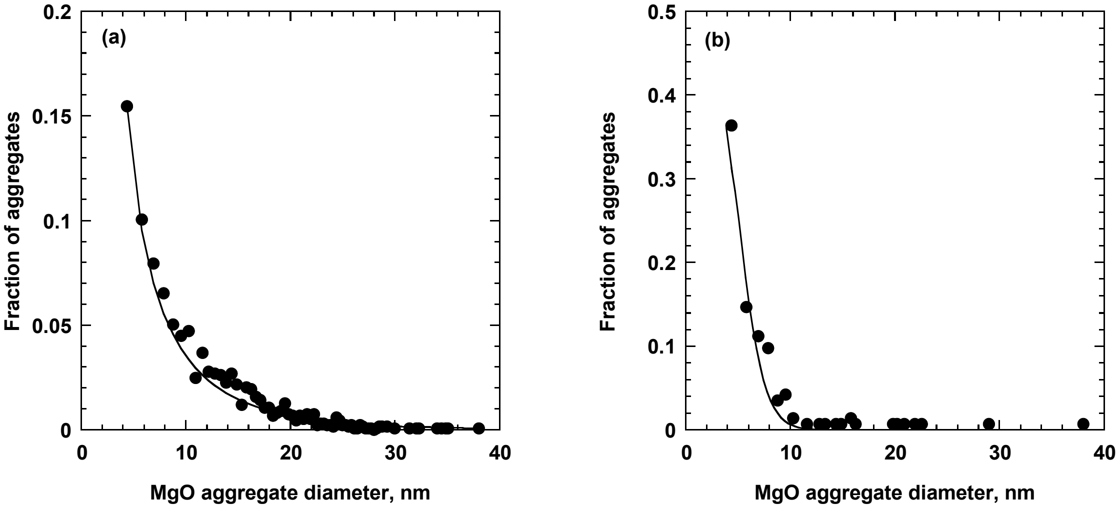

Figure 8.5. MgO aggregate diameter distribution from tapping mode phase profiles of PB containing (a) 10 nominal volume percent MgO and (b) 13 nominal volume percent MgO. The solid line represents a Weibull distribution with parameters of v = 3.0 nm, β = 1.92 ± 0.66 and α = 0.75 ± 0.32 for plot (a) and v = 3.0 nm, β = 2.57 ± 0.83 and α = 1.32 ± 0.50.[16,17] The error in the Weibull distribution parameters was determined by the least-squares fit method described by Bevington.[4]

Figure 8.5 presents the estimated characteristic particle diameter distribution for the nanoparticles and nanoparticle aggregates in Figures 8.4b and 8.4c and compares them to the best fit of a Weibull distribution to the data (*i.e.,* Eq. (3.4)).[21,31,32] A spherical model is used in calculating the aggregate diameters. The average aggregate diameter, $\bar{d}$, was estimated from the Weibull distribution as follows:[31]

$$\bar{d} = \sum_{j=1}^{h} d_j F_j \tag{8.1}$$

where h is the number of bins used in the AFM particle analysis, (*i.e.,* 100). The nanoparticle aggregates in Figures 8.4b and 8.4c have an average characteristic diameter $\bar{d}$ determined from the Weibull distribution of 7 nm ± 6 nm and 7 nm ± 3 nm, respectively. These results are consistent with the $\bar{d}$ calculated by Eq. (3.5) where the average particle diameter is 11 nm ± 6 nm and 8 nm ± 4 nm for PB films containing 10 and 13 nominal volume percent MgO, respectively. Since the smallest structures the AFM can resolve (*i.e.,* 2 nm) are similar to the nanoparticle diameter, a significant population of particles may not be resolved in these experiments, which would cause the experimentally derived $\overline{d}$ to be larger than the true average particle diameter in the nanocomposite.

Inter-aggregate spacing, d_a, can be estimated by assuming that the aggregates are spherical and dispersed in a body centered cubic structure:

$$d_a = \overline{d}\left[\left(\frac{\pi}{6\phi_F^N}\right)^{\frac{1}{3}} - 1\right] \tag{1.2}$$

d_a does not change significantly when either nominal or true volume fraction MgO (*i.e.,* the particle concentration that accounts for any void volume in the nanocomposite)[11] is used in Eq. (1.2). A discussion regarding the differences between true and nominal volume fraction MgO in nanocomposites is provided below. The assumption of a body centered cubic aggregate structure is made solely to simplify estimating d_a. However, more realistic particle distributions (*e.g.,* a random aggregate distribution)[33] yield very similar values for d_a. For the PB film containing 10 nominal volume percent MgO, d_a is approximately 8 nm, and d_a is 4 nm for PB films containing 13 nominal volume percent MgO. These values are comparable to the estimated inter-aggregate distances reported in the literature for similar systems, as shown in Table 8.2.[11,12] Interparticle spacing in these nanocomposites are quite small even at moderate particle loadings. These interparticle spacings are comparable in magnitude to the structural features of PB molecules; for example, the radius of gyration of 1,2-polybutadiene used in this study is 8.5 nm.[12,34]

One might anticipate that particles dispersed throughout the particle matrix at such short interparticle spacings should influence polymer chain packing, chain mobility, and gas transport properties.

Table 8.2. Nanoparticle average aggregate diameter and estimated interparticle spacing in various nanocomposites[11,12]

Polymer	Particle	$\phi_F^N \times 100(\%)$	$\overline{d}$, nm	d_a, nm	Area % nanoparticles
PTMSP[13]	TiO_2	3	7 ± 3	9	4
PTMSP[13]	TiO_2	10	12 ± 8	11	16
PB[14]	TiO_2	10	9 ± 4	7	6
PB	MgO	10	11 ± 6	8	16
PB	MgO	13	8 ± 4	4	18

Note: TiO_2 nanoparticles were approximately 3 nm in primary particle diameter.[11,12]

Although TEM cannot resolve individual nanoparticles, it can characterize micron size nanoparticle aggregates. Figure 8.6 presents the TEM images for samples containing 10 and 20 nominal volume percent MgO. The dark regions are electron rich (*i.e.,* particle rich) and the lighter colored regions are electron poor (*i.e.,* polymer or voids). Figure 8.6a shows numerous well-dispersed nanoparticle aggregates with characteristic dimensions in the sub-micron and micron range.

The nanoparticle aggregates in the sample containing 20 nominal volume percent MgO are larger and less uniformly dispersed than those in the film containing 10 nominal volume percent MgO. The larger aggregate size in the more highly concentrated sample may be due, in part, to more incomplete mixing in the sample containing a higher concentration of particles, since sample viscosity increased with increasing particle concentration. The presence of large aggregates of particles could, in turn, promote the formation of large nanoparticle aggregates at the expense of smaller aggregates or individually dispersed particles.[35]

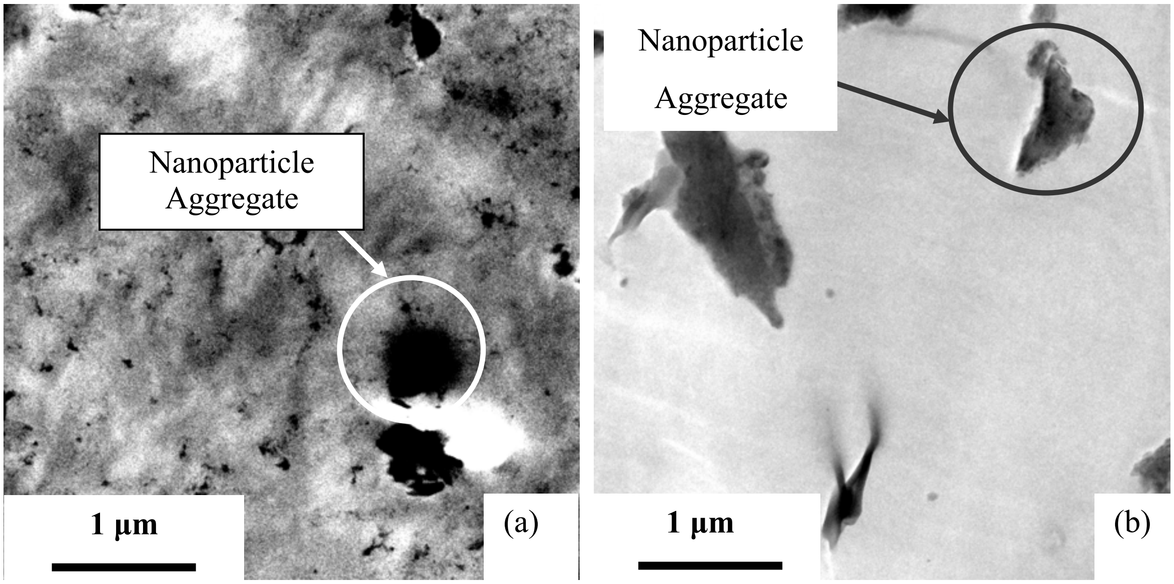

Figure 8.6. TEM images of (a) PB containing 10 nominal volume percent MgO, and (b) PB containing 20 nominal volume percent MgO.

Nanocomposite density and void volume

Based upon the density data presented below, the inclusion of nanoparticles in PB results in the formation of voids in the sample. This point is readily apparent if one compares the experimentally-determined density of the nanocomposite samples to the so-called additive density, ρ_{Add}, which is the density that a nanocomposite sample would have if the polymer and particles each exhibited their pure component properties:[12]

$$\rho_{Add} = \phi_F^N \rho_F + \left(1-\phi_F^N\right)\left(\phi_C \rho_C + \left(1-\phi_C\right)\rho_A\right) \tag{2.21}$$

where ϕ_C is the crystalline phase volume percent from WAXD (*cf.*, Table 8.1), and ρ_F is the pure filler density. Figure 8.7 presents the experimentally determined density, ρ_{Exp}, as a function of particle content in the sample. As nanoparticle concentration increases, the experimental density deviates more and more from the additive model given by Eq. (2.21).

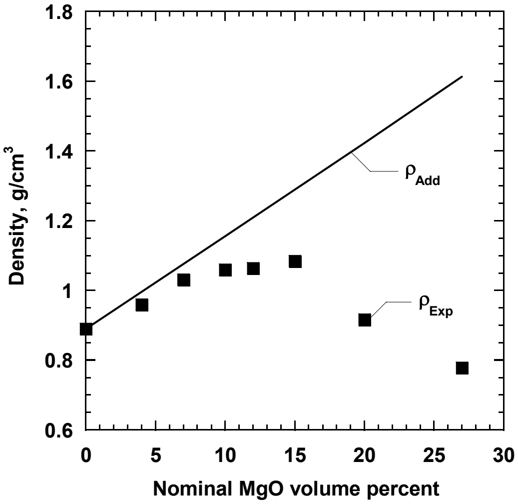

Figure 8.7. Effect of MgO concentration on composite density (ρ_{Exp}, ■). The solid line represents the additive density, ρ_{Add}, calculated according to Eq. (2.21).

The departure of ρ_{Exp} from ρ_{Add} can be characterized in terms of the "void" volume fraction, ϕ_V, in the sample:[11]

$$\phi_V = \left(1 - \frac{\rho_{Exp}}{\rho_{Add}}\right) \tag{2.22}$$

Using the data in Figure 8.7, the void volume was calculated and is presented as a function of particle loading in Figure 8.8. At loadings of approximately 25 nominal volume percent MgO, the void volume percent is approximately 52%, so most of the sample is voids at the highest loadings considered. Other nanocomposite systems also exhibit an increase in void volume fraction with increasing particle loading, and various groups have assigned the voids to the polymer-particle interface,[36] polymer free volume,[27] or interparticle spaces.[25] Based on the information available, we cannot definitively assign the voids in MgO filled PB nanocomposites to any one or combination of these locations. However, it is quite clear that including these very small particles in the polymer results in strong deviations away from the additive density model presented above.

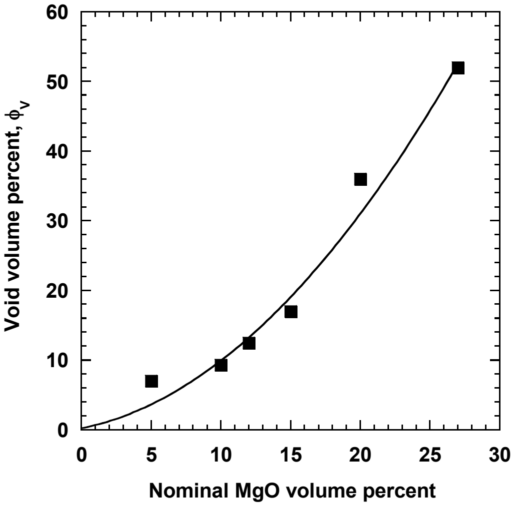

Figure 8.8. Void volume percent of PB/MgO nanocomposite films as calculated from the data in Figure 8.7 using Eq. (2.22). The solid line is drawn to guide the eye.

Given the non-negligible volume of voids in the nanocomposites, the true and nominal volume fraction of MgO are not the same. The true volume fraction of MgO in the PB matrix, ϕ_F^T, may be calculated as follows:[11]

$$\phi_F^T = \phi_F^N \left(1 - \phi_V\right) \tag{2.23}$$

The maximum difference ϕ_F^N between and ϕ_F^T occurs at the maximum particle loadings, where ϕ_F^N is 27 percent and ϕ_F^T is 13 percent, according to Eq. (2.23) and the data in Figures 8.7 and 8.8.

Gas permeability

In MgO filled PB films, CO_2, N_2, and CH_4 permeability increases with increasing particle loading, as presented in Figure 8.9. The CO_2, CH_4, and N_2 permeability values are approximately 10, 17, and 18 times higher, respectively, in PB containing 27 nominal volume percent MgO than in unfilled PB. Gas permeability values are considerably higher for the nanocomposite samples than predicted by Eq. (2.26) for heterogeneous films with an impermeable discontinuous phase.

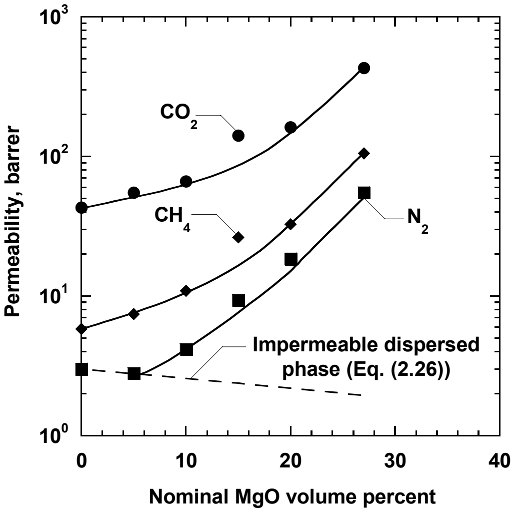

Figure 8.9. Effect of MgO concentration on CO_2 (●), CH_4 (♦), and N_2 (■) permeability at $\Delta p = 6$ atm. Measurements were conducted at 35 °C and at a downstream pressure less than 0.01 atm. The dashed line represents Bruggeman's model for N_2 in the limit where the nanoparticles are treated as an impermeable dispersed phase (*i.e.*, Eq. (2.26)) present at levels corresponding to the nominal volume fraction loading of particles in the polymer. The solid lines are drawn to guide the eye.

In previous studies involving dispersion of nanoparticles in PB, the increase in gas permeability with increasing particle loading could be rationalized using Bruggeman's model if the model were applied in the limit where the dispersed phase was much more permeable than the matrix (*i.e.,* Eq. (2.27)), and the dispersed phase volume fraction was set equal to the volume fraction of voids in the sample.[12] This approach was applied to the data from the present study. The results are presented in Figure 8.10, which shows the correlation between relative CO_2, CH_4, and N_2 permeability (*i.e.,* permeability in a composite sample relative to that of unfilled PB) and void volume. The dashed line represents Eq. (2.27) when the dispersed phase volume fraction is set equal to the void volume fraction (*i.e.,* $\phi_D = \phi_V$). Interestingly, Eq. (2.27) captures the observed trend in permeability at low void volumes but does not increase as strongly with void volume as the void volume percent increases beyond approximately 10%.

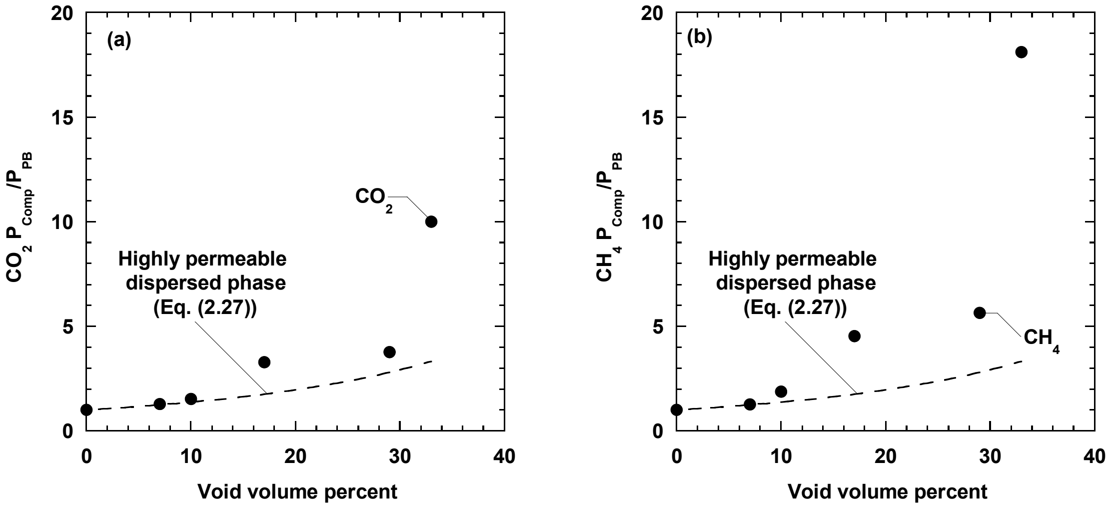

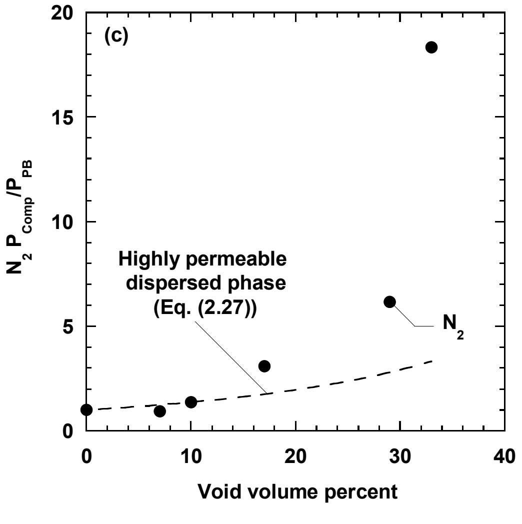

Figure 8.10. Permeability of nanocomposite samples, P_{Comp}, relative to the permeability of nitrogen in 1,2-polybutadiene, P_{PB} for: (a) CO_2, (b) CH_4, and (c) N_2. The dashed line represents Bruggeman's model in the limit where the dispersed phase is highly permeable (*i.e.,* Eq. (2.27)). The volume fraction of the dispersed phase in this model was set equal to the void volume estimated from the density data (*i.e.*, Eq. (2.22)). The experimental permeability data were collected at 35 ^{o}C and $\Delta p = 6$ atm.

The strong increase in permeability values at high particle loadings could suggest that the particles were introducing transmembrane defects.[37] In this case, the gas transport properties would be expected to be more similar to the properties observed with either Knudsen diffusion or Poiseuille flow.[10] In the case of Poiseuille flow, gas permeability would be pressure dependent.[11] Figure 8.11 presents the influence of upstream pressure on gas permeability for PB and PB filled MgO. Permeability values for the unfilled polymer are similar to the values from Naito *et al.*, who reported CO_2, CH_4, and N_2 permeability coefficients of 43, 5.6, and 1.9 barrer, respectively, in PB.[38] Although CO_2 permeability does increase with pressure, this behavior may be attributed to CO_2 induced plasticization.[12] Both CH_4 and N_2 permeabilities are independent of pressure, which suggests that gas transport in the nanocomposite does not follow Poiseuille flow.

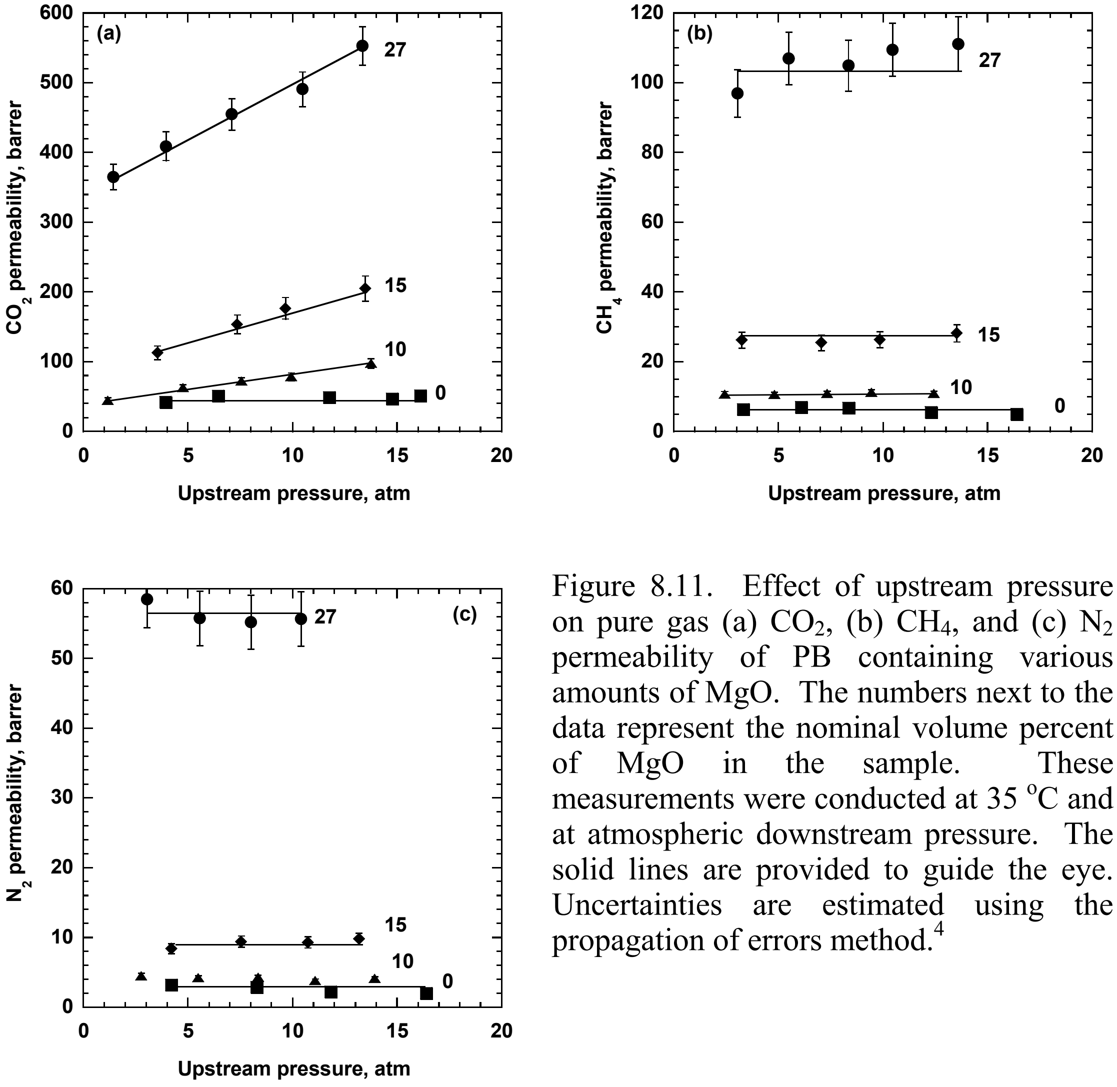

Figure 8.11. Effect of upstream pressure on pure gas (a) CO_2, (b) CH_4, and (c) N_2 permeability of PB containing various amounts of MgO. The numbers next to the data represent the nominal volume percent of MgO in the sample. These measurements were conducted at 35 °C and at atmospheric downstream pressure. The solid lines are provided to guide the eye. Uncertainties are estimated using the propagation of errors method.[4]

The gas selectivities expected in films containing transmembrane defects could be either the Knudsen, $\alpha^{K}_{A/B}$, or Poiseuille limit, $\alpha^{P}_{A/B}$. The Knudsen limit is:[39]

$$\alpha^{K}_{A/B} = \sqrt{\frac{M_B}{M_A}} \tag{4.1}$$

where M_A and M_B are the molar masses of gases A and B, respectively.[60] The Poiseuille selectivity limit for gases tested individually is:[60]

$$\alpha^{P}_{A/B} = \frac{\mu_B}{\mu_A} \tag{4.2}$$

where μ_A and μ_B are the viscosities of gas A and B, respectively.[60] However, if gases are tested in mixtures and undergo Poiseuille flow, then the observed selectivity would be 1. Figure 8.12 presents pure gas selectivity values for the gas pairs considered as a function of increasing particle loading. Table 8.3 presents a comparison of the pure gas selectivity values in unfilled PB, PB filled with the highest content of particles considered (27 nominal volume percent), and the Knudsen and Poiseuille limits, calculated based on Equations (4.1) and (4.2). In the case of CO_2/N_2 and CO_2/CH_4, selectivity decreases with increasing particle loading, but never reaches values that are consistent with either Poiseuille or Knudsen flow, suggesting that the films are free from macroscopic, trans-film defects. The CH_4/N_2 selectivity did not deviate significantly from 2 (*i.e.,* the unfilled polymer CH_4/N_2 selectivity) with increasing particle concentration, indicating that methane and nitrogen permeability exhibited essentially the same relative dependence on particle content. Based on the lack of pressure dependence for CH_4 and N_2 permeabilities and the strong deviations between the selectivity values observed in the nanoparticle-filled samples and the selectivity values expected for flow through pores, the presence of MgO nanoparticles increases permeability without introducing trans-film defects in amounts sufficient to drive selectivity to values consistent with pore flow models, such as Knudsen flow.[10,12]

Table 8.3. Comparison of pure gas selectivity values in unfilled and filled 1,2-polybutadiene with values expected for Knudsen and Poiseuille flow at 35°C

Gas Pair	Knudsen Selectivity	Poiseuille Selectivity	Unfilled PB	PB filled with 27 nominal vol. % MgO
CO_2/N_2	0.8	1.2	14	7.8
CO_2/CH_4	0.6	0.7	7.4	4.1
CH_4/N_2	1.3	0.6	1.9	1.9

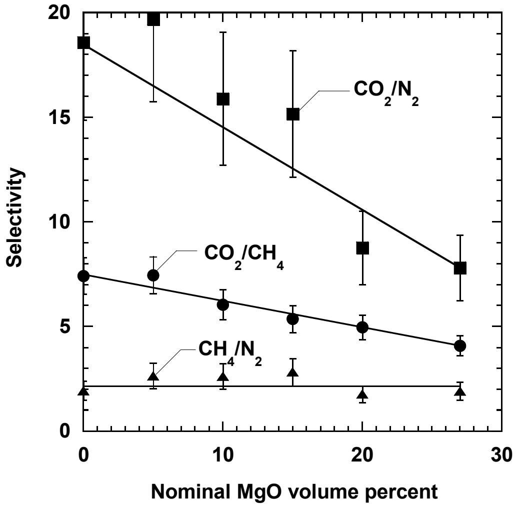

Figure 8.12. Effect of MgO concentration on pure gas CO_2/N_2 (■), CO_2/CH_4 (●), and CH_4/N_2 (▲) selectivity at Δp = 6 atm. Measurements were made at 35 °C and a downstream pressure less that 0.01 atm. The trend lines are drawn to guide the eye. Uncertainties are estimated using the propagation of errors method.[4]

Gas solubility

The Freundlich isotherm is an empirical model used to characterize the effect of pressure on the amount of gas adsorbed on mineral surfaces, C_F:[42]

$$C_F = Kp^{\frac{1}{n}} \tag{4.4}$$

where K and n are temperature dependent fitting parameters,[42] and p is the gas pressure. In contrast to models such as the Langmuir isotherm, the Freundlich isotherm does not predict a limit to the adsorbed gas concentration at increasing pressure.[42] Eq. (4.4) has been used to model gas adsorption on TiO_2 nanoparticles in polymer-based nanocomposites, and we use it in this study as well.[11,12,42] The concentration of light gases in rubbery polymers usually obeys Henry's Law:[5]

$$C = k_D p \tag{7.3}$$

where k_D is the Henry's Law constant, and p is the gas pressure. The CO_2, CH_4, and N_2 Freundlich equation parameters for adsorption on MgO nanoparticles and the Henry's law parameters for sorption in unfilled PB are presented in Table 8.4.[12,16] The Henry's Law values listed in Table 8.4 are similar to those reported in the literature.[38]

Table 8.4. Freundlich isotherm parameters for adsorption onto MgO and Henry's law sorption parameters for 1,2-polybutadiene

Penetrant	K, $\frac{\text{cm}^3\left(\text{STP}\right)}{\text{cm}^3\text{MgO atm}^{\frac{1}{n}}}$	n, -	$k_D, \frac{\text{cm}^3(\text{STP})}{\text{cm}^3\text{PB atm}}$ (Matteucci *et al.*)	$k_D, \frac{\text{cm}^3(\text{STP})}{\text{cm}^3\text{PB atm}}$ (Naito *et al.*)
N_2	31 ± 7	2.6 ± 0.2	0.03 ± 0.01	0.04
CH_4	50 ± 8	2.5 ± 0.2	0.21 ± 0.01	0.23
CO_2	63 ± 10	3.4 ± 0.2	0.71 ± 0.06	0.81

Freundlich isotherm parameters were obtained from experimental results at 35 °C. Uncertainties were estimated using the least-squares fit method.[21] Matteucci *et al.* reported Henry's law parameters for light gases in 1,2-polybutadiene at 35 °C[12], while the values reported by Naito et al. were determined at 25 °C.[38]

Gas sorption in polymer crystals is typically negligible as compared to the equivalent amorphous polymer.[43] Therefore, the Henry's law parameter for the amorphous polymer phase in a nanocomposite, $k_{D,A}$, can be estimated as follows:[44]

$$k_{D,A} = \frac{k_D}{1-\phi_{C,0}} \tag{7.4}$$

where $\phi_{C,0}$ (cm^3 crystals / cm^3 polymer) is the crystalline polymer volume fraction of the polymer.

The adsorption isotherms for CO_2, CH_4, and N_2 at 35 °C on MgO nanoparticles are presented in Figure 8.13. The amount of gas sorbed per unit volume of particles is orders of magnitude higher than the amount of gas sorbed per unit volume of polymer. To put these sorption values in perspective, Table 8.5 presents the amounts of various gases sorbed onto the particles and in the polymer. In some cases, the particles sorb more than 2 orders of magnitude more gas per unit volume than the polymer.

Table 8.5. CO_2, CH_4, and N_2 concentration on MgO nanoparticles and PB at 35 °C and 0.9 atm as determined by low pressure sorption experiments.

Penetrant	$C_F, \frac{\text{cm}^3(\text{STP})}{\text{cm}^3\text{MgO}}$	C, $\frac{\text{cm}^3(\text{STP})}{\text{cm}^3\text{PB}}$
N_2	30 ± 4	0.03 ± 0.01
CH_4	48 ± 5	0.18 ± 0.01
CO_2	67 ± 7	0.63 ± 0.06

Uncertainties were estimated using the propagation of errors method.[21]

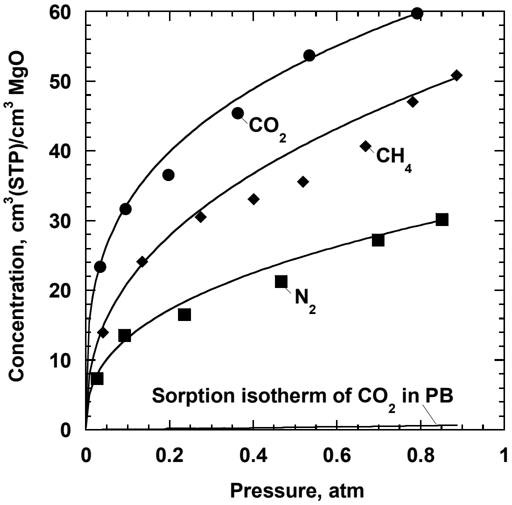

Figure 8.13. Pure gas CO_2 (●), CH_4 (♦), and N_2 (■) adsorption isotherms on MgO and CO_2 sorption isotherm in PB at 35 °C.[30] The CO_2 sorption isotherm was estimated by Eq. (7.3) using the Henry's law parameters from Matteucci *et al.*[30] listed in Table 8.4. The lines are drawn to assist the reader.

Figure 8.14 presents the sorption isotherms for CO_2, CH_4, and N_2 in PB and nanocomposites containing various concentrations of MgO. Gas sorption in the nanocomposites was consistently higher than in unfilled PB, as might be expected given that the particles inherently sorb much more gas than the polymer. If the concentration of gas sorbed by the particles, polymer, and voids in the nanocomposite sample were equal to their pure component values (*i.e.,* if the observed nanocomposite sorption were the additive sum of the contributions of each of the constituent components, weighted according to their concentration), then the gas concentration in the composite, C_C, would be given by:[11]

$$C_C = \left(\phi_F^N K p^{\frac{1}{n}} + \left(1-\phi_F^N\right)\left(1-\phi_C\right) k_{D,A} p \right)\left(1-\phi_V\right) + \frac{p\phi_V}{RT} \tag{7.5}$$

The final term in Eq. (7.5) accounts for the concentration of gas in the void space according to the gas law.[40] Based upon calculations using the parameters in Table 8.4 and the void volume values from Figure 8.8, the sorption of gas on the nanoparticle surface dominates overall nanocomposite sorption in Eq. (7.5). For example, at 1 atm, Eq. (7.5) predicts that the adsorption of CO_2 on the nanoparticle surface would account for approximately 78 % of the gas sorbed into a nanocomposite containing 5 nominal volume percent MgO and 5 volume percent voids.

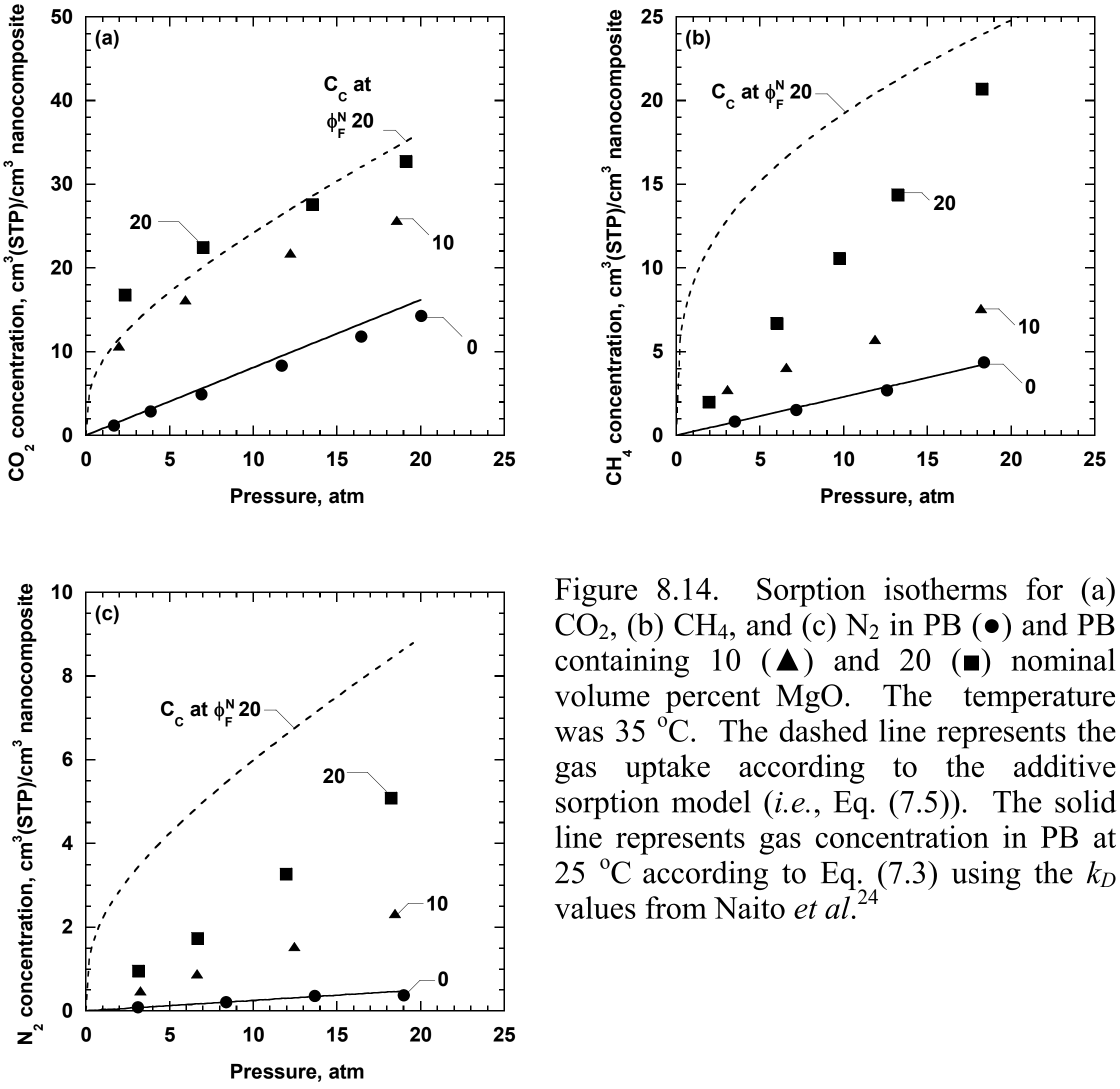

Figure 8.14. Sorption isotherms for (a) CO_2, (b) CH_4, and (c) N_2 in PB (●) and PB containing 10 (▲) and 20 (■) nominal volume percent MgO. The temperature was 35 °C. The dashed line represents the gas uptake according to the additive sorption model (*i.e.*, Eq. (7.5)). The solid line represents gas concentration in PB at 25 °C according to Eq. (7.3) using the k_D values from Naito *et al.*[24]

Qualitatively, the gas uptake increases with increasing particle content, consistent with the trend anticipated by Eq. (7.5). Quantitatively, however, Eq. (7.5) overestimates the CH_4 and N_2 concentration in the nanocomposites, which may be due to wetting of the nanoparticle surface by the polymer.[11,45] Polymers are known to interact with particles and can readily adsorb on particle surfaces.[46] The absorbed polymer chains occupy sorption sites on the particle surface that could otherwise adsorb gas.[45] Eq. (7.5) provides a reasonably good quantitative estimate of CO_2 uptake in the nanocomposites. It is not clear why Eq. (7.5) provides a better estimate of CO_2 uptake than it does of the non-polar gases.

The differences between the gas uptake predicted by Eq. (7.5) and the values presented in Figure 8.14 could come from the extrapolation of the gas sorption on the particles beyond 1 atm. Values of gas uptake of the particles are only available up to 1 atm. Therefore, the estimation of the particle contribution to overall nanocomposite gas uptake depends on the ability for Eq. (4.4) to accurately model the gas sorption behavior at pressures well in excess of the original data. Any inaccuracy in the extrapolation could contribute to the observed differences between the experimental data and Eq. (7.5).

The presence of nanoparticles in PB substantially increases CO_2, CH_4, and N_2 solubility. Figure 8.15 presents gas solubility in PB as a function of MgO particle concentration. Solubility was estimated by linearly interpolating the concentration data (*cf.*, Figure 8.14) to 6 atm and applying Eq. (2.8). The CO_2 solubility is 3.6 $cm^3/(cm^3$(nanocomposite) atm) in films containing 27 nominal MgO volume percent, which is 5.1 times the CO_2 solubility in unfilled PB at 6 atm and 35 ^oC. In films containing 27 nominal volume percent MgO, CH_4 solubility is 1.2 $cm^3/(cm^3$(nanocomposite) atm) at 6 atm and 35 ^oC, which is 6 times the solubility of CH_4 in unfilled PB (*i.e.,* 0.21 cm^3(STP)/(cm^3 atm)). The N_2 solubility in PB films containing 27 nominal volume percent MgO was 0.54 $cm^3/(cm^3$ nanocomposite atm) at 6 atm and 35 ^oC, which is 21 times higher than the N_2 solubility in unfilled PB. The increase in solubility is due mainly to adsorption of gas by the particles. Based on the values in

Table 8.5, the particles (at the conditions presented in Table 8.5) sorb approximately 100, 270, and 1000 times more CO_2, CH_4, and N_2 than unfilled PB, respectively.

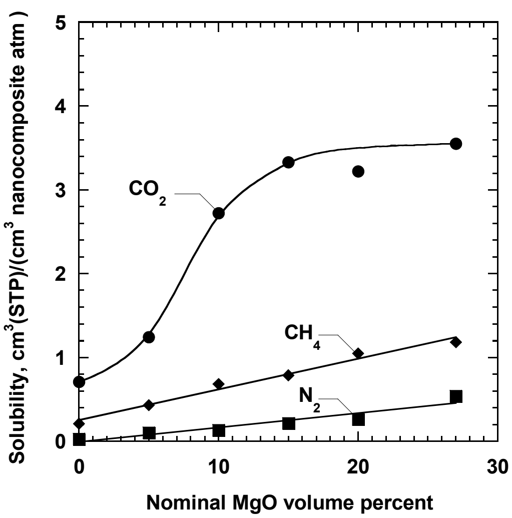

Figure 8.15. Effect of MgO concentration on CO_2 (●), CH_4 (♦), and N_2 (■) solubility at 6 atm and 35 °C. Solubility values were estimated using Eq. (2.8), and concentration values were linearly interpolated to 6 atm. Trend lines are drawn to guide the eye.

Figure 8.16 presents diffusion coefficients calculated using Eq. (2.9), using permeability coefficients from experimental data at 35 °C and $\Delta p = 6$ atm and solubility values from Figure 8.15. Gas diffusion coefficients initially decrease with increasing particle loading, which may be attributed to the presence of impermeable particles, which would increase the tortuosity of the diffusion pathway a penetrant gas would take to cross the film, or to a reduction in bulk polymer chain mobility, as indicated by the increase in T_g as shown in Table 8.1. At particle loadings above 10 nominal volume percent MgO, the gas diffusion coefficients increased with increasing particle concentration. The creation of void space within the composite could contribute to increases in diffusion coefficients with increasing particle content, which corresponds to increasing levels of voids in the samples.

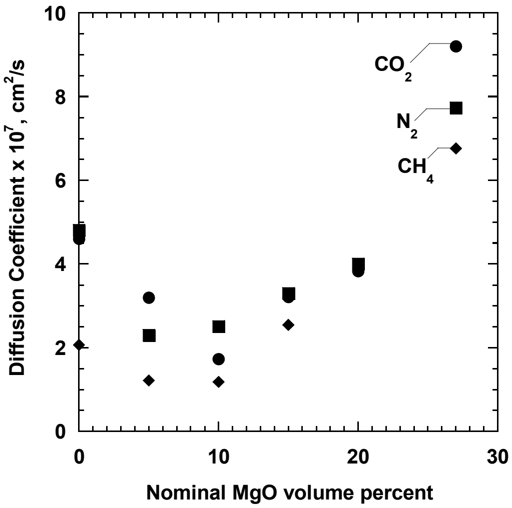

Figure 8.16. Effect of MgO concentration on CO_2 (●), CH_4 (♦), and N_2 (■) diffusion coefficients at $\Delta p = 6$ atm, calculated according to Eq. (2.9). Permeability values used in this calculation are from experimental data at 35 °C and $\Delta p = 6$ atm, and the solubility coefficients are reported in Figure 8.15.

Mixed gas transport

Often pure gas permeability does not accurately predict gas transport properties in mixed gas systems.[5,47] The CO_2/CH_4 mixed gas permeability behavior in PB containing 20 nominal volume percent of MgO is exhibited in Figure 8.17. Fugacity is used to report these results to compensate for any non-ideal behavior in the gas mixtures. Fugacity was determined using the Soave-Redlich-Kwong (SRK) equation based on the total pressure and the mole fraction of CO_2 or CH_4 in the feed and permeate.[48]

As indicated in Figure 8.17, the permeability of both CO_2 and CH_4 increases with increasing CO_2 partial pressure. For example, the CH_4 permeability increases from 30 barrer to 41 barrer as CO_2 fugacity increases from 1.6 atm to 12 atm. Such behavior is often ascribed to plasticization, and it generally occurs when one or more of the penetrant gases is present at sufficiently high concentrations within the polymer matrix to increase polymer chain mobility.[70-72] The pure gas nanocomposite CO_2 permeability also increases with increasing CO_2 fugacity, suggesting that the increase in CH_4 permeability with increasing CO_2 fugacity in the mixture is due to the presence of CO_2.

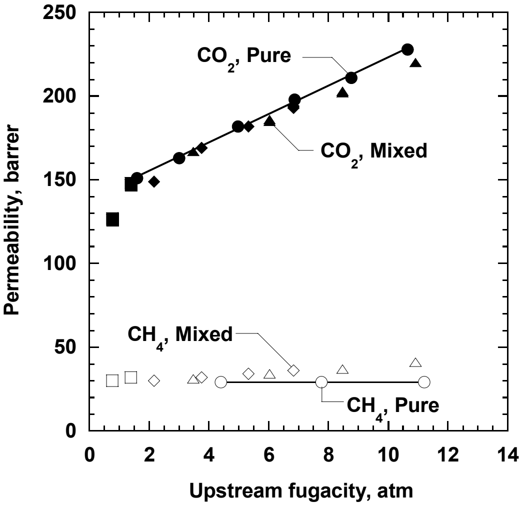

Figure 8.17. CO_2 (●) and CH_4 (○) pure gas permeability coefficients and CO_2 and CH_4 mixed gas permeability coefficients in 1,2-polybutadiene containing 20 nominal volume percent MgO at 35 ^{o}C. The fugacity was varied by varying total feed pressure and by using gas mixtures of the following compositions: 20/80 (■,□), 50/50 (♦,◊), and 80/20 (▲,Δ) (mol/mol) CO_2/CH_4. CO_2 and CH_4 permeability coefficients are represented by the filled and unfilled symbols, respectively. For the pure gas permeability data, the fugacity axis in this plot is the pure gas fugacity. The mixture permeation data for both CO_2 and CH_4 are plotted as a function of CO_2 fugacity in the feed gas mixture. Trend lines are drawn to assist the reader.

Figure 8.18 presents pure and mixed gas CO_2/CH_4 selectivity as a function of upstream CO_2 fugacity. In the pure gas case, selectivity increases with increasing CO_2 fugacity since CO_2 permeability increases with increasing CO_2 fugacity. In the mixed gas case, the selectivity is lower than the pure gas case. Moreover, the selectivity increases with increasing CO_2 fugacity up to about 4 atm, primarily because CH_4 permeability is approximately constant over this range of CO_2 fugacity values, but CO_2 permeability increases steadily, as shown in Figure 8.17. At higher CO_2 fugacity values, the mixed gas selectivity reaches a maximum and decreases slightly with increasing CO_2 fugacity. This result occurs because CH_4 permeability begins to increase with increasing CO_2 fugacity, suggesting the onset of CO_2-induced plasticization at CO_2 fugacities beyond about 4 atm. The increase in selectivity with increasing CO_2 fugacity at low CO_2 fugacity values may be due to more favorable adsorption of CO_2 on the particles in the gas mixture (*i.e.,* an increase in the CO_2/CH_4 solubility selectivity) as CO_2 fugacity increases, though this hypothesis is speculative at this time and has not been proven.

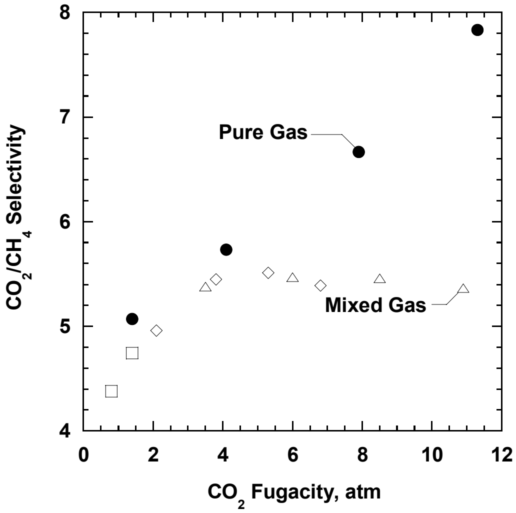

Figure 8.18. Effect of upstream CO_2 fugacity on pure and (●) mixed gas CO_2/CH_4 selectivity in 1,2-polybutadiene containing 20 nominal volume percent MgO at 35 °C. The CO_2 fugacity was varied by varying total feed pressure and by using gas mixtures of the following compositions: 20/80 (□), 50/50 (◊), and 80/20 (Δ) (mol/mol) CO_2/CH_4. The mixture selectivity data are plotted as a function of CO_2 fugacity in the feed gas mixture. The pure gas selectivity value at 1.4 atm is calculated from the pure gas CH_4 permeability value at 4.1 atm, since pure gas CH_4 permeability is pressure independent.

CONCLUSIONS

MgO filled PB nanocomposites exhibited higher permeability than the unfilled polymer. As particle loading increased, nanocomposite density deviated from the additive density model, which indicated that voids were present in the nanocomposite films. As the void concentration increased, gas permeability increased. The increase in permeability was partially due to increases in gas solubility coefficients that occurred as MgO concentration in the nanocomposites increased. Diffusion coefficients were lower than in the unfilled polymer at low particle loading, but increased at higher loadings to levels that were higher than the unfilled polymer at the highest particle loadings considered. For instance, in a PB film containing 27 nominal volume percent MgO, about 60 % of the CH_4 permeability increase, relatively to an unfilled sample, can be attributed to an increase in solubility, while the remaining 40 % of the increase can be attributed to an increase in the methane diffusion coefficient.

REFERENCES

(1) Baker, R. W., Future directions of membrane gas separation technology, *Industrial and Engineering Chemistry Research* **2002**, *41*, 1393-1411.

(2) Powell, C. E.; Qiao, G. G., Polymeric CO_2/N_2 gas separation membranes for the capture of carbon dioxide from power plant flue gases, *Journal of Membrane Science* **2006**, *279*, 1-49.

(3) Freeman, B. D., Basis of permeability/selectivity tradeoff relations in polymeric gas separation membranes, *Macromolecules* **1999**, *32*, 375-380.

(4) Robeson, L. M., Correlation of separation factor versus permeability for polymeric membranes, *Journal of Membrane Science* **1991**, *62*, 165-185.

(5) Matteucci, S.; Yampol'skii, Y. P.; Freeman, B. D.; Pinnau, I. *Transport of gases and vapors in glassy and rubbery polymers*, In Materials Science of Membranes for Gas and Vapor Separations; Yampol'skii, Y. P.; Freeman, B. D.; Pinnau, I., Eds.; John Wiley and Sons: London, 2006; pp 1-48.

(6) Park, H. B.; Jung, C. H.; Lee, Y. M.; Hill, A. J.; Pas, S. J.; Mudie, S. T.; van Wagner, E.; Freeman, B. D.; Cookson, D. J., Polymers with cavities tuned for fast selective transport of small molecules and ions, *Science* **2007**, *318*, 254-258.

(7) Vu, D. Q.; Koros, W. J.; Miller, S. J., Mixed matrix membranes using carbon molecular sieves I. Preparation and experimental results, *Journal of Membrane Science* **2003**, *211*, 311-334.

(8) He, Z.; Pinnau, I.; Morisato, A., Nanostructured poly(4-methyl-2-pentyne)/silica hybrid membranes for gas separation, *Desalination* **2002**, *146*, 11-15.

(9) Merkel, T. C.; Freeman, B. D.; Spontak, R. J.; He, Z.; Pinnau, I.; Meakin, P.; Hill, A. J., Ultrapermeable, reverse-selective nanocomposite membranes, *Science* **2002**, *296*, 519-522.

(10) Merkel, T. C.; He, Z.; Pinnau, I.; Freeman, B. D.; Hill, A. J.; Meakin, P., Effect of nanoparticles on gas sorption and transport in poly(1-trimethylsilyl-1-propyne), *Macromolecules* **2003**, *36*, 6844-6855.

(11) Matteucci, S.; Kusuma, V.; Sanders, D.; Swinnea, S.; Freeman, B. D., Gas transport in TiO_2 nanoparticle filled poly(1-trimethylsilyl-1-propyne), *Journal of Membrane Science* **In Press**.

(12) Matteucci, S.; Kusuma, V. A.; Swinnea, S.; Freeman, B. D., Light gas permeability, solubility and diffusion in 1,2-polybutadiene containing brookite nanoparticles, *Polymer* **Submitted**.

(13) Barsema, J. N.; Balster, J.; Jordan, V.; van der Vegt, N. F. A.; Wessling, M., Functionalized carbon molecular sieve membranes containing Ag-nanoclusters, *Journal of Membrane Science* **2003**, *219*, 47-57.

(14) Kang, Y. S.; Kang, S. W.; Kim, H.; Kim, J. H.; Won, J.; Kim, C. K.; Char, K., Interaction with olefins of the partially polarized surface of silver nanoparticles activated by *p*-benzoquinone and its implications for facilitated olefin transport, *Advanced Materials* **2007**, *19*, 475-479.

(15) Paul, D. R.; Kemp, D. R., Diffusion Time Lag in Polymer Membranes Containing Adsorptive Fillers, *Journal of Polymer Science, Polymer Symposia* **1973**, *41*, 79-93.

(16) Matteucci, S.; Kusuma, V.; Kelman, S.; Freeman, B. D., Gas transport properties in MgO nanoparticle filled poly(1-trimethylsilyl-1-propyne), *Polymer* **Submitted**.

(17) Mekhemer, G. A. H.; Halaway, S. A.; Mohamed, M. A.; Zaki, M. I., Qualitative and quantitative assessments of acid and base sites exposed on polycrystalline MgO surfaces: Thermogravimetric, calorimetric, and in-situ FTIR spectroscopy study combination, *Journal of Physical Chemistry Part B* **2004**, *108*, 13379-13386.

(18) Stark, J. V.; Park, D. G.; Lagadic, I.; Klabunde, K. J., Nanoscale metal oxide particles/clusters as chemical reagents. Unique surface chemistry on magnesium oxide as shown by enhanced adsorption of acid gases (sulfur dioxide and carbon dioxide) and pressure dependence, *Chemistry of Materials* **1996**, *8*, 1904-1912.

(19) Matteucci, S.; van Wagner, E.; Swinnea, S.; Freeman, B. D.; Sakaguchi, T.; Masuda, T., Desilylation of substituted polyacetylenes in the presence of nanoparticles, *Macromolecules* **2007**, *40*, 3337-3347.

(20) Obata, Y.; Tosaki, C.; Ikeyama, M., Bulk properties of syndiotactic 1,2-polybutadiene. I. Thermal and viscoelastic properties, *Polymer Journal* **1975**, *7*, 207-216.

(21) Bevington, P. R.; Robinson, D. K. Data Reduction and Error Analysis for the Physical Sciences, 3rd ed.; McGraw-Hill, Inc.: New York, 2003.

(22) Dhoot, S. N.; Freeman, B. D.; Stewart, M.; Hill, A. J., Sorption and transport of linear alkane hydrocarbons in biaxially oriented poly(ethylene terephthalate), *Journal of Polymer Science Part B: Polymer Physics* **2001**, *39*, 1160-1172.

(23) Rittigstein, P.; Torkelson, J. M., Polymer-nanocomposite interfacial interactions in polymer nanocomposites: Confinement effects on glass transition temperature and suppression of physical aging, *Journal of Polymer Science Part B: Polymer Physics* **2006**, *44*, 2935-2943.

(24) Tasagaropoulos, G.; Eisenberg, A., Dynamic mechanical study of the factors affecting the two glass transition behavior of filled polymers. Similarities and differences with random ionomers, *Macromolecules* **1995**, *28*, 6067-6077.

(25) Takahashi, S.; Paul, D. R., Gas permeation in poly(ether imide) nanocomposite membranes based on surface-treated silica. Part 1: Without chemical coupling to matrix, *Polymer* **2006**, *47*, 7519-7534.

(26) Lape, N. K.; Nuxoll, E. E.; Cussler, E. L., Polydisperse flakes in barrier films, *Journal of Membrane Science* **2004**, *236*, 29-37.

(27) Merkel, T. C.; Freeman, B. D.; Spontak, R. J.; He, Z.; Pinnau, I.; Meakin, P.; Hill, A. J., Sorption, transport, and structural evidence for enhanced free volume in poly(4-methyl-2-pentyne)/fumed silica nanocomposite membranes, *Chemistry of Materials* **2003**, *15*, 109-123.

(28) Sengupta, R.; Bandyopadhyay, A.; Sabharwal, S.; Chaki, T. K.; Bhomick, A. K., Polyamide-6,6/in situ silica hybrid nanocomposites by sol-gel technique: synthesis, characterization, and properties, *Polymer* **2005**, *46*, 3343-3354.

(29) Ma, D.; Akpalu, Y. A.; Li, Y.; Siegel, R. W.; Schadler, L. S., Effect of titania nanoparticles on the morphology of low density polyethylene, *Journal of Polymer Science Part B: Polymer Physics* **2005**, *43*, 488-497.

(30) Yang, H.; Bhimaraj, P.; Yang, L.; Siegel, R. W.; Schadler, L. S., Crystal growth in alumina/poly(ethylene terephthalate) nanocomposite films, *Journal of Polymer Science Part B: Polymer Physics* **2007**, *45*, 747-757.

(31) Olkin, I.; Gleser, L. J.; Derman, C. Probability Models and Applications, 2nd ed.; Macmillan College Publishing Company: New York, 1980.

(32) Weibull, W., A statistical distribution function of wide applicability, *Journal of Applied Mechanics* **1951**, *18*, 293-297.

(33) Mackay, M. E.; Dao, T. T.; Tuteja, A.; Ho, D. L.; Van Horn, B.; Kim, H.-C.; Hawker, C. J., Nanoscale effects leading to non-Eistein-like decrease in viscosity, *Nature Materials* **2003**, *2*, 762-766.

(34) Gestoso, P.; Nicol, E.; Doxastakis, M.; Theodorou, D. N., Atomistic Monte Carlo simulation of polybutadiene isomers: *cis*-1,4-polybutadiene and 1,2-polybutadiene, *Macromolecules* **2003**, *36*, 6925-6938.

(35) Osman, M. A.; Atallah, A., interparticle and particle-matrix interactions in polyethylene reinforcement of viscoelasticity, *Polymer* **2005**, *46*, 9476-9488.

(36) Hill, R. J., Diffusive permeability and selectivity of nanocomposite membranes, *Industrial and Engineering Chemistry Research* **2006**, *45*, 6890-6898.

(37) Wijmans, J. G.; Baker, R. W. *The solution-diffusion model: A unified approach to membrane permeation*, In Materials Science of Membranes for Gas and Vapor Separation; Yampol'skii, Y. P.; Pinnau, I.; Freeman, B. D., Eds.; John Wiley & Sons: London, 2006; pp 159-190.

(38) Naito, Y.; Kamiya, Y.; Terada, K.; Mizoguchi, K.; Wang, J.-S., Pressure dependence of gas permeability in a rubbery polymer, *Journal of Applied Polymer Science* **1996**, *61*, 945-950.

(39) Lindbrathen, A.; Hagg, M.-B., Glass membranes for purification of aggressive gases: Part II. Adsorption measurements and diffusion coefficient estimations, *Journal of Membrane Science* **2005**, *259*, 154-160.

(40) Bird, R. B.; Stewart, W. E.; Lightfoot, E. L. Transport Phenomena, 2nd ed.; John Wiley & Sons: New York, 2002.

(41) Breck, D. W. Zeolite Molecular Sieves: Structure, Chemistry, and Use; John Wiley & Sons: New York, 1974.

(42) Do, D. D. Adsorption Analysis: Equilibria and Kinetics; Imperial College Press: London, 1998; Vol. 2.

(43) Weinkauf, D. H.; Paul, D. R. *Effects of structural order on barrier properties*, In Barrier Polymers and Structures; Koros, W. J., Ed.; American Chemical Society: Washington, D.C., 1990; pp 60-91.

(44) Michaels, A. S.; Bixler, H. J., Solubility of gases in polyethylene, *Journal of Polymer Science* **1961**, *50*, 393-412.

(45) Barrer, R. M.; Barrie, J. A.; Rogers, M. G., Heterogeneous membranes: Diffusion in filled rubber, *Journal of Polymer Science, Part A: Polymer Chemistry* **1963**, *1*, 2565-2586.

(46) Kraus, G. *Interactions between elastomers and reinforcing fillers*, In Reinforcement of Elastomers; Kraus, G., Ed.; John Wiley & Sons: New York, 1965; pp 125-152.

(47) Bos, A.; Punt, I. G. M.; Wessling, M.; Strathmann, H., Suppression of CO_2-plasticization by semiinterpenetrating polymer network formation, *Journal of Polymer Science: Part B: Polymer Physics* **1998**, *36*, 1547-1556.

(48) Raharjo, R. D.; Lin, H.; Sanders, D. F.; Freeman, B. D.; Kalakkunnath, S.; Kalika, D. S., Relation between network structure and gas transport in crosslinked poly(propylene glycol diacrylate), *Journal of Membrane Science* **2006**, *283*, 253-265.

(49) Visser, T.; Koops, G. H.; Wessling, M., On the subtle balance between competitive sorption and plasticization effects in asymmetric hollow fiber gas separation membranes, *Journal of Membrane Science* **2005**, *252*, 265-277.

(50) Staudt-Bickel, C.; Koros, W. J., Improvement of CO_2/CH_4 separation characteristics of polyimides by chemical crosslinking, *Journal of Membrane Science* **1999**, *155*, 145-154.

(51) Koros, W. J.; Hellums, M. W. *Transport Properties*, In Encyclopedia of Polymer Science and Engineering, 2nd ed.; John Wiley and Sons: New York, 1989; Vol. Suppl. Vol., pp 724-802.

Chapter 9: Conclusions and Recommendations

The gas transport and morphological properties of nanoparticle filled polymers has been investigated. Below is a brief summary of the conclusions from Chapters 4 through 8, as well as recommendations for future work.

CONCLUSIONS

Particle dispersion

Atomic force microscopy and transmission electron microscopy demonstrated the extent of nanoparticle dispersion in poly(1-trimethylsilyl-1-propyne) and 1,2-polybutdiene filled with periclase and brookite nanoparticles. Some of the nanoparticles in the brookite filled films and 1,2-polybutdiene filled with periclase dispersed into aggregates with effective diameters on the order nanometers. Weibull distributions characterized the particle size distributions from atomic force tapping mode phase profiles. These aggregates were estimated to have interaggregate spacings below 10 nanometers, which are similar to the dimensions of various polymer dimensions (*i.e.,* persistence length and radius of gyration). These nanoparticle filled materials also exhibited aggregates that were on the order of microns in characteristic dimensions in addition to the nanometer sized aggregates. Periclase filled poly(1-trimethylsilyl-1-propyne) only exhibited the micron sized nanoparticle agglomerates.

Density measurements indicated that dispersing nanoparticles into polymer matrixes also created a substantial amount of void space within the films, except at very low loadings of brookite in poly(1-trimethylsilyl-1-propyne). The two microscopic techniques used in these studies did not conclusively demonstrate the location of the voids, although assignments of void space to interparticle spacing or at the polymer-particle interface are consistent with the literature.[1,2] The void space increased with increasing particle loading, and in some cases (*i.e.,* nanoparticle filled poly(1-trimethylsilyl-1-propyne)) the voids comprised over half of the nanocomposite volume.

Gas transport properties

Nanocomposite light gas permeability increased with increasing particle loading, regardless of polymer or particle chemistry. The nanocomposite permeability behavior for filled poly(1-trimethylsilyl-1-propyne) is in good agreement with Bruggeman's model for a highly permeable dispersed phase, whereas for permeability in filled 1,2-polybutadiene Bruggeman's model predicts the correct trend for permeability, but the values predicted by the model are much lower than those observed experimentally. The films were defect free as demonstrated by comparing the permeability pressure dependence and ideal gas selectivity to those that are predicted for porous materials (*i.e.,* Knudsen or Poiseuille flow regimes). The permeability behavior has been largely attributed to an increase in solubility and diffusion coefficients. The increase in diffusion coefficients was ascribed to diffusion in the nanocomposite void space. Solubility increased with increasing particle loading, and the extent to which it increased permeability varied with the polymer-particle system.

Nanoparticle reactivity

The brookite nanoparticles were demonstrated to be inert in the environments tested in this research (*i.e.,* dispersed in toluene or the polymers, exposed to high pressure light gases). Periclase did react with water to form brucite. Brucite was able to remove trimethylsilyl groups from select polymers and model compounds. Poly(1-phenyl-2-[(*p*-trimethylsilyl)phenyl]acetylene) desilylated by the MgO particles was insoluble in several solvents that dissolve the unfilled polymer.

RECOMMENDATIONS FOR FUTURE WORK

Mixed gas sorption and permeation

The results from our studies suggest that the particles and nanocomposites may interact with gases differently depending on the penetrant gas, particle surface chemistry and the polymer matrix. It would be very informative to determine how gases compete in a mixed gas environment for sorption sites on nanoparticle surfaces, and how this may vary with surface chemistry, lattice structure and/or adsorbent partial pressure. Although there is substantial literature for competitive sorption on mineral surfaces at low pressures (*i.e.,* < 0.1 atm),[3,4] a systematic study of this competitive sorption at pressures and temperatures that are relevant to potential membrane applications would facilitate the selection of nanoparticles in the future.

Currently, pure gas experiments do not necessarily give a full view of the complexity or capabilities of mineral filled nanocomposites. Mixed gas sorption and permeation experiments on nanocomposite materials may demonstrate the importance of nanoparticle adsorption of gases to permeability and true selectivity. Any competition between penetrant gases or between penetrants and the polymer for nanoparticle sorption sites could significantly influence the outcome of the nanocomposite mixed gas behavior, and such competition may only be observed in mixed gas experiments.

Particle size

There is currently a disconnect between gas transport behavior in polymeric based materials filled with particles that are well below 100 nanometers in diameter and those filled with particles with characteristic diameters on the order of microns or larger. In nanocomposites, permeability can increase or decrease depending on particle orientation,[5] dispersion,[6] or interaction with the polymer,[7] whereas permeability in composites containing micron scale particles has been shown to decrease with increasing particle loading.[8]

It would be useful to determine how particle size influences gas transport properties. Both periclase and brookite nanoparticles are commercially available in a number of particle sizes, which would allow for the study of how surface area or interparticle spacing may affect gas transport properties. Nanoparticle surface area may influence the concentration of gas that the nanoparticles can adsorb per volume, which may, in turn, render the particle phase adsorption behavior insignificant in comparison to the polymer phase. Particle size may also influence the void volume concentration in nanocomposites by either limiting the surface area where polymer-particle dewetting occurs, or by increasing the size of the interparticle voids in highly compact nanoparticle aggregates. However, if the particles are individually dispersed, increasing the particle size would be expected to increase the interparticle distance. In either case, there is significant need to understand the effects of filler size on gas transport properties in order to facilitate the efficient design of mixed matrix membranes.

Particle surface chemistry

The surface science and catalyst communities have dedicated extensive amounts of time and effort to characterize the interaction of various metal and metal oxides with permanent gases.[4,9-11] Many of these metallic materials have recently become available commercially as nanoparticles. It is feasible to use alternative nanoparticles to influence the sorption characteristics of penetrant gases in a similar many as has been proposed for acid gas-basic nanoparticle interactions. For instance, silicon dioxide nanoparticles have an acidic surface chemistry,[4] which may act to repel acid gases. Incorporating these particles into an appropriate polymer may increase the non-polar gas/acid gas selectivity. The study of how nanoparticle surface chemistry affects nanocomposite gas transport properties is a necessary step in understanding gas transport in heterogeneous materials.

REFERENCES

(1) Takahashi, S.; Paul, D. R., Gas permeation in poly(ether imide) nanocomposite membranes based on surface-treated silica. Part 1: Without chemical coupling to matrix, *Polymer* **2006**, *47*, 7519-7534.

(2) Hill, R. J., Diffusive permeability and selectivity of nanocomposite membranes, *Industrial and Engineering Chemistry Research* **2006**, *45*, 6890-6898.

(3) Outka, D. A.; Madix, R. J., The Oxidation of Carbon Monoxide on the Au(110) Surface, *Surface Science* **1987**, *179*, 351-360.

(4) Auroux, A.; Gervasini, A., Macrocalorimetric study of the acidity and basicitiy of metal oxide surfaces, *Journal of Physical Chemistry* **1990**, *94*, 6371-6379.

(5) Lape, N. K.; Nuxoll, E. E.; Cussler, E. L., Polydisperse flakes in barrier films, *Journal of Membrane Science* **2004**, *236*, 29-37.

(6) Qiu, J.; Zheng, J.-M.; Peinemann, K.-V., Gas transport properties in a novel poly(trimethylsilylpropyne) composite membrane with nanosized organic filler trimethylsilylglucose, *Macromolecules* **2006**, *39*, 4093-4100.

(7) Merkel, T. C.; Freeman, B. D.; Spontak, R. J.; He, Z.; Pinnau, I.; Meakin, P.; Hill, A. J., Ultrapermeable, reverse-selective nanocomposite membranes, *Science* **2002**, *296*, 519-522.

(8) Barrer, R. M.; Barrie, J. A.; Rogers, M. G., Heterogeneous membranes: Diffusion in filled rubber, *Journal of Polymer Science, Part A: Polymer Chemistry* **1963**, *1*, 2565-2586.

(9) Backx, C.; De Groot, C. P. M.; Biloen; Sachtler, W. M. H., Interaction of O_2, CO_2, CO, C_2H_4, and C_2H_4O with Ag(100), *Surface Science* **1983**, *128*, 81-103.

(10) Barteau, M. A.; Madix, R. J., The Adsorption of CO, O_2, and H_2 on Pt(100)-(5x20), *Surface Science* **1981**, *102*, 99-117.

(11) Carnes, C. L.; Klabunde, K. J., Unique chemical reactivities of nanocrystalline metal oxides toward hydrogen sulfide, *Chemistry of Materials* **2002**, *14*, 1806-1811.

Bibliography

MSDS Monoethanolamine, **2004**, Equistar, pp 1-9

Ajjou, A. N.; Alper, H., Catalitic oxidation of polybutadienes based on a Wicker-type reaction, *Macromolecules* **1996**, *29*, 5072-5074.

Atteya, M.; Klabunde, K. J., Nanoscale metal oxide particles as chemical reagents. Heats of adsorption of heteroatom-containing organics on heat-treated magnesium oxide samples of various surface areas, *Chemistry of Materials* **1991**, *3*, 182-187.

Auroux, A.; Gervasini, A., Macrocalorimetric study of the acidity and basicity of metal oxide surfaces, *Journal of Physical Chemistry* **1990**, *94*, 6371-6379.

Backx, C.; De Groot, C. P. M.; Biloen; Sachtler, W. M. H., Interaction of O_2, CO_2, CO, C_2H_4, and C_2H_4O with Ag(100), *Surface Science* **1983**, *128*, 81-103.

Baker, R. W., Future directions of membrane gas separation technology, *Industrial and Engineering Chemistry Research* **2002**, *41*, 1393-1411.

Baker, R. W. Membrane Technology and Applications, 2nd ed.; McGraw-Hill: New York, 2004.

Barrer, R. M.; Barrie, J. A.; Rogers, M. G., Heterogeneous membranes: Diffusion in filled rubber, *Journal of Polymer Science, Part A: Polymer Chemistry* **1963**, *1*, 2565-2586.

Barsema, J. N.; Balster, J.; Jordan, V.; van der Vegt, N. F. A.; Wessling, M., Functionalized carbon molecular sieve membranes containing Ag-nanoclusters, *Journal of Membrane Science* **2003**, *219*, 47-57.

Barteau, M. A.; Madix, R. J., The adsorption of CO, O_2, and H_2 on Pt(100)-(5x20), *Surface Science* **1981**, *102*, 99-117.

Bartik, T.; Happ, B.; Iglewsky, M.; Bandmann, H.; Boese, R.; Helmbach, P.; Hoffmann, T.; Wenschuh, E., Synthesis and characterization of bis(phosphine)nickel(0) complexes containing nonsymmetrically substituted acetylenes, *Organometallics* **1992**, *11*, 1235-1241.

Berchtold, K. A.; Young, J. S.; Dudeck, K. W.; Acquaviva, J.; Onorato, F.; Hopkins, S. D. In *Fifth Annual Conference on Carbon Capture & Sequestration*: Alexandria, VA, 2006.

Beruto, D. T.; Botter, R., Liquid-like H_2O adsorption layers to catalyze the $Ca(OH)_2/CO_2$ solid-gas reaction and to form a non-protective solid product layer at 20^oC, *Journal of the European Ceramic Society* **2000**, *20*, 497-503.

Bevington, P. R.; Robinson, D. K. Data Reduction and Error Analysis for the Physical Sciences, 2nd ed.; McGraw-Hill, Inc.: New York, 1992.

Bird, R. B.; Stewart, W. E.; Lightfoot, E. L. Transport Phenomena, 2nd ed.; John Wiley & Sons: New York, 2002.

Bondar, V.; Freeman, B. D.; Pinnau, I., Gas transport properties of poly(ether-b-amide) segmented block copolymers, *Journal of Polymer Science Part B: Polymer Physics* **2000**, *38*, 2051-2062.

Bondar, V. I.; Freeman, B. D.; Pinnau, I., Gas sorption and characterization of poly(ether-b-amide) segmented block copolymers, *Journal of Polymer Science: Part B: Polymer Physics* **1999**, *37*, 2463-2475.

Bos, A.; Punt, I. G. M.; Wessling, M.; Strathmann, H., Suppression of CO_2-plasticization by semiinterpenetrating polymer network formation, *Journal of Polymer Science: Part B: Polymer Physics* **1998**, *36*, 1547-1556.

Bouma, R. H. B.; Checchetti, A.; Chidichimo, G.; Drioli, E., Permeation through a heterogeneous membrane: The effect of the dispersed phase, *Journal of Membrane Science* **1997**, *128*, 141-149.

Brandon, D.; Kaplan, W. D. Microstructural Characterization of Materials; John Wiley and Sons: New York, 1999.

Breck, D. W. Zeolite Molecular Sieves: Structure, Chemistry, and Use; John Wiley & Sons: New York, 1974.

Bryant, G.; Martin, S.; Budi, A.; van Megen, W., Accurate measurement of small polydispersities in colloidal suspensions, *Langmuir* **2003**, *19*, 616-621.

Carnes, C. L.; Klabunde, K. J., Unique chemical reactivities of nanocrystalline metal oxides toward hydrogen sulfide, *Chemistry of Materials* **2002**, *14*, 1806-1811.

Chaudhary, D. S.; Prasad, R.; Gupta, R. K.; Bhatacharya, S. N., Clay intercalation and influence on crystallinity of EVA-based clay nanocomposites, *Thermochimica Acta* **2005**, *433*, 187-195.

Chien, J. C. W.; Wnek, G. E.; Karasz, F. E.; Hirsch, J. A., Electrically conducting acetylene-methylacetylene copolymers. Synthesis and properties, *Macromolecules* **1981**, *14*, 479-485.

Colthup, N. B.; Daly, L. H.; Wiberly, S. E. Introduction to Infrared and Raman Spectroscopy, 2nd ed.; Academic Press: New York, 1975.

Coluccia, S.; Boccuzzi, F.; Ghiotti, G.; Morterra, C., Infrared study of hydrogen adsorption on MgO, CaO, and SrO, *Journal of the Chemical Society, Faraday Transactions 1: Physical Chemistry in Condensed Phases* **1982**, *78*, 2111-2119.

De Sitter, K.; Winberg, P.; D'Haen, J.; Dotremont, C.; Leysen, R.; Martens, J. A.; Mullens, S.; Maurer, F. H. J.; Vankelecom, I. F. J., Silica filled poly(1-trimethylsilyl-1-propyne) nanocomposite membranes: Relation between gas transport and structural characteristics, *Journal of Membrane Science* **2006**, *278*, 83-91.

Dhoot, S. N.; Freeman, B. D.; Stewart, M.; Hill, A. J., Sorption and transport of linear alkane hydrocarbons in biaxially oriented poly(ethylene terephthalate), *Journal of Polymer Science Part B: Polymer Physics* **2001**, *39*, 1160-1172.

Do, D. D. Adsorption Analysis: Equilibria and Kinetics; Imperial College Press: London, 1998; Vol. 2.

Erdohelyi, A.; Anneser, E.; Bauer, T.; Stephan, K.; Borgmann, D.; Wedler, G., Interaction of carbon dioxide and oxygen on iron films at 273 K, *Surface Science* **1990**, 57-66.

Ferrari, A. M.; Soave, R.; D'Ercole, A.; Pisani, C.; Giamello, E.; Pacchioni, G., Theoretical characterization of charge-transfer reactions between N_2 and O_2 molecules and paramagnetic oxygen vacancies on the MgO surface, *Surface Science* **2001**, 83-97.

Freeman, B. D., Basis of permeability/selectivity tradeoff relations in polymeric gas separation membranes, *Macromolecules* **1999**, *32*, 375-380.

Freeman, B. D.; Pinnau, I., Separation of gases using solubility-selective polymers, *Trends in Polymer Science* **1997**, *5*, 167-173.

Freeman, B. D.; Pinnau, I. *Polymeric materials for gas separations*, In Polymer Membranes for Gas and Vapor Separation, ACS Symposium Series; Freeman, B. D.; Pinnau, I., Eds.: Washington, D.C., 1999; Vol. 733, pp 1-27.

Freund, H.-J.; Roberts, M. W., Surface chemistry of carbon dioxide, *Surface Science Reports* **1996**, *25*, 225-273.

Fujita, S.-I.; Takezawa, N., Difference in the selectivity of CO and CO_2 methanation reactions, *Chemical Engineering Journal* **1997**, *68*, 63-68.

Gerstein, M.; Tsai, J.; Levitt, M., The volume of atoms on the protein surface: Calculated from simulation, using Voronoi Polyhedra, *Journal of Molecular Biology* **1995**, *249*, 955-966.

Gestoso, P.; Nicol, E.; Doxastakis, M.; Theodorou, D. N., Atomistic Monte Carlo simulation of polybutadiene isomers: *cis*-1,4-polybutadiene and 1,2-polybutadiene, *Macromolecules* **2003**, *36*, 6925-6938.

Ghosal, K.; Freeman, B. D., Gas separation using polymer membranes: An overview, *Polymers for Advanced Technology* **1994**, *5*, 673-697.

Gregg, S.; Ramsay, J. D., Adsortpion of carbon dioxide by magnesia studied by use of infrared and isotherm measurements, *Journal of Chemical Society A* **1970**, 2784-2787.

Harnau, L.; Winkler, R. G.; Reineker, P., Comment on "Chain motion in an unentangled polyethylene melt: A critical test of the Rouse Model by molecular dynamics simulations and neutron spin echo spectroscopy:, *Physical Review Letters* **1999**, *82*, 2408.

He, Z.; Pinnau, I.; Morisato, A., Nanostructured poly(4-methyl-2-pentyne)/silica hybrid membranes for gas separation, *Desalination* **2002**, *146*, 11-15.

Helmy, R.; Wenslow, R. W.; Fadeev, A. Y., Reaction of organosilicon hydrides with solid surfaces: An example of surface-catalyzed self-assembly, *Journal of the American Chemical Society* **2004**, *126*, 7595-7600.

Henglein, F. A.; Scheinost, K., Substituted silyl derivatives of pectin and glucose, *Makromolekulare Chemie* **1956**, *21*, 59-73.

Henis, J. M. S. *Commercial and practical aspects of gas separation membranes*, In Polymeric Gas Separation Membranes; Paul, D. R.; Yampolskii, Y. P., Eds.; CRC Press: Boca Raton, 1994; pp 441-512.

Hill, R. J., Diffusive permeability and selectivity of nanocomposite membranes, *Industrial and Engineering Chemistry Research* **2006**, *45*, 6890-6898.

Horiuchi, T.; Hiroaki, H.; Takehisa, F.; Kubo, Y.; Horio, M.; Suzuki, K.; Mori, T., Effect of added basic metal oxides on CO_2 adsorption on alumnia at elevated temperatures, *Applied Catalysis A: General* **1998**, *167*, 195-202.

Houghton, J. T. Climate Change 2001: The Scientific Basis; Cambridge University Press: Cambridge, 2001.

Iraqi, A.; Cole-Hamilton, D. J., Preparation and reactivity of polyepoxides and polyketones: Catalytic oxidation of polybutadienes, *Journal of Material Chemistry* **1992**, *2*, 183-190.

Joensen, F.; Rostrup-Nielsen, J. R., Conversion of hydrocarbons and alcohols for fuel cells, *Journal of Power Sources* **2002**, *105*, 195-201.

Kang, Y. S.; Kang, S. W.; Kim, H.; Kim, J. H.; Won, J.; Kim, C. K.; Char, K., Interaction with olefins of the partially polarized surface of silver nanoparticles activated by *p*-benzoquinone and its implications for facilitated olefin transport, *Advanced Materials* **2007**, *19*, 475-479.

Kohl, A.; Nielsen, R. Gas Purification, 5th ed.; Gulf Publishing Company: Houston, 1997.

Koper, O. B.; Lagadic, I.; Volodin, A. M.; Klabunde, K. J., Alkaline-earth oxide nanoparticles obtained by aerogel methods. Characterization and rational for unexpectedly high surface chemical reactivities, *Chemistry of Materials* **1997**, *9*, 2468-2480.

Koros, W. J.; Chan, A. H.; Paul, D. R., Sorption and transport of various gases in polycarbonate, *Journal of Membrane Science* **1977**, *2*, 165-190.

Koros, W. J.; Hellums, M. W. *Transport Properties*, In Encyclopedia of Polymer Science and Engineering, 2nd ed.; John Wiley and Sons: New York, 1989; Vol. Suppl. Vol., pp 724-802.

Kraus, G. *Interactions between elastomers and reinforcing fillers*, In Reinforcement of Elastomers; Kraus, G., Ed.; John Wiley & Sons: New York, 1965; pp 125-152.

Krook, M.; Morgan, G.; Hedenqvist, M. S., Barrier and mechanical properties of injection molded montromorillonite/polyesteramide nanocomposites, *Polymer Engineering and Science* **2005**, *45*, 135-141.

Lape, N. K.; Nuxoll, E. E.; Cussler, E. L., Polydisperse flakes in barrier films, *Journal of Membrane Science* **2004**, *236*, 29-37.

Leclerc, M.; Prud'homme, R. E.; Soum, A.; Fontanille, M., Determination of the geometric structure of substituted polyacetylenes: polymethylacetylene, polypentylacetylene, and poly(tert-butylacetylene). *Journal of Polymer Science Part B: Polymer Physics Edition* **1985**, *23*, 2031-2041.

Lee, W. M., Selection of barrier materials from molecular structure, *Polymer Engineering and Science* **1980**, *20*, 65-69.

Lin, H.; Freeman, B. D., Gas solubility, diffusivity and permeability in poly(ethylene oxide), *Journal of Membrane Science* **2004**, *239*, 105-117.

Lin, H.; van Wagner, E.; Freeman, B. D.; Roman, I., High performance polymer membranes for natural-gas sweetening, *Advanced Materials* **2006**, *18*, 39-44.

Lin, H.; van Wagner, E.; Freeman, B. D.; Toy, L. G.; Gupta, R. P., Plasticization-enhanced hydrogen purification using polymeric membranes, *Science* **2006**, *311*, 639-642.

Lindbrathen, A.; Hagg, M.-B., Glass membranes for purification of aggressive gases: Part II. Adsorption measurements and diffusion coefficient estimations, *Journal of Membrane Science* **2005**, *259*, 154-160.

Litynski, J. T.; Klara, S. M.; McIlvried, H. G.; Srivastava, R. D., An overview of terrestrial sequestration of carbon dioxide: The United States Department of Energy's Fossil Energy R&D Program, *Climatic Change* **2006**, *74*, 81-95.

Liu, L.; Qi, Z.; Zhu, X., Studies on nylon 6/clay nanocomposites by melt-intercalation process, *Journal of Applied Polymer Science* **1998**, *71*, 1133-1138.

Ma, D.; Akpalu, Y. A.; Li, Y.; Siegel, R. W.; Schadler, L. S., Effect of titania nanoparticles on the morphology of low density polyethylene, *Journal of Polymer Science Part B: Polymer Physics* **2005**, *43*, 488-497.

Mackay, M. E.; Dao, T. T.; Tuteja, A.; Ho, D. L.; Van Horn, B.; Kim, H.-C.; Hawker, C. J., Nanoscale effects leading to non-Eistein-like decrease in viscosity, *Nature Materials* **2003**, *2*, 762-766.

Masuda, T.; Isobe, E.; Higashimura, T., Polymerization of 1-(trimethylsilyl)-1-propyne by halides of niobium(V) and tantalum(V) and polymer properties, *Macromolecules* **1985**, *18*, 841-845.

Matteucci, S.; Kusuma, V.; Sanders, D.; Swinnea, S.; Freeman, B. D., Gas transport in TiO_2 nanoparticle filled poly(1-trimethylsilyl-1-propyne), *Journal of Membrane Science* **In Press**.

Matteucci, S.; Raharjo, R.; Kusuma, V. A.; Swinnae, S.; Freeman, B. D., Permeability, solubility and diffusion coefficients in 1,2-polybutadiene containing magnesium oxide, **In Preparation**.

Matteucci, S.; van Wagner, E.; Swinnea, S.; Freeman, B. D.; Sakaguchi, T.; Masuda, T., Desilylation of substituted polyacetylenes in the presence of nanoparticles, *Macromolecules* **2007**, *40*, 3337-3347.

Matteucci, S. T.; Kusuma, V.; Freeman, B. D., Gas transport properties in MgO nanoparticle filled poly(1-trimethylsilyl-1-propyne), **Submitted**.

Matteucci, S. T.; Kusuma, V.; Sanders, D.; Swinnea, S.; Freeman, B. D., Gas transport in TiO_2 nanoparticle filled poly(1-trimethylsilyl-1-propyne), **Submitted**.

Matteucci, S. T.; Yampol'skii, Y. P.; Freeman, B. D.; Pinnau, I. *Transport of gases and vapors in glassy and rubbery polymers*, In Materials Science of Membranes for Gas and Vapor Separations; Yampol'skii, Y. P.; Freeman, B. D.; Pinnau, I., Eds.; John Wiley and Sons: London, 2006; pp 1-48.

McDowell, C. C.; Coker, D. T.; Freeman, B. D., An automated spring balance for kinetic gravimetric sorption of gases and vapors in polymers, *Review of Scientific Instruments* **1998**, *69*, 2510-2513.

Meixner, D. L.; Arthur, D. A.; George, S. M., Kinetics of desorption, adsorption, and surface diffusion of CO_2 on MgO(100), *Surface Science* **1992**, *261*, 141-154.

Mekhemer, G. A. H.; Halaway, S. A.; Mohamed, M. A.; Zaki, M. I., Qualitative and quantitative assessments of acid and base sites exposed on polycrystalline MgO surfaces: Thermogravimetric, calorimetric, and in-situ FTIR spectroscopy study combination, *Journal of Physical Chemistry Part B* **2004**, *108*, 13379-13386.

Merkel, T. C.; Bondar, V.; Nagai, K.; Freeman, B. D., Sorption and transport of hydrocarbon and perfluorocarbon gases in poly(1-trimethylsilyl-1-propyne), *Journal of Polymer Science: Part B: Polymer Physics* **2000**, *38*, 273-296.

Merkel, T. C.; Freeman, B. D.; Spontak, R. J.; He, Z.; Pinnau, I.; Meakin, P.; Hill, A. J., Ultrapermeable, reverse-selective nanocomposite membranes, *Science* **2002**, *296*, 519-522.

Merkel, T. C.; Freeman, B. D.; Spontak, R. J.; He, Z.; Pinnau, I.; Meakin, P.; Hill, A. J., Sorption, transport, and structural evidence for enhanced free volume in poly(4-methyl-2-pentyne)/ fumed silica nanocomposite membranes, *Chemistry of Materials* **2003**, *15*, 109-123.

Merkel, T. C.; He, Z.; Pinnau, I.; Freeman, B. D.; Hill, A. J.; Meakin, P., Effect of nanoparticles on gas sorption and transport in poly(1-trimethylsilyl-1-propyne), *Macromolecules* **2003**, *36*, 6844-6855.

Merkel, T. C.; He, Z.; Pinnau, I.; Freeman, B. D.; Meakin, P.; Hill, A. J., Sorption and transport in poly(2,2-bis(trifluoromethyl)-4,5-difluoro-1,3-dioxole-*co*-tetrafluoroethylene) containing nanoscale fumed silica, *Macromolecules* **2003**, *36*, 8406-8414.

Mezzasalma, S. A., Percolating behavior of solid bimodal (polymethylmethacrylate + inert) particle packings during polymerization, *Journal of Colloid and Interface Science* **1997**, *195*, 51-58.

Michaels, A. S.; Bixler, H. J., Solubility of gases in polyethylene, *Journal of Polymer Science* **1961**, *50*, 393-412.

Minhas, B. S.; Matsura, T.; Sourirajan, S., Formation of asymmetric cellulose acetate membranes for the separation of carbon dioxide-methane gas mixtures, *Industrial and Engineering Chemistry Research* **1987**, *26*, 2344-2348.

Nagai, K.; Masuda, T.; Nakagawa, T.; Freeman, B. D.; Pinnau, I., Poly[1-(trimethylsilyl)-1-propyne] and related polymers: Synthesis, properties and functions, *Progress in Polymer Science* **2001**, *26*, 721-798.

Nagai, K.; Nakagawa, T., Effects of aging on the gas permeability and solubility in poly(1-trimethylsilyl-1-propyne) membranes synthesized with various catalysts, *Journal of Membrane Science* **1995**, *105*, 261-272.

Nagai, K.; Sugawara, A.; Kazama, S.; Freeman, B. D., Effects of physical aging on solubility, diffusivity, and permeability of propane and *n*-butane in poly(4-methyl-2-pentyne), *Journal of Polymer Science Part B: Polymer Physics* **2004**, *42*, 2407-2418.

Naito, Y.; Kamiya, Y.; Terada, K.; Mizoguchi, K.; Wang, J.-S., Pressure dependence of gas permeability in a rubbery polymer, *Journal of Applied Polymer Science* **1996**, *61*, 945-950.

Natta, G., Determination of the polypropylene crystallinity, *Atti della Accademia Nazionale dei Lincei Rendiconti-Classe de Scienze Fisiche-Matematiche and Naturali* **1957**, *22*, 11-17.

Natta, G.; Corradini, P., The structure of crystalline 1,2-polybutadiene and of other "syndiotactic polymers", *Journal of Polymer Science* **1956**, *20*, 251-266.

Niki, A.; Masuda, T.; Higashimura, T., Effects of organometallic cocatalysts on the polymerization of distributed acetylenes by tantalum chloride and niobium clhoride, *Journal of Polymer Science Part A: Polymer Chemistry* **1987**, *25*, 1553-1562.

Obata, Y.; Tosaki, C.; Ikeyama, M., Bulk properties of syndiotactic 1,2-polybutadiene. I. Thermal and viscoelastic properties, *Polymer Journal* **1975**, *7*, 207-216.

O'Brien, K. C.; Koros, W. J.; Barbari, T. A., A new technique for the measurement of multicomponent gas transport through polymeric films, *Journal of Membrane Science* **1986**, *29*, 229-238.

Olkin, I.; Gleser, L., J.; Derman, C. Probability Models and Applications, 2nd ed.; Macmillan College Publishing Company: New York, 1980.

Onishi, H.; Egawa, C.; Aruga, T.; Iwasawa, Y., Adsorption of sodium atoms and oxygen-containing molecules on magnesia(100) and (111) surfaces, *Surface Science* **1987**, *191*, 479.

Osman, M. A.; Atallah, A., interparticle and particle-matrix interactions in polyethylene reinforcement of viscoelasticity, *Polymer* **2005**, *46*, 9476-9488.

Outka, D. A.; Madix, R. J., The oxidation of carbon monoxide on the Au(110) surface, *Surface Science* **1987**, *179*, 351-360.

Pacchioni, G., Physisorbed and chemisorbed CO_2 at surface and step sites of MgO(100) surface, *Surface Science* **1993**, *281*, 207-219.

Pacchioni, G.; Ricart, J. M.; Illas, F., Ab initio cluster model calculations of chemisorption of CO_2 and SO_2 probe molecules on MgO and CaO (100) surfaces. A theorhetical measure of oxide basicity, *Journal of the American Chemical Society* **1994**, *116*, 10152-10158.

Paparazzo, E.; Fanfoni, M.; Severini, E., Studies on the structure of the SiOx/SiO_2 interface, *Applied Surface Science* **1992**, *56-58*, 866-872.

Patel, N. P.; C., M. A.; Spontak, R. J., Highly CO_2-permeable and -selective membranes derived from crosslinked poly(ethylene glycol) and its nanocomposites, *Advanced Functional Materials* **2004**, *15*, 699-707.

Paul, D. R.; Kemp, D. R., Diffusion time lag in polymer membranes containing adsorptive fillers, *Journal of Polymer Science, Polymer Symposia* **1973**, *41*, 79-93.

Pavlov, G. M.; Zaitseva, I. I.; Michailova, N. A.; Rjumtsev, E. I., Molecular characteristic of poly(1-trimethylsilyl-1-propyne) in dilute solutions, *Polymer* **2004**, *45*, 1159-1166.

Paul, D. R.; Yampol'skii, Y. P. *Introduction and Perspective*, In Polymeric Gas Separation Membranes; Paul, D. R.; Yampolskii, Y. P., Eds.; CRC Press: Boca Raton, 1994; pp 1-81.

Peterson, D. R., The determination of crystallinity in polymers, **1957**, The Dow Chemical Company, Research Report SL 87902,

Petropoulos, J. H. *Mechanisms and theories for sorption and diffusion of gases in polymers*, In Polymeric Gas Separation Membranes; Paul, D. R.; Yampol'skii, Y. P., Eds.; CRC Press, Inc.: Boca Raton, 1994; pp 17-82.

Pierce, A. E. Silylation of Organic Compounds; Pierce Chemical Company: Rockford, Illinois, 1968.

Pinnau, I.; Toy, L. G., Transport of organic vapors through poly(1-trimethylsilyl-1-propyne), *Journal of Membrane Science* **1996**, *116*, 199-209.

Powell, C. E.; Qiao, G. G., Polymeric CO_2/N_2 gas separation membranes for the capture of carbon dioxide from power plant flue gases, *Journal of Membrane Science* **2006**, *279*, 1-49.

Qiu, J.; Zheng, J.-M.; Peinemann, K.-V., Gas transport properties in a novel poly(trimethylsilylpropyne) composite membrane with nanosized organic filler trimethylsilylglucose, *Macromolecules* **2006**, *39*, 4093-4100.

Raharjo, R. D.; Lin, H.; Sanders, D. F.; Freeman, B. D.; Kalakkunnath, S.; Kalika, D. S., Relation between network structure and gas transport in crosslinked poly(propylene glycol diacrylate), *Journal of Membrane Science* **2006**, *283*, 253-265.

Raharjo, R. D.; Lee, H. J.; Freeman, B. D.; Sakaguchi, T.; Masuda, T., Pure gas and vapor permeation properties of poly[1-phenyl-2-[p-(trimethylsilyl)phenyl]acetylene] (PTMSDPA) and its desilylated analog, poly[diphenylacetylene] (PDPA), *Polymer* **2005**, *46*, 6316-6324.

Rao, M. B.; Sircar, S., Performance and pore characterization of nanoporous carbon membranes for gas separation, *Journal of Membrane Science* **1996**, *110*, 109-118.

Rasmussen, P. B.; Kazuta, M.; Chorkendorff, I., Synthesis of methanol from a mixture of H_2 and CO_2 on Cu (100), *Surface Science* **1994**, *318*, 267-280.

Ratcliffe, C. T.; Diaz, A.; Nopasit, C.; Munoz, G. In *Laurence Reid Gas Conditioning Conference*: Norman, OK, 1999; pp 118-140.

Reinking, L., Examples of Image Analysis Using ImageJ, *Online:* http://rsweb.nih.gov/ij/docs/pdfs/examples.pdf **2001**, 1-2.

Ren, M.; Chen, Q.; Song, J.; Zhang, H.; Sun, X.; Mo, Z.; Zhang, H.; Zhang, X.; Jiang, L., Crystallization kinetics and melting behaviors of syndiotactic 1,2-polybutadiene, *Journal of Polymer Science Part B: Polymer Physics* **2005**, *43*, 553-561.

Rethwisch, D. G.; Dumesic, J. A., Effect of metal-oxygen bond strength on properties of oxides. 1. Infrared spectroscopy of adsorbed CO and CO_2, *Langmuir* **1986**, *2*, 73-79.

Rittigstein, P.; Torkelson, J. M., Polymer-nanocomposite interfacial interactions in polymer nanocomposites: Confinement effects on glass transition temperature and suppression of physical aging, *Journal of Polymer Science Part B: Polymer Physics* **2006**, *44*, 2935-2943.

Robeson, L. M., Correlation of separation factor versus permeability for polymeric membranes, *Journal of Membrane Science* **1991**, *62*, 165-185.

Rollason, R. J.; Plane, J. M. C., A kinetic study of the reactions of MgO with H_2O, CO_2, and O_2: Implications for magnesium chemistry in the mesosphere, *Physical Chemistry Chemical Physics* **2001**, *3*, 4733-4740.

Sakaguchi, T.; Yumoto, K.; Shiotsuki, M.; Sanda, F.; Yoshikawa, M.; Masuda, T., Synthesis of poly(diphenylacetylene) membranes by desilylation of various precursor polymers and their properties, *Macromolecules* **2005**, *38*, 2704-2709.

Sanders, E. S.; Koros, W. J.; Hopfenberg, H. B.; Stannett, V., Pure and mixed gas sorption of carbon dioxide and ethylene in poly(methyl methacrylate), *Journal of Membrane Science* **1984**, *18*, 53-74.

Sasaki, T.; Sunago, H.; Hoshikawa, T., Multiple melting behavior of syndiotactic 1,2-polybutadiene, *Polymer Engineering and Science* **2003**, *44*, 629-638.

Sengupta, R.; Bandyopadhyay, A.; Sabharwal, S.; Chaki, T. K.; Bhomick, A. K., Polyamide-6,6/in situ silica hybrid nanocomposites by sol-gel technique: synthesis, characterization, and properties, *Polymer* **2005**, *46*, 3343-3354.

Shantarovich, V. P.; Kevdina, I. B.; Yampolskii, Y. P.; Alentiev, A. Y., Positron annihilation lifetimes of high and low free volume glassy polymers: Effects of free volume sizes on the permeability and permselectivity, *Macromolecules* **2000**, *33*, 7453-7466.

Sherrill, A. B.; Barteau, M. A., Oligomerization of trimethylsilyl acetylene to form large molecules on reduced surfaces of TiO_2 (001), *Journal of Molecular Catalysis A: Chemical* **2002**, *184*, 301-310.

Shutov, F. A. *Cellular structures and properties of foamed polymers*, In Handbook of Polymeric Foams and Foam Technology; Klempner, D.; Frisch, K. C., Eds.; Hanser Publishers: New York, 1991; pp 17-46.

Silverstein, R. M.; Webster, F. X. Spectrometric Identification of Organic Compounds, 6th ed.; John Wiley & Sons: New York, 1998.

Sommer, L. H. Stereochemistry, Mechanism, and Silicon; McGraw Hill: New York, 1965.

Sone, T.; Asako, R.; Masuda, T.; Tabata, M.; Wada, T.; Sasabe, H., Polymerization of o-trifluoromethyl(phenylacetylene) initiated by [Rh(norbornadiene)Cl]$_2$ and MoCl$_4$-*n*-Bu$_4$Sn-EtOH catalysts. Formation of order and disorder trans sequences., *Macromolecules* **2001**, *34*, 1586-1592.

Stark, J. V.; Park, D. G.; Lagadic, I.; Klabunde, K. J., Nanoscale metal oxide particles/clusters as chemical reagents. Unique surface chemistry on magnesium oxide as shown by enhanced adsorption of acid gases (sulfur dioxide and carbon dioxide) and pressure dependence, *Chemistry of Materials* **1996**, *8*, 1904-1912.

Staudt-Bickel, C.; Koros, W. J., Improvement of CO_2/CH_4 separation characteristics of polyimides by chemical crosslinking, *Journal of Membrane Science* **1999**, *155*, 145-154.

Stern, S. A.; Gareis, P. J.; Sinclair, T. F.; Mohr, P. H., Performance of a versatile variable-volume permeability cell. Comparison of gas permeability measurements by the variable-volume and variable-pressure methods, *Journal of Applied Polymer Science* **1963**, *7*, 2035-2051.

Stewart, C.; Hessami, M.-A., A study of methods of carbon dioxide capture and sequestration--The sustainability of a photosynthetic bioreactor approach, *Energy Conversion and Management* **2005**, *46*, 403-420.

Takahashi, S.; Goldberg, H. A.; Feeney, C. A.; Karim, D. P.; Farrell, M.; O'Leary, K.; Paul, D. R., Gas barrier properties of butyl rubber/vermiculite nanocomposite coatings, *Polymer* **2006**, *47*, 3083-3093.

Takahashi, S.; Paul, D. R., Gas permeation in poly(ether imide) nanocomposite membranes based on surface-treated silica. Part 1: Without chemical coupling to matrix, *Polymer* **2006**, *47*, 7519-7534.

Tanem, B. S., Sample preparation and AFM analysis of heterophase polypropylene system, *Polymer* **2003**, *44*, 4283-4291.

Tasagaropoulos, G.; Eisenberg, A., Dynamic mechanical study of the factors affecting the two glass transition behavior of filled polymers. Similarities and differences with random ionomers, *Macromolecules* **1995**, *28*, 6067-6077.

Teplyakov, V. V.; Durgaryan, S. G., Correlation analysis of permeation parameters for polymers, *Vysokomolekuliarnye Soedineniia, A* **1984**, *26*, 1498-1505.

Teplyakov, V. V.; Meares, P., Correlation aspects of the selective gas permeabilities of polymeric materials and membranes, *Gas Separation & Purification* **1990**, *4*, 66-73.

Teplyakov, V. V.; Roizard, D.; Farve, E.; Khotimsky, V. S., Investigations on the peculiar permeation properties of volatile organic compounds and permanent gases through PTMSP, *Journal of Membrane Science* **2003**, *220*, 165-175.

Teraguchi, M.; Masuda, T., Poly(diphenylacetylene) membranes with high gas permeability and remarkable chiral memory, *Macromolecules* **2002**, *35*, 1149-1151.

Toy, L. G.; Nagai, K.; Freeman, B. D.; Pinnau, I.; He, Z.; Masuda, T.; Teraguchi, M.; Yampolskii, Y. P., Pure-gas and vapor permeation and sorption properties of poly{1-phenyl-2-[*p*-(trimethylsilyl)phenyl]acetylene] (PTMSDPA), *Macromolecules* **2000**, *22*, 2516-2524.

Tsuchihara, K.; Masuda, T.; Higashimura, T., Polymerization of silicon-containing diphenylacetylenes and high gas permeability of the product polymers, *Macromolecules* **1992**, *25*, 5816-5820.

Utamapanya, S.; Klabunde, K. J.; Schlup, J. R., Nanoscale metal oxide particles/clusters as chemical reagents. Synthesis and properties of ultrahigh surface area magnesium hydroxide and magnesium oxide, *Chemistry of Materials* **1991**, *3*, 175-181.

van der Marck, S. C., Percolation thresholds of the duals of the face-centered-cubic, hexagonal-close-packed, and diamond lattices, *Physical Review E* **1997**, *55*, 6593 LP - 6597.

Visser, T.; Koops, G. H.; Wessling, M., On the subtle balance between competitive sorption and plasticization effects in asymmetric hollow fiber gas separation membranes, *Journal of Membrane Science* **2005**, *252*, 265-277.

von Wroblewski, S., Ueber die natur der absorption der gase durch flussigkeiten unter hohen drucken, *Ann Physik u Chem* **1879**, *8*.

Vu, D. Q.; Koros, W. J.; Miller, S. J., Mixed matrix membranes using carbon molecular sieves II. Modeling permeation behavior, *Journal of Membrane Science* **2003**, *211*, 335-348.

Vu, D. Q.; Koros, W. J.; Miller, S. J., Mixed matrix membranes using carbon molecular sieves I. Preparation and experimental results, *Journal of Membrane Science* **2003**, *211*, 311-334.

Wan, T.; Wang, Y.-C.; Feng, F., Preparation of titanium dioxide/polyacrylate nanocomposites by sol-gel process in reverse micelles and *in situ* photopolymerization, *Journal of Applied Polymer Science* **2006**, *102*, 5105-5112.

Wang, J. A.; Novaro, O.; Bokhimi, X.; Lopez, T.; Gomez, R.; Navarrete, J.; Llanos, M. E.; Lopez-Salinas, E., Structural defects and acidic and basic sites in sol-gel MgO, *Journal of Physical Chemistry B* **1997**, *101*, 7448-7451.

Wang, Z. F.; Wang, B.; Qi, N.; Zhang, H. F.; Zhang, L. Q., Influence of fillers on free volume and gas barrier properties in styrene-butadiene rubber studied by positrons, *Polymer* **2005**, *46*, 719-724.

Weibull, W., A statistical distribution function of wide applicability, *Journal of Applied Mechanics* **1951**, *18*, 293-297.

Weinkauf, D. H.; Paul, D. R. *Effects of structural order on barrier properties*, In Barrier Polymers and Structures; Koros, W. J., Ed.; American Chemical Society: Washington, D.C., 1990; pp 60-91.

Westlinning, H.; Fleischhauer, H. *Properties of White Reinforcing FIllers in Elastomers*, In Reinforcement of Elastomers; Kraus, G., Ed.; John Wiley and Sons: New York, 1965; pp 425-490.

White, L. S.; Blinka, T. A.; Kloczewski, H. A.; Wang, I., Properties of a polyimide gas separation membrane in natural gas streams, *Journal of Membrane Science* **1995**, *103*, 73-82.

Wiederhorn, S.; Fields, R.; Low, S.; Bahng, G.; Wehrstedt, A.; Hahn, J.; Tomota, Y.; Miyata, T.; Lin, H.; Freeman, B. D.; Aihara, S.; Hagihara, Y.; Tagawa, T. *Mechanical Properties*, In Springer-Handbook of Materials Measurement Methods; Czichos, H.; Smith, L. E.; Saito, T., Eds., 2005; pp 283-397.

Wijmans, J. G.; Baker, R. W. *The solution-diffusion model: A unified approach to membrane permeation*, In Materials Science of Membranes for Gas and Vapor Separation; Yampol'skii, Y. P.; Pinnau, I.; Freeman, B. D., Eds.; John Wiley & Sons: Chichester, West Sussex, England, 2006; pp 159-190.

Wind, J. D.; Paul, D. R.; Koros, W. J., Natural gas permeation in polyimide membranes, *Journal of Membrane Science* **2004**, *228*, 227-236.

Xu, M.; Iglesia, E., Readsorption and adsorption-assisted desorption of CO_2 on basic solids, *Journal of Physical Chemistry Pary B* **1998**, *102*, 961-966.

Yang, H.; Bhimaraj, P.; Yang, L.; Siegel, R. W.; Schadler, L. S., Crystal growth in alumina/poly(ethylene terephthalate) nanocomposite films, *Journal of Polymer Science Part B: Polymer Physics* **2007**, *45*, 747-757.

Yang, J.; Lee, C.-H., Adsorption dynamics of a layered bed PSA for H_2 recovery from coke oven gas, *AIChE Journal* **1998**, *44*, 1325-1334.

Yin, D.; Zhang, Y.; Pend, Z.; ZHang, Y., Effect of fillers and additives on the properties of SBR vulcanizates, *Journal of Applied Polymer Science* **2003**, *88*, 775-782.

Yu, Y.; Guo, Q.; Liu, S.; Wang, E., Partial dissociation of water on a MgO(100) film, *Physical Review B* **2003**, *68*, 1-4.

Zecchina, A.; Lofthouse, M. G.; Stone, F. S., Reflectance spectra of surface states in magnesium oxide and calcium oxide, *Journal of the Chemical Society, Faraday Transactions 1: Physical Chemistry in Condensed Phases* **1975**, *71*, 1476-1490.

Zecchina, A.; Stone, F. S., Reflectance spectra of surface states in strontium oxide and barium oxide, *Journal of the Chemical Society, Faraday Transactions 1: Physical Chemistry in Condensed Phases* **1976**, *72*, 2364-2374.

Zimmerman, C. M.; Singh, A.; Koros, W. J., Tailoring mixed matrix composite membranes for gas separations, *Journal of Membrane Science* **1997**, *137*, 145-154.

Vita

Scott Tyson Matteucci, son of Arthur and Sandra Matteucci, was born on October 2, 1976 in Great Falls, Montana. Scott graduated from Great Falls High School in 1995. He earned a Bachelor of Science and Engineering in Chemical Engineering in 1999 from Princeton University, and later that year he began working for Solvay Engineered Polymers as a technical associate in Grand Prairie, Texas. In 2001, Scott was promoted to research engineer at Solvay and worked in that role until 2002. He entered the Graduate School at The University of Texas at Austin in 2002. On March 13, 2004, Scott married Michal Elizabeth Porter, and on December 28, 2006 their daughter, Ondine Magnolia Matteucci was born. Upon graduation with his Ph. D. Scott plans to begin work with The Dow Chemical Company in Midland, Michigan.

Permanent Address:
3440 6th Avenue S.
Great Falls, MT 59401

This dissertation was typed by the author.